Analyse d'images de microscopie 3D : de l'amélioration des images à l'analyse quantitative des tissus artériels

Zeineb Nejim

N° d'ordre NNT: 2022LYSEM016

THÈSE de DOCTORAT DE L'UNIVERSITÉ DE LYON

opérée au sein de

École des Mines de Saint-Étienne

École Doctorale N° 488

(Sciences, Ingénierie, Santé)

Spécialité de doctorat: Sciences des images et des formes

Soutenue publiquement le 01/07/2022, par:

Zeineb Nejim

Analyse d'images de microscopie 3D : de l'amélioration des images à l'analyse quantitative des tissus artériels

—

3D microscopy image analysis: from image enhancement to quantitative analysis of arterial tissues

---

Devant le jury composé de:

CLAUSEL Marianne	Professeure	Université de Laurraine	Présidente et rapporteuse
COURBEBAISSE Guy	Ingénieur de recherche HDR	INSA de Lyon	Rapporteur
FOURNEL Thierry	Professeur	Université Jean Monnet	Examinateur
NAIT SIDI MOH Ahmed	Professeur	Université Jean Monnet	Examinateur
MORIN Claire	Maître-assistante	Mines Saint-Etienne	Examinatrice
NAVARRO Laurent	Maître de recherche	Mines Saint-Etienne	Directeur de thèse

Spécialités doctorales	Responsables :	Spécialités doctorales	Responsables
SCIENCES ET GENIE DES MATERIAUX	K. Wolski Directeur de recherche	MATHEMATIQUES APPLIQUEES	O. Roustant, Maître-assistant
MECANIQUE ET INGENIERIE	S. Drapier, professeur	INFORMATIQUE	O. Boissier, Professeur
GENIE DES PROCEDES	F. Gruy, Maître de recherche	SCIENCES DES IMAGES ET DES FORMES	JC. Pinoli, Professeur
SCIENCES DE LA TERRE	B. Guy, Directeur de recherche	GENIE INDUSTRIEL	N. Absi, Maitre de recherche
SCIENCES ET GENIE DE L'ENVIRONNEMENT	D. Graillot, Directeur de recherche	MICROELECTRONIQUE	Ph. Lalevée, Professeur

EMSE : Enseignants-chercheurs et chercheurs autorisés à diriger des thèses de doctorat (titulaires d'un doctorat d'État ou d'une HDR)

ABSI	Nabil	MR	Génie industriel	CMP
AUGUSTO	Vincent	CR	Image, Vision, Signal	CIS
AVRIL	Stéphane	PR2	Mécanique et ingénierie	CIS
BADEL	Pierre	MA(MDC)	Mécanique et ingénierie	CIS
BALBO	Flavien	PR2	Informatique	FAYOL
BASSEREAU	Jean-François	PR	Sciences et génie des matériaux	SMS
BATTON-HUBERT	Mireille	PR2	Sciences et génie de l'environnement	FAYOL
BEIGBEDER	Michel	MA(MDC)	Informatique	FAYOL
BLAYAC	Sylvain	MA(MDC)	Microélectronique	CMP
BOISSIER	Olivier	PR1	Informatique	FAYOL
BONNEFOY	Olivier	PR	Génie des Procédés	SPIN
BORBELY	Andras	MR(DR2)	Sciences et génie des matériaux	SMS
BOUCHER	Xavier	PR2	Génie Industriel	FAYOL
BRODHAG	Christian	DR	Sciences et génie de l'environnement	FAYOL
BRUCHON	Julien	MA(MDC)	Mécanique et ingénierie	SMS
CAMEIRAO	Ana	MA(MDC)	Génie des Procédés	SPIN
CHRISTIEN	Frédéric	PR	Science et génie des matériaux	SMS
DAUZERE-PERES	Stéphane	PR1	Génie Industriel	CMP
DEBAYLE	Johan	MR	Sciences des Images et des Formes	SPIN
DEGEORGE	Jean-Michel	MA(MDC)	Génie industriel	Fayol
DELAFOSSE	David	PR0	Sciences et génie des matériaux	SMS
DELORME	Xavier	MA(MDC)	Génie industriel	FAYOL
DESRAYAUD	Christophe	PR1	Mécanique et ingénierie	SMS
DJENIZIAN	Thierry	PR	Science et génie des matériaux	CMP
BERGER-DOUCE	Sandrine	PR1	Sciences de gestion	FAYOL
DRAPIER	Sylvain	PR1	Mécanique et ingénierie	SMS
DUTERTRE	Jean-Max	MA(MDC)		CMP
EL MRABET	Nadia	MA(MDC)		CMP
FAUCHEU	Jenny	MA(MDC)	Sciences et génie des matériaux	SMS
FAVERGEON	Loïc	CR	Génie des Procédés	SPIN
FEILLET	Dominique	PR1	Génie Industriel	CMP
FOREST	Valérie	MA(MDC)	Génie des Procédés	CIS
FRACZKIEWICZ	Anna	DR	Sciences et génie des matériaux	SMS
GARCIA	Daniel	MR(DR2)	Sciences de la Terre	SPIN
GAVET	Yann	MA(MDC)	Sciences des Images et des Formes	SPIN
GERINGER	Jean	MA(MDC)	Sciences et génie des matériaux	CIS
GOEURIOT	Dominique	DR	Sciences et génie des matériaux	SMS
GONDRAN	Natacha	MA(MDC)	Sciences et génie de l'environnement	FAYOL
GONZALEZ FELIU	Jesus	MA(MDC)	Sciences économiques	FAYOL
GRAILLOT	Didier	DR	Sciences et génie de l'environnement	SPIN
GROSSEAU	Philippe	DR	Génie des Procédés	SPIN
GRUY	Frédéric	PR1	Génie des Procédés	SPIN
HAN	Woo-Suck	MR	Mécanique et ingénierie	SMS
HERRI	Jean Michel	PR1	Génie des Procédés	SPIN
KERMOUCHE	Guillaume	PR2	Mécanique et Ingénierie	SMS
KLOCKER	Helmut	DR	Sciences et génie des matériaux	SMS
LAFOREST	Valérie	MR(DR2)	Sciences et génie de l'environnement	FAYOL
LERICHE	Rodolphe	CR	Mécanique et ingénierie	FAYOL
MALLIARAS	Georges	PR1	Microélectronique	CMP
MOLIMARD	Jérôme	PR2	Mécanique et ingénierie	CIS
MOUTTE	Jacques	CR	Génie des Procédés	SPIN
NAVARRO	Laurent	CR		CIS
NEUBERT	Gilles			FAYOL
NIKOLOVSKI	Jean-Pierre	Ingénieur de recherche	Mécanique et ingénierie	CMP
NORTIER	Patrice	PR1	Génie des Procédés	SPIN
O CONNOR	Rodney Philip	MA(MDC)	Microélectronique	CMP
PICARD	Gauthier	MA(MDC)	Informatique	FAYOL
PINOLI	Jean Charles	PR0	Sciences des Images et des Formes	SPIN
POURCHEZ	Jérémy	MR	Génie des Procédés	CIS
ROUSSY	Agnès	MA(MDC)	Microélectronique	CMP
ROUSTANT	Olivier	MA(MDC)	Mathématiques appliquées	FAYOL
SANAUR	Sébastien	MA(MDC)	Microélectronique	CMP
SERRIS	Eric	IRD		FAYOL
STOLARZ	Jacques	CR	Sciences et génie des matériaux	SMS
TRIA	Assia	Ingénieur de recherche	Microélectronique	CMP
VALDIVIESO	François	PR2	Sciences et génie des matériaux	SMS
VIRICELLE	Jean Paul	DR	Génie des Procédés	SPIN
WOLSKI	Krzystof	DR	Sciences et génie des matériaux	SMS
XIE	Xiaolan	PR0	Génie industriel	CIS
YUGMA	Gallian	CR	Génie industriel	CMP

Mise à jour : 30/08/2018

3D microscopy image analysis: from image enhancement to quantitative analysis of arterial tissues

Zeineb Nejim

01/07/2022

Abstract

Abstract

The human body is a complex structure composed of multiple cells, organs and tissues. The cardiovascular system is responsible of transferring nutrients and oxygen to all the body and the aorta plays an essential role. The upper portion of the aorta, called ascending thoracic aorta, is a critical section since it has to support the high pressure blood pumped by the heart. This is made possible thanks to the micro-structure of the aortic wall, mainly composed of fibers (collagen and elastin). With aging, changes may occur on the aortic micro-structure and may cause some diseases such as aneurysms. Studying this microstructure is helpful to understand its functions. To this end, several imaging modalities were used in the literature especially the multi-photon microscopy and Second Harmonic Generation (SHG) because of its good resolution in 3D. However, SHG images may present some artifacts such as noise in addition to some discontinuities on certain fibers. The study of this micro-structure is based on the quantitative analysis of acquired 3D images in order to extract information related to the geometry and the morphology of collagen fibers as well as the composition of the considered specimen.

The goal of this thesis is, in the first place, to enhance 3D second harmonic generated images of collagen fibers in order to make them more suited for a potential quantitative analysis. To this end, a combination of a 3D directional filter (to deal with fibers discontinuities) and a 1D and a 3D top-hat transforms (to reduce the noise) is proposed. The second part of this thesis is focused on the quantitative analysis of these images and in particular, orientations' estimation of collagen fibers in the 3D space. A new approach based on deep learning is introduced. A dataset of 3D images of synthetic fibers is developed to ensure the learning phase of the proposed neural network.

Résumé

Le corps humain est une structure complexe composée de plusieurs cellules, tissus et organes. Le système cardiovasculaire est responsable du transfert de l'oxygène et des nutriments vers tout le corps et l'aorte y joue un rôle essentiel. La portion supérieure de l'aorte, appelée aorte thoracique ascendante, est assez critique puisqu'elle doit supporter la pression élevée du sang pompé par le cœur. Ceci est possible grâce

à la micro-structure de l'aorte qui est principalement composée de fibres (collagène et élastine). Cependant, avec le vieillissement, des changements peuvent toucher cette micro-structure et causer des pathologies comme les anévrismes. L'étude de cette micro-structure est nécessaire pour comprendre ses fonctions. Ceci est possible grâce à plusieurs modalités d'imagerie notamment la microscopie à deux photons et la génération de seconde harmonique puisqu'elle offre une bonne résolution en 3D. Cependant, les images collectées peuvent présenter plusieurs artéfacts comme du bruit et des discontinuités au niveau de quelques fibres. L'étude de cette micro-structure est basée sur l'analyse quantitative des images acquises afin d'extraire des informations relatives à la géométrie et la morphologie des fibres ainsi que la composition du spécimen considéré.

Cette thèse a pour objectif, en premier lieu, d'améliorer des images 3D de seconde harmonique de fibres de collagène afin de les rendre exploitables pour une éventuelle analyse quantitative. Pour se faire, une combinaison d'un filtre directionnel 3D (pour remédier au problème de discontinuité) et de transformées "top-hat" à une et trois dimensions (pour réduire le bruit) est proposée. En second lieu, l'intérêt est porté sur l'analyse quantitative de ces images et en particulier l'estimation de l'orientation des fibres de collagène dans l'espace 3D. Une nouvelle approche basée sur l'apprentissage profond est présentée. Une base de données contenant des images 3D de fibres synthétiques est développée pour assurer la phase d'apprentissage du réseau de neurones proposé.

Dedication

To my grandfathers

Acknowledgments

My PhD, a life-changing experience, is comming to an end. I would like to start thank Mrs. Marianne Clausel and M. Guy Courbebaisse for accepting to review my manuscript in such a short notice. I would also want to express my grattitude to M. Thierry Fournel and M. Ahmed Nait Sidi Moh for accepting to by part of my jury. This project would not have been possible without the support of many people. I would like to extend my sincere thanks to my adviser, Laurent Navarro, who was always available for any question or needed guidance through out the entire period I spent on this work. I would also like to thank Claire Morin for all the help with manuscript revisions and for accepting to join my PhD commitee. Besides, I special thank goes to Pierre Badel, who also was one of my advisers at a certain time, for all his comments and advices.

I am also grateful for all the good moments I shared in the CIS. I would like to thank Françoise, Amélie, Nathalie H. and Marlène for their help and support for the administrative part. I want also to thank Jérôme, Woo-suck, Baptiste Pierrat, Stéphane, Miquel, Vincent and Raksmey for their availability and advices. I could not have undertaken this journey without the best office-mate of all times: Laure! Thanks for your good mood and for all the loughs that we shared. I am extremely grateful for all the great friends I met during the last 3 years: Asma the fellow Tunisian, Mohamed always available for a chat, Solmaz my office-mate for 3 days, Jay the bravest person ever, Danielle the astronomy lover, Brooks my lunch partner before covid, Bastien the runner, Jules always ready to help, Chen the nice guy, Cristina the owner of SHG images. Thanks to every single person who made this experience as delightful as possible: Romain, Afaf, Joan, Rada, Daniele, Ozge, Cyriac, Nilson, Hugo, Omar, Habib, Long, Baptiste, Joseph, Aïcha and Ali. I hope I did not forget anybody.

Finally, I am grateful for my family's unconditional, unequivocal, and loving support. Thank you for believing in me and for your eternal encouragement.

Contents

List of figures

List of tables

Acronyms

1D: one dimension
2D: two dimensions
3D: three dimensions
ATA: Ascending Thoracic Aorta
ATAA: Ascending Thoracic Aortic Aneurysms
BN: Batch Normalization
CCD: Charge Coupled Device
CLAHE: Contrast Limited Adaptive Histogram Equalization
CNN: Convolutional Neural Networks
Conv: Convolution
CT-scan: Computed Tomography scan
DFT: Discrete Fourier Transform
DWT: Discrete Wavelet Transform
ECM: Extra-Cellular Matrix
FC: Fully Connected
FFM: Fast Marching Method
FFT: Fast Fourier Transform
FNN: Feed-forward Neural Network
FOS: First-Order Statistics
FT: Fourier Transform
FWHM: Full-Width at Half-Maximum
GCA: Giant Cell Arteritis
GLCM: Gray Level Co-occurrence Matrix
GPU: Graphics Processing Unit
HT : Hough Transform
K-NN: K-Nearest Neighbors
LSCM: Laser Scanning Confocal Microscope
MLU: Medial Lamellar Units
MR: Magnetic Resonance
MSLE: Mean Squared Logarithmic Error
NA: Numerical Aperture
NLO: Non-Linear Optical
OCT: Optical Coherence Tomography

OPD: Optical Path Difference
PBS: Phosphate Buffer Saline
PCA: Principal Component Analysis
PSF: Point Spread Function
PVC: PolyVinyl Chloride
QI: Quasi-Instantaneous
ReLU: Rectified Linear Unit
RNN: Recurrent Neural Networks
ROI: Region Of Interest
RT : Radon Transform
SE: Structuring Element
SEM: Scanning Electron Microscopy
SHG: Second Harmonic Generation
SNN: Spiking Neural Networks
SOS: Second-Order Statistics
TBF: Two-Photon Fluorescence
VSMC: Vascular Smooth Muscle Cells
WT: Wavelet Transform
WTH: White Top-Hat
XRCT: X-rays Computed Tomography

Introduction

The human body is a highly complex structure which is composed of cells, tissues and organs. This structure can be divided into different systems where each one of them is responsible of one function. Among these system, there is the circulatory or cardiovascular system which ensures the circulation of the blood from the heart to the rest of the body and the reverse path through a network of blood vessels. The occurrence of any pathology along this system can be very serious and may even lead to death. These pathologies are referred to as cardiovascular diseases. One complex and dangerous cardiovascular disease is the ascending aortic thoracic aneurysm. It corresponds to a bulge in the ascending part of the aorta, the largest artery of the human body. This condition can grow over time because of the weakening of the aortic wall. Several risk factors are linked to aortic aneurysms, one can site smoking, atherosclerosis, hypertension and drug abuse. Ascending thoracic aortic aneurysms raised the interest of the bio-mechanical community because of the fact that researchers can recover the damaged tissue from patients who had surgery to remove the aneurysm since this pathology exposes the patient to some risks such as the rupture and the dissection. The dissection corresponds to a tear in the inner layer of the aorta which may prevent blood from reaching vital organs while the rupture consists in a sudden burst of the aortic wall. In both cases, the probability that the patient dies is very high and unfortunately, no significant symptoms are experienced by the patient. Thus, it is complicated to diagnose the condition medically.

In order to prevent the aorta in general and the ascending aorta in particular from aneurysms, it is interesting to study its micro-structure and especially collagen fibers since they are responsible of the mechanical resistance of the aorta. Early studies conducted on this protein led to the characterization at the microscopic scale (around 30 μm) of many tissues composed essentially of collagen by the mean of histology. This technique consists in studying the microscopic structure of biological tissues and the relations between individual elements [LAS15]. It involves a chemically destructive process which can only be performed on *ex vivo* samples where a slicing step is needed which prevents from three dimensional observations. The process can also have an impact on the micro-structure of the considered specimen. For example, a freezing process of the tissue is used for visualization purposes, which may destroy some of its components. Its use remains, however, a standard for pathology diagnoses in clinics. Hence, the study of the micro-structure evolution of a biological system

ex vivo under a mechanical load is impossible with histology. In order to deal with this issue, new imaging techniques have been tested and proved their efficiency. Among those imaging modalities, one can cite first Scanning Electron Microscopy (SEM) [Pra+03 ; OKH82]. It allows obtaining images with a resolution of $1-20$ nm but it lacks in-depth signal: only the peripheral surface can be imaged accurately. As a remedy, other techniques would ideally ensure a precise quantification of the collagen fibers within the volume of the material as oriented structures in space in an adapted scale ($1-100$ μm). For instance, X-rays Computed Tomography (XRCT) and X-rays micro-tomography are well suited for quantifying collagen's network because they allow capturing their micro-structure through larger fields of view (up to 1.7mm x 1.7mm) as compared to other microscopy techniques [Wal+15 ; Bai+18 ; Dis+17]. In addition, it offers a resolution of $20-100$ μm, though a compromise between resolution and field of view must be made. However, the addition of X-ray contrast agents may change the behavior of the specimen components, restraining their use. Optical Coherence Tomography (OCT) [Fuj+00] has been used as an alternative [Bab+14 ; Ugr+09]. Just like XRCT, OCT provides a resolution of $1-15$ μm but it does not allow to capture individual components of a specimen. This makes quantitative analysis hard to achieve such as for aortic ostial lesions where it is not possible to clear the blood at the entrance to neighboring arteries. It is dependent on the considered biological tissue scattering and absorption. Yet, it is possible to use optical clearing agents to reduce light scattering but it can have an impact on the tissue structure. Recently, a strong interest was shown toward fluorescence microscopy, which requires the use of stains, but has limited physico-chemical modification of biological tissues. For instance, confocal microscopy was often used [Wu+03 ; Ste+08] because of its resolution of around 160 nm and its capability to capture images through the specimen depth. Later, the emergence of powerful lasers enabled multi-photon microscopy. This imaging technique, with [Pol+13 ; Che+12 ; Yeh+02] or without polarizer [Cav+17 ; APB19], does not harm the sample because it is less exposed to the laser. It offers a scale for representation of the order of a microometer and a resolution up to $150-200$ nm. Besides, it allows imaging deeper into the sample and thus collecting more images in the depth (up to 500 μm [YLP14]). Additionally, collagen fibers react to multi-photon laser by generating second harmonics across the spectral region between 400 and 500 nm [The+06]. This property, called Second Harmonic Generation (SHG) is an asset to capture images of collagen fiber only, as this signal is specific and can be separated from other signals.

The cited imaging modalities introduced some improvement on how to capture sufficiently good images to extract information related to the structure and the function of collagen fibers. Studying the organization of the collagen fibers is of interest in biomedical research since it allows diagnosing fibrosis [Cam11 ; Str+07] or analyzing their interaction with cancerous cells [Bre+14]. Moreover, in [Bro+03], the authors tried to quantify the dynamics of collagen modification in tumors *in vivo* after pharmacologic intervention. Besides, other researchers focused on the quantification of fiber orientation in order to study structure-to-function relationships such as in pressurized vessels [APB19 ; Cav+17 ; Sch+13], or waviness and density in

order to identify the impact of sample aging [SM17 ; Wu+16]. However, this type of quantification is complicated and requires dedicated methods. To-date, the conducted research in this field succeeded in characterizing collagen structures only in 2D planes although those tissues are three-dimensional.

Keeping all the above in mind, this thesis is directed to investigate the following hypothesis:

Research hypothesis: The collagen fibers network extracted in three dimensions from SHG stacks is a better and more accurate alternative to determine its geometry in the space.

The hypothesis was tested through realising the following research objectives:

— Considering the collagen network as a three dimensional volume.

— Improving SHG stacks of collagen fibers using three dimensional image processing techniques

— Evaluating collagen fibers orientations in the three dimensional space using deep learning

— Validating the proposed approach by comparing it with other techniques from the literature

In addressing the previously mentioned objectives, this thesis is divided into 5 chapters, outlined in the following manner. All the chapters are reported essentially in English along with a short abstract at the beginning written in French.

— Chapter 1 explores the medical and technical context on which the study is based. A detailed review of the relevant collagen fibers imaging modalities in addition to commonly used image improvement techniques is presented.

— Chapter 2 explores the development a new approach to improve the SHG stacks based on combination of three dimensional image processing techniques.

— Chapter 3 explores the existent approaches to extract quantitative information from SHG images in addition to the different quantitative information that raises the interest of researchers in general. A detailed review of these two aspects is reported.

— Chapter 4 presents a new approach based on deep learning to estimate collagen fibers orientations in the three dimensional space. For this matter, a synthetic dataset of three dimensional images of fibers was developed.

— Chapter 5 presents a comparison of the proposed deep learning approach with some existing methods.

— Finally a detailed description of the main findings, limitations, and future prospects is reported.

The project was carried out at CIS (Centre Ingénierie et Santé), in particular the STBio (soft tissue biomechanics) group; which is an integral part of the university École Nationale Supérieure des Mines de Saint-Étienne.

Introduction

Le corps humain est une structure très complexe qui est composée de cellules, tissus et organes. Cette structure peut être divisée en différents systèmes où chacun est responsable d'une certaine fonction. Parmi ces systèmes, il y a le système cardiovasculaire qui assure la circulation du sang du cœur au reste du corps et le trajet inverse. Ce système est composé d'un réseau de vaisseaux sanguins (artères et veines). L'apparition d'une pathologie le long de ce réseau peut être grave et peut même causer la mort du patient. Ces maladies, dont fait partie l'anévrisme de l'aorte thoracique ascendante, sont appelées maladies cardio-vasculaires. Il s'agit d'une dilatation de la portion ascendante de l'aorte qui est la plus large artère du corps humain. Cette pathologie peut s'aggraver au cours du temps à cause de l'affaiblissement de la paroi aortique. Plusieurs facteurs de risque sont liés à l'anévrisme aortique en général comme le tabac, l'athérosclérose, l'hypertension et l'abus de drogue. L'anévrisme de l'aorte thoracique ascendante a suscité l'intérêt de la communauté biomécanique puisqu'il est possible de prélever la partie endommagée de l'aorte des patients qui subissent une intervention chirurgicale pour enlever l'anévrisme en question. Cette intervention est nécessaire pour prévenir des risques de complications comme la dissection et la rupture de l'aorte. La dissection correspond à une déchirure au niveau de la couche interne de l'aorte qui peut empêcher le sang d'atteindre les organes vitaux. Quant à la rupture, elle consiste en un brusque éclatement de la paroi aortique. Dans les deux cas, la probabilité que le patient décède est très élevée. Malheureusement, l'anévrisme de l'aorte n'est accompagné d'aucun symptôme significatif, ce qui rend son diagnostic compliqué.

Afin de prévenir les anévrismes de l'aorte en général et plus particulièrement celui de l'aorte thoracique ascendante, il est intéressant d'étudier sa micro-structure et en particulier les fibres de collagène car elles sont responsables de la résistance mécanique de l'aorte. Les premières études portées sur cette protéine ont permis, en utilisant l'histologie, de caractériser plusieurs tissus biologiques composés principalement de fibres de collagène à une échelle microscopique (autour de 30 μm). Cette technique permet d'étudier la structure microscopique des tissus biologiques et les relations entre les différents éléments [LAS15]. Elle n'est appliquée que sur une tranche de l'échantillon ce qui ne permet pas une observation en trois dimensions. Elle nécessite un processus chimique destructif qui peut être appliqué à des échantillons *ex vivo* uniquement et peut avoir un impact sur la micro-structure. Par

exemple, l'échantillon peut être gelé pour permettre une bonne visualisation mais ce processus peut nuire à la micro-structure. Malgré ses inconvénients, l'histologie reste une méthode de référence pour le diagnostic des pathologies de l'aorte. Cependant, il est impossible d'étudier l'évolution de la micro-structure d'un tissu biologique *ex vivo* quand il est soumis à une charge mécanique en utilisant l'histologie. Pour remédier à ce problème, plusieurs techniques d'imagerie ont été testées et ont prouvé leur efficacité. Parmi ces techniques, on peut, tout d'abord, citer la microscopie électronique à balayage [Pra+03 ; OKH82]. Ce type de microscopie permet d'obtenir des images avec une résolution de $1 - 20$ nm mais seulement la surface périphérique peut être observée. D'autres modalités d'imagerie ont permis d'acquérir des images à trois dimensions pour une quantification fine des fibres de collagène contenues dans un certain volume à une échelle adaptée (autour de $1 - 100$ μm). Par exemple, la tomodensitométrie à rayons X est adéquate pour quantifier le réseau de collagène puisqu'elle permet de capturer sa structure à travers un champ de vision (jusqu'à 1.7mm x 1.7mm) plus large que pour d'autres types d'imagerie [Wal+15 ; Bai+18 ; Dis+17]. De plus, elle offre une résolution de $20 - 100$ μm, mais un compromis entre la résolution et le champ de vision doit être fait. D'autre part, la tomodensitométrie à rayons X nécessite l'injection d'un agent de contraste dans l'échantillon à étudier ce qui peut changer son comportement et restreindre son utilisation. La tomographie par cohérence optique [Fuj+00] a été utilisée comme une alternative [Bab+14 ; Ugr+09]. Tout comme la tomodensitométrie à rayons X, la tomographie par cohérence optique offre une résolution de $1 - 15$ μm mais ne permet pas la capture des composants individuels du spécimen. Ceci rend l'analyse quantitative difficile à effectuer comme pour les lésions ostiales aortiques où il est impossible de distinguer le sang à l'entrée des artères voisines. L'efficacité de cette méthode dépend de la diffusion et de l'absorption du tissu biologique à étudier. Il est possible d'utiliser un éclaircissant optique pour réduire la diffusion de la lumière mais il peut impacter la structure du spécimen. Récemment, la microscopie à fluorescence qui, certes, exige l'utilisation d'un agent de coloration, est devenue une référence pour l'étude de la micro-structure des tissus biologiques puisque les colorants utilisés ne causent que peu de modification physico-chimique de la micro-structure. Par exemple, la microscopie confocale a souvent été utilisée [Wu+03 ; Ste+08] puisqu'elle offre une résolution de 160 nm et permet d'acquérir des images en profondeur. Plus tard, avec l'émergence des lasers puissants notamment les lasers femto-secondes, la microscopie multiphotonique a vu le jour. Cette technique d'imagerie, avec [Pol+13 ; Che+12 ; Yeh+02] ou sans polariseur [Cav+17 ; APB19], limite la détérioration de l'échantillon puisqu'il est exposé moins longtemps au laser. Cette modalité d'imagerie offre une échelle de représentation de l'ordre du micromètre et une résolution qui peut atteindre $150 - 200$ nm. De plus, elle permet d'acquérir des images encore plus en profondeur (jusqu'à 500 μm [YLP14]). D'autre part, les fibres de collagène réagissent au laser femto-seconde en générant de secondes harmoniques dans la région spectrale située entre 400 et 500 nm [The+06]. Cette propriété est un atout qui permet d'acquérir des images contenant uniquement les fibres de collagène puisque le signal de seconde harmonique généré peut être séparé des autres signaux.

Les modalités d'imagerie citées précédemment ont permis d'acquérir de meilleures

images des fibres de collagène afin d'extraire des informations fiables concernant ces fibres. Un intérêt majeur est porté sur l'étude de l'organisation des fibres de collagène puisqu'elle permet de diagnostiquer les fibroses [Cam11 ; Str+07] et d'analyser l'interaction des fibres avec les cellules cancéreuses [Bre+14]. De plus, dans [Bro+03] par exemple, les auteurs ont tenté de quantifier la dynamique des modifications au niveau des fibres de collagène dans les tumeurs *in vivo* après une intervention pharmacologique. Par ailleurs, d'autres recherches ont porté sur la quantification des orientations des fibres afin d'étudier leur relation structure-fonction comme par exemple au niveau de vaisseaux sous pression [APB19 ; Cav+17 ; Sch+13] ou pour étudier l'ondulation des fibres afin d'identifier son impact sur le vieillissement du spécimen considéré [SM17 ; Wu+16]. Cependant, cette quantification nécessite des méthodes dédiées qui peuvent être assez complexes. A ce jour, les recherches menées dans ce domaine ont réussi à caractériser les fibres de collagène principalement en deux dimensions malgré leur structure tridimensionnelle.

En gardant ces éléments à l'esprit, cette thèse vise à étudier l'hypothèse suivante:

Hypothèse de recherche: Le réseau de fibres de collagène étant une structure tridimensionnelle, l'étude de l'orientation de ces fibres doit se faire en trois dimensions afin de mieux les caractériser.

L'hypothèse a été testée en réalisant les objectifs de recherche suivants :

— Considérer le réseau de collagène comme un volume tridimensionnel.

— Améliorer les images de seconde harmonique tridimensionnelles des fibres de collagène en utilisant des techniques de traitement d'images en trois dimensions.

— Évaluer les orientations des fibres de collagène dans l'espace tridimensionnel en utilisant l'apprentissage profond.

— Valider l'approche proposée en la comparant à d'autres méthodes de la littérature.

En abordant les objectifs ci-dessus, cette thèse se divise en 5 chapitres, répartis de la manière suivante. Tous les chapitres sont rédigés en anglais et sont accompagnés d'un succinct résumé en français au début.

— Le chapitre 1 explore le contexte médical et technique sur lequel cette étude est basée. Une revue détaillée des modalités d'imagerie utilisées pour l'acquisition d'images de collagène ainsi que les méthodes les plus communes d'amélioration de ces images est présentée.

— Le chapitre 2 explore le développement d'une nouvelle approche pour améliorer les images de seconde harmonique de fibres de collagène basée sur une combinaison de plusieurs techniques de traitement d'images tridimensionnelles.

— Le chapitre 3 examine les approches existantes d'extraction d'informations quantitatives à partir d'images de seconde harmonique ainsi que les différentes métriques qui on suscité un intérêt majeur au sein de la communauté scientifique. Une revue détaillée de ces deux aspects est présentée.

— Le chapitre 4 présente une nouvelle approche basée sur l'apprentissage profond visant à estimer les orientations des fibres de collagène dans l'espace tridimen-

sionnel. A cette fin, un jeu de données d'images synthétiques contenant des fibres a été développé.

— Le chapitre 5 présente une comparaison de l'approche basée sur l'apprentissage profond présentée dans le chapitre 4 avec quelques méthodes de la littérature.

— Finalement, une description détaillée des principaux résultats, des limites ainsi que des perspectives est rapportée.

Le projet a été réalisé au Centre Ingénierie et Santé (CIS), en particulier au sein du groupe STBio (biomécanique des tissus mous), qui fait partie de l'École Nationale Supérieure des Mines de Saint Étienne.

Chapter I

State of the Art

Contents of the chapter

I.1 Résumé du chapitre

La circulation sanguine est un phénomène complexe qui est assuré par un réseau de vaisseaux. Le cœur permet de pomper le sang vers le reste du corps à travers l'aorte. Une portion critique de l'aorte correspond à sa partie ascendante qui se trouve directement après la valve aortique qui reçoit le flux puissant de l'éjection systolique. Par conséquent, cette portion peut être sujette à différentes maladies comme les anévrismes. Pour comprendre les mécanismes et le comportement du tissu aortique, il faut analyser sa micro-structure en particulier les fibres de collagène. Pour se faire, plusieurs techniques d'imagerie ont été utilisées notamment la microscopie de seconde harmonique. Dans cet état de l'art, une description de l'anatomie et de la physio-pathologie du système cardiovasculaire humain est présentée. De plus, une revue des principales technique d'imagerie utilisée dans l'acquisition d'images de fibres de collagène est introduite ainsi que quelques unes des méthodes de traitement d'images les plus implémentées pour l'amélioration des images de seconde harmonique.

I.2 Abstract of the chapter

Blood circulation in the human body is a complex event which is ensured by a network of vessels. The heart pumps the blood and the aorta transfer it to the rest of the body. A critical part of the aorta is the ascending thoracic one since it receives a powerful blood flux of the systolic ejection. Thus, it can be subject to several diseases such as aneurysms. In order to understand the mechanics of the aortic tissue and its behaviour, it is important to analyze its micro-structure, in particular, collagen fibers. For this matter, several imaging modalities have been used such as Second Harmonic Generation (SHG) microscopy. In this state-of the art, a report of the anatomy and physio-pathology of the human cardiovascular system is proposed. Besides, a review of the main imaging modalities used to acquire collagen fibers images is introduced as well as some of the main image processing techniques used to improve SHG images.

I.3 Introduction

The human body is a complex system where the heart pumps oxygen and nutrient rich blood to the rest of the body. This function is ensured by the circulatory system and primarily by the aorta. This artery is composed of three layers namely the intima, the media and the adventitia. The aorta is a large elastic artery which mechanical function are really important to a proper functioning of the organism and its physiological and mechanical functions are ensured by its micro-structure. This micro-structure is composed of collagen, elastin and smooth muscle cells. The aorta, as any other vessel, can suffer from different pathologies among which one can cite aneurysms and in particular, the ascending thoracic aortic aneurysm located in the ascending part of the aorta. This condition, if not treated on time, can cause the patient's death.

The analysis of the aortic micro-structure aroused great interest in the bio-mechanical community. Researchers showed that this micro-structure is mainly composed of elastic and collagen fibers and smooth muscle cells. Collagen plays an important role in holding the aorta together. Besides, many imaging modalities were used to capture the essence of aortic micro-structure anatomy and behaviour. The most promising one is the two-photon microscopy and second harmonic generation. This technique allows us to collect 3D images of collagen fibers. However, these images have some artifacts (blur, noise, discontinuities in the fibers, etc.).

In this chapter, a brief introduction on the anatomy, physiology and composition of the aorta is provided. Next, an overview of the different diseases that may affect the aorta will be exposed with a special focus on ascending thoracic aortic aneurysm which is in the center of the present thesis. Then, an overview of the different imaging modalities that were used in the literature to capture the aortic micro-structure is introduced. Finally, a review of the main image processing techniques implemented in the literature to improve second harmonic generated images is reported.

I.4 Anatomy and physio-pathology of the human cardiovascular system

The human cardiovascular system, also called vascular or circulatory system, is the system of the human body that allows the transportation of oxygen, hormones, carbon dioxide, nutrients and blood cells through blood to and from cells. This operation helps in stabilizing temperature and pH, maintaining homeostasis and fighting diseases. It keeps blood (between 4 and 6 L) in continuous motion: the blood's total volume performs a cycle from and to the heart in around one minute on average for a healthy man [Ste99].

I.4.1 Anatomy of the human cardiovascular system

The human cardiovascular system is a closed system composed of the heart, the blood and blood vessels. It aims, through blood, to carry nutrients and oxygen to

the body organs and remove carbon dioxide and other wastes.

I.4.1.1 Overview

The heart, which is the pump of the human body, is a cone-shaped muscular organ. Its main function consists in keeping blood circulating through the cardiovascular system. It can be found in the mediastinum which is the thoracic cavity between the lungs. Its size is around 9 cm wide and 14 cm long for an average adult which is similar to the size of a fist [AFM17]. Four chambers composes the heart: two thin-walled atria and two thick-walled ventricles, figure I.1. During the cardiac cycle, the right atrium receives blood poor in oxygen from the entire body through the major veins: the superior vena cava and the inferior vena cava. This blood passes to the right ventricle through the tricuspid valve. Once it is full, the ventricle contracts and pumps the blood toward the lungs for reoxygenation. The left atrium receives oxygen-rich blood from the pulmonary veins and sends it to the left ventricle through the bicuspid valve. The cycle ends when the left ventricle pumps the blood into the aorta, [Mad02]. The cardiac cycle can be divided into two main phases: the diastole phase when the blood flows to the atria and the systole phase when the blood leaves the ventricles.

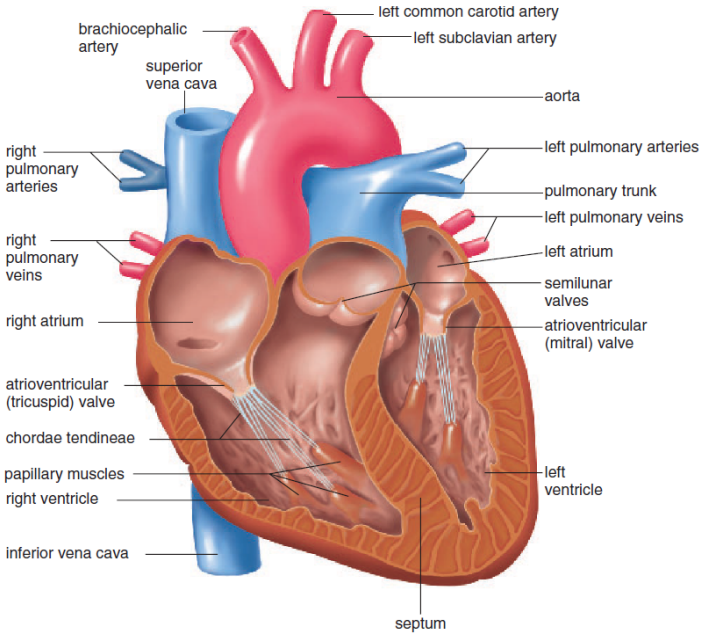

FIGURE I.1 – The heart's internal view, [Mad02]

The vessels are tube-like structures that form a closed system which carries blood to and from the heart. Their size decreases as they move away from the heart. Blood is transported through vessels under high pressure which imply that vessels walls need to be strong and elastic. They can be categorized into veins and arteries (figure I.2, [FRW17]).

Arteries (respectively veins) give rise to even smaller arteries (respectively veins), also called arterioles (respectively venule), figure I.3, [Van02]. This transition is gradual through a progressive thinning of the vessel wall and the decrease of the

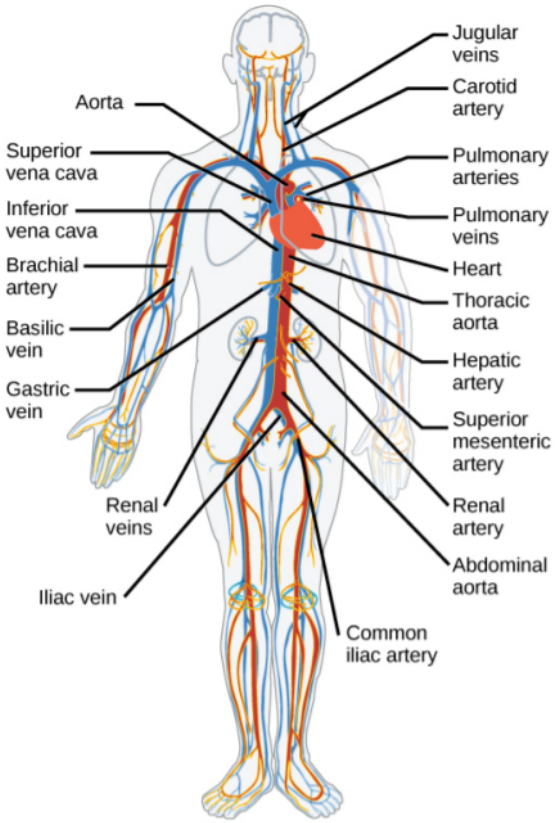

FIGURE I.2 – Vascular system: arteries in red and veins in blue

lumen's size (the size of the inside space of the vessel). Arterioles carry blood to microscopic vessels known as capillaries which ensure not only the nourishment and the oxygenation of tissues, but also the elimination of the carbon dioxide and wastes by sending them through venules and then veins [RB11].

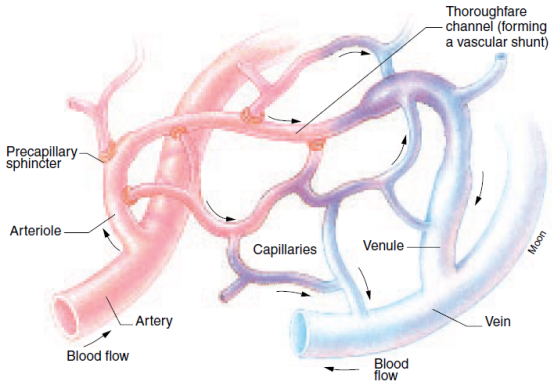

FIGURE I.3 – Micro-circulation at the capillary level

I.4.1.2 Arterial system

The arterial system is composed of two kinds of arteries: pulmonary arteries and systemic arteries. The pulmonary arteries are low-presser arteries that carry blood poor in oxygen from the heart to the lungs. On the other hand, systemic arteries carry blood rich in oxygen, under high pressure, from the heart to the rest of the

body. The pulse that can be felt over an artery close to the skin, is generated by the expansion and contraction of the arterial tissue when the heart pushes blood into arteries through the aorta [RB11]. Systemic arteries can be divided into elastic and muscular arteries depending on their relative composition of elastic and muscle tissue. Typically, large arteries are elastic arteries and small arteries are muscular arteries. Small arteries and arterioles can be seen as valves allowing to carry blood to capillaries. Their strong muscular wall is capable of expanding to many times its diameter and also closing the path to blood in order to control the blood flow to the capillaries.

I.4.1.3 Aorta

The aorta is the largest systemic artery in the human body. It supplies the body with oxygen-rich blood. It also allows to maintain the blood pressure thanks to its elasticity. The aorta will be in the center of our research.

I.4.1.3.a Anatomy

The aorta arises from the heart's left ventricle upward and then loops 180 degrees to continue its path toward the diaphragm and then to the rest of the body. In the connection between the aorta and the left ventricle, there is a three-part valve which prevent the blood from going back to the heart. The aorta is not only the largest artery but also the thickest one. In fact, its length is around 30 to 40 cm, its average diameter is around 3 cm [Ita+02] with a thickness of 2 to 3 mm [Erb01]. Thus, the aorta can be divided into 3 regions: the Ascending Thoracic Aorta (ATA), the aortic arch and the descending aorta, figure I.4 [KKA21].

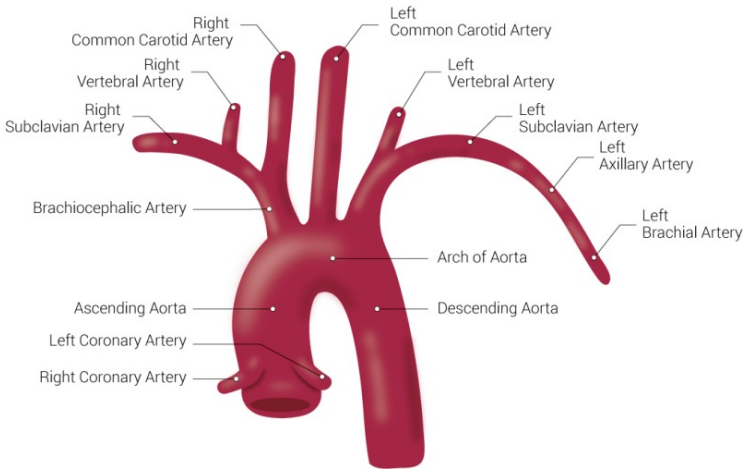

FIGURE I.4 – Regions of the aorta

The ATA, sizing between 5 cm and 7 cm [Dag11], is enveloped in a pericardial sheath and twisted around the pulmonary trunk. Its average diameter is estimated to be 3.3 cm but varies with respect to some personal characteristics such as the sex, the age and the mass index. An exhaustive description of the diameter variation in the ascending aorta is reported by Goldfinger et al. [Gol+14]. It can be divided into two sections namely the aortic root and the tubular ascending aorta. The first section

starts from the aortic annulus and ends with sinotubular junction. It contains the aortic annulus, the aortic valve, the Valsalva sinuses and the begining of the coronary arteries. The normal average diameter of the sinotubular junction represents usually 85% of the aortic annulus diameter. Regarding the second section, it extends to the inferior boarder of the left sternocostal junction. There are no branches arising from this part of the aorta.

The aortic arch is positioned above the bifurcation of the pulmonary trunk, the left pulmonary artery, the left main bronchus and some nerves. It starts when the ascending aorta leaves the pericardium. From the aortic arch arise some arteries that carry blood to the upper body, namely the brachiocephalic trunk, the left common carotid artery and the left subclavian artery. In fact, the brachiocephalic trunk supplies blood to the right side of the head and the right arm. Regarding the left common carotid artery, it transfer blood to the left side of the head. Last but not least, the left subclavian artery provides blood to the left arm [Nat+09].

The descending aorta starts at the level of the forth thoracic vertebra and ends with the medial sacral artery and the common iliac arteries at the level of the forth lumbar vertebra. It can be divided into descending thoracic and abdominal aorta separated by the diaphragm [RB11]. Other arteries arise from the descending aorta and carry blood to the internal organs and the thorax. Once it reaches the abdomen, the aorta bifurcates into two branches named iliacs in order to supply blood to the legs.

I.4.1.3.b Composition

The arterial wall is a complex structure. Its micro-structure varies alongside the vascular tree and also depends on the sex, age and medical condition of each individual. The aorta is not any different. However, like any other artery, the aorta is composed of three layers, also called tunicae. These layers are: the tunica intima (I), the tunica media (M) and the tunica adventitia (A), figure I.5 [GOH06].

tunica intima The internal layer is called the intima and is the thinnest layer. It consists of a layer of endothelial cells which can be seen as a semi-selective biological boundary between the vessel lumen and surrounding tissue since it controls the transit of white blood cells in and out the bloodstream [RF95] [Sur+96]. The aorta contains also a sub-endothelial layer which is formed by connective tissues and some oriented smooth muscle cells [Hum02]. The contact between the intima and the blood is ensured by the endothelium which prevents blood clotting. The tunica intima and the tunica media are separated by the internal elastic lamina which is difficult to seperate from the tunica media. This lamina can be seen as a fenestrated layer of elastin that not only allows the circulation of nutrients and electrolytes between the two tunicae but also prevents the migration of smooth muscle cells.

tunica media The middle layer is the media and is the thickest layer. It is composed of elastin, collagen bundles and smooth muscle cells. Elastin and smooth muscle cells form what is called Medial Lamellar Units (MLU) or also muscoloe-

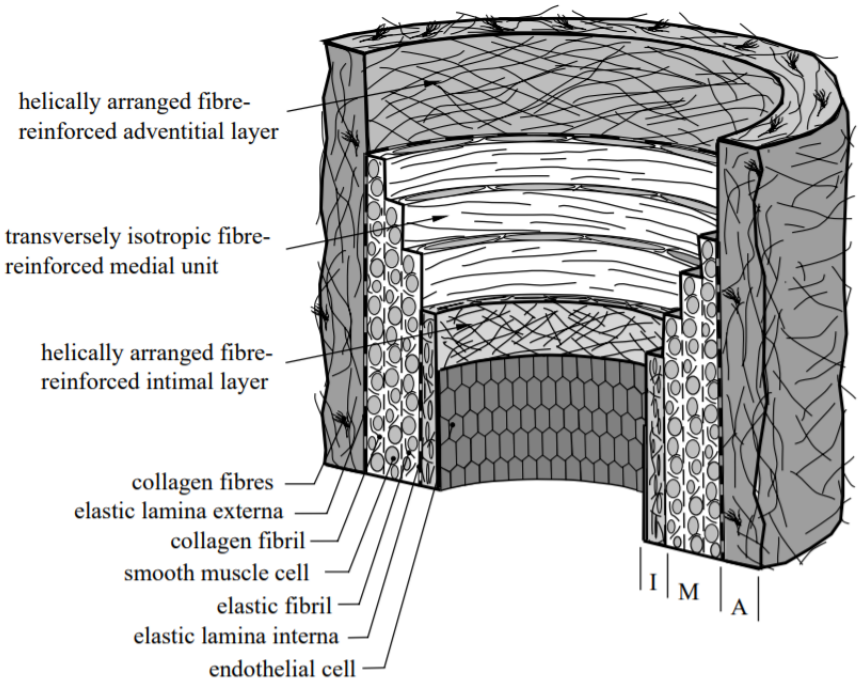

FIGURE I.5 – Layers of arteries

lastic fascicles. MLUs are disposed concentrically. One MLU is composed of two parallel circumferentially-oriented thick lamellae of elastin which present rounded fenestration and enclosed smooth muscle cells. Clark and Glagov [CG85] introduced a schema I.6 of the tunica media structure. In this figure, Ce designates smooth muscle cell, E is for elastin and F is for collagen bundles. The number of MLUs depends on the thickness of the aorta and, thus, decreases with the distance from the heart. The smooth muscle cells allow to maintain the blood pressure in arteries. The outtermost sheet of elastin, known as the external elastic lamina, separates the media from the adventitia and is generally considered as a part of the tunica media.

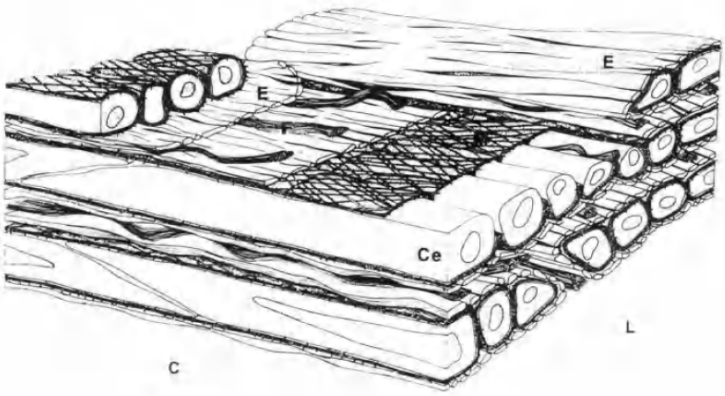

FIGURE I.6 – Representation of the structure of the tunica media

tunica adventitia The outer layer is the tunica adventitia and is the strongest layer. It contains fibrous connective tissue (mainly type I collagen fibers and elastin), nerves and fibroblasts. An additional characteristic of this layer is that it contains

small blood vessels known as the vasa vasorum that supply the aortic wall. However, the intima and the media are nourished from the blood carried by the vessel. The collagen fibers have an axial orientation. They are oriented axially, are undulated in the basal state and are organized in bundles [Hum02]. However, this organization varies during the cardiac cycle, going from undulated to straight configuration. Regarding the elastin, they are different from those observed in the tunica media. They have been described as ribbons, tangled and twisted, with sporadic branches [CHH77]. Those fibrous connections make the tunica adventitia strong and thus, protect the aorta from over expansion. It plays a protective role just like the epicardium to the heart. The fibroblast ensures a function of regalution of the connective tissues.

I.4.1.3.c Micro-structure

As seen in the previous section, the aorta is composed mainly of three micro-structure: collagen, elastin and muscle cells.

Collagen Collagen is the most abundant protein in the human body. It ensures the strength and elasticity of the body's connective tissues. It can be divided into different types. Around 90% of the collagen in the human body are collagen type I (skin, tendons and ligaments), II (cartilages) and III (scar tissue, vessel walls) [Lod+00]. It is mostly found in the form of fibers. However, to be more accurate, it is important to recall that the structures which can be seen in microscopic images depend on the imaging scale and what we are observing: one can see bundles composed of collagen fibrils at a scale of 20 μm or directly collagen fibrils at a scale of 100 nm. For simplicity, the bundles are also often called collagen fibers, and their typical dimensions are in the order of one to a few tens of micrometer in diameter and several hundreds of micrometer in length. Figure I.7 shows a simplified sketch of the organization of collagen fibers in tendons which can be generalized to other types of biological tissues.

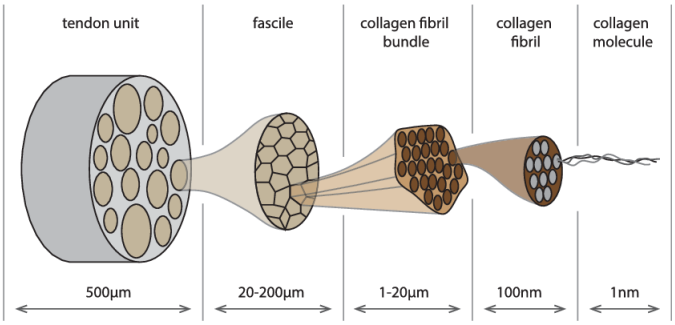

Figure I.7 – Collagen fibers organization [Kar+17]

The fibrils fundamental structural unit is a triple helix with a length of 300 nm and a diameter of 1.5 nm [Lod+00]. It composed of three left-handed helical polypeptide chains (α-chains). As any protein, collagen is formed by a sequence of amino-acids. This sequence is made from a succession of triplets Gly-Xaa-Yaa, where

Gly stands for glycyl and Xaa and Yaa positions are respectively occupied by propyl and hydroxyprolyl residues [VG91].

Collagen fibrils are synthesized by the smooth muscle cells in the intima and the media but by the fibroblasts in the adventitia. The polypeptide chains form the procollagen. These molecules lose their non-collagenous domains through a synthetic proteinases. This leads to the creation of tropocollagen, see figure I.8. The collagen type is determined by how the α-chains are assembled.

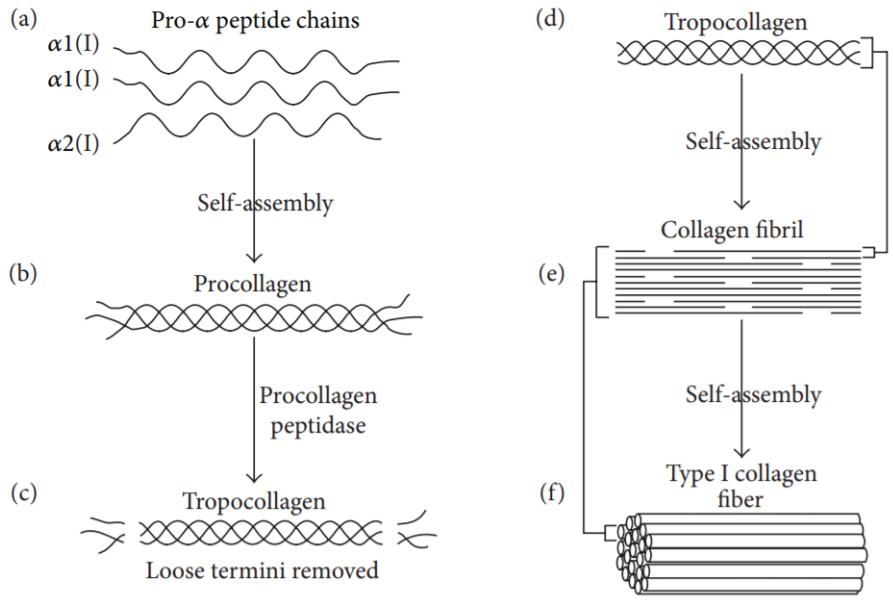

FIGURE I.8 – Collagen synthesis [KMW13] (a) three peptide chains to form procollagen, (b) procollagen, (c) formation of tropocollagen after procollagen removed its termini, (d) tropocollagen, (e) tropocollagen self-assemble to form a collagen fibril and (f) collagen fibrils self-assemble to form collagen fibers

The study of these fibers, which are essential to the proper functioning of tissues, is fundamental in understanding the etiology of pathologies, their evolution, and in improving their clinical diagnosis and management. In fact, Berillis et al. [Ber13] showed that collagen types and quantities along the aorta depends on age, sex, position along the aorta and pathologies. It is a multidisciplinary field which involves mechanics, image processing, chemistry, biology, etc. Relevant researches targeting this aspect require both suitable imaging techniques and reliable image analysis methods.

Elastin The elastic fibers are one of the principle structures of the Extra-Cellular Matrix (ECM). They are responsible of the elastic characteristic of biological tissue, especially the aorta. They are composed of a microfibrillar component and an amorphous component. The amorphous component is referred to as elastin fibers. A polypeptide chain of amino acid residues, mainly glycine, alanine, and proline, forms these fibers [Hum02]. Smooth muscle cells and fibroblasts ensure the synthesis of elastin fibers.

Regarding elastic fibers synthesis, elastin chains are transformed into proelastin which is cross-linked to form a more stable molecule. Elastic fibers result in a mesh of

highly cross-linked structure of elastin. These fibers diameter varies between 0.2 and 0.5 μm and can be considered as forming networks or sheets. What is interesting about elastic fibers is that they can be uniaxially extended up to 150% of their original length when collagen fibers only reaches 10% [Hum02]. Unfortunately, like any other protein, the concentration of elastic fibers decreases with age.

Smooth Muscle cells Vascular Smooth Muscle Cells (VSMC) represents the major component of medium and large arteries [Hu+19]. they count for about 25 to 60% of the arterial dry weight. They have a spindle-shaped structure with a diameter of 5 μm and a length of 100 μm [Hum02]. However, they are slightly thicker around the nucleus. Usually, VSMCs are positioned such that the thicker portion of one cell is next to the thinner portion of surrounding cells. Each VSMC is composed of a contractile apparatus (i.e. actin and myosin filaments) enveloped in a non-muscle cytoskeleton. The cytoskeleton is mainly composed of actin filaments, smooth muscle myosin and intermediate filaments.

In elastic arteries, such as the aorta, VSMCs in the tunica media are usually organized in layers, which are separated by thin (around 3 μm) sheets of elastin. It is responsible of the synthesis of procollagen. This synthesis lasts between 10 and 60 minutes [Hum02].

I.4.2 Arterial diseases

Arterial diseases refer to vascular diseases that may affect arteries. Unfortunately, they affects more and more individuals. They are often related to other diseases such as diabetes and heart failure and are closely linked with turbulence in the blood flow. The aorta, as any other artery, can be the subject of multiple diseases. In most cases, these diseases can cause the patient's death. In this section, we will introduce different vascular diseases that may occur in the aorta and then we will focus on ascending thoracic aortic aneurysm, which is related to the work presented in this thesis.

I.4.2.1 Aortitis

Aortitis designates all forms of inflammation that may occur in the aorta. This inflammation can be classified into two categories: infectious and more frequently, non-infectious inflammation. Infectious inflammations are commonly caused by syphilis tuberculosis, salmonella and other bacteria [GC08]. On the other hand, non-infectious inflammation are mainly caused by the large vessel vasculitides [GB10], Giant Cell Arteritis (GCA) [KE10] and Takayasu arteritis [JLG02].

Aortitis clinical presentation differ from a person to another and depends on its causes. Symptoms may involve back or chest pain and acute severe aortic insufficiency (such as aortic dissection and rupture) [GC08]. It may also lead to the formation of aneurysms and thrombosis.

I.4.2.2 Atherosclerosis

Atherosclerosis is the most common aortic disease. It may affect all types of vessels from thin to large ones. It is a chronic and progressive disease, which consists of plaques build-up in the arteries wall. For the aorta, the consequences of atherosclerosis are based on changes within the tunica media. This deposit is formed of lipids, cholesterol, calcium and inflammatory cells named macrophages, [Agg+09], see figure I.9 [Fog]. As a consequence, the concerned artery can get partially or completely obstructed leading to ulceration or thrombosis.

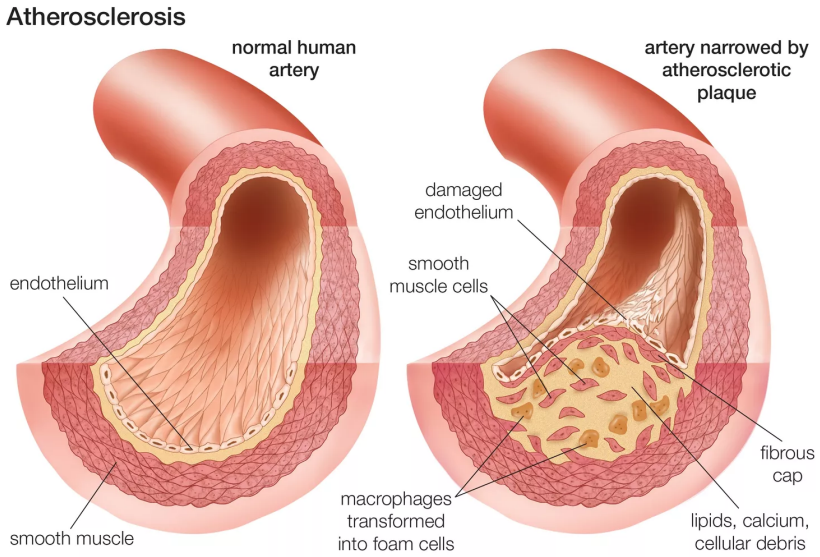

FIGURE I.9 – Comparison between healthy artery and an artery with atherosclerosis

Atherosclerosis is caused by a complex interaction between genetic heritage and environmental factors. The risk and the severity of this pathology can be increased by smoking, diabetes mellitus, dyslipidemia and hypertension [DDD19].

Atherosclerosis in the aorta is generally characterized as mild, moderate or severe [DDD19]. It does not usually affect the ascending aorta except when the patient suffers from diabetes, previous aortitis or familial hyperlipoproteinemia. Severe forms of atherosclerosis which often affect the abdominal aorta may cause aneurysm formation, luminal obstruction or distal emboli.

I.4.2.3 Hypertension

Hypertension or high blood pressure is a very common disease. It is considered by the World Health Organization as a cause of 54% of strokes and 47% of cases of ischemic heart disease. It is considered as a risk factor for cardiovascular morbidity and mortality [JKR18]. We can define hypertension as an elevation of blood pressure. Usually, systemic hypertension corresponds to a systolic pressure higher than 160mmHg or a diastolic pressure greater than 90mmHg or both [Hum02].

Many factors can cause hypertension. One can cite genetics, bad diet, stress, tabacco, some drugs and substances, improper functioning of some organs such as the heart, the kidney or the nervous system or even the vasculature. When resulting

from a distinct disease, hypertension is qualified as secondary. On another hand, hypertension can have a bad impact on the vessels and cause additional problems. In fact, it may lead to a thickening of the tunica media.

I.4.2.4 Aortic aneurysm

Aneurysms correspond to a local dilation up to 50% of the aortic wall normal diameter. Normal aortic diameter depends on the age and the sex of patients, see figure I.10 [Gol+14]. In fact, it increases with age and men usually have larger aortas than women. Aneurysms may occur in different parts of the aorta (e.g. thoracic and abdominal aneurysms). It is caused by a loss of strength of the aortic wall. In this case, a high pressure can make the aortic tissue bulge. The loss of strength is due to the elastic fibers degeneration and smooth muscle cells dropout. This phenomena is called cystic medial degeneration.

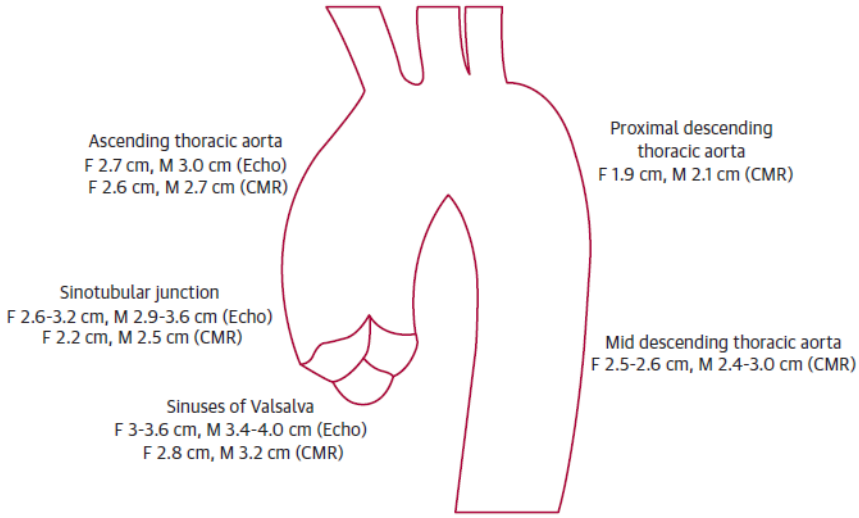

FIGURE I.10 – Normal sizes of diameters of the different parts of the thoracic aorta with respect to age and sex and the used imaging modality (M: male, F: female, Echo: echocardiography and CMR: cardiac magnetic resonance

This pathology can be fatal if not treated. In fact, aneurysms can dissect and rupture and thus, cause the patient's death. It is considered as one of the principal causes of death among seniors in developed countries. For example, in 2019, aortic aneurysms and aortic dissections caused more than 9000 deaths in the United States where 59% of them were men [CHP]. In this thesis, we focus on the study of ascending thoracic aortic aneurysms which we will describe in the next paragraph.

I.4.2.5 Ascending Thoracic Aortic Aneurysms (ATAA)

ATAA are a type of aortic aneurysms that occurs in the ascending thoracic aorta. More than 50% of thoracic aortic aneurysms are localized in the ascending part of the aorta. Studies showed that men and women are equally affected by this condition. However, the age of diagnosis is 10 years higher for women [Clo+99 ; Sal+15].

I.4.2.5.a Symptoms

Ascending thoracic aortic aneurysms are commonly asymptomatic, and are usually discovered accidentally on imaging exams [DDD19]. The dilation of the ascending aorta is an indolent long process. However, as they progress in size, some symptoms may come out. In fact, patients may experience chest pain, back pain, dysphagia, dyspnea and transient neurologic deficit. Besides, ATAAs may have some secondary effects such as aortic regurgitation (when the heart's aortic valve doesn't close tightly). In this case, a diastolic murmur can be detected during physical examination [Iss05]. In some extreme cases, when the ATAA suffers from an acute dissection or a rupture, a sudden and severe anterior chest pain may affect the patient.

I.4.2.5.b Risk factors

As any disease, there are many factors that may increase the risk of getting an ATAA. Among the basic ones, we can cite smoking, aging, diabetes and less commonly atherosclerosis. However, the most dangerous one is hypertension. In fact, when the blood leaves the heart with a high pressure, it will apply a high tension on the ascending aorta which may eventually weaken the aorta and thus make it dilate.

Some genetic conditions, such as Marfan and Ehlers-Danlos syndromes, may also cause ATAAs. Indeed, cystic medial degeneration is correlated with these conditions. In these cases, the amount of elastic fibers in the aorta decreases and thus, leads to increase stiffness and dilation [Iss05]. Bicuspid aortic valve is also associated with many cases of ATAAs. Nistri et al. [Nis+99] analyzed echocardiographies of young people with normally functioning bicuspid aortic valves and found out that 52% of them had aortic dilatation.

I.4.2.5.c Diagnosis

ATAA diagnosis is usually accidental. Physicians discover the presence of an ATAA when they ask their patient to do some imaging exams for other issues. Here, we will focus on the different imaging modalities used to confirm the diagnosis of an ATAA.

Thoracic aortic aneurysms is general can be seen on chest X-ray since they cause a widening of the mediastinal silhouette, a tracheal deviation or an enlargement of the aortic knob [Iss05]. However, enlarged mediastinal silhouette does not necessarily mean that there is a thoracic aortic aneurysm. That's why, CT-Scans may be a good alternative to diagnose ATAAs and better define the aortic anatomy. CT-Scans allows a 3D reconstruction of the aorta and its branches which enhances the measurement of aneurysms and the detection of dissections [Sal+15]. Another used method is MR angiography, see figure I.11. This imaging modality, even though its spatial resolution is less than CT-scans and echocardiography, offers a good reconstruction of the aorta's anatomy.

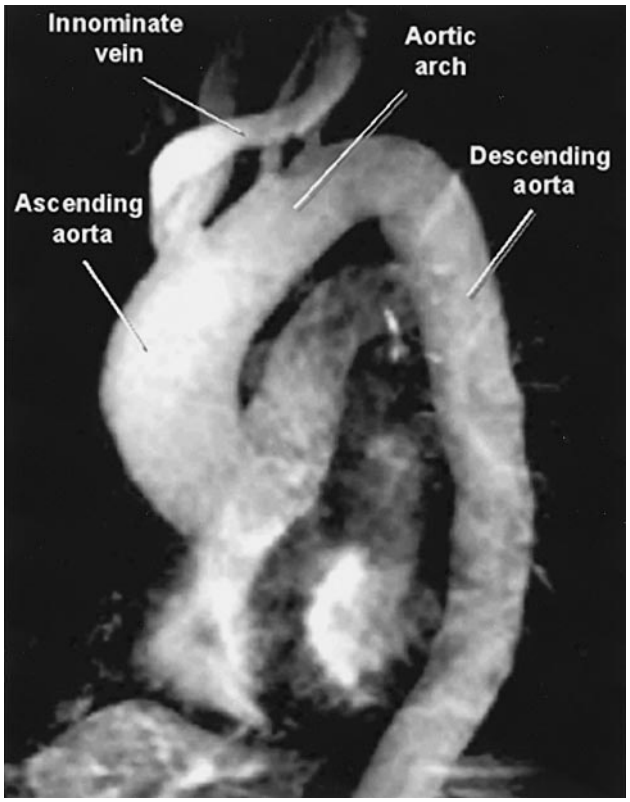

Figure I.11 – MR angiogram showing a ATAA of 4.7cm of diameter

I.4.2.5.d Complications

ATAAs can cause multiple complications. In some cases, those complications are similar to stroke symptoms (i.e. weakness or paralysis of one side of the body, difficulty speaking, etc). Besides, as mentioned above, ATAAs can be accompanied by an aortic regurgitation. This condition can induce heart failure, infections that affect the heart, such as endocarditis and even death.

The main complications with ATAAs is dissection and rupture. A dissection in the ascending part of the aorta, which corresponds to a tear in the lining of the aorta, will weaken the artery and may cause its rupture. The rupture will undoubtedly cause an internal bleeding. In this case, if the patient is not addressed immediately, he/she will certainly die.

I.4.2.5.e Treatment

The only treatment of ATAAs is surgery. However, in order to decide if the patient needs surgery or not, the clinician must determine the diameter of the ATAA. If the latter is greater than 5.5cm for patients without Marfan syndrome and 5cm for patient with Marfan syndrome [DDD19], the physician will proceed to a surgical intervention. This intervention consists in taking off the aneurysm and replacing it by a prosthesis. It is a heavy surgery which requires bypass and its mortality in larger center is estimated to vary between 3% and 5% [Iss05].

For patients that do not qualify for an ATAA repair, it is necessary to monitor them with CT-scans or MR angiographies. The frequent examinations allow clinician

to intervene when necessarily and prevent complications. Besides, it is also important to manage risk factors with those patients by helping them quit smoking, control their blood sugar and their blood pressure.

I.4.2.6 Aortic dissection

Aortic dissection is a dangerous condition. It may be lethal for the patient if not treated on time. Aortic dissection corresponds to a tear in the tunica intima. This allows the blood to fill up between the tunica intima and the tunica media. This phenomena causes the two layers to separate and dissect.

Aortic dissection affects especially men and persons being over 60 years old. Hypertension is considered as one of the main risk factors related to this condition which causes a continuous stress on the inner layer of the aorta. Among the other risk factors, one can cite aneurysms, fatty plaques, defects of the aortic valve and genetics (e.g. Marfan syndrome [JD05] and Ehlers-Danlos syndrome [PJ08]).

For thoracic dissection, we use two common classifications, see figure I.12 [Gol+14] :

— The DeBakey classification: It categorises dissections with respect to their location in the aorta;

— The Stanford classification: It categorizes dissection depending on their relation to the ascending aorta (A dissection when the dissection occurs in the ascending section of the aorta and B dissection when the dissection occurs elsewhere);

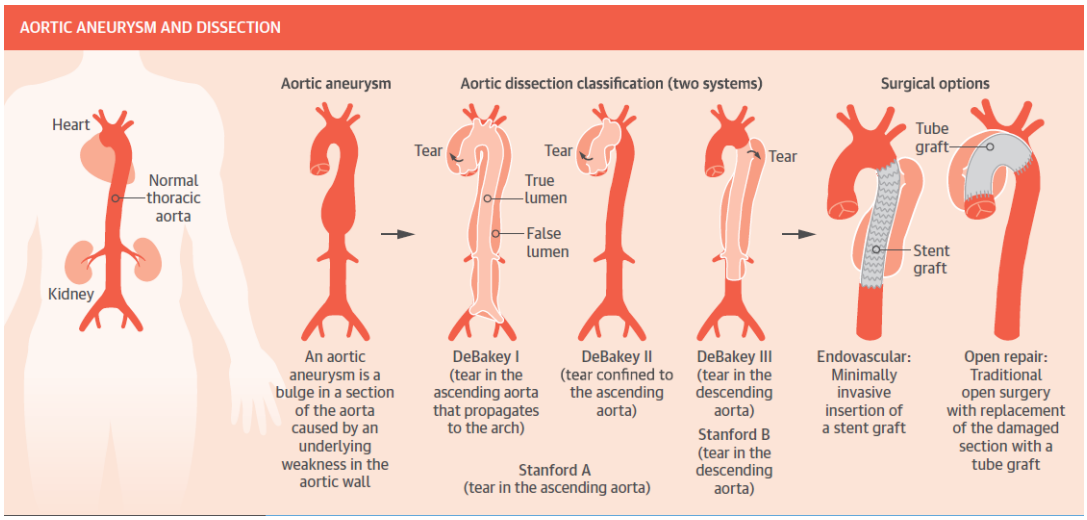

FIGURE I.12 – Global view on different aortic dissection and their treatment

Regarding the symptoms, aortic dissections are usually considered as a silent condition but acute types of dissections can cause severe chest pain spreading to the neck, the jaw and the back, shortness of breath and loss of conscience. Besides, patients may get the same symptoms as a stroke such as a sudden difficulty of speaking, visual loss and weakness on one side of the body [HCC16].

I.5 Mechanical characteristics of the arterial tissue

Mechanobiology has shown that the behaviour of cells and tissues is governed by mechanical stress and strain in addition to genetic and chemical stimuli [Mor+21]. The observation of the mechanical stimuli is highly dependent on the chosen scale of observation. It can be global to the considered specimen or local to focus on a small portion. Besides, it also depend on whether one wants to focus on the macro or the micro-structure of the chosen biological tissue or cell. For example, in order to understand the mechanism leading to aortic aneurysms, it is important to focus on the mechanics of the tissue's micro-structure (mainly collagen and elastin fibers). In particular, collagen fiber characteristics and behaviour in soft tissues have been in the center of many researches [SM17 ; APB19 ; Cav+17 ; Bre+14 ; Koc+14 ; Hil+12 ; Cho+14] since this protein is responsible of tissues' strength.

Multiple studies, in clinical and laboratory settings, have been conducted in order to understand the mechanical characteristics of the arterial wall. They aimed at understanding relationships between diameter, orientations, compliance, stiffness, waviness and forces and pressures to which the aortic wall is subjected. Here we present a brief description of the main experiments conducted for this purpose.

I.5.1 *In vivo* experiments

The determination of the stress and strain of an artery *in vivo* is very limited [VYP73 ; SKK04 ; GST19]. However, one can extract other valuable information from this type of tests. On can site blood pressure, state of diseases, diameter and changes in the aortic geometry and responses to external stimuli. For this matter, several imaging modalities are used such as ultrasounds [Åst+03 ; Dis+20], CT-scan [Lar+11 ; Mey+20] and magnetic resonance imaging (MRI) [Dra+02 ; Fer+22]. For example, the authors of [Fer+22] used a deep neural network to estimate wall shear stress from four-dimensional flow MRI. The wall shear stress corresponds to the force applied by the blood flow on the vessel wall. On another hand, Astrand et al. [Åst+03] used ultrasound images of healthy individuals to determine the diameter of several arteries. It is also possible to use the previously introduced imaging modalities to measure the evolution of the artery's diameter between the diastole and systole phases which is helpful to estimate the circumferential stiffness. The change in the artery's diameter is estimated to be up to 10 - 15% in the pulmonary aorta, 6 - 10% in the carotids, and 2 - 5% in the aorta [HR02].

To our knowledge, the majority of the *in vivo* experiments focused on the mechanical characteristics proper to the considered soft tissue. They are not suitable to understand the material behavior of the arterial wall. In fact, in order to analyze the micro-structure, imaging modalities with high resolution are needed. Some papers succeeded in capturing images of collagen fiber from skin *in vivo* using second harmonic generation microscopy. However, no mechanical characteristics were estimated [Tan+13 ; Yas+18].

I.5.2 *Ex vivo* experiments

Multiple types of *ex vivo* experiments have been conducted on soft tissues in general and the aortic wall in particular to study the passive mechanical properties of these tissues. These experiments are usually a combination of manual and computer assisted manipulations for precision purposes. In order to properly study the multi-axial behaviour of the arterial wall, several testing protocols have been proposed and can be divided into three main categories:

1. Uniaxial testing: It is a simple testing protocol to obtain stress-strain curves and, thus, has been widely used [Oka+02 ; Mat+09 ; Hol+05]. For these setups, specimens are prepared from cylindrical portions from arteries and opened longitudinally [Cho+09]. The specimen is, then, fixed delicately using screwed clamps. One must pay attention to avoid the sample from slipping in the tension's direction. It is possible to perform uniaxial test on both the axial and circumferential directions [Cho+09].

   Soft tissues in general, and the aorta in particular, have a non-linear stress-stretch response with a low and a high modulus regimes. The main purpose of this test is to characterize the mechanical response of the considered specimen as well as to help assessing failure properties. In fact, one can estimate the level of mechanical stimulus which will damage the tissue. García-Herrera et al. [Gar+12] have reported that arterial tissue tensile strength is higher in the circumferential direction when compared to the axial direction. Regarding aneurysmal aortas, Cavinato et al. [Cav+19] showed that they are much stiffer than healthy samples.

2. Biaxial testing: It consists in stretching a portion of a soft tissue in two orthogonal directions at the same time. It is possible to use a different stretch for each direction. The sample is, then, stretched in the plane. Biaxial testing allows to assess the anisotropy and heterogeneity of arterial walls [Som+10]. Besides, they proved that, when using the same stretch, the circumferential direction is characterized with a stiffer response than the axial direction [Cav+19]. In [ZBD09], the authors reported that the stiffness of the tissue decreases when its temperature increases but no significant change was observed for specimens that have been frozen and refrigerated. Besides, they proved that, for biaxial testing, the effect of the strain rate is negligible. Regarding arterial rupture, Duprey et al. [Dup+16] showed that it occurs with a crack perpendicular to the axial direction.

3. Inflation testing: Since uniaxial and biaxial testings do not take into consideration arterial geometry, inflation testing was introduced to mimic the effect of the blood pressure on arterial wall. Two possible setups are possible: (i) bulge tests where samples are subjected to a constant pressure all over one side [Cav+17 ; Rom+14] and (ii) tension-inflation testing where samples are subjected to tension-inflation in cylindrical form [WP88 ; Gen+13]. For both configurations, it is possible to use a saline solution or air to apply pressure on the sample. For tension-inflation testing, the arterial mechanical response is characterized by the changes of the diameter of the artery which depends

on the applied pressure. It is also characterized by the changes of the reaction force along the sample axis. Digital image correlation was used to estimate stress and strain fields in the sample during the inflation.

I.5.3 Macroscopic mechanical properties of the arterial wall

The arterial wall, such as any other soft tissue, can be characterized through a set of mechanical properties. Researchers tried over the years to determine the geometrical and material properties of cardiovascular tissues by modeling their behaviour through equations taking into consideration stress and strain. These models proved the following properties:

— Elasticity: Arteries elastic responses varies along the vascular network and depends on the age and the considered specie. Arteries diameter undergoes some fluctuations while no noticeable change is reported in the axial direction.

— Non-linearity: The stress-strain response of aortic tissues is highly nonlinear. Besides, when the physiological pressure arises, aortic tissues are characterized by a quick stiffening. This nonlinear behaviour can be observed in any load direction [Cho+09].

— Anisotropy: This property is mainly introduced by the presence of fibers within the micro-structure of aortic tissues. It describes a material whose mechanical response is independent of the load's direction. Patel et al. [PFJ69] conducted a study on arterial anisotropy and suggested that the wall is cylindrically orthotropic.

— Heterogeneity: When considering the microscopic level, it is obvious that healthy aortic walls are not homogeneous. In fact, they are composed of multiple constituents and their distribution varies from a layer to another. Davis et al. [Dav+16] demonstrated the heterogeneity of the arterial wall at the millimeter scale.

— Viscosity: Across the arterial wall, energy transmission is divided into parts: Some energy is stored in the tissue and can potentially be restored because of the tissue's elasticity. The rest of the energy is dissipated because of the tissue's viscosity. This phenomena has been studied by Bergel et al. [Ber60] through the examination of static and dynamic viscoelastic behavior in dog arteries. This property is interesting to understand the mechanisms behind aortic degenerative diseases.

— Incompressibility: The arterial tissue can be considered as a mixture composite structure where the solid part is represented by collagen and elastin fibers in addition to smooth muscle cells. Even though arteries are not really incompressibile, they appear to be incompressible under several loading conditions. Girerd et al. [Gir+92] demonstrated that the volume of the aorta does not change in the range of physiological loading.

— Residual stress: It corresponds to the stress existing in a body when no external load is applied. It participates in maintaining the homeostatic state in arteries [Car+09]. It was first observed in arteries by Bergel et al. [Ber60].

I.5.4 Limitation of the macro-characterization of arterial tissues

The macro-analysis of the arterial wall is important to globally characterize it. In fact, to study the evolution of aneurysms for example, it is important to have an idea on the mechanical response of arteries. However, to explain this response, a deeper look into the micro-structure is necessary. For arterial tissues, one needs to consider fiber reorientation and recruitment processes. These phenomena are caused by the reaction of the hierarchically organized micro-structure to mechanical loads [Mor+21].

In recent years, many researchers attempted to develop models of soft tissues in general and aortas in particular. These models need to take into consideration the microscopic arrangement and its influence on the macroscopic mechanical response. Continuum thermomechanics have been used to develop soft tissue models with relevant micro-structure features that are responsible of the macroscopic behaviour [VH18 ; MAH18]. Models based on the strain energy function have been developed to describe arterial walls deformations [VYP73 ; TH87 ; FFP79]. It was also generalized to shear deformations [Den+94]. The cited models are adequate to describe the global microscopic mechanical response but they miss information relevant to the micro-structure.

Hence, new models, referred to as structural models have been developed to generate more general continuum models where fibers rearrangement is coupled with the global mechanical response. To capture the anisotropy of arterial tissues, models of fiber-reinforced materials are generally used. Here, the global mechanical response to the rearrangment of the arterial wall micro-structure is considered in the strain energy function. For example, Holzapfel et al. [HGO00] proposed a hyperelastic model to describe the arterial wall where the preferred fiber directions are incorporated as a structural parameter.

I.6 Imaging modalities

In order to develop accurate model of the aorta mechanical response, it is interesting to study the aortic wall micro-structure and quantify it. By analyzing this micro-structure, it is possible to understand the aging process of the aorta and thus, determine its relationship with vascular diseases and especially aneurysms. For this matter, multiple imaging modalities have been used in the literature. In this section, we will exhibit the main imaging techniques that were used to analyse collagen fibers in biological tissues.

I.6.1 Histology

Histology, also referred to as microscopic anatomy, is a branch of biology studying the microscopic anatomy of biological tissues. It consists in observing a slice of a biological tissue using light or electron microscopy. The result of this observation is a 2D image. However, it is possible to reconstruct a 3D image by combining 2D

images of multiple slices. An example of the histology of the aortic wall can be seen in figure I.13 [Slo]. One can capture the details of a biological tissue thanks to the light attenuation when it passes through the specimen.

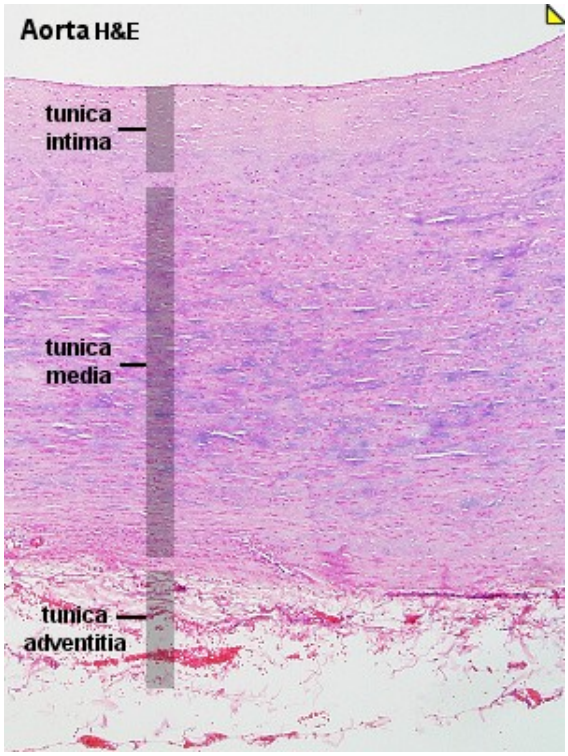

Figure I.13 – Histological section of human aorta

In order to proceed to a histological study of a biological tissue, the latter needs to be prepared properly. First, it is necessary to cut the specimen into thin slices so the light can get through it. However, this may damage the tissue and cause tears, fractures and folds in the slices [Wal+15]. Then, the specimen needs to be treated chemically to enhance the contrast between the different micro-structures of the considered tissue. For this matter, staining techniques are used. It is also common to freeze the tissue using some chemical products such as formalin and paraffin [Wal+15]. Nevertheless, the use of those product is not without harm to the tissue. In fact, they may cause variation in the tissue's thickness [Smo+17 ; LL96].

I.6.2 Optical Coherence Tomography (OCT)

Initially, tomography refers to the reconstruction of cross-sectional images of a certain object from its projections. It was described by J. Radon [Rad83] in 1917. However, the use of tomography in medical imaging came later. It led to different configurations depending on the nature and characteristics of the light used for projections. Besides, data acquisition can be performed by reflected or transmitted radiation.

OCT [Hua+91] is a new type of optical imaging modality. It is used to capture cross-sectional tomographic plane or volume of biological tissues and their micro-structure. The principle is similar to ultrasound but offers a higher resolution (between 1 and 15 μm) [Fuj+00]. This imaging modality is non-invasive, based

on measuring optical reflections and can be used on *in vivo* and *ex vivo* specimens. Most OCT systems use continuous wave short coherent length light but they can also perform with short-pulse light [BT02]. OCT was initially used to image different types of biological tissues such as the retina and different eye structures and it still has a wide application in ophthalmology since there is no need for a physical contact to perform an OCT.

The first step towards the construction of a tomographic image using OCT consists in measuring the axial range within the specimen. Spatial information related to the micro-structure of the considered biological tissue is determined by the diffusion of the optical signal through the tissue. In fact, measuring the echo time delay of the back-scattered signal is transformed into spatial information following the formula $\Delta T = z/v$ where z is the distance traveled by the echo time delay, v is the light velocity and ΔT is the echo time delay. In OCT, the mechanisms governing the transverse and axial resolutions are independent. In fact, the coherence length of the light source determines the axial resolution while the focusing properties of an optical beam determines the transverse resolution.

Regarding aortic imaging, OCT allows observing native aortic tissues and their micro-structure [Rea+13] and evaluating the mechanical properties of the aorta [Aco+18]. However, limitations in the resolution of the OCT prevents it from capturing the individual components of the aortic wall during loading and its main advantage relies in having a large field of view to have a more global idea about what is happening [Fuj+00].

I.6.3 X-ray micro-tomography

X-ray micro-tomography is an imaging technique that is able to penetrate in the depth of a tissue with a micro spatial resolution (between 1 to 50 μm [Bar+]). Thus, it is possible to recover good 3D images. During the scanning, the specimen is rotating and is irradiated with X-rays.

Besides, it provides larger fields of view (up to 1.7mm x 1.7mm) as compared to other imaging modalities [Wal+15], [Bai+18], [Dis+17], though a compromise between resolution and field of view must be made. X-ray micro-tomography is characterized by a lesser reflection and a higher transmission. In fact, the images captured with this technique have a high contrast which corresponds to the high absorption of the captured specimen. This implies that the quality of the image closely depends on the considered specimen. For example, X-ray micro-tomography works better on hard tissues than on soft tissues.

In order to improve the images of soft tissues, some contrast agents may be injected. However, these substances may change the behaviour of the specimen components. In fact, they may damage the biological tissue, alter its mechanics and make it shrink [Bai+18 ; Hel+18 ; She+16]. Figure I.14 shows an example of X–ray micro-tomography without the use of X-ray contrast agents of a rat large artery embedded in paraffin [Wal+15]. Despite its good resolution, X–ray micro-tomography is still limited to histologically fixed unloaded and loaded specimens.

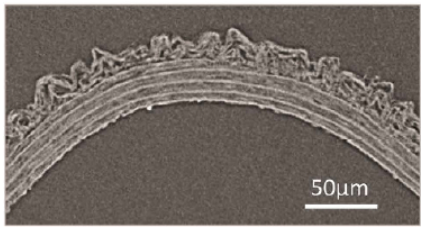

FIGURE I.14 – Virtual radial slice of a rat large artery

I.6.4 Confocal microscopy

Confocal microscopy is a type of fluorescence microscopy. It was first introduced in 1955 by Marvin Minsky and was patented in 1961 [Min19]. Minsky replaced the condenser of conventional microscopes by a lens identical to the objective lens. Besides, he introduced a first pinhole on the axis of the microscope to limit the field of illumination and a second one on the focal plane of the reflected beams from the specimen, the specimen being placed on the focal plan of the lens. The second pinhole play the role of rejecting the rays not coming directly from the focal point. The first Laser Scanning Confocal Microscope (LSCM) was developed by David Egger and Paul Davidovits in 1969 [DE69] and was based on Minsky's patent. Later, with the technological advances related to lasers and computers, LSCMs have evolved and became an efficient tool to capture micro-structures in biological applications. Figure I.15 [SW05] shows a simplified setup of a LSCM. Here, the laser beams passes through the pinhole and the dichroic mirror, are reflected by two rotating mirrors converging through a lens to a point on the specimen. This point reflects also the beam (under another wavelength) which goes through the rotating mirrors, the dichroic mirror and the exit pinhole before reaching the detector. Other variants of confocal microscopes exist such as multiple-beam confocal microscope using Nipkow Disk which was proposed by Milan Hadravsky and Mojmir Petran in 1968 [Pet+68].

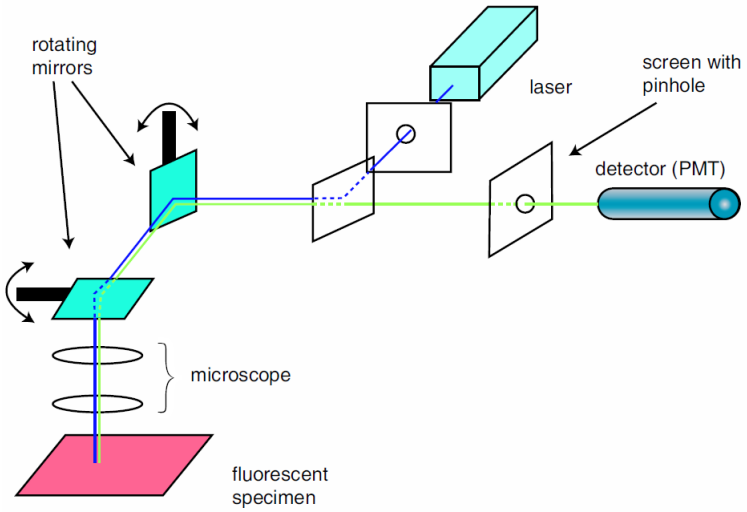

FIGURE I.15 – Comparison between different imaging modalities with respect to their resolution and image penetration

Confocal microscopy offers many advantages in comparison with other imaging

modalities. In fact, it has a higher resolution and a higher image penetration than OCT, see figure I.16 [DF08]. That is why, it makes capturing the micro-structure of the aorta in 3D possible under good conditions and thus, analyze their behaviour. For this matter, the choice of the pinhole aperture is essential. In addition, the specimen should not be exposed to the laser beams for too long because it might get photo-bleached. It is interesting to use confocal microscopy in a fluorescent mode imaging with different fluorophore markers in order to distinguish between the different component of the specimen. However, since this technique scans the specimen point by point, it can easily become computationally expensive. Besides, the depth penetration is limited and depends on the considered specimen and the wavelength [Got+16].

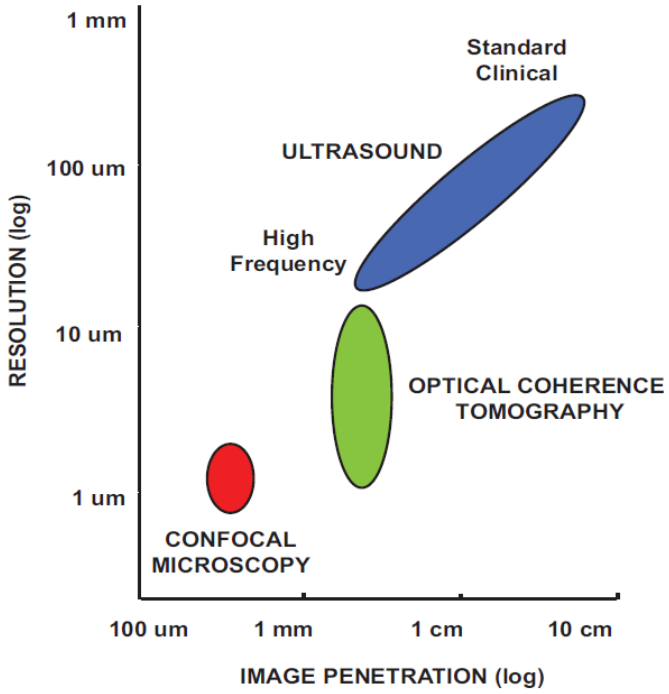

FIGURE I.16 – Comparison between different imaging modalities with respect to their resolution and image penetration

I.6.5 Two-photon microscopy and second harmonic generation

Optical harmonics were first discovered in the 1960s when the high-intensity pulsed lasers have been invented. It was Franken who observed Second Harmonic Generation (SHG) in crystalline quartz by using a Q-switched ruby laser [Fra+61]. It became a very used method to characterize the second order Non-Linear Optical (NLO) response of emerging materials, especially organic NLO materials. It led to an increase of its use in different fields such as biomedical research [Ost13]. One of those organic materials of interest is collagen which drew the attention of several scientists. The non-linear polarization of a material is defined as:

$$P = \chi^{(1)}E^1 + \chi^{(2)}E^2 + \chi^{(3)}E^3 + ... \tag{I.1}$$

where P is the total induced polarization, $\chi^{(i)}$ is the ith-order nonlinear susceptibility, and E is the electric field vector of incident light [Boy08]. For SHG signals, $\chi^{(2)}$, which characterizes the material of the studied interface [She89] is strictly positive.

SHG imaging in biology was reported by Freund in 1986 [FDS86] when he tried to characterize the polarity of collagen fibers in a rat-tail tendon. A more recent practical implementation was reported by Campagnola in 2002 [Cam+02] where they succeeded in imaging biological tissue at high resolution and fast acquisition rate. In order to collect SHG images of collagen in biological tissues, a two-photon light microscopy has been developed. This imaging technique is based on the excitation of a molecule to a virtual state by two photons which are then converted into a single photon of exactly total energy at double frequency, without absorption or reemission of photons, see figure I.17. For two-photon excitation, photons in the infrared spectral range are used under highly intense laser illumination (for example Ti:sapphire lasers). Infrared photons are chosen because of their low energy. When the energy gap between the ground state and the excited state is smaller than the sum of the energy of the two photons, the non-linear process can occur. In this case, the probability that a fluorescent molecule absorbs simultaneously two infrared photons is a quadratic function of the excitation radiance [So02].

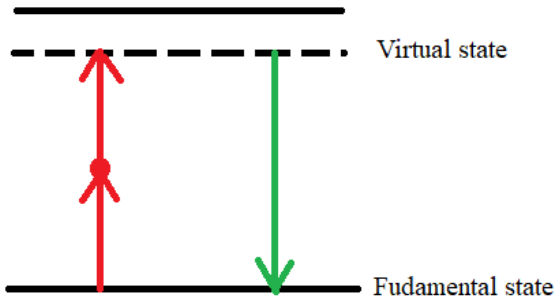

FIGURE I.17 – Simplified Jablonski diagram of the two-photon excitation process

The possibility to take microscopic images in three dimensions (i.e. depth discrimination) is considered as one of the most interesting properties of two-photon microscopes. It originates from the almost absence of out-of-focus light resulted by the reflection. 80% or more of the total fluorescence signal may be cramped in a region of 1μm thickness around the focal plane of a two-photon excitation [So02]. Notable two-photon excitation occurs where the photon density is high. It corresponds to the focal volume of the microscope which can be as small as $0.1\mu m^3$ [ZWW03], i.e. the generation of fluorescent signal is limited to a restricted zone. Thus, it is possible to reach several hundreds of micrometers in the depth of the specimen. It was even possible to reach an imaging depth of $1.6mm$ in mouse cortex [KHX11]. The laser needs to scan the entire specimen in the three dimensions to generate a 3D image, which may involve relatively long acquisition times according to the volume size and acquisition parameters. Finally, the use of two low energy

photons limits the risk of photo-damage of the sample [SY06]. In addition, it maximizes the probability of detecting photons per excitation event in the right spot and, thus, minimizes photo-bleaching (when the molecule looses its ability to fluoresce) and photo-toxicity.

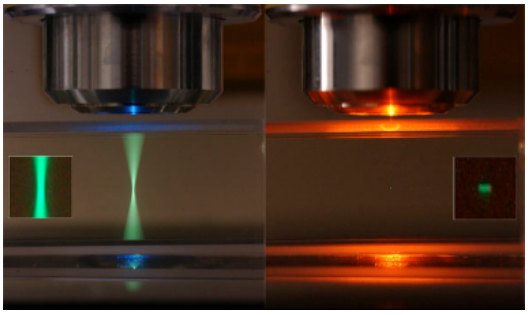

FIGURE I.18 – Left: one-photon excitation. Right: two-photon excitation (Image by Steve Ruzin and Holly Aaron, UC Berkeley)

I.7 Pre-processing techniques

In order to process an SHG image or stack and to extract as much accurate information as possible, it is important to remove the noise that is present. SHG images of tissues present usually Poisson noise because of their poor signal to noise ratio [Bre+14]. Common methods in pre-processing SHG images are introduced in the following.

I.7.1 Median Filter

It is a simple and widely used filter to reduce noise in images and to smooth them. Median filter [HYT79] is a non-linear smoothing filter. The value of each pixel in the image is replaced by the median value of pixel's intensity in a previously defined neighborhood of size $m * m$. In other words, The intensity values of the pixels in the considered neighborhood are sorted, then the median value is assigned to the pixel being processed. This way, pixels which are darker or brighter than their surroundings and cover an area of $m^2/2$ will be removed with a median filter of size $m * m$ [Tya18]. To process peripheral pixels, it is necessary to pad with zeros the image borders.

Median filters work well for removing random salt and pepper noises [GW18]. However, this kind of filter does not allow the suppression of Gaussian noise [OZV95] which can be dealt with through deconvolution. They do not reduce the difference in brightness of images and hence, preserve edges. However, when the signal-to-noise ratio of the image is small, or the neighborhood is too large, median filters tend to delete useful information and produce false noise edges.

I.7.2 Contrast enhancement

The recognition of image features depends on the image contrast. However, the contrast can be distorted by the imaging system because of poor illumination conditions. For this purpose histogram equalization is widely used. A well acquired gray-scale image should cover black and white pixels. It is also better that the image's shades are evenly distributed (i.e. the image histogram is uniform). Many contrast transforms can be used for this purpose such as histogram equalization, adaptive histogram equalization and Contrast Limited Adaptive Histogram Equalization (CLAHE) [MA18]. Here, we will focus on the CLAHE algorithm which is very used in SHG imaging [Koc+14 ; Hu+12].

CLAHE [Piz+87] is a variant of adaptive histogram equalization. It consists in computing histograms of distinct regions and using them to redistribute the pixels intensity values of the image. The difference between CLAHE and other adaptive histogram equalization algorithms is that it clips the histogram at a pre-defined value (i.e. if a histogram bin is higher than the clip limit, those pixels are clipped and uniformly shared with other bins before proceeding to the histogram equalization). It operates on small regions of the image called tiles. To remove the artificial boundaries between the different tiles, bi-linear interpolation is used.

CLAHE is a good technique to improve local contrast and to enhance edges. Compared to other adaptive histogram equalization techniques, it limits the noise amplification. However, if the image is too noisy, a phenomena of noise amplification may occur. The combination of CLAHE, median filter and edge sharpener (such as high-pass filters) can be successful to maintain the image high spatial frequency content.

I.7.3 Directional filters

When there is a need to study oriented features in an image, directional filters [BS92] can be used. They consist in a filter bank containing lines in different directions. They can be used to detect edges or to identify object orientations. Those filters have wedge-shaped pass-band spectral regions, and are therefore usually referred to as wedge or fan filters [SF96]. Wedge filters are also a filter bank where each filter represents a region of the space shaped as a wedge, *figure* I.19. Those filters work as a pass-band filters where each filter of the bank focuses on the corresponding region in the image. When the orientation of the wedge is known, the determination of object directions is straightforward.

Wedge filters are an easy to implement and efficient tool to study oriented objects in images. However, in order to have a fine description of the image features, it is necessary to have thin wedges in as many directions as possible which will add more computational costs.

I.7.4 Gradient magnitude

The gradient vector is a fundamental approach for finding extrema of a continuous and smooth function in space [HHH09]. Gradient direction gives information

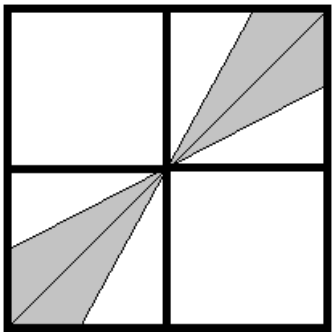

FIGURE I.19 – Ideal wedge filter with given aperture, and a certain angle

FIGURE I.20 – SHG of a human aorta

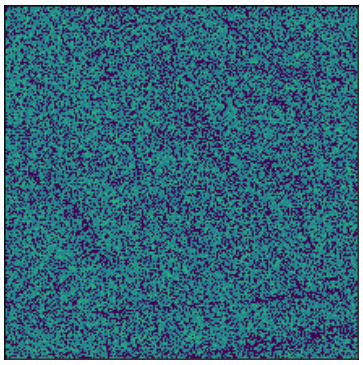

FIGURE I.21 – Gradient magnitude

FIGURE I.22 – Gradient magnitude of a noisy SHG image

about the direction where the function is growing fast while the gradient magnitude indicates how fast does the intensity change. Hill et al. [Hil+12] for example used the gradient vector to detect the edges of the image as a first step to determine fiber directions. The gradient is defined as the partial derivatives of a function with respect to all its components. For 2D images, the gradient is usually achieved by the convolution of the image by a couple of filters based on the Sobel filter [Sob14] or the Prewitt operator [Pre70].

The fact that small displacements are considered to compute the gradient allows to capture as much details as possible in any direction. The gradient works fine with clear images without much noise. However, if the considered image is noisy, the gradient will not bring any useful information. *figure* I.22.

I.7.5 Frangi filter

The Frangi filter [Fra+98] was first developed to be a vessel enhancement filter. However, it was used to detect both vessel-like and tube-like structures in images. Because of the collagen fibers morphology, which can be assimilated to tubes, the Frangi filter was used to extract the fibers from SHG images.

The Frangi filter is based on the computation of the image's hessian matrix. In the proposed framework, the derivative of an image corresponds to its convolution with derivatives of Gaussians. The second derivative of a Gaussian kernel *figure* I.23a allows to measure the contrast between the region in and out of a range $(-s, s)$, s

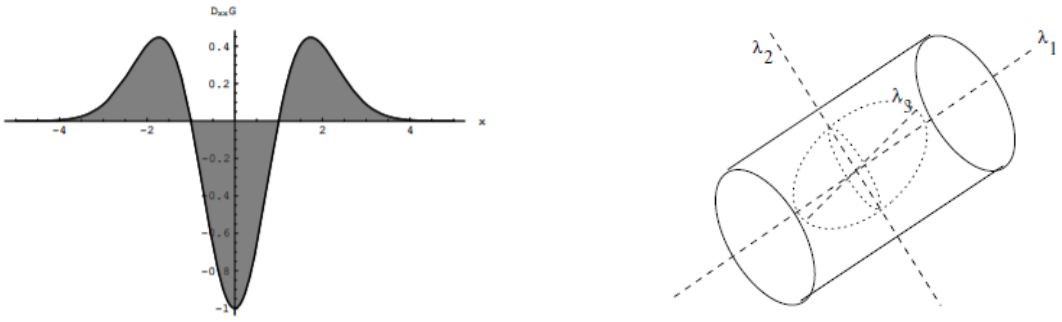

(a) (b)

FIGURE I.23 – (a) Second derivative of a Gaussian kernel, (b) Ellipsoid described by the eigenvalues

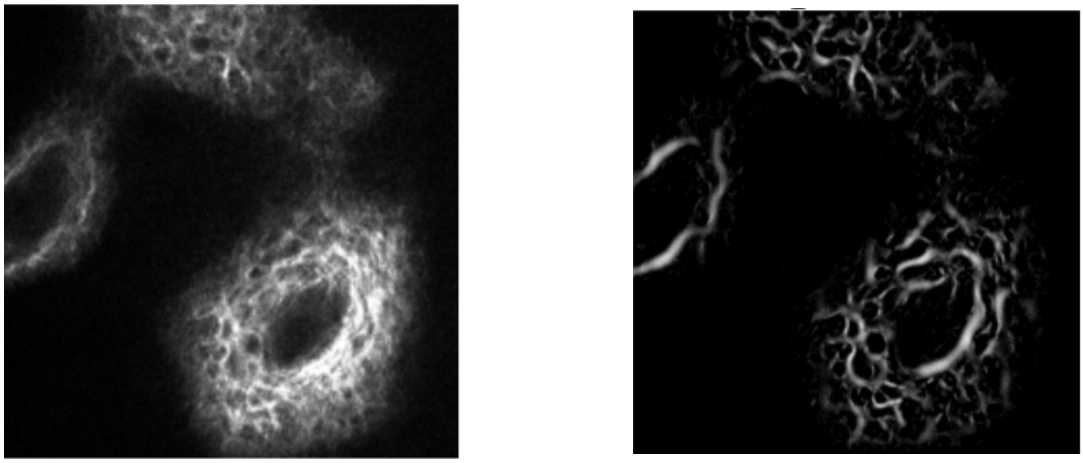

(a) (b)

FIGURE I.24 – (a) Original image, (b) Result after Frangi filter

being the standard deviation of the Gaussian. Through the analysis of the eigenvalues of the image's hessian matrix, it is possible to extract the direction of the smallest vessel's curvature which corresponds to the main directions in which the local second order structure of the image can be decomposed [Fra+98]. The eigenvalue decomposition gives three orthonormal directions *figure* I.23b which allow to describe vessels in images.

Figure I.24 shows the results of the work of Cai et al. [Cai+14] when they applied Frangi filter on SHG images of human skin. The use of multiscale Frangi filter, through the analysis of the eigenvalues of the hessian matrix, makes it possible to capture the smallest details of an image and thus, avoid the application of different filters of different sizes. However, the Frangi filter may not take into consideration any object in the image which does not have a circular cross-section.

I.8 Overview

The review of the state of the art presents us with a good understanding of the complexity surrounding 3D imaging of arterial micro-structure. The aorta, as

an important artery, may suffer from different conditions and thus, put in danger individual's life. The choice of ATAAs to focus on in this thesis is based on the possibility to recover ascending aortic healthy and aneurysmal tissues from the hospital to image them and analyze them. As seen in this chapter, SHG images are not always ready to be analyzed. In fact, artifacts are often present on the images especially on its 3D component. These stacks can be noisy, blurry and even present some black regions. Besides, in the literature, most of the attempts to improve these images were only applied on 2D images without taking into consideration the 3D nature of the micro-structure. The first part of this thesis aims at addressing these problems by realizing the following aspect:

Develop a new approach to improve the SHG stacks: To this aim, many image processing techniques were tested and we finally propose a combination of a top hat transform to reduce the noise and a 3D directional filter to reconstruct the fibers in case of discontinuities (presence of black spots). The results will be exposed in the following chapter.

Chapter II

From raw to enhanced images: A story to tell

Contents of the chapter

II.1 Résumé du chapitre

Les maladies cardiovasculaires, comme l'anévrisme de l'aorte thoracique ascendante, sont déclenchées au niveau de la micro-structure. Afin d'acquérir des images de cette micro-structure, et en particulier les fibres de collagène, la microscopie de seconde harmonique est utilisée. Cependant, ces images présentent généralement des artéfacts notamment du bruit, du flou et des discontinuités au niveau de certaine fibres. Traiter ces artéfacts peut s'avérer complexe et nécessiter une combinaison de plusieurs techniques. Pour se faire, une approche basée sur des filtres directionnels 3D pour reconstruire les fibres de collagène et des transformées "top-hat" à une et trois dimensions pour réduire le flou et le bruit est proposée. Cette approche a été appliquée sur des images de seconde harmonique 3D et a montré de bons résultat quant à la restitution du réseau de collagène.

II.2 Abstract of the chapter

Vascular diseases, such as the ascending thoracic aortic aneurysm, are triggered at a micro-structural level. To capture this micro-structure, in particular collagen fibers, SHG microscopy is used. However, the resulting 3D images usually presents some artifacts namely blur, noise and fibers' discontinuities. Dealing with all these issues may be complex and need a combination of multiple techniques. For this matter, an approach based on 3D directional filters to reconstruct collagen fibers as well as 1D and 3D white top-hat transforms to deal with the noise and the blur is proposed. This approach was performed on 3D images and provided a good restitution of the collagen network.

II.3 Introduction

The aortic wall is a complex structure composed of three heterogeneous layers namely the intima, the media and the adventitia. A strong interest was shown toward the study of the micro-structure of the adventitia for mechanical purposes, especially to characterize traumatic aortic injuries and conditions such as aneurysms and dissections.

As we have seen in the previous chapter, the analysis of 3D collagen SHG images can be difficult because of occurring artifacts. This statement is, in particular, applicable to collagen SHG images of the ascending thoracic aorta. Therefore, it is important to improve these images in order to properly characterize the aortic micro-structure. The artifacts in SHG images may have a strong impact on the quantitative analysis of collagen fibers. In fact, among these artifacts, one can cite fibers discontinuities which lead to a wrong estimation of the collagen density. In addition, the noise and the blur occurring in SHG images may lead to inaccurate results in relation with fibers' size, fibers' orientation and even fibers' waviness.

In this chapter, we start by describing the available 3D collagen SHG images and the acquisition process. These images were taken by Cavinato et al. [Cav+17]. Then, we will introduce some new approaches to deal with the artifacts on the stacks. Our approaches focus on the entire 3D stacks unlike the majority of the techniques in the literature where the authors processed the stacks slice by slice. Finally, we analyze the effect of our filters parameters on the volume fraction of the collagen on images of rabbit carotid arteries [Kra+17].

II.4 Description of the available 3D images

Images we used in the present work have been acquired in the lab. For more details on the images, please refer to [Cav+17].

II.4.1 Acquisition

The aorta is a complex structure composed of three layers. All the images treated in this thesis focus on the tunica adventitia since it is the last layer before complete dissection and rupture. Collagen fibers of the adventitia layer hold the aorta together. Here, we use SHG imaging to capture collagen fibers of different types of ascending aortas.

II.4.1.1 The specimen

The conducted study includes three types of specimen:

— Porcine aortas were collected from a slaughterhouse from domestic pigs aged between 6 and 12 months. Aortas were cut along the longitudinal direction. Specimen had a square shape with 45mm long.

— Fresh non-aneurysmal human aortas were collected via the French voluntary body donation program from the Department of Anatomy of the University of Saint-Etienne.

— Unruptured human ATAAs were collected from patients having elective surgery to replace the aneurysmal segment of the aorta with a graft. The collections and the experiments on the specimens respects a protocol approved by the Institutional Review Board of the University Hospital Center of Saint Etienne.

Specimens were placed in Phosphate Buffer Saline (PBS) in the refrigerator under a temperature of 4°C for 12 hours maximum. Before proceeding to tests, the external edges of the adventitia were glued with ethyl cyanoacrylate on a 30mm diameter PVC support appended to the inflation device. To track the regions of interest under the microscope, fluorescent micro-particle was placed using a micro-needle to mark its center on the outer part of the tissue. The maximum radius in the axial-circumferential plane was about 300 μm.

II.4.1.2 The setup

The collected specimens are imaged by a multi-photon microscope with a certain protocol. In this section, we exhibit the characteristics of the used microscope in addition to the bulge inflation test protocol.

II.4.1.2.a Multi-photon microscopy

The used multi-photon microscopy is a LEICA TCS SP2 upright confocal microscopy system equipped with a water immersion objective (HCX APO L UVI ×20 NA0.5). The laser source is a Ti:Sapphire femtosecond laser Chameleon Vision I from COHERENT, Inc. The best compromise between SHG signal and two photon fluorescence (TPF) was reached with an excitation wavelength of 830nm. SHG signal was collected between 375 and 425nm while TPF signals were collected between 560 and 700nm. The scanned volumes is 750 × 750 × dz μm^3. dz can vary between 100μm and 500μm with respect of the permeability of the sample. For each specimen, Cavinato et al. [Cav+17] proceeded to two scans after stabilization: one of a stack placed 750μm away from the ROI marker and an adjacent stack 1.4 mm away from it. The numerical resolution of the images is 1024x1024pixels. Regarding the z-step, it corresponds to 1μm. At each z-step, each line of the specimen was scanned twice and the average was retained.

Small motions may occur during the acquisition and distort it. To deal with this issue, two quasi-instantaneous (QI) scans with a z-step equal to 15μm were taken just before and after each main scan. These QI scans aim at providing data to determine the needed z-correction to balance a possible z-motion. For more details, refer to [Cav+17].

II.4.1.2.b Bulge inflation test

Before starting the acquisition, the intimal side of the specimen is glued on another PVC support. Then, it is assembled and tightened via a tightening nut to the bulge inflation device, figure II.1. This ensures a hermetic closure for the intimal surface while the adventitial surface is exposed. Cavinato et al. [Cav+17] used PBS to cover the exposed adventitial surface during all the test duration. In order to inflate and control the specimen volume, an automatic water pumping system (WPI®, NE-501 Multi-Phaser) commanded with a LabVIEW program to inject water at a constant rate (2 mL/min for human specimens and 30 mL/min for porcine specimens). A pressure transducer (Omega®) was used to record pressure values. When a pressure of interest is reached, the water injection stops and the volume is kept constant.

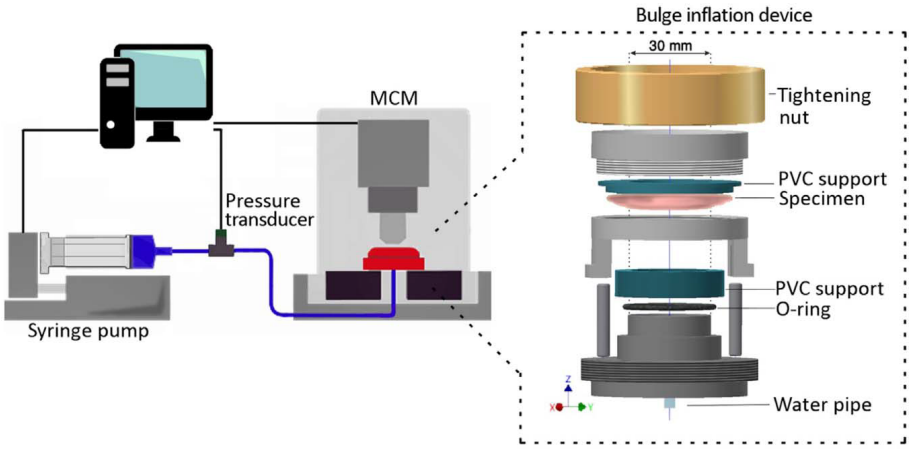

FIGURE II.1 – Experimental setup to perform the bulge inflation test

The choice of pressures fell on the values of 200 and 450 mmHg because the authors wanted to evaluate a wall stress state close to diastolic-systolic conditions (around 120 mmHg) in addition to state beyond the physiological range.

II.4.2 Characteristics of collagen SHG images

Most of the available SHG images have a dimension of 1024 by 1024 pixels and between 50 and 300 slices per stack. Slices are taken with 1μm step. 1024 pixels correspond to 750μm. These stacks show dense undulated collagen fiber bundles. The stacks taken under a mechanical load show that the collagen fibers become straight following a preferred direction. When we visually analyze the 3D stacks, we can see that there are some artifacts. In fact, we can observe on some stacks the occurrence of some black regions and shadows. In addition, we can notice the presence of a multiplicative noise and some blur.

II.4.2.1 Shadows

Collagen fibers network is a 3D structure. The fibers are undulated and do not have necessarily a preferred direction. The creation of 3D stacks is performed slice

by slice. When capturing a slice in the depth of the specimen, the laser of the microscope needs to pass through the fibers present in the superior slices. However, the beams are backscatterd by the fibers and thus, prevented from reaching the fibers beneath which will not be illuminated. This explains the presence of shadows. In other terms, these shadows come from the presence of collagen fiber above the capture slice. Figure II.2 shows an image with some shadows.

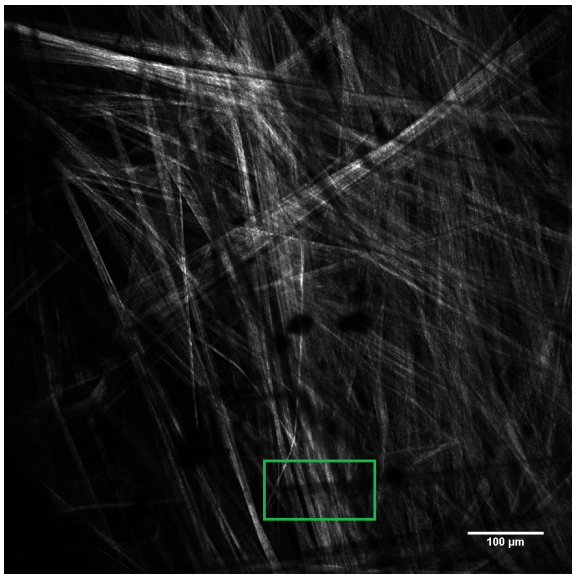

FIGURE II.2 – Example of an image with some shadows on different fibers

II.4.2.2 Black spots

On some of the available stacks, we noticed the presence of some black spots, see figure II.3. This artifact is not proper to the specimen and is not introduced by the microscope. In fact, these regions are most probably due to the presence of dust or water when proceeding to the acquisition. Besides, if we look through the different slices of a stack having a black region, we can see that this spot is always present in the same place or a little bit displaced. This displacement is probably due to some vibrations that made the dust move during the acquisition.

II.4.2.3 Noise

A very common type of noise in SHG images is the Poisson noise [Bre+14] also called shot noise. This noise is introduced by the Charge Coupled Device (CCD) which is usually the detector in two-photon microscopes. It is due to the low-light conditions caused by the low number of photons. It is multiplicative noise and can be modeled by a Poisson process expressed by the equation:

$$P(X = k) = \frac{e^{-\lambda}\lambda^k}{k!} \tag{II.1}$$

where λ is the mean and k is the expected value.

This type of noise is associated with the particle nature of light. It actually occurs in optical devices when counting photons at the level of the detector. Unlike

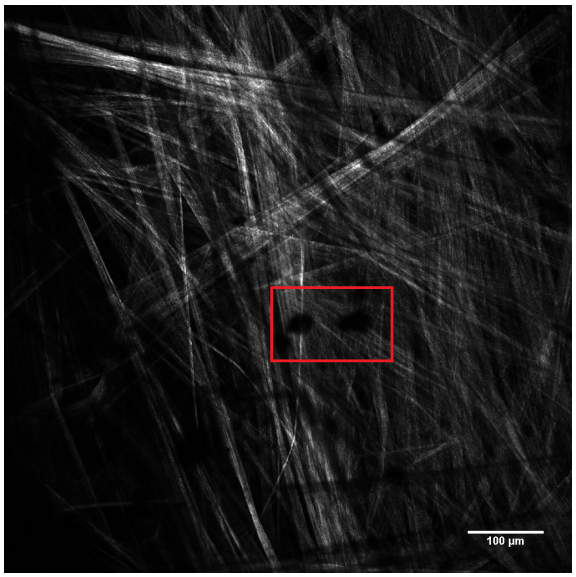

Figure II.3 – Example of an image with some black regions

the Gaussian noise, the Poisson noise is a signal dependent noise. In fact, it depends on the image brightness. Figure II.4 emphasize on a section extracted from an SHG image of human aortic collagen fibers.

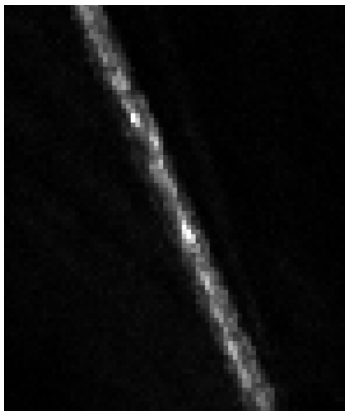

Figure II.4 – A portion of a collagen fiber extracted from an SHG image. The intensity of the pixels forming this fiber is not homogeneous which is caused by the Poisson noise.

II.4.2.4 Blur

SHG images are taken by a microscope which, as any optical system, introduces some blur. This blur is caused by the Point Spread Function (PSF). This function is specific to the used microscope.

II.4.2.4.a Definition of the PSF

PSF is the image of a point source of light imaged by an optical system. It represents the 3D diffraction pattern of light emitted from an infinitely small point source in the specimen and transmitted to the image plane through a high Numerical

Aperture (NA) objective. The choice of the NA parameter is very important since it affects the quality of the recovered image and thus, its resolution, see figure II.5 [Mic].

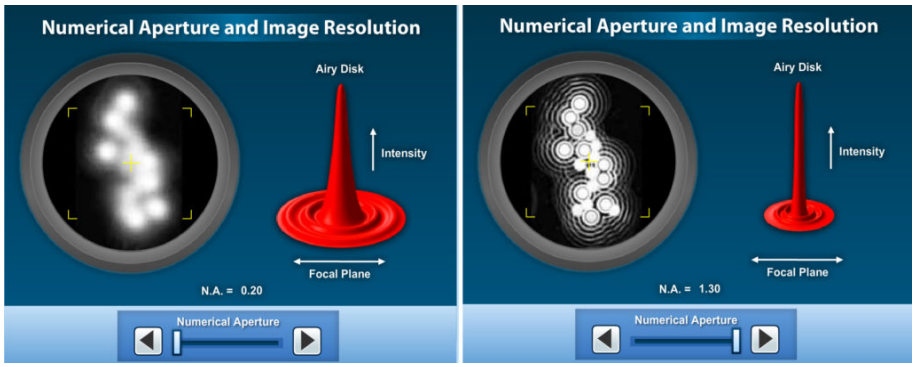

FIGURE II.5 – Relationship between NA and the image resolution

The airy disk presented in red in figure II.5 corresponds to how the microscope sees a point. In fact, the laser beam converges and interfere at the focal point and leads to the creation of diffraction pattern of concentric rings of light surrounding a central bright disk. The radius of this disk is determined by the NA. Low NA corresponds to large disks, figure II.6 [Oly], thus, to a bad resolution. The microscope spatial resolution can be determined through the Full-Width at Half-Maximum (FWHM). This metric is the width of the airy disk when its values equal to half its maximum.

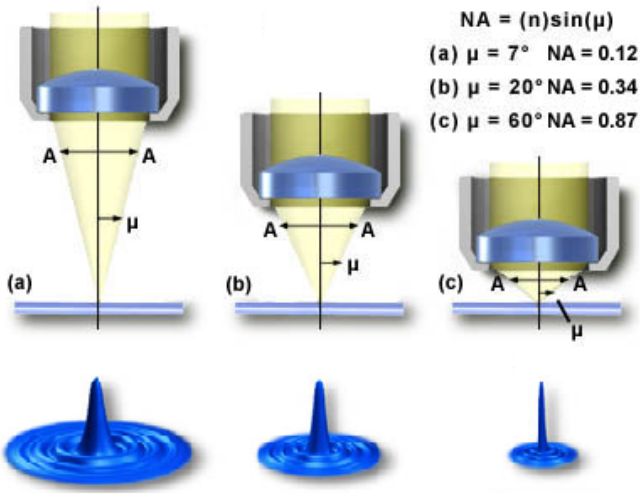

FIGURE II.6 – Relationship between NA and the image resolution

The PSF can be determined by three methods:

— experimentally: for two-photon microscopes, it is possible to insert a microsphere of fluorescent substance in a specimen and image it with the microscope. Then, from this image, it is possible to extract the needed information to characterize the PSF (mainly the FWHM).

— theoretically: It is possible to use the Gibson and Lanni model [GL91] which is based on the computation of the Optical Path Difference (OPD) between

the design conditions and experimental conditions of the objective.

— analytically: it is possible to perform a blind deconvolution. Here, one can start with an estimation of the PSF and then update it with respect to some constraints and by applying an expectation maximization algorithm.

II.4.2.4.b Effect of the PSF

An image is a convolution of the object to capture and the PSF and can be symbolically represented as:

$$Image(x, y, z, t) = object(x, y, z, t) * PSF(x, y, z, t) \tag{II.2}$$

where x, y and z are the coordinates of a voxel of the image and t is the time.

In the Fourier domain, this equation will be:

$$FT(Image(x, y, z, t)) = FT(object(x, y, z, t)) \times FT(PSF(x, y, z, t)) \tag{II.3}$$

where FT stands for Fourier Transform.

3D PSFs in microscopy usually have rice seed shape. In fact, the refractive index mismatch in biological tissues causes some spherical aberrations. This leads to a degradation of the focus especially along the optical axis. Thus, the PSF is extended along this axis [Jin+20 ; Lef+21]. It introduces some blur on the 3D volume. Its effect is small on the 2D plan but is wider along the z axis. That is why the impact of the PSF on the 2D slices of the stack is not very obvious but if one proceeds to a depth descrimination of the stack, one can see that the fibers are very blurred.

II.5 Blur removal through the PSF

SHG stacks in general, and those we consider in this work in particular, show that the PSF has a rice seed shape. As said previously, the PSF introduces some blur. Therefore, by estimating the PSF, we can recover a cleaner image.

II.5.1 On synthetic images

In order to analyze the effect of the PSF on SHG images, we first created SHG synthetic images. This makes it possible to overcome acquisition problems and give the opportunity to focus on the mathematical operations before dealing with real SHG images.

II.5.1.1 PSF creation

The creation of the PSF is based on 2 different Gaussians. We start by creating a classical 2D Gaussian defined on a 1024x1024 support (because most of the available SHG images have these dimensions), see figure II.7a. As a rice seed, this Gaussian has a small variation. In order to have a 3D PSF, we multiply our 2D Gaussian by a uni-dimensional Gaussian with a larger variation, see figure II.7b. This Gaussian has

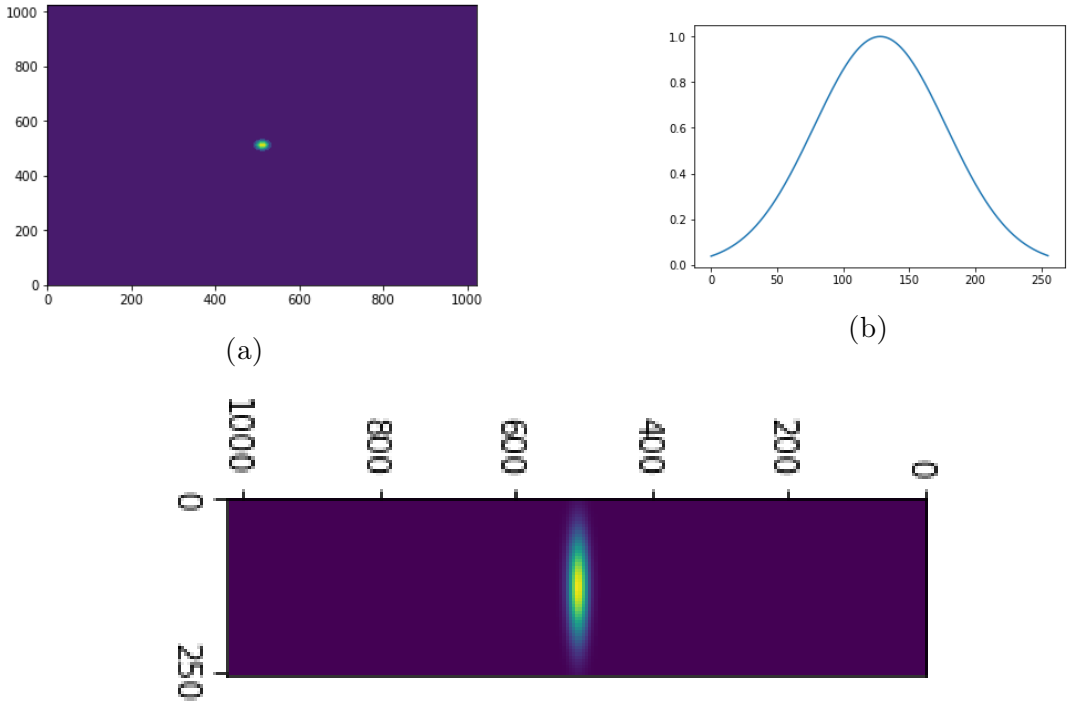

FIGURE II.7 – (a) 2D Gaussian, (b) 1D Gaussian and (c) cross-sectional view

a support of 256. In other terms, each slice of our 3D PSF is the product of the 2D Gaussian by a value of our sampled uni-dimensional Gaussian. The cross-sectional view is showed in figure II.7c. As intended, the resulting PSF has a rice seed shape.

II.5.1.2 Downgrading the image

Once the image is created, one can downgrade an image by convolving it with the PSF. For this matter, we created a synthetic 3D stack where different undulated fibers are lined up in the same direction and separated by the same distance, see figure II.8. We have to mention that the aim behind this synthetic image is to master the mathematical operations to downgrade (i.e. convolution) and recover an image (i.e. deconvolution). This means that the synthetic image does not have to be similar to real ones.

The created image is then convolved by the defined PSF. This operation corresponds to the product of the Fast Fourier Transform (FFT) of the image by the FFT of the PSF. For more details on the FFT see chapter 3. The convolution is a mathematical operation that is equivalent, on a digital support, to adding each voxel of the image to its neighbours weighted by the kernel. It corresponds to applying a Gaussian filter with different standard deviations on the 3D image. Inverse FFT is then applied on the resulting product to recover a downgraded image. In figure II.9, we show the effect of different PSFs on the created image. Theses tests were conducted on 3D artificial stacks of dimensions $(128, 128, 32)$.

From figure II.9, we can clearly see the effect of the different sizes of PSF. It is important to say that, for visualization purposes, the chosen values are exaggerated

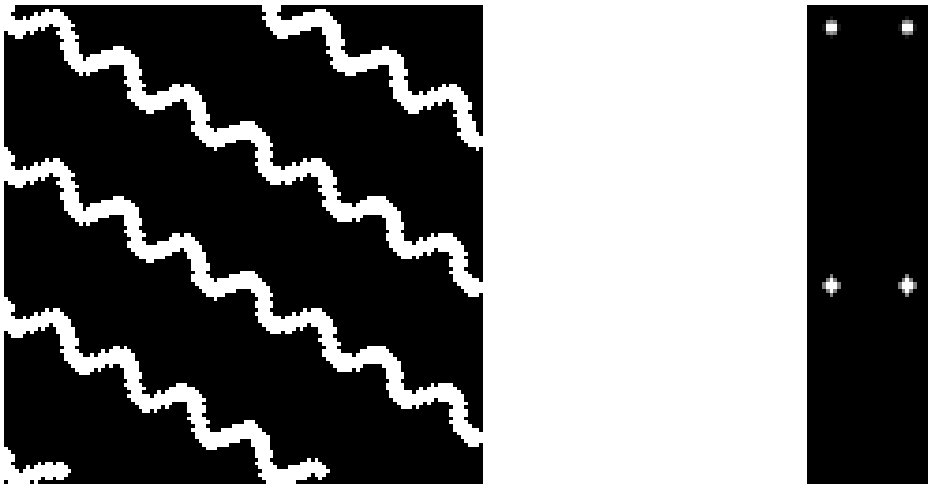

(a) (b)

FIGURE II.8 – Example of a virtual image where (a) is a slice of the virtual stack where there are some fibers and (b) is a section of the stack along the z axis.

compared to real PSFs. Figures II.9a and II.9b show a "small" PSF makes the slice a little blurrier that the original one, figure II.8a. However, on the section along the z axis at $y = 70$, we can see that the fibers sections are wider and we notice also the appearance of some other bright pixels which correspond to the some wider (due to the convolution) fiber portion which is close to the section plan. Moreover, a high variance on a certain axis corresponds to a dispersion of bright pixels on the same direction, see figures II.9b, II.9d and II.9f.

II.5.1.3 Recovering the initial image

In order to recover the initial image, we need to perform the inverse operation. We deconvolve the image by the PSF used to degrade it. In the Fourier domain, it corresponds to a division of the FFT of the downgraded image by the FFT of the PSF and is expressed by:

$$FT(Image(x, y, z, t)) = FT(downgradedImage(x, y, z, t))/FT(PSF(x, y, z, t)) \tag{II.4}$$

Even though, mathematically speaking, multiplying then dividing an image by the same quantity will have the same image as a result. However, since the PSF is very sparse, one can encounter some problems during the division. That is why, the deconvolution will certainly introduce some noise. We tested the deconvolution with different PSF variations and we exhibit the results in figure II.10. After some tests, we were able to determine the maximum size (standard deviation) of the PSF to be able to recover a decent image. All the tests were conducted on 3D images.

The deconvolution gives satisfying results in general. We noticed that it is possible to recover the initial image from the downgraded one when the PSF variations in the (x,y) plan are smaller than 4. Indeed, figures II.10c and II.10d show that the deconvolution did not work well for PSF variances equal to $(10, 10, 4)$. However, the

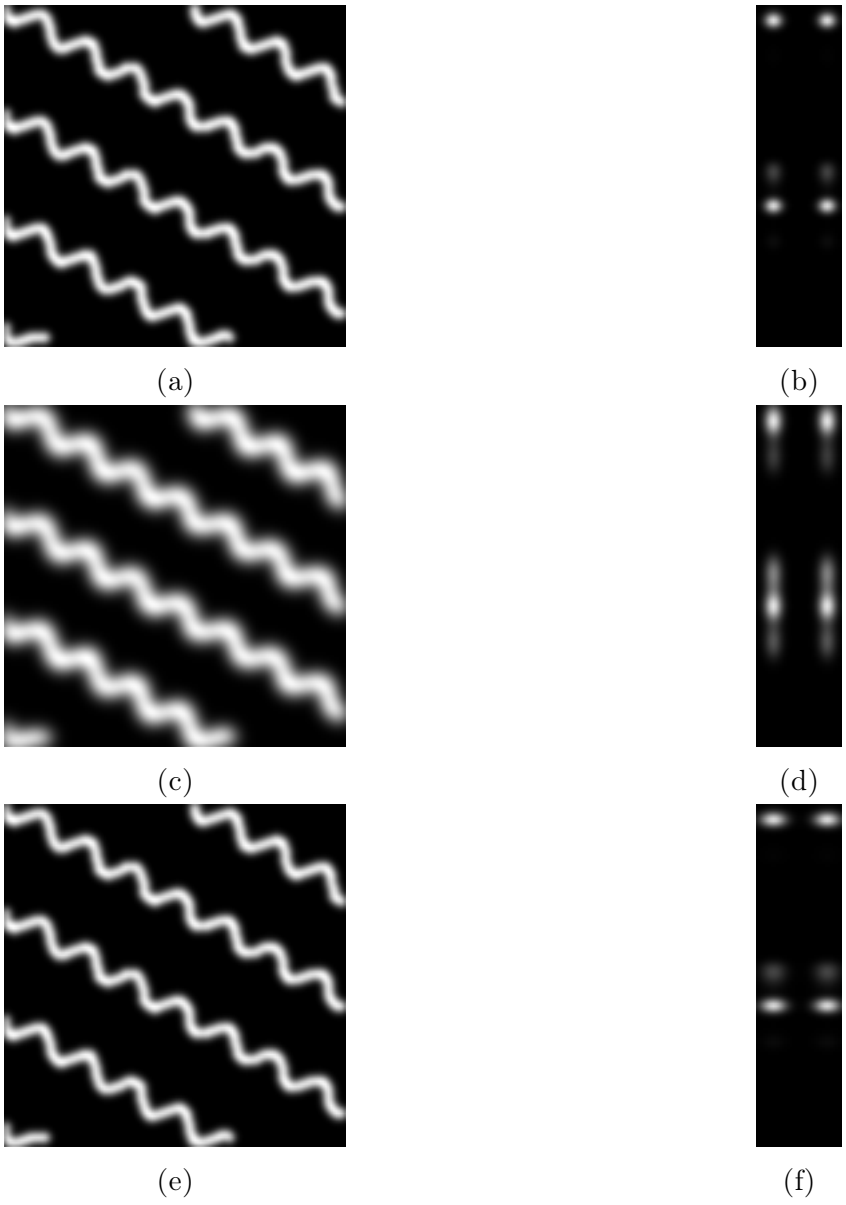

(a) (b) (c) (d) (e) (f)

FIGURE II.9 – Impact of the variance parameter of the PSF on the artificial stack. (a) and (b) correspond respectively to a slice of the stack where the fibers are the brightest and the corresponding section at $y = 70$ for a variance equal to $(2, 2, 4)$, (c) and (d) correspond respectively to a slice of the stack where the fibers are the brightest and the corresponding section at $y = 70$ for a variance equal to $(10, 10, 4)$ and (e) and (f) correspond respectively to a slice of the stack where the fibers are the brightest and the corresponding section at $y = 70$ for a variance equal to $(2, 2, 10)$

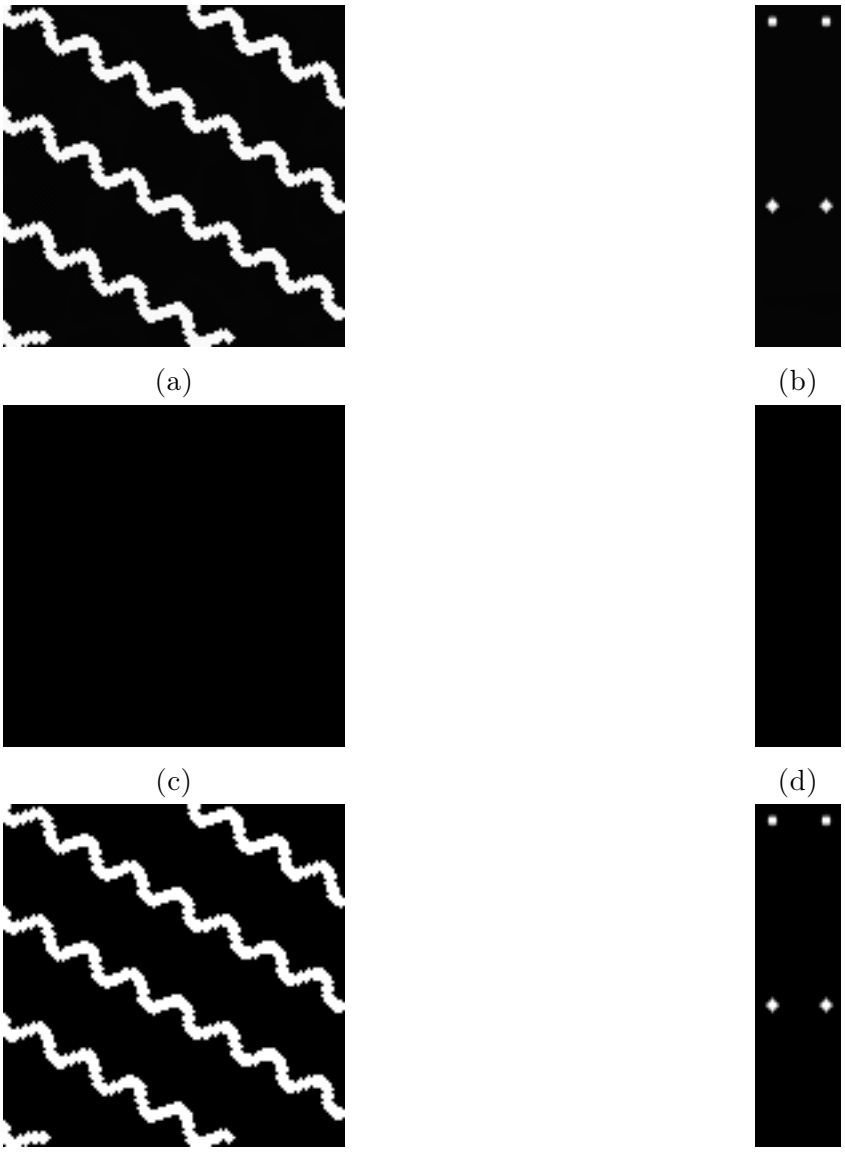

(a) (b) (c) (d) (e) (f)

Figure II.10 – Results of the deconvolution process on different convolved images. (a) and (b) correspond respectively to a slice of the stack where the fibers are the brightest (slice number 6) and the corresponding section at $y = 70$ for variances equal to $(2, 2, 4)$, (c) and (d) correspond respectively to the slice number 6 and the corresponding section at $y = 70$ for variances equal to $(10, 10, 4)$ and (e) and (f) correspond respectively to the slice number 6 and the corresponding section at $y = 70$ for variances equal to $(2, 2, 10)$

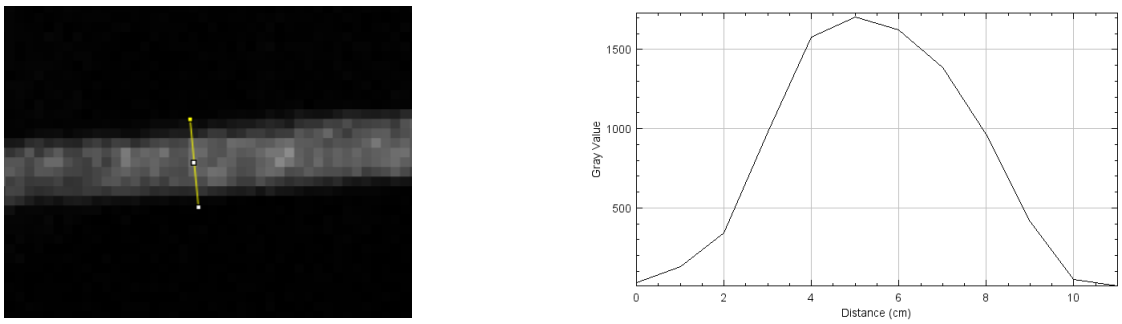

(a) (b)

FIGURE II.11 – (a) Example of a single fiber where a yellow line is draw. This line corresponds to the direction along which the intensity evaluation profile is extracted. (b) Intensity profile of one collagen fiber.

variance along the z axis does not have any impact on the result on the deconvolution. In fact, we conducted several tests with fixed (x,y) variances = 2 and varying variance along the z axis (i.e. 4, 10, 20 and 50). Some examples are presented in figures II.10a and II.10b as well as II.10e and II.10f. In all these cases, we succeeded in recovering the initial image from the downgraded one.

II.5.2 On real images

Once we mastered the computational implementation of the 3D convolution and the 3D deconvolution, we conducted the same tests on real SHG images.

II.5.2.1 PSF estimation and deconvolution

We tried to estimate the PSF from a real SHG stack. For this matter, we supposed that collagen fibers have a cylindrical shape (i.e. having a disk for a cross-section). We chosed one slice of the stack where we can distinguish clearly one fiber. We then recovered the variation profile of the intensity of the pixels forming this fiber. This profile certainly needs to be perpendicular to the fiber. Figure II.11 shows an example of fiber to be considered and the corresponding intensity profile.

Since the effect of the PSF is practically nonexistent in the (x,y) plan, we focused only on its effect in the stack's depth. Because we assume that collagen fibers are cylindrical, the chosen collagen fiber needs to have the same intensity profile along the z axis. However, due to the effect of the microscope's PSF, this profile is larger. Thus, we perform a deconvolution of the real intensity profile by the expected one (i.e. the profile captured from a slice). This way, we can recover an estimation of the z-profile of the PSF which is supposed to have a Gaussian shape. This can be summed up in the equation:

$$FT(IntP(z,t)) = FT(IntP_exp(z,t)) \times FT(PSF(z,t)) \tag{II.5}$$

$$\Updownarrow$$

$$FT(PSF(z,t)) = FT(IntP(z,t))/FT(IntP_exp(z,t)) \tag{II.6}$$

where:

— $IntP$: is the wide intensity profile.

— $IntP_exp$ is the expected intensity profile

— PSF(z,t) is the z-profile of the PSF

II.5.2.2 Results

Both intensity profiles of the fiber were approximated to two generalized Gaussian distributions. Figure II.12 shows an example of an intensity profile as well as its approximation. Once the estimation of the z-PSF has been done, one can reconstruct the 3D PSF by assuming the 2D PSF has the same standard deviations as the intensity profile extracted from the 2D image. We proceed then to the deconvolution of the stack by the estimated PSF.

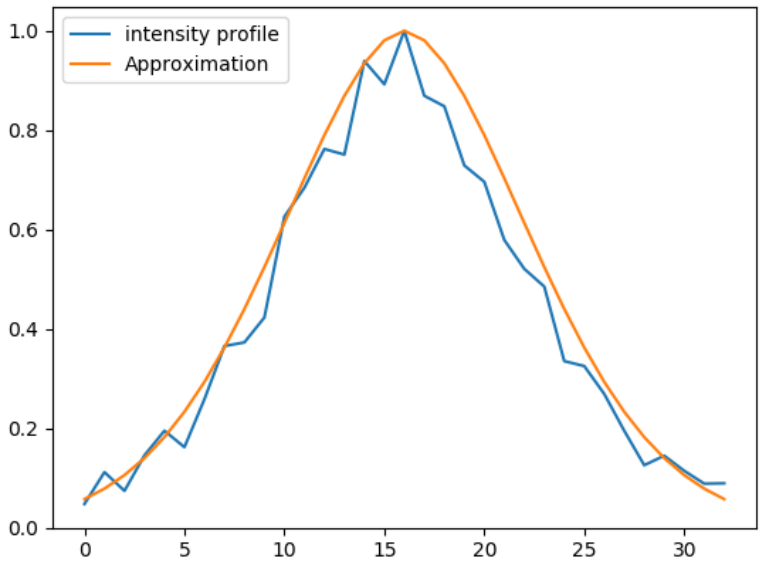

FIGURE II.12 – Example of an intensity profile of a collagen fiber extracted along the z axis in addition to its generalized Gaussian approximation.

Collagen fibers have usually a diameter around 10 pixels. The intensity profile extracted in the (x,y) plan is defined on 11 pixels while it is defined on around 33 pixels along the z axis. This way, we are certain that it covers any potential exceeding. Certainly, the intensity profile is wider along the z axis because of the effect of the PSF. The main issue with this methodology consists in finding the best approximation. The deconvolution was performed in the Fourier domain. It is interesting to mention that, the support of the result of the deconvolution is equal to the sum of supports of both intensity profiles. Figure II.13 shows both approximations of intensity profiles of one fiber in addition to the result of the deconvolution previously described. The result of the deconvolution corresponds to the actual PSF along the z axis.

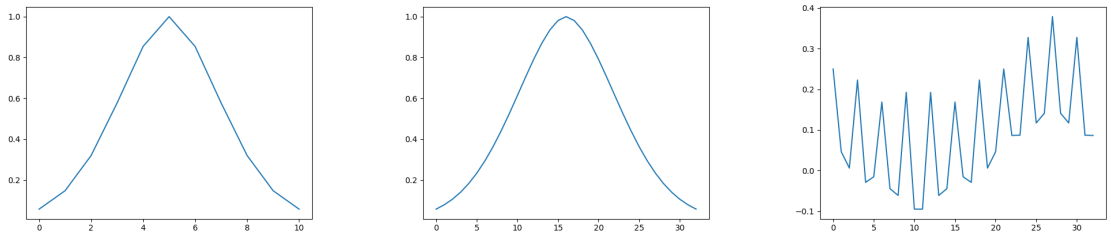

(a) (b) (c)

FIGURE II.13 – Approximations of different intensity profiles: (a) approximation of the intensity profile extracted in the (x,y) plan, (b) approximation of the intensity profile along the z axis and (c) result of the deconvolution of (b) by (a)

The present approach did not succeed in recovering a clean Gaussian as a result of the deconvolution, figure II.13c. This random result is probably due to the non-smoothness of the the intensity profile approximation in the (x,y) plan. In fact, the deconvolution in general enhances the noise. We tried multiple times to better approximate this profile but we did not succeed. Thus, the approach based on the deconvolution of real images by the PSF of the microscope aiming at improving them was forsaken.

II.6 Shadows and black spots removal

As shown in sections 2.2.2.1 and 2.2.2.2, SHG images may present some shadows and black regions. To deal with this problem, we needed to develop an algorithm that aims at reconstructing the fibers when there are discontinuities. Here, we will present our algorithm which is based on directional filters.

II.6.1 2D directional filter

The first attempt was to apply a 2D directional filter on all the slices of each stack and see if we are able to reconstruct the fibers while taking the fibers orientations in the space.

II.6.1.1 Specifications

A 2D directional filter is a bank of 2D filters. Each one of these filters is an image containing one segment of a length l and tilted with an angle α. l is the same for all the filters. At first, we need to define the number of angles we want to include in our analysis. In more details, if we want to take into consideration d directions, α will be equal to $k \times \frac{2\pi}{d}$ where k is an integer varying between 0 and $d-1$. In order to simplify computations, we divide the number of directions by 2 if it is even. Then, for each pixel of the slice, we select the portion of the image centered on this pixel and having the same dimensions as the created filters. This portion is afterwards multiplied by each one of the filters. For each multiplication, we compute

the mean intensity value. Finally the pixel's value is updated with the maximum of the calculated means. Mathematically, it is expressed as:

$$imF(x,y) = \max(mean(im(x,y) \times DirFilter_i(x,y))) \tag{II.7}$$

where imF is the filtered image, im is the original image, $DirFilter_i$ is the filter number i of the filter bank, $i \in [0, numberofdirections]$

The choice of the segment's length l has a strong impact on the resulting image and the fibers reconstruction. In fact, the length needs to be equal to at least the double of the discontinuity to fill. Regarding the choice of the number of directions, the higher is the number of the directions, the more precise is the reconstruction. In fact, directional filter aims at reconstructing the fibers with respect to their neighborhood. Thus, if we consider more angles, our reconstruction will be sharper.

II.6.1.2 Results

The 2D directional filter works well to recover fibers continuities in the 2D plan. Figure II.14 shows an example of an image after the application of a 2D directional filter. One can see that the black regions present in the original image were suppressed. This is also valid for shadows. Besides, we were also able to delete fibers that are not relevant to the slice we are treating. It may introduce some smoothing effect but it does not drastically affect the global shape of the fibers. Besides, there is no notable impact on the fibers orientations in the space.

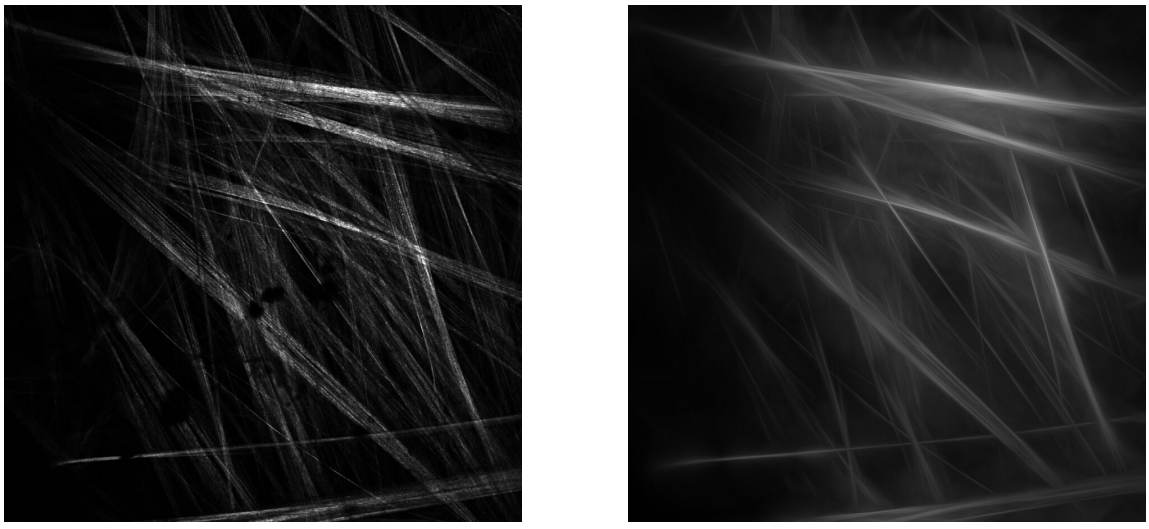

(a) (b)

FIGURE II.14 – (a) Original image, (b) Result after 2D Directional filter

In figure II.15, we shows another example of a segment of a collagen fiber where occurs a discontinuity in addition to the resulting image after the application of the 2D directional filter. As we can see, the fiber is reconstructed. Besides, the result can be harmonized a little bit more by applying a median filter. Furthermore, we were able to delete some fibers that are not relevant to the considered slice.

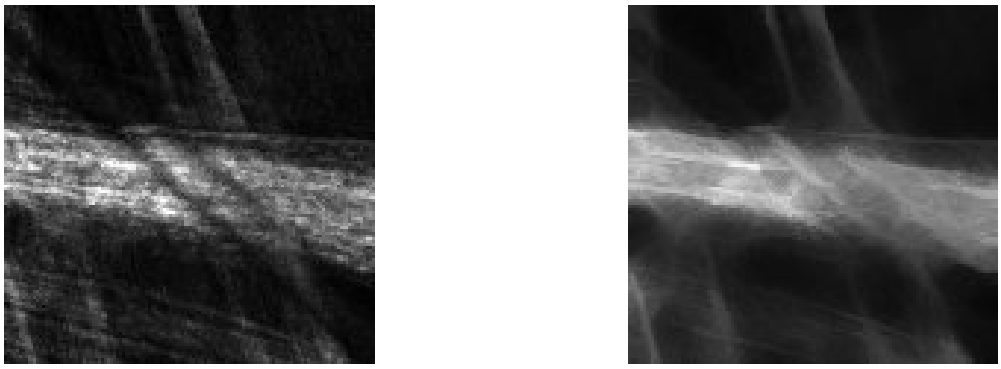

(a) (b)

FIGURE II.15 – (a) Original image, (b) Result after 2D Directional filter

II.6.2 3D directional filter

Here, we implement a 3D directional filter for the same purpose: reconstructing collagen fibers with discontinuities. It is important to mention that the 3D version is more computationally expensive than the 2D one.

II.6.2.1 Specifications

The 3D directional filter has the same specifications as the 2D version but with some tilt added along the z axis. Usually, in biological tissues, collagen fibers are not very tilted along the z axis (less than 5°). For this reason, we decide to introduce three different tilt angles: 1.5°, 3° and 4.5°. Thus, the number of direction is multiplied by four. Regarding the length of the filters, it follows the same characteristics as for 2D directional filters.

II.6.2.2 Results

Regarding collagen fibers reconstruction, the 3D directional filter achieve as good results as the 2D version. Figure II.16 shows the result after applying a 3D directional filter.

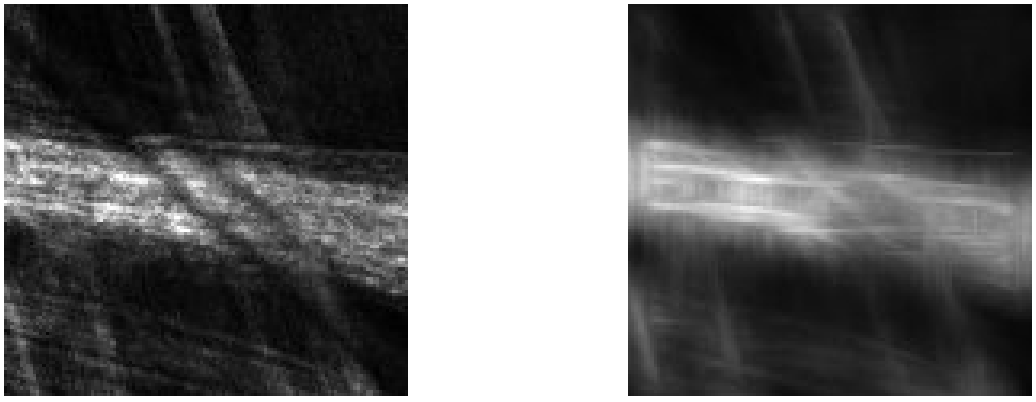

(a) (b)

FIGURE II.16 – (a) Original image, (b) Result after 3D Directional filter

The main contribution of the 3D directional filter is that we can distinguish a certain tilt along the z axis. In fact, if we analyze a section of the stack along one fiber, see figures II.17c and II.17f, we can notice that the fiber is quite tilted along the z axis.

II.6.3 Comparison

In order to compare the two types of filter, we applied them both on the same small part of an image where one can clearly see a fiber with at least one discontinuity. Then, we section the slice along the collagen fiber. This way, we can analyze the fiber's behaviour in the space. As previously introduced, the 3D directional filter allows having a better view of the collagen fiber orientations in the entire space, see figure II.17.

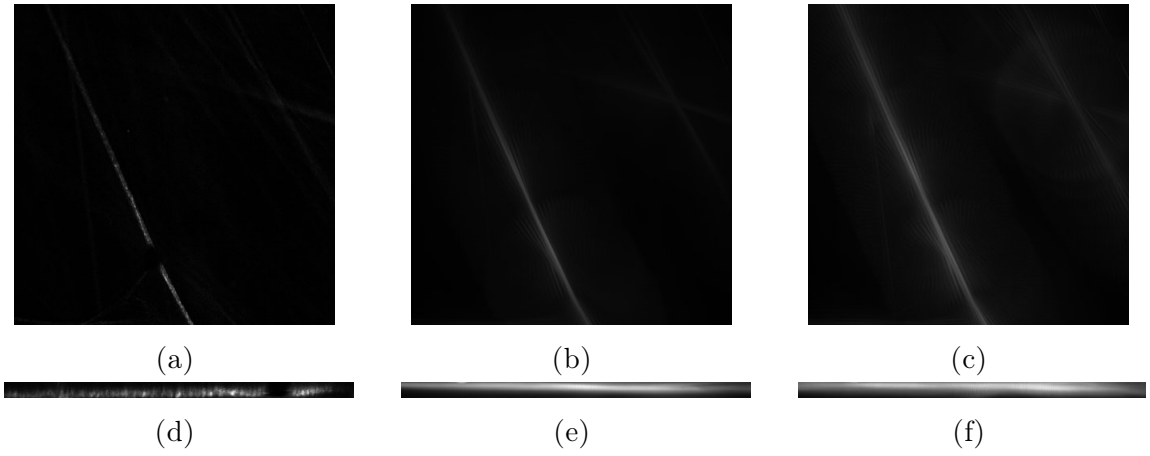

Figure II.17 – (a) Original image, (b) Result after 2D Directional filter and (c) Result after 3D Directional filter

However, these kind of filters may introduce some artifacts due to the effect of the bright pixels surrounding the fiber. The 3D directional filter introduces more artifacts than the 2D one since the number of surrounding pixels to take into consideration is higher (the neighbouring pixels in the 3D space). In fact, if we chose a high number of directions, the number of surrounding pixels will increase. The filter's length also has an impact on the result and the occurring artifacts. As a matter of fact, in the case there is a large discontinuity and some small one, if we use a high length, which allows to reconstruct the large discontinuity, on the small discontinuities, it adds some artifacts caused by some far fibers. In order to deal with this issue, it is possible to apply some morphological filters.

It is important to mention that the proposed directional filter works perfectly with straight fibers but may encounter some issues with undulated ones. In fact, for undulated fibers, if there is a large discontinuity, the proposed filter will reconstruct this fiber with a straight line without taking into consideration its real geometry. In order to deal with this problem, it is possible to apply a directional filter with small length subsequently. This way, the fiber is reconstructed step by step and thus, in a closer way to reality.

II.7 Noise reduction

Poisson noise is is dominant in SHG images of collagen fibers. After a deep investigation on the possible methods used to deal with it, we finally used the top-hat transform on the available 3D stacks. In the following, a description of the method as well as the results of its application will be exhibited.

II.7.1 Top-hat transform

The top-hat transform is a morphological operator based on erosion and dilation. We selected the white top-hat (WTH) as it is adapted to our case (white fibers over black background). It is defined as the difference between the input image and the results of its opening by some structuring element. It is expressed as:

$$WTH(Im) = Im - (Im \circ SE) \tag{II.8}$$

where Im is the image, SE is the structuring element and $\circ$ denotes the opening transform.

WTH keeps elements of the image that do not fit into the structuring element and that are brighter than their surroundings. It is usually used for uniforming illumination.

II.7.1.1 3D top-hat

We apply the 3D top-hat transform on a 3D stack. Here the structuring element is cube-shaped. It is expressed as:

$$WTH(Im(x,y,z)) = Im(x,y,z) - (Im(x,y,z) \circ SE(x,y,z)) \tag{II.9}$$

We conducted multiple tests on several stacks. Figure II.18 exhibits three results using structuring elements of sizes 7, 14 and 21.

The analysis of figure II.18 shows that the size of the SE has obviously a strong impact on the image. In fact, for higher sizes of SE, we notice that there are more fibers left on the slice than with lower sizes. This can also be seen on the section images. Besides, the noise present at the bottom of the stack remains whatever is the SE's size. The used 3D WTH has a cube as a structuring element. However, since the noise in SHG images is higher along the z axis, it is complicated to achieve a good reconstruction. When we compare the different results with the original stack, we notice that the 3D WTH may keep, in certain slices, some fibers which normally belong to a superior slice. In fact, when the size of the structuring element is not properly chosen, the algorithm will not succeed in dealing with the noise along the z axis even if, visually, the result is satisfying in the (x,y) plan.

II.7.1.2 1D top-hat

In order to deal with the unwanted presence of some fibers, we decided to apply a 1D WTH along the z axis. This transform consider the 3D stack as a set of lines. For

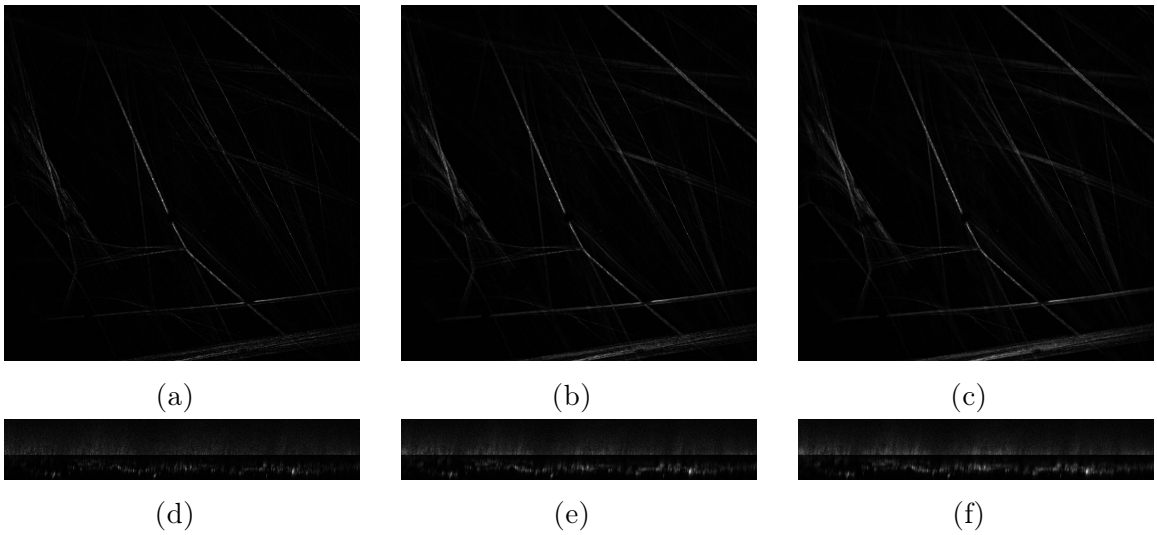

(a) (b) (c)

(d) (e) (f)

Figure II.18 – Impact of the SE size on the result: (a) result using a SE of size 7 pixels, (b) result using a SE of size 14 pixels, (c) result using a SE of size 21 pixels, (d) section along the z axis result using a SE of size 7 pixels, (e) section along the z axis result using a SE of size 14 pixels and (f) section along the z axis result using a SE of size 21 pixels

each line, it allows to deal with the noise occurring on it while preserving collagen fibers. The uni-dimensional top hat works the same as the 3D one except that the structuring element is also uni-dimensional and we apply it on along the z axis. It can be expressed as:

$$WTH(Im(x_i, y_j, z)) = Im(x_i, y_j, z) - (Im(x_i, y_j, z) \circ SE) \tag{II.10}$$

where i,j $\in$ 0...1023 which corresponds to the dimension of the images. This way, we focus more on the noise present in the z direction.

Tests on different stacks using different sizes of SE were conducted and the results are quite satisfying. With a structuring element of a size equal or slightly higher than the fiber's depth, the recovering of collagen fibers works well. In fact, this configuration allows to keep collagen fibers and delete the noise occurring in each line along the z axis. Figure II.19 shows an example of stack before and after the application of the 1D top-hat transform. The shown results corresponds to structuring element of a size of 12 pixels. The irrelevant fibers were deleted. In addition, from figures II.19c and II.19d, one can clearly see the fibers without all the noise present in the original image.

In figure II.20 we present another example of stack where we applied a 1D WTH of a size of 12 pixels. Here, we chose randomly the slice to show. If we compare figures II.20a and II.20b, we may think that the uni-dimensional top-hat transform suppresses important information. However, figures II.20a and II.20b, which correspond to a 3D view of the entire stack, show that our transform keeps the necessary information to recover a good 3D reconstruction and thus, a proper segmentation of the collagen fibers.

Several tests were conducted on different stacks and with different SEs. 1D WTH works well on all stacks. However, one should pay attention to fibers continuity that

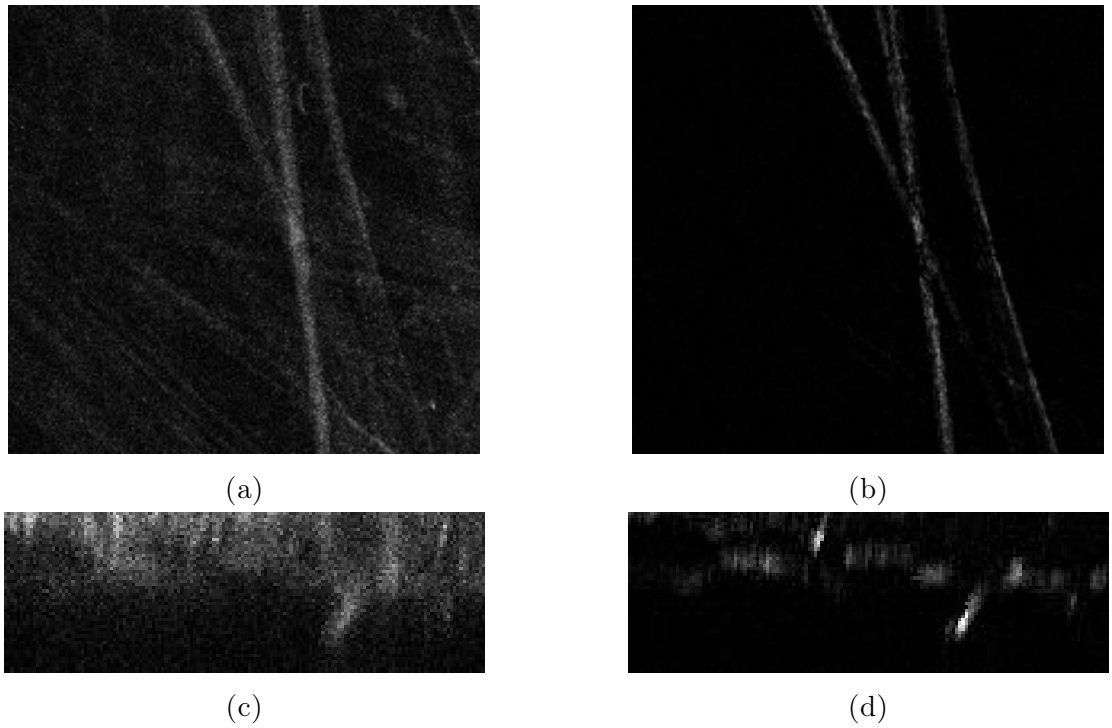

(a) (b)

(c) (d)

FIGURE II.19 – (a) original image, (b) result after 1D WTH, (c) section of the original stack and (d) section of the 1D WTH resulting stack

may be impacted by the size of the SE.

II.7.1.3 Comparison

The result of the 3D top-hat presents more noise than the result of the 1D top-hat, see figure II.21. In fact, by analyzing figure II.21a, one can clearly see that the 3D version keeps more fibers that the 1D WTH. However, the visual analysis of the original stack confirms that the fibers kept by the 3D WTH are not relevant to the slice we are studying. Thus, 1D WTH keeps the needed information in the 2D plan and suppress most of the noise which makes the fibers more distinguishable for the human eye.

In addition, when focusing on stacks sections on $x = 512$ and along the y axis, it is obvious that the fibers section are sharper and the noise is less present after the application of 1D WTH than with 3D WTH.

II.8 Combination of both techniques

Because of the artifacts that may be introduced by the directional filters, it is wiser to apply the top-hat transform before the application of the directional filter in order to limit the noise as much possible. In fact, when applied subsequently, those two techniques ensure a good reconstruction of the fibers with a minimum noise. Therefore, it is possible to apply once again a top-hat transform but this time in 3D after the directional filter. This way, the artifacts introduced by the directional filter are reduced. Figure II.22 shows the results after the application of each filter.

In this example, we used a 1D top-hat transform of size 11, a directional filter of length 120 and covering 101 directions as well as a 3D top-hat transform of size 2.

By reducing the noise, the 3D directional filter introduces less artifacts. Meanwhile, it may add some smoothing effect which can be seen when sectioning the stack as well as some artifacts caused by the considered high number of directions. This issue can be dealt with by using a 3D white top-hat transform. A small size of the structuring element for the 3D top-hat transform is chosen to reduce the noise as much as possible. This way, we recover a perfectly reconstructed fiber which can be later segmented easily.

II.9 Effect of the used filters on the collagen volume fraction

Because some information related to the stretch of the tissues during mechanical load are missing, in this section, we decided to work on 3D collagen SHG images of rabbit carotid artery provided by Krasny et al. [Kra+17]. In this dataset, we have multiple stacks which were captured under different loads. The idea here is to implement the top-hat transform with several sizes and to see its impact on the collagen volume fraction. In order to calculate the volume fraction, the stacks were segmented using Otsu's thresholding method after the application of each top-hat transform.

Furthermore, it is necessarily to establish a relationship between the volume fraction and the load applied on the aortic tissue. For this matter, we assume that the volume fraction of collagen fibers remains stable regardless of the mechanical load. In this case, the volume of the aortic tissue does not vary. This means that, when under load, the length of the specimen increases while the width and the depth vary accordingly. Thus, in terms of images, the x and y dimensions do not change since we are focusing on a small portion of the specimen. However, the z dimension should decrease with respect to the applied mechanical load. Unfortunately, it is not the case for some stacks. Figure II.23 shows two examples of the volume fraction evolution according to the size of the top-hat structuring element and the applied load.

One can notice in figure II.23 that, for each slice, the different curves have almost the same shape. But, unlike what is expected, there is no intersection point between all of them. From both figures II.23a and II.23b, one can say that the volume fraction drastically decreases when the mechanical load increases. This proves that the previous assumption claiming that the volume fraction is constant is not valid. In fact, even visually, one can clearly see that there is less collagen fibers when the specimen is under high loads. Besides, it is interesting to mention that, for some aortic tissue, the captured stacks according to different loads seems to not correspond to the exact same portion. The displacement during the acquisition may also have an impact on the volume fraction since we are comparing two stacks of two different specimen portions. To properly study the evolution of the volume fraction, it may be judicious to redo the acquisition while paying more attention to the portion to

capture. Unfortunately, for time consideration, that was not conducted in this PhD work.

II.10 Conclusion

In this chapter, we presented some new approaches to deal with the artifacts occurring in SHG images. The 3D directional filter showed satisfying results in reconstructing discontinuous collagen fibers. For the noise removal, we propose to perform a white top-hat transform on the SHG images. The uni-dimensional WTH gives excellent results in deleting the majority of the noise while keeping all the needed information to properly reconstruct a 3D view of the collagen fibers. This way, the segmentation becomes easy to perform. Besides, the combination of the WTH and 3D directional filters gives good results in both fiber reconstruction and noise reduction. The application of a 3D top-hat transform after the directional filter allows to deal with the artifacts introduced by the directional filter. With this in mind, the choice of the size of the structuring element of the WTH is really important in order to keep a consistent volume fraction. That is why, we conducted some tests on rabbit carotid arteries to evaluate the effect the size of the structuring element of the WTH on the collagen volume fraction. Unfortunately, these tests were not as conclusive as we expected.

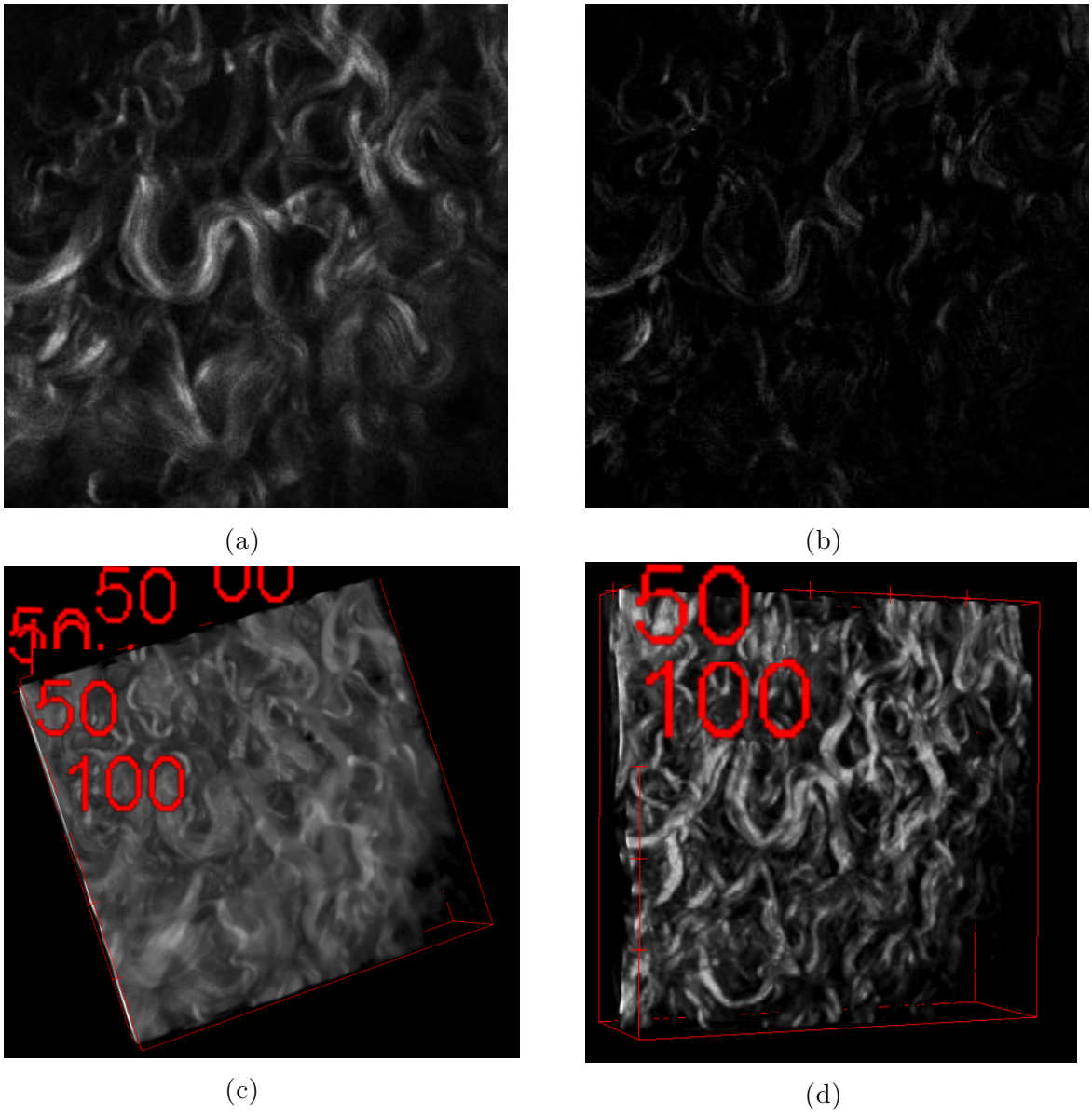

(a) (b)

(c) (d)

Figure II.20 – (a) Original crop, (b) Result after applying 1D WTH of size 12 (c) 3D view of the original crop (d) 3D view of the crop after applying 1D WTH of size 12

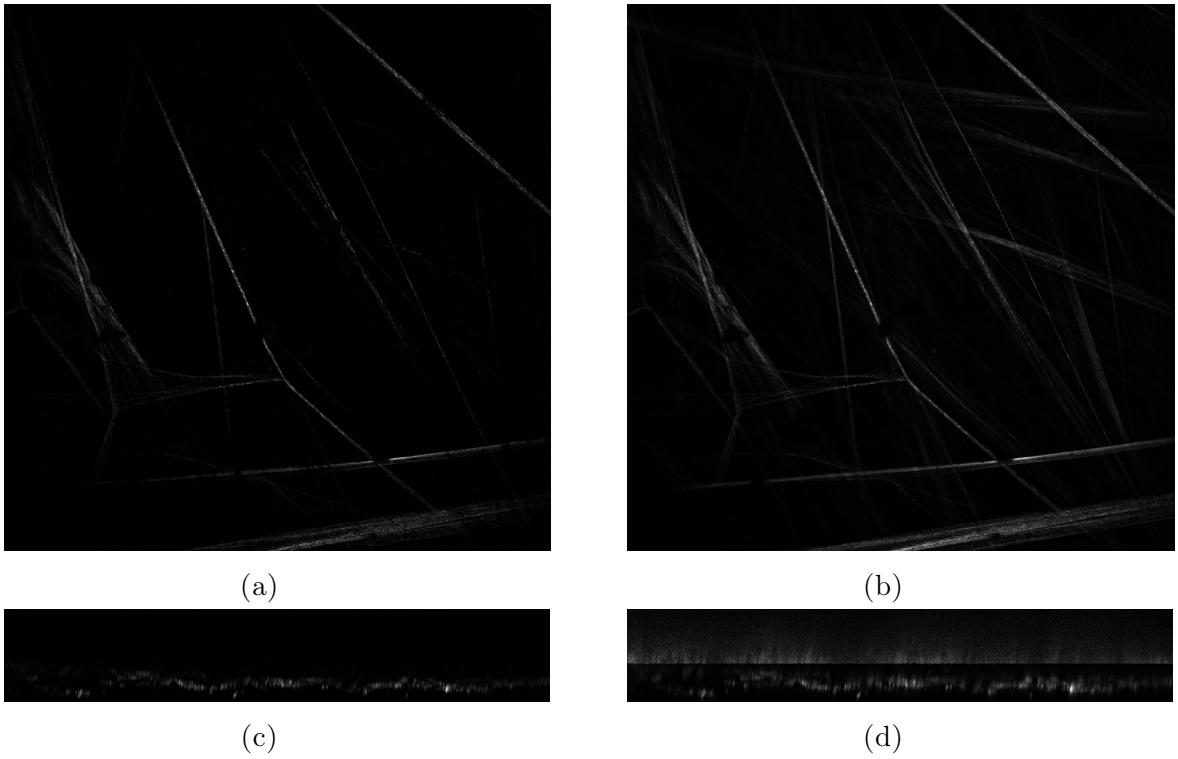

(a) (b)

(c) (d)

FIGURE II.21 – (a) Result after applying 1D WTH, (b) Result after applying 3D WTH (c) Section in the middle of the stack after the application of 1D WTH and (d) Section in the middle of the stack after the application of 3D WTH

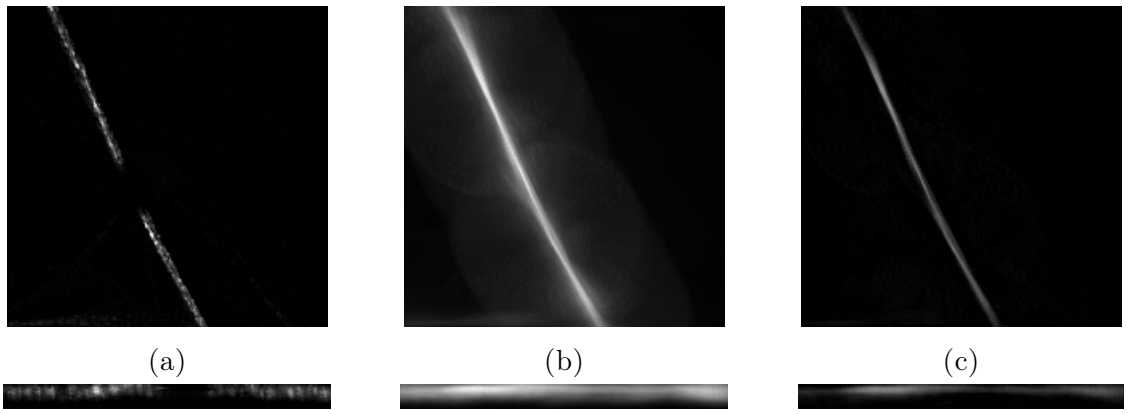

(a) (b) (c)

(d) (e) (f)

FIGURE II.22 – Results of the consecutive application of directional filters and top-hat transforms: (a) result using a SE of size 11, (b) result after using a 3D directional filter, (c) result after applying a 3D top-hat of size 2, (d) section of the fiber in (a) along the z axis, (e) section of the fiber in (b) along the z axis and (f) section of the fiber in (c) along the z axis

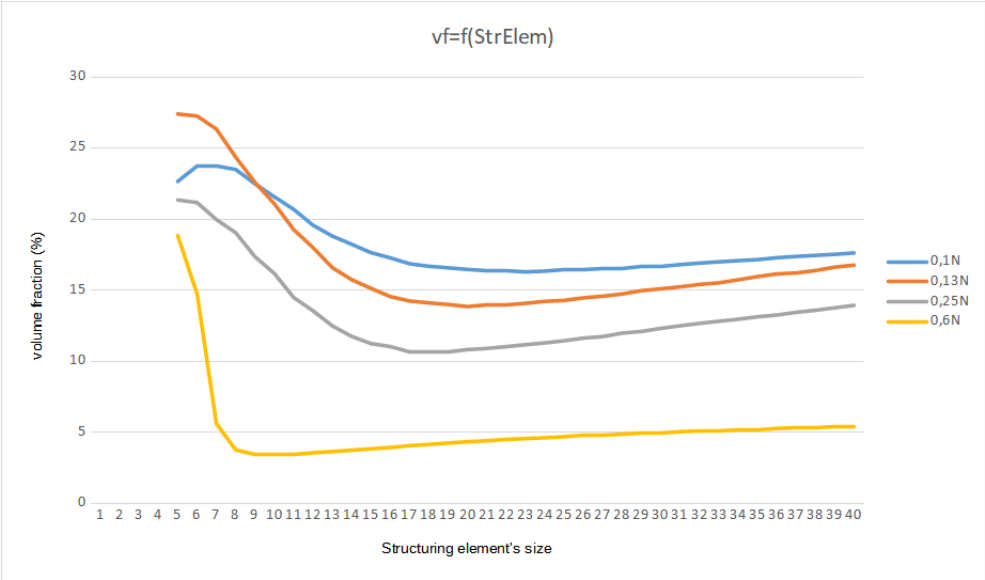

(a)

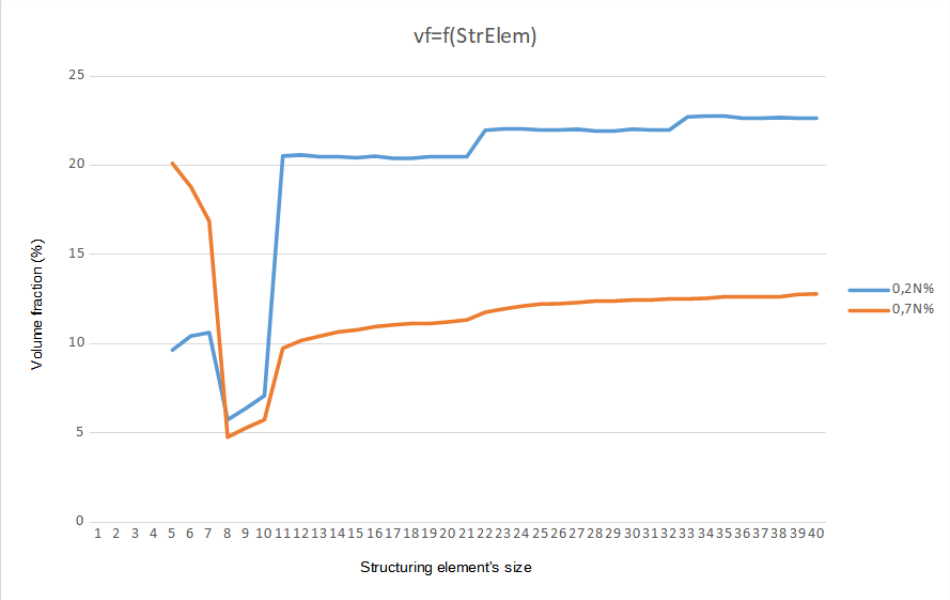

(b)

FIGURE II.23 – Two examples of the evolution of the collagen volume fraction according to the size of the top-hat structuring element

Chapter III

Quantitative analysis of SHG images: A state of the art

Contents of the chapter

III.1 Résumé du chapitre

Les fibres de collagène représentent le composant majeur de la matrice extracellulaire chez les mammifères. Par conséquent, l'étude de ces fibres est importante en vue de la caractérisation des tissus de connection. La microscopie basée sur la génération de seconde harmonique a souvent été utilisée pour acquérir des images de ces fibres à partir de tissus biologiques. L'analyse quantitative de ces images permet une fiable caractérisation des fibres de collagène. Plusieurs techniques ont été développées afin d'extraire des informations relatives aux fibres à partir d'images de seconde harmonique. Le présent état de l'art couvre les principales méthodes de traitement d'images qui ont servi à l'analyse quantitative d'images de microscopie de seconde harmonique ainsi que les différentes métriques pouvant être extraites de ce type d'images.

III.2 Abstract of the chapter

Collagen fibers represent the major component of the extracellular matrix in mammals in general. Thus, studying it is important to characterize connective tissues. For this matter, SHG microscopy was often used to capture these fibers in biological tissues and quantitative analysis of SHG images offers a reliable characterization of them. Different approaches have been developed in order to extract information from SHG images. This state-of-the-art covers the different image processing techniques used to quantitatively analyze SHG images as well as the multiple quantitative metrics that can be extracted from this type of images.

III.3 Introduction

Collagen fibers ensure keeping the arteries in general and the aorta in particular strong and holding it together. Understanding their geometry, morphology, composition and behaviour is a challenge facing the scientific community. In the literature,

multiple image processing techniques were used for this purpose. These techniques can be divided into two different categories namely techniques used to transform the image into another domain where it is possible to extract some quantitative information, and techniques aiming at selecting and extracting information directly from raw or pre-processed images. Meanwhile, these techniques did not include deep learning which, despite its great potential, is not widely used on SHG images.

It is important to mention that the choice of the image processing technique to use is very dependent on the information we want to extract or estimate. In fact, it depends on the scale one wants to analyze (i.e. global or local information). For example, regarding orientation estimation, the Fast Fourier Transform (FFT) is often used. It allows to recover a distribution of orientations describing the fibers in the considered image. On the other hand, for more local metrics like fiber sizes and lengths, statistics are often used.

In the present chapter, a focus is made on the analysis of those SHG images of collagen fibers and the different techniques that have been developed to extract information aiming at characterizing these fiber networks. A special emphasis is put on the accurate quantification of several quantities such as the fiber orientation, waviness and dimensions in addition to the collagen density. To this aim, the chapter is organized as follow: first, we will cover the question of how to extract quantitative information from collagen SHG images by describing some of the main image processing techniques used in the literature. Then, we will give a brief introduction of deep learning and the different possibilities it offers. Finally, we will go through the literature to present the used techniques and categorize them with respect to the information we want to extract from SHG images.

III.4 Goals behind the quantitative analysis of collagen fibers

The quantification of collagen fibers in biological tissues in general and in the arterial wall in particular can be used for different aims:

— For mechanical characterization: As introduced in section 2 of the first chapter, the orientation of collagen fibers can be taken into consideration to model the mechanical response of the considered specimen in the best way possible [HGO00 ; Mor+21].

— For organizational characterization: It is possible to follow the evolution of collagen fibers orientations when a biological tissue is under a mechanical load which can help with understanding the behaviour of the sample through aging and potential pathologies [GMM18 ; Bay+09].

— For morphological characterization: In fact, by quantifying collagen fibers features (length, diameter), it is possible to understand the impact of aging on the micro-structure [Wu+11 ; Wu+16].

— For composition characterization: It is possible to use the density of collagen in certain biological tissues and compare it with other samples to identify

cancerous cells [Hom+08 ; Ros+20].

III.5 How can quantitative information from SHG images be extracted?

The study of collagen fibers in the aortic wall is based on quantitative analysis of these micro-structures. For this matter, there are plenty of image processing techniques that help deducing and extracting important metrics from SHG images of collagen fibers. These techniques can be divided into two categories: (i) techniques based on image transformations where images are transformed into other representations and (ii) techniques aiming at selecting and extracting information from raw images. In this section, we will exhibit some of the main methods used to quantitatively analyze collagen fibers from SHG images.

III.5.1 Image transformations

A strong interest has been shown in signal decomposition because of the uneven distribution of signal energy in the frequency domain. It consists in dividing the signal spectrum into its sub-spectra, which are then treated individually [Aka01]. Signal decomposition has been used for many applications such as compression and feature extraction. For image analysis, and particularly for studying the collagen fibers in SHG images, several image decomposition methods have been used: the Fast Fourier Transform (FFT), the Wavelet Transform (WT), the Radon Transform (RT) and the Hough Transform (HT). Those methods will be summed up in table III.1.

III.5.1.1 Fast Fourier Transform (FFT)

The FFT is an efficient method to study the distribution of the pixels in an image in general. The FFT image represent a map of spatial frequencies of the initial image. It can be used with SHG images of highly oriented collagen fibers or not.

The Fourier Transform (FT) was initially used to characterize linear systems and to identify their frequency components that make a continuous waveform [Ber69]. To process images, the Discrete Fourier Transform (DFT) is used. This transform shares most of the continuous FT properties except that it is performed on finite intervals.

The DFT coefficients can be computed by the Fast Fourier Transform (FFT) which is a computationally cheap and fast algorithm originally introduced in 1965 by Cooley and Turkey [CLW69]. Different approaches can be chosen to compute the FFT [Rad68 ; Blu70 ; Bru78 ; Riv77]. For instance the Rivard [Riv77] algorithm decomposes the 2D FFT into two successive one-dimensional FFT.

Let f be the discrete function for which we want to compute the DFT. In one-dimensional space, the input of this function represents the time. The result of the DFT of f is a function of frequency.

It consists in combining vertical and horizontal 1D DFT of an array into one 2D transform that makes sense. One can first perform a 1D DFT over horizontal lines of an image (*figure* III.1). The result is a matrix M where the first column contains the zero frequencies which represent the average value of the intensity of each line. The k^{th} column represents the $k-1^{th}$ order harmonics of the line. Following this scheme, we are able to describe the intensity changes in the horizontal direction without taking into consideration the vertical changes [Zon04].

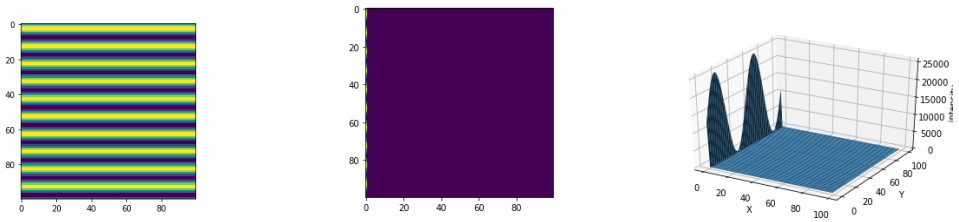

(a) (b) (c)

Figure III.1 – (a) Second derivative of a Gaussian kernel, (b) Ellipsoid described by the eigenvalues

To complete the 2D DFT, an additional 1D DFT is performed on the columns of M. In fact, any column can be considered as a function at a constant frequency and thus, one can apply a 1D DFT on it. This is possible because of the separability property of the DFT. The transform of any column of M is a spectrum of constant amplitude harmonics that may be combined to recover the column again. The zero-frequency component of the vertical 1D DFT is the average of all the zero frequency components of the entire horizontal transforms. It corresponds to the average intensity of the whole image.

The 2D FFT is an efficient operator to characterize an image and to capture the variation of its texture (*figure* III.1b). However, the notion of space is lost when the transition from space to frequency is performed. In fact, the 2D Fourier transform gives information about global changes in frequency without any knowledge regarding the section of the image corresponding to the frequency's change. Besides, Fourier transform may not work accurately to reconstruct an image which is highly non-smooth [JH13].

III.5.1.2 Wavelet Transform

Wavelet methods have become a powerful tool in image processing during the last twenty years. This is due to their ability to analyze non-stationary structures and characterize local properties. An image is mapped to a phase space which is parametrized by a scale/size/resolution and a time/space parameters. Wavelet transform is an alternative to the Fourier transform which characterizes the image in a time/space frequency space [Dah+08].

The word "wavelet" is synonym to "small wave". It was first introduced by Grossmann in 1984 [GM84]. It is introduced as an alternative to Fourier series and an elegant multi-resolution signal processing tool thanks to its ability to naturally vary the time-frequency resolution [Aka01]. It is a mathematical function of zero average

used to divide a function into components at different scales. Each scale is computed using a specific wavelet generated from an initial function named *mother wavelet* by dilation and translation. Figure III.2 shows some frequently used mother wavelets [SHB08]. These functions are defined in 1D as:

$$\psi_{(a,b)}(t) = \frac{1}{\sqrt{a}}\psi(\frac{t-b}{a}) \tag{III.1}$$

where a and b are the dilation and translation parameters. The dilation allows to carry out a multi-scale analysis and enables to capture small details. Thanks to this feature, wavelet transforms can be used for filtering, feature detection and compression.

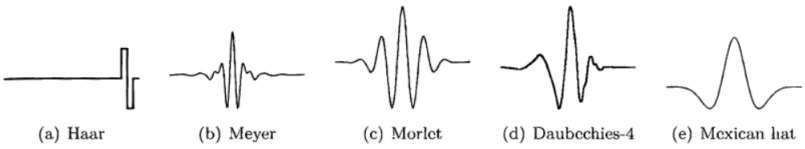

FIGURE III.2 – Famous wavelets

It is possible to perform a wavelet decomposition of an image (in 2D or even for higher dimensions) in order to compress the data or to obtain a vector of features which characterizes the data in a basis of wavelet. It is helpful to capture the orientations changes in an image. For this matter, we need to perform a 2D Discrete Wavelet Transform (DWT). As for the 2D FFT, it can be generated using the horizontal and vertical 1D DWT. In the case of images, the transformation scale in both direction is usually the same which simplifies the computations and gives square transforms.

The main advantages of the wavelet transform is that it provides a localization in both space and frequency domains. The wavelet transform allows to capture small and coarse details. Indeed, wavelet transforms over-perform traditional Fourier transforms in representing functions with sharp peaks discontinuities and in correctly decomposing and reconstructing non-stationary, non-periodic and finite signals [JH13]. In addition, it is possible to recover a good approximation of the initial image with few components which is not the case of the Fourier Transform. It can also be used to detect discontinuities and irregularities in signals. However, this technique is computationally expensive for fine decomposition. The choice of the mother wavelet and the number of decompositions can highly influence the result.

III.5.1.3 Radon Transform

The Radon transform is a mathematical transformation based on projections which is the basis of Computed Tomography (CT). It can also be used to detect edges. For SHG images, the Radon transform was usually used on the result of a FFT of the image to detect the fibers orientation.

The Radon transform consists in performing different projections of an image according to different angles. The resulting projection corresponds to the line integral

(i.e. the sum of the pixels intensities in every direction) [Dea07]. For an image f(x,y), its radon transform can be expressed as:

$$RT(\rho,\theta) = \int_{-\infty}^{\infty}\int_{-\infty}^{\infty} f(x,y)\delta(\rho - x\cos\theta - y\sin\theta)dxdy \tag{III.2}$$

where δ is the Dirac function and $\rho = x\cos\theta + y\sin\theta$

In other terms, the RT maps an image from Cartesian coordinates to polar ones. This transform can also be applied to 3D images. In this case, the integral is taken over planes. The RT data is usually referred to as sinograms.

The use of a FFT gives qualitative information about the fibers orientations. To deal with this issue, it is possible to apply an RT on the result of the FFT. Since it is based on projections, it gives quantitative information for each considered angle. It is important to have a sufficient number of angles to get accurate results in detecting and extracting the fiber orientations.

III.5.1.4 Hough Transform (HT)

The Hough transform [Hou62] was first introduced to detect lines in images. this algorithm was then simplified by duda et al. [DH72] and generalized to detect circles and curves.

The original HT algorithm assumes that every line in an image can be represented by a unique couple (slope, intercept). Duda et al. [DH72] changed this representation by the couple (angle, distance), where the angle and the distance correspond to the polar coordinates of a considered line in the image (the distance being the distance between the image origin and its projection on the line). A matrix called accumulator is created where its axes correspond to the parameters characterizing the line. Thus, for each pixel of the image, the accumulator is incremented for all possible lines passing through that pixel. The presence of an edge corresponds to a high value position in the accumulator [Lea92]. A reconstruction of the initial image is possible by retrieving the parameters corresponding to the peaks in the accumulator.

The HT gives good results when applied on an image where the edges were already detected. It works fine with noisy data. This method allows to reconstruct an edge if it is discontinuous when performing the edge detection algorithm. As a consequence, the application of the HT needs a prior step to detect the edges but does a good job in correcting those detected edges. For linear objects, the HT is a good method to detect edges orientation directly from the accumulator matrix. However, its effectiveness depends on the considered image: if two objects are aligned in an image, the HT will exhibit them as one.

III.5.1.5 Summary

The advantages and drawbacks of image transformations previously cited are applicable to SHG images. In fact, this type of images can be seen as an object (collagen fibers) and a background. The image's quality can vary with the noise and the blur. Thus, to analyze collagen fibers, one needs transformations that are able to extract information from SHG images. Some of these transformations certainly

depend on how fine one wants the analysis to be. In table III.1, we present a summary on the advantages and drawbacks of the previously mentioned transformations.

TABLE III.1 – Image transformation methods

Methods	Output	Advantages	Drawbacks
FFT	Complex representation of the image in the frequency domain	Captures the variation of the image texture	Loses spatial information Doesn't work properly with highly non-smooth images
WT	Decomposed image	Provides a localization in both space and frequency domains Detects discontinuities and irregularities Captures small and coarse details	The result highly depends on the choice of the mother wavelet Is computationally expensive for fine decomposition
RT	Projection data	Gives information with respect to the angle of projection	Depends on the chosen number of angles Is computationally expensive for fine analysis
HT	Polar map of the image	Corrects properly the detected edges Can be used to estimate objects orientations	Works better on detected edges Doesn't distinguish between objects if they are aligned

III.5.2 Information selection and extraction

After the pre-processing of an image, the SHG image analysis needs to extract as much valuable information as possible. For this matter, it is possible to extract these information through a spatial characterization or a statistical one. For both types of characterizations, many methods can be used. Some of them are detailed hereafter and will be summed up in table III.2.

III.5.2.1 Spatial information selection

To analyze an image, it is important to consider the spatial distribution of the pixel intensity. This is possible through several techniques: (i) segmentation, which transforms an SHG image into a binary image where only the collagen fibers are represented; (ii) skeletonization, which determines the center line of the collagen fibers in the SHG images and thus, allows to extract geometrical information about the fibers.

III.5.2.1.a Pixel-based segmentation

This type of segmentation aims to gather pixels corresponding to an object and mark them. It is based on their intensity similarity and spatial proximity. The (automatic) thresholding segmentation is the easiest method for image segmentation. Otsu thresholding algorithm [Ots79] is the most used one, especially on SHG images, because of its simplicity in addition to the fact that it works particularly well when the considered image contains two classes (an object and the background). Its principle is to find the threshold that maximizes the interclass variance of a two-classes histogram. In addition to this method, several other approaches exist to compute the threshold such as entropy-based thresholding [Kha+15], [LLF04], minimum error thresholding [KI86], moment-preserving thresholding [Tsa85] and fuzzy set thresholding [Tiz05]...

Thresholding decomposes the image gray scale information with respect to gray level of targeted objects. There are two types of thresholding segmentation: global and local. The global threshold looks at the global picture: it divides the image into two regions (background and target) regardless of the positions of objects. On the contrary, local thresholding looks for a threshold in a neighborhood around any pixel of the image.

The main advantages of thresholding techniques are their simplicity and their fast computation. This type of segmentation works well when the image's histogram presents two or more peaks. However, it is highly sensitive to the tackled problem and is specific to the considered image. In addition, it takes only into consideration the intensity of the pixel/voxel and not its spatial information which makes this method highly sensitive to noise [YH17]. In fact, small areas or isolated pixels can be classified as independent regions even though they represent noise or belong to another region. Besides, to segment SHG stacks where the pixels intensity decreases with depth, it is complicated to find a threshold that takes into consideration that phenomenon.

III.5.2.1.b Region-based segmentation

Unlike pixel-based segmentation which classifies a pixel based on its intensity value without taking into consideration the spatial context, region-based segmentation looks for pixels having similar features. Several techniques belong to this category such as region growing algorithm [AB94 ; MGM06], split and merge algorithm [DR03 ; CA10] and clustering [TS11]. Our interest is paid to the region growing algorithm since it has been used in quantifying SHG images of collagen.

First, the user selects initial seed points to be in a region. Then the algorithm checks iteratively if the adjacent pixels should be added to the region according to one or several of available criteria (gray scales texture, intensity, color, etc.) [YH17]. The algorithm then continues with the added pixels; it is an iterative algorithm. Many criteria can be used to determine if a pixel belongs to a region . For example, one can consider the difference between the considered pixel and the seed point values and check if it is smaller than a given value. Moreover, it is possible to choose more than one criterion for regional growth segmentation

Region-based segmentation allows to partition the image into sub-regions. However, those methods depend on the choice of seed points and do not work properly on non-smoothly varying regions. Besides, a threshold is needed as a criterion to construct the regions, thus, its choice is important. Finally, it is a local technique with no global view on the image and it is sensitive to noise which may lead to an over-segmentation.

III.5.2.1.c Edge-based segmentation

An important feature carrying information about objects is their borders i.e. the discontinuities in the pixels' intensity. To detect the gray levels discontinuities, the most common approach is based on detecting edges, which represents a set of connected pixels forming a boundary between two regions [GW18]. There is a gap between the pixels values of two adjacent regions. Those discontinuities can be either step edges or line edges. Step edges are characterized by the sudden change in the pixel intensity from a region to another. Line edges correspond to a sudden change of the pixel values followed by another sudden change to return to the initial value within a short distance [SR09]. However, in real images, it is impossible to find those types of edges because of the smoothing introduced by the optical systems (the effect of the PSF of the used microscope in the case of SHG images for example) or by the low frequency components of images. One can find ramp edges instead of step edges and roof edges instead of line edges, where the pixel intensity changes occur over a finite distance, figure III.3.

Such gaps can usually be detected with the help of differential operators such as the Sobel operator [Sob14], the Laplacian and the Laplacian of gaussians (also called Marr-Hildreth operator) [AR05], the Prewitt operator [Pre70] or the Kirsch operator [Kir71]. More sophisticated techniques such as the Hough transform were also used to determine image edges [Hou62]. Once the edges are detected, mathematical morphology operators (erosion, dilation, opening, closing, etc.) are used to

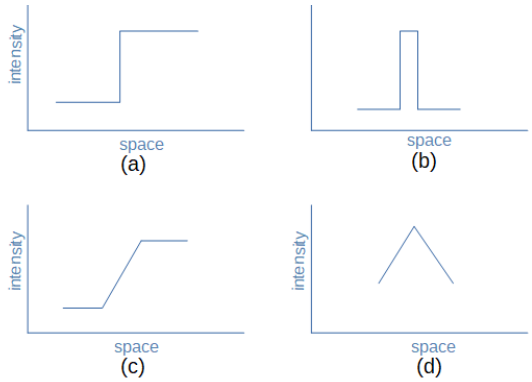

FIGURE III.3 – Edges types: (a) Step edge (b) Line edge (c) Ramp edge and (d) Roof edge

fill the targeted regions and, thus, segment the image.

Edge-based segmentation is a high-level segmentation approach similar to the way humans perceive an image. It works well on images with high contrast. However, it is highly sensitive to noise. It is centered on local information and does not take into consideration the global view. In addition, it doesn't work well to detect corners and when the contrast is low.

III.5.2.1.d Fast Marching Method (FMM)

The fast marching algorithm [MS96] allows to track objects boundary. It was initially developed to follow an interface or contour propagating under a speed function F [Car10] and was then used in medical applications. The FMM is a discretized and computationally optimized version of the level set method [OS88]. It aims at spreading an initial surface until it covers the entire surface of interest (the collagen fibers in our case) by solving the Eikonal equation:

$$|\nabla T|F = 1 \tag{III.3}$$

where T(x,y) is the time when the curve crosses the point (x,y).

It is based on computing a distance map between the initial surface and its surroundings. The surrounding points are divided into three regions: the accepted points, the narrow band and the far region. Initially, the accepted point region is the initial surface. The narrow band constitutes the closest pixel to the initial front. The far region is what is left of the image. The Eikonal equation is solved on the edge points of the initial surface. The points that satisfy this equation are then added to the initial surface and the same steps are applied again until there is no more points that may be added to the accepted point set.

The algorithm gives good results when the image is very distinct from its background. Besides, the use of such algorithm does not need a prior setting of the parametric representation of the surface contour to be followed: this technique is robust with respect to the topology to be analyzed. However, it relies entirely on a physical interpretation of the problem characterized by the isotropic front propagation of the initial surface [Cri09]. Besides, the use of the first-order neighbors (only

four neighbors) introduces errors in the computation of the travel-time from a point to another.

III.5.2.1.e CT-FIRE

The CT-FIRE is an algorithm introduced by Bredfeldt et al. [Bre+14] that enables the extraction of fibers through their skeletons. It was developed to extract collagen fibers from SHG images in order to estimate their orientation and geometric information.

This algorithm is based on two steps. The first one is a filtering using Curvelet Transform (CT). Curvelet filters were introduced by Starck et al. [SCD02] in order to overcome the limitation of highlighting lines and edges. The curvelet transform is a wavelet transform except that instead of the wavelets, curved functions called curvelets are used. The second step consists in applying the fiber extraction algorithm FIRE developed by Stein et al. [Ste+08]. It describes the fibers as a set of n vertices and p paths. Every path corresponds to a fiber characterized by k vertex identifiers ($p^i = {n_1}^i; {n_2}^i; ..., {n_k}^i$). The image is smoothed using a Gaussian filter before segmenting it through thresholding. Then, for each pixel of the segmented image, the euclidean distance map is computed. This map is used to identify the center lines of the fibers. Once the center lines identified, short non relevant fibers are deleted and close fibers are connected.

The CT step introduced in the CT-FIRE algorithm improved the result of the fibers extraction compared to the classic FIRE algorithm [Ste+08]. It provides better results when the collagen fibers are densely packed. However, for highly noisy images, other pre-processing techniques may be needed before applying the CT-FIRE algorithm. It also does not work well on images where the fibers are wavy and present a lot of intersections.

III.5.2.2 Statistical features extraction

The analysis of an image texture covers the region-specific identification of higher order properties which are hard to detect visually. Texture analysis leads to the definition of statistically uniform regions of an image based on the intensity distribution [Dud+19]. Statistical approaches that have been used to analyze SHG collagen images can be divided into three categories: first order statistics, second order statistics and directional statistics.

III.5.2.2.a First-Order Statistics (FOS)

First-order statistics estimates parameters derived directly from the image statistics. They are often used to simply describe the image intensity distribution. However, they ignore the spatial correlations between the pixels of the image. In other terms, FOS describes the probability to observe a pixel having a certain intensity in any position in the image. It includes *intensity distribution histogram* and standard parameters such as *mean*, *standard deviation*, *skewness* and *kurtosis* (respectively first, second, third and fourth statistical moments). Those metrics, in addition to

second-order statistics have been used for example by Wu et al. [Wu+16] to extract SHG image features changes that are associated to collagen aging process. In more details:

— *The intensity distribution histogram* is a representation of the number of pixels in an image with respect to their values. It is a useful tool to detect saturation effects in an image (i.e. presence of pixels with maximum intensity), to deduce the brightness (the image is bright if the histogram values are more concentrated around high values) and to check the contrast (if the values of the histogram are spread out without a noticeable peak);

— The *mean*, calculated from the pixels' intensity or from the probability distribution of the pixels' intensity, is used to evaluate the presence of one texture in the image. It consists in dividing the sum of pixels forming an image by the total number of pixels. With this value, one can compare it to other neighbouring pixels' intensity to determine if they belong to the same texture or not;

— The *standard deviation* captures how the pixels are spread out with respect to their intensity. A low standard deviation means that the pixels' values are around the mean value. A high standard deviation means that the pixels' values are dispersed from the mean value;

— The *skewness* evaluates the histogram's lack of symmetry and allows to characterize the slope of the image histogram with respect to the central line. The skewness of a normal distribution is equal to zero. A negative (resp. positive) skewness denotes an image for which the majority of pixels have values smaller (resp. greater) than the mean value. However, if the image data is multi-modal, the skewness sign can be affected;

— The *kurtosis* describes how much a distribution is concentrated around a peak (the mean) and allows to evaluate the efficiency of a denoising algorithm; There is a relation between asymmetry and the value of the *kurtosis*. In fact, when an image in asymmetrical, its histogram is wider, thus, its kurtosis is greater.

FOS are easy and fast to calculate. However, their interpretation is not always simple. They give global information and cannot be used to quantify local information (unless the initial image is divided into several ROIs).

III.5.2.2.b Second-Order Statistics (SOS)

Second-order statistics estimate parameters from the matrix generated by performing a correlation between the image pixels. It studies, in particular, the topology of one region compared to the image. Here we talk about texture analysis. This technique is usually used to describe and characterize a local area in an image through the use of Gray Level Co-occurrence Matrix (GLCM) [HSD73] and some statistics:

— The *GLCM* evaluates the spatial relationships between the values of the pixel intensity. It is a squared matrix of dimension equal to the number of gray levels in the considered image (for example, 256 for 8 bit images). The parameters

that will be presented subsequently [Iqb+21] can be calculated from the initial image but they are more relevant when they are performed on the GLCM.

— The *energy* (also called uniformity) allows to evaluate the uniformity of the image meaning that it detects disorders in the image textures. It is computed as the square root of the sum of square elements in GLCM. When the considered window is ordered, the energy is high;

— The *inverse difference moment (IDM)* measures the local homogeneity of an image. It is more sensitive to the presence of elements near the diagonal in the GLCM. When the IDM value increases, it means that the incidence of pixels' pairs co-occurrence is enhanced which means that IDM is high when the image is homogeneous. In other terms, its maximum is reached when elements in the image are the same;

— The *inertia* (also called contrast) allows to study local variations in an image by measuring the spatial frequency of the considered image. It represents the difference between the highest and lowest intensities of the neighbouring pixels. It is highly sensitive to large differences in the GLCM values and has a strong correlation with the lowest and highest values in a ROI. An image having a low inertia is characterized by a GLCM concentration term around the principle diagonal. Inertia and the IDM are inversely correlated;

— The *correlation* characterizes the gray levels linear dependency on specified pixels on an image (i.e. the repetitive nature of the texture element position). Correlation between pixels implies that there is a linear relationship between 2 adjacent pixels within the considered window. A low correlation texture means a low predictability of pixel relationships. Pixels are usually more highly correlated with close pixels than with distant ones;

— The *entropy* focuses on the randomness of regions in an image with respect to its neighborhood in terms of intensity distribution and thus, allows to detect subtle variations in the GLCM. Low entropy values correspond to a uniform and homogeneous image while high values correspond to unequal pixels intensity. Complex textures usually have high entropy. Entropy is strongly and inversely correlated to energy.

Texture analysis is widely used to measure a variety of characteristics or properties such as the way the studids material behaves and breaks, its structure etc. In the case of SHG images, it helps with studying the morphology of collagen fibers. Texture analysis can be performed on an entire image but it is more interesting to use it on a localized area in order to capture morphological changes. This technique allows seeing morphological modifications in the collagen structure (for example to make a comparison between a benign and a malignant tumor) such as in [Mos+13] but it does not give information about their geometric and composition information. In fact, GLCM and SOS focus mainly on the relations between neighbouring pixels which are suitable to study fiber local features.

III.5.2.2.c Directional statistics

Directional statistics focuses on observations that have directions. These observations usually lie whether on the circumference of a circle (circular statistics) or on the surface of a sphere or a hypersphere (spherical statistics) [LV17]. Statistical analysis of directional data became more used after Fisher's paper [Fis53] where he explained the need to consider the curved nature of the sample space. Several directional distributions emanated from Fisher's contribution. They are based on the extension of classical concepts from multivariate analysis (e.g. point estimation, regression, multi-sample testing procedure) to directional setting [PG20 ; Mar+08 ; MJ00].

In the following, we will focus on the *Von Mises distribution* which has been used to extract quantitative information from SHG images of collagen fibers.

The Von Mises distribution is considered as a flexible circular distribution. It is useful for a circle from a statistical inference point of view [MJ00]. It represents the maximum entropy distribution for circular data when the first circular moment real and imaginary parts are specified. It is characterized by two parameters, a location parameter $\mu \in [-\pi, \pi]$ and a concentration parameter κ. κ is positive and it allows to regulate the concentration of the distribution around μ. The probability density function of a Von Mises distribution is defined as:

$$g(\theta) = \frac{1}{2\pi I_0(\kappa)} \exp(\kappa \cos(\theta - \mu)) \tag{III.4}$$

where I_0 is the modified Bessel function of order 0 and of the first kind. This distribution was later generalized to higher dimensions by Von Mises and Fisher and thus, was named von Mises-Fisher distribution. For a bivariate Von Mises distribution, its probability density function is proportional to:

$$\begin{aligned} g(\theta, \psi) \propto \exp(\kappa_1 \cos(\theta - \mu_1) + \kappa_2 \cos(\psi - \mu_2) \\ +(\cos(\theta - \mu_1), \sin(\theta - \mu_1)) A (\cos(\psi - \mu_2), \sin(\psi - \mu_2))^T) \end{aligned} \tag{III.5}$$

The Von Mises distribution can also be referred to as the circular normal distribution. To characterize collagen in SHG images, it is possible to evaluate the fiber dispersion and its diameter by fitting a Von Mises distribution.

It is an interesting tool to study 3D images because it can be generalized to high dimensions without using a lot of parameters. However, for SHG images of collagen, this method assumes that all the fibers belong to a single family (i.e. having the same orientation).

III.5.2.3 Summary

Same as for image transformations, the cited information selection and extraction methods previously mentioned are well-suited for SHG images. CT-FIRE has even been developed for SHG images. This type of images, which are composed of collagen fibers and a background, is perfect for binary segmentation. Besides, the use of statistics is very compatible with the nature of these fibers (undulated, straight, noisy, discontinuous, etc.) since it allows to study their structure and texture. In

table III.2, we present a summary of the advantages and drawbacks of methods previously described.

TABLE III.2 – Information selection and extraction methods

Methods	Output	Advantages	Drawbacks
Thresholding	Binary image	Is simple and fast Works well for images having an histogram with distinct peaks Is a global method	Is highly sensitive to noise Is specific to the considered image
Region-based segmentation	Binary image	Allows to partition the image Works properly on smoothly varying regions	Depends on the choice of the seed points Is local technique with no global view
Edge-based segmentation	Binary image	Is a high-level segmentation approach Works well on images with good contrast	Is highly sensitive to noise Does a poor job detecting corners
FMM	Segmented image	Gives good results when the image is very distinct from its background Is robust and fast	Is a static technique The first-order nature introduces errors in computation
CT-FIRE	Fibers' skeleton	Works well on images of densely packed collagen fibers	Needs sometimes some additional preprocessing
FOS	Statistical information	Are fast and easy to implement	Give global information
SOS	Statistical information	Capture changes in images	Only give information on the fibers texture

Methods	Output	Advantages	Drawbacks
Directional statistics	Mathematical function	Fit well the orientation distribution profile of collagen fibers Can be generalized to higher dimensions with few parameters	Assume that the fibers follow one direction

III.5.3 The case of deep learning

Recently, in all fields of image analysis and processing, deep learning has emerged and has shown great results in different applications such as segmentation, regression and classification. Certainly, the use of deep learning on 3D images and SHG images is still limited but it shows promising results.

III.5.3.1 Definition

Deep learning is a sub-field of machine learning based on artificial neural networks with more than one hidden layer. These networks were developed to mimic the behaviour of the human brain by learning from a certain amount of data to do a certain task (predict, segment, classify, etc.). There are three different types of learning:

— supervised learning: it is an approach to make a system learn from a labeled dataset. The system is trained until it can detect interesting features and the relationship between the input data and the output labels. It is well suited for classification and regression applications. It aims at giving a meaning to the data in a specific context. Here, we need an expert to label the data correctly. Supervised learning is interesting to implement especially because it can give human-like judgment on the data. However, if the system is not trained with enough data in terms of number and categories, it will not perform well.

— unsupervised learning: unlike the supervised learning, for unsupervised learning, we do not have the equivalent of output label. It aims at modeling the underlying structure or distribution in the data in order to learn more information about the data. It is referred to as unsupervised because there is no need to have an expert to train the algorithm. In fact, the algorithm learns by its own. It is good for clustering and association applications. Certainly, it is interesting to use unsupervised learning when no labeled data and no expert are available. However, it can be slow and computationally complex. Besides, the risk of inaccurate results is higher and a human intervention is needed to validate the output.

— reinforcement learning: Inspired from behavioural psychology, it allows the system to learn from an interactive environment using feedback from its actions and experiences. It aims at learning the best action model to maximize the agent reward, the reward corresponding to the feedback from the environment. The feedback can obviously be rewarding positive behaviour of punishing negative behaviour. It is interesting to use reinforcement learning because it shows great results in learning from its environment. However, it presents some drawbacks: it may lose too much time if it does not proceed to the best actions.

With the development of fast computers and powerful GPUs, even deeper and more efficient neural networks have appeared. In fact, to ensure the proper functioning of the proposed network, it needs to learn from a high amount of data that covers all the possible changes related to our output. For this purpose, regarding the hardware, we need more performing GPUs and preferably higher memory. This

configuration allows the training of neural networks in a descent amount of time. This way, deep learning networks can reach a very high accuracy and can be very fast too. Besides, unlike other machine learning algorithms, deep learning performance increases when the amount of data increases too.

III.5.3.2 Basic principles

Deep neural networks are composed of an input layer, an output layer and multiple hidden layers. Each layer contains several neurons. A neuron can be seen as a mathematical function. It collects information following a specific architecture and aims at mimicking how the human brains learn. The neuron has three components: (i) a number of input connections with some weights, (ii) a number of output connections and (iii) an activation function, see figure III.4.

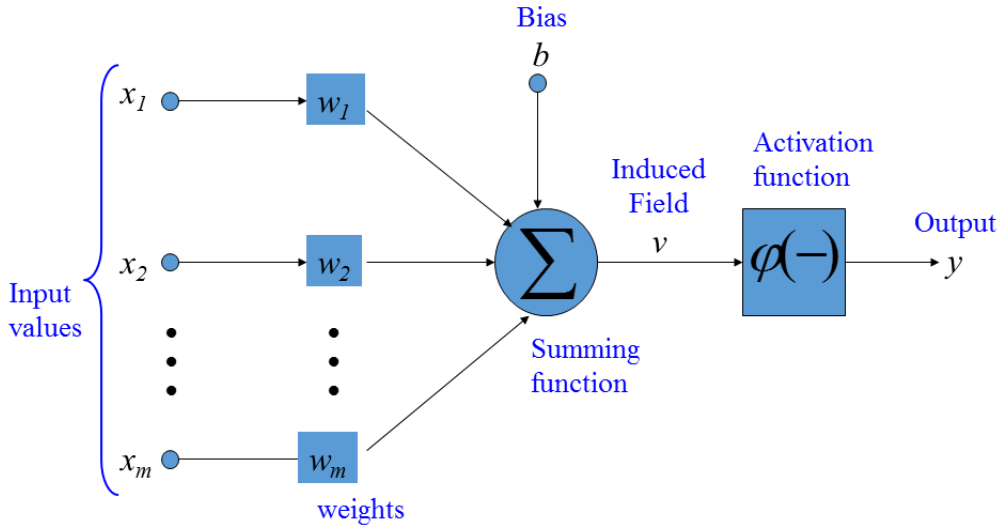

FIGURE III.4 – Graphical representation of an artificial neuron

The mathematical model of the output signal of a neuron j is expressed as:

$$y_j(w_j, b_j, x_j) = \varphi(b_j + \sum_{k=1}^{m} x_{jk}.w_{jk}) \tag{III.6}$$

where x_{jk} is the input signal from the neuron i to neuron j, $x_j = [x_{j1}, x_{j2}, ..., x_{jm}]$ is input signal vector of the neuron j, $w_j = [w_{j1}, w_{j2}, ..., w_{jm}]$ is the corresponding input weight vector, b_j is the bias of neuron j, and $\varphi()$ is a nonlinear activation function. The bias aims at shifting the activation function but it can be critical for proper learning. The activation function is a function aiming at helping the network learn complex patterns from the data. Basically, it is responsible of the nature of the value one wants to feed to the following neuron. In other terms, for each neuron, the activation function takes its input and convert it to a new value to transmit it to the following neuron. The main feature of an activation function is that it can introduce some non-linearity into a neural network. Among the classical activation functions, the most straightforward is the Heaviside step function which indicates if a neuron is firing or not. The choice of the activation function depends on the

desired objective (computational power, analytic tractability, and the type of the desired output signal (logistic or continuous) [Che+17]). Regarding the weights, they emphasize the most relevant inputs and penalize the less relevant inputs.

There are many types of neural networks. One can cite:

— Feed-forward Neural Network (FNN): It is the most classical architecture of neural networks. Here, there are only connections between each neuron and the neurons in the following layer. It is a unidirectional connection and there is no connection between neurons in the same layer. This explains the designation "feed-forward". This way, information propagates from the input layer to the output layer through the hidden layers. Figure III.5 shows an example of a simple FNN with two hidden layers.

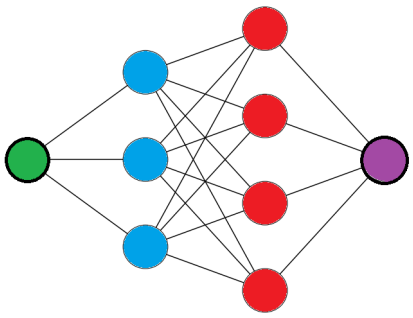

FIGURE III.5 – Graphical representation of a simple FNN

— Recurrent Neural Networks (RNN): They are usually used when the inputs and outputs of a certain neuron are dependent. This architecture allows connections between a neuron in a certain layer to a neuron in previous layers. This way, the output of the neural network not only depends on the current input but also on the historical input. In fact, it uses sequential information and exploits dynamic temporal behaviors. It can be seen as an artificial neural network that has memory. RNNs are usually used in time-related applications. However the learning process may take more time than for FNNs because each output of the activation function depends on data series recorded in RNNs.

— Spiking Neural Networks (SNN): SNNs are inspired from biological neural networks and the neuron activation. In fact, in biological neural networks, the communication between neurons is done through spikes. The voltage of a neuron is disrupted by incoming signals. Then, when the voltage reaches a certain threshold, the neuron transmits a short and high signal, which explains the designation "spike". After firing a spike, the neuron enters in a rest moment during which it cannot fire again. The use of this kind of spikes can improve the dynamics of the SNN. Thus, SNNs are faster than FNNs or RNNs and have higher information carriage capacity. In fact, SNNs can use lesser number of neurons than traditional neural networks. Besides, they can be used for real-time applications. However, the training process can become more time-consuming and more challenging.

III.5.3.3 Possible applications

Deep learning can be used for different purposes. In fact, it mainly depends on the result we want to achieve. Here, we will focus on three applications, namely image generation, regression, classification and segmentation. The list is obviously non exhaustive.

III.5.3.3.a Regression

Regressive networks are often used for prediction and estimation purposes. In this section, we will obviously focus on 2D and 3D images, which corresponds to the SHG images data. Regarding the output, it is a vector of one or multiple values (corresponding to the number of neurons in the output layer. The network is usually composed of 2 parts: convolutional layers and fully connected layers. The convolutional layers aims at convolving the input and passing it to the next layer. This way, the network is able to reduce the dimensions of the input and recover a feature vector which capture all the needed information to describe the initial image. This vector is then fed to some fully connected layers which aim at giving an estimation of a certain measure to be extracted. For example, regarding SHG images of collagen fibers, regression can be used to estimate the average fiber orientation, the average fiber diameter or the density. With this in mind, it has to be mentioned that, as far as we know, there were no publications that used regressive models to estimate measures from SHG images of collagen fibers. Through our literature review, we did not find any paper that used a regressive deep network to estimate information about collagen fibers. However, as an example of regression, on can cite [LLS17] where the author used a deep regressive network to estimate stress-strain responses of a chemically-treated collagenous tissue through SHG images.

III.5.3.3.b Classification

Classification consists of calculating a probability that an image represents a certain class. The common types of inputs are 2D or 3D images. Regarding the output, it is a vector of N probabilities, N being the number of classes to be considered. Classification neural networks are also composed of two parts: some convolutional layers to extract a feature vector from the input and some fully connected layers which map the feature vector to a vector of probabilities. For this matter, the soft max function is usually used as activation function of the output layer. Classification using deep learning is often used in medical imaging. For example, classification networks can be used to say if the images presents some anomalies or not (e.g. cancer). As far as we know, there are no direct application of classification on SHG images of collagen fibers. With this in mind, one can see the problem of orientation estimation as a classification problem. In fact, one can choose N orientations and classify the images with respect to fibers orientations. Regarding SHG images of collagen, classification represents the application that was mostly used. One can cite the work of Huttunen [Hut+18], where the authors classified SHG images using a CNN whether they represent healthy or cancerous ovaries.

III.5.3.3.c Segmentation

Segmentation consists in separating the different components of an image, like, for example, separating the object from its background. Again, inputs consist in 2D or 3D images. Regarding the output, it is an image with the same dimensions as the input. Classification neural networks are usually composed of two major parts: the first one is based on convolution and aims at extracting a feature vector from the input and the second part is based on deconvolution and aims at reconstructing a segmented image from the feature vector. To proceed to proper segmentation, the number of elements that one wants to extract from the image has to be fixed (in the case of SHG images, one can for example work with two elements which are the collagen fibers and the background). Segmentation using deep neural networks is often used in medical imaging and showed very good results. Performing algorithms exist for both 2D and 3D images. One can cite the work of [Sch+19], where a comparison of different 2D and 3D methods aiming at estimating local orientations was proposed.

III.6 Information to be extracted from SHG

In order to analyze and understand how collagen fibers behave when they are under a mechanical load, it is necessary to quantify them using some relevant information. In the literature, researchers focused on three types of information that can be extracted from SHG images of collagen fibers: its geometry, its composition and its morphology. However, they dealt with different types of input data (thus the output data were different) at different scales of measure. In the present section, we will exhibit how those information were extracted through the literature. It is important to say that we only found one paper in the literature where the authors used some deep learning to quantitatively analyze collagen fibers.

III.6.1 Geometric information (orientation, waviness)

A strong attention in the biomedical community is paid to geometric information of the collagen fibers. Changes in their geometric characteristics when they are under a mechanical load can actually be seen with a naked eye on SHG image, hence, the will to quantify it. Besides, their arrangement has a strong impact on the tissue's bio-mechanics.

III.6.1.1 Scale of measure

Orientation, waviness and curvature are the important Geometric information about collagen fibers. Orientation is usually calculated globally but sometimes, researchers shows interest in specific regions in an image and therefore they focus on the local directions. On the other hand, waviness and curvature are determined locally.

III.6.1.1.a Local characterization

The study of collagen fibers in biological tissues showed that those fibers are crimped and undulated. Thus, it is important to characterize their shapes. For this matter, several techniques have been proposed.

For the estimation of the fiber waviness, one needs to start by extracting the fibers. Sugita et al. [SM17] proposed an automated algorithm to compute the waviness of the collagen fibers. For this purpose, they determined the centers of the fibers as the pixels with a local maximum intensity. Then, they computed the length of the fiber as the distance between all the centers of a same fiber. Finally, they estimated the waviness as a ratio between the euclidean distance between the first and the last centers of one fiber and its length.

The CT-FIRE algorithm [Bre+14] is one of the techniques used to improve the images by extracting the fibers. Bredfeldt et al. used also their algorithm to extract the collagen fibers and then estimated the waviness. CT-FIRE was also used by [Bes+19] to extract the collagen fibers in renal cells carcinoma and by [Zho+17] in gastric cancer in order to characterize their organization and their straightness.

It is also possible to segment the SHG images and extract the collagen fibers using other methods such as the skeletonization. Koch et al. [Koc+14] proposed a new approach based on the application of several filters before segmenting the images. They used sequentially a CLAHE, a histogram adjustment and a Frangi filter to reduce the noise and enhance the fibrous information. Then, a threshold was applied to recover a binary image where the fibers are well defined. Finally, they applied mathematical morphology operators to retrieve the fibers skeleton.

Techniques which were not initially developed for quantifying collagen in SHG images were also used. The most known one is the NeuronJ plugin [Mei+04] of ImageJ software. This plugin was designed to characterize neurons which have a linear shape. NeuronJ was used for tracing the fibers and analyzing their waviness [Zya+17 ; Cho+14], [Zei+13]. Besides, a 3D implementation of this technique was proposed and tested on SHG images. For example, to determine the fiber arc length, Hill et al. [Hil+12] proceeded to a reconstruction of the SHG stack using a fast marching algorithm to trace the fibers.

Once an accurate extraction of the collagen fibers is reached, it is possible to compute the waviness as a ratio between the euclidean distance between the starting and ending points of a fiber and its actual length [Hil+12 ; Koc+14 ; APB19]. The estimation of those distances is done manually using ImageJ (National Institutes of Health, Bethesda, MD, USA) or Imaris (Bitplane, CT, USA).

The waviness in the 3D space was also investigated by Luo et al. [LCK17]. They proceeded to a 3D skeletonization based on the fast marching algorithm. The waviness computation is similar to what has been explained before, except that the considered points have 3D coordinates.

Regarding the local orientation, some interesting techniques were tested on collagen gels and showed their efficiency. One can cite the work of Bayan et al. [Bay+09] where they used the Hough transform on different small partitions of the SHG image to determine the dominant local orientation of the considered fiber. The size of the

partitions is chosen such as they are likely to contain a linear fiber. The SHG images were pre-processed to delete the noise through an adaptive thresholding and the application of an erosion and a dilation if needed.

It is also possible to evaluate orientations after fibers extraction. In [Koc+14], the authors used the segmented skeleton to calculate the local orientation as the angle of the tangent line between the first and last points in a considered segment. Some other researchers used the FFT to evaluate the local orientation, [Siv+10 ; RMT09 ; Amb+12a ; LAT12]. For example, Rao et al. [RMT09] focused on the preferred orientation and the maximum spatial frequency of some regions in the SHG images. To determine those metrics, they computed the 2D FFT of the considered regions. The FFT gives the perpendicular angle to the dominant direction. To have a better quantitative approximation, one can fit the probability distributions of fiber orientations using one Gaussian function [SM17]. It is also possible to apply a 3D FFT on the entire stack to evaluate the fibers most frequent direction in the space [LAT12]. However, the poor resolution of the SHG images in the third dimension may have a bad impact on the result of the 3D FFT to estimate fiber directions in space.

Wavelet transforms were also used for the direction's estimation [Til+14]. The properties of the wavelet transform allow to capture small details and thus estimate correctly the orientation of the fibers. For this matter, the local coefficients of the wavelet transform were calculated and then clustered using K-Nearest Neighbors (K-NN) [Alt92] and Principal Component Analysis (PCA) [Pea01].

Image gradient is an efficient method to estimate orientations. This technique was initially developed by Chaudhuri et al. [CKS93]. It consists in computing the gradient of the image to detect edges and then to keep only the most relevant direction. The proposed method is similar to the Hough transform. It was later applied to biological tissues [Kar+98] and to SHG images in particular such as in [Hil+12 ; Phi+14 ; Kab+13 ; SBZ15]. In [Kab+13], the authors focused on a ROI from initial SHG image where fibers have a pronounced dominant direction and calculated its 2D gradient to estimate the fiber's orientation. Gradient calculation has proven its efficiency over time to estimate orientations. For this purpose, it is possible to combine it with its related weighted 2D structure tensors at each pixel. This has been implemented in the powerful plugin OrientationJ available in ImageJ. Cavinato et al. [Cav+17] used this plugin to extract the orientation distribution histogram which was fitted using Gaussian functions to accurately quantify the dominant fibers directions. In [ÁB15], the authors also used it on the images structure tensor.

Even though most of the proposed methods that have been used to quantify collagen fiber orientation were performed in 2D, some researcher such as Liu at al. [Liu+18] took into consideration the collagen fiber distribution in the 3D space. They used the 3D directional variance algorithm to identify each pixel orientation and then estimate the entire fiber orientation.

More recently with the emergence of deep learning algorithms, some authors applied this technique to estimate local orientations of collagen fibers. For example, in [Sch+19], a comparison of different 2D and 3D methods aiming at estimating local orientations was reported. Besides, the authors introduced a new modality to

transfer 2D weights to 3D weight in different network architectures to perform a segmentation of some images with respect to local orientations.

III.6.1.1.b Global characterization

Most of the scientific contributions aiming at extracting quantitative information from SHG images of collagen fibers in biological tissues focused on the fibers orientation.

It is possible to determine fiber orientations using the FFT. It is the most used technique for this matter [APB19; Bue+13; Chi10; Cho+14; LCD19; LAT12; Rob+16; Siv+10; Wu+11; Pij+19; For+21]. This approach is also called FT-SHG imaging [Amb+12a]. In [LCD19], the authors used the FFT on each image of corneal lamellae stacks and then performed a segmentation on the transformed images to only keep the dominant fiber directions. Once the segmentation achieved, it is possible to recover the angle distribution that corresponds to each image. It is then possible to evaluate the variation of the angles while going deeper in the stack. Germann et al. [GMM18] used the same methodology as Bueno et al. [Bue+13], based on some pre-processing (noise reduction and edge sharpening) and a FFT to extract the orientation of collagen fibers in SHG corneal images.

Usually, the use of the FFT is sufficient to estimate fiber directions but it can be useful to make the procedure more automated. For example, Ayyalasomayajula et al. [APB19] extracted the distribution using a finite mixture of Von Mises distribution to fit the orientation distribution extracted from the FFT in order to determine the global mean orientation. Others, such as [Sch+13] and [Pol+13] used a classical Von Mises distribution for the same purpose. It is also possible to use a Gaussian function for the fitting such as in [Amb+12b] where the authors tested the FT-SHG on several human breast tissues. In some papers [Bri+15; Tan+14; Wu+11; Krö+21], the focus was oriented toward the result of the FFT where an ellipse was superimposed. The major axis of this ellipse corresponds to the orthogonal of the dominant direction if the ratio between the major and the minor axes is high. Otherwise, there is no preferable orientation. Besides, it may be useful to use the Radon transform on the 2D FFT of the SHG images [McL15], [Meg+12] since, unlike the FFT, it provides quantitative information for each discrete angle. It is also common to use wedge filters after the FFT and then fit the orientation distribution with a Von Mises distribution to better estimate the orientation [Pol+13; Sch+13; Nie+16]. In [Zei+17], the author applied an FFT on the images. Then, they improved the result of the transform by smoothing and enhancing it.

Directional filters were also used to determine the local orientation of the collagen fibers. Wen et al. [Wen+14] proposed an approach based on those filters with different scales to determine the collagen fibers orientation in ovarian cancer. They extracted a histogram of the frequency of occurrence of individual patterns in an image. A nearest neighbor classification was then performed on the extracted histograms to distinguish between human normal and high grade malignant ovarian tissues.

Some local techniques such as texture analysis have been used to quantify and

describe the main fiber orientation. They showed their efficiency and they may be also more precise than the classic FFT. In fact, Hu et al. [Hu+12] proposed a new approach for texture analysis based on orientation-dependent gray level co-occurrence matrix. They used their algorithm on ex vivo rat tendons to study the dominant collagen fiber direction. For this matter, they focused on the correlation feature of the GLCM.

III.6.1.2 Input data nature (2D / projected 3D / 3D)

The determination of the orientation and the waviness of collagen fibers can be done using different types of input. Multi-photon microscopes allow to go deeper in the tissue, and one can recover 3D stacks of images. However, most of the proposed techniques in the literature were limited to the image plane.

Generally, 2D images are used. For example, Zyablitskaya et al. [Zya+17] used 2D SHG image of rabbit sclera to estimate the waviness of the collagen fibers. In addition, to assess the accuracy of their measurements, they calculated the average value on 10 SHG images. Ayyalasomayajula et al. [APB19] used 2D images but limited their study to 10 slices of the stack. Then, the global orientation was set as the average of the computed orientations.

However, for the computation of the waviness of the collagen fibers, some papers processed 3D images such as in [Hil+12], so they were able to characterize this metric in 3D in arterial tissues. In this paper, the waviness was computed from a 3D reconstruction of the SHG images by tracing the fibers using a 2D marching algorithm. This is possible because the waviness estimation is based on coordinates which can be deduced from 3D SHG images. Meanwhile, an accurate 3D reconstruction of the SHG image may be hard to get because of the poor data resolution in the third dimension.

Regarding the orientation measurements, Hill et al. [Hil+12] and Cavinato et al. [Zha20] used a 2D superimposed projection of the 3D stack of SHG images. Phillippi et al. [Phi+14] succeeded in evaluating both collagen and elastin fibers in the aorta using superimposed 2D image stacks. The dominant orientation from a projection of all the SHG stack images can be extracted to recover a 2D image that contains all information from the entire stack [Hri+18]. However, it is more common to use 2D images to estimate the orientation [Bue+13 ; Kab+13] and look at its evolution with respect to the stack depth [LCD19].

Some studies showed that the collagen fiber orientation in the axial–radial direction is negligible [HH12 ; WM09]. However, in [LAT12], the authors proposed a 3D FFT approach to evaluate the fiber dominant orientation in 3D stacks of SHG images. SHG stacks were also used to determine the waviness of the fibers such as in [LCK17]. Bivariate Von Mises distribution was used by the authors of [Nie+16] on 3D stacks of collagen in the aorta to fit the in-plane and out-of-plane collagen fiber orientations.

III.6.1.3 Output data nature

The outputs of all the methods cited above can be divided into two types: a single value or an orientation distribution (i.e. a list). For example, the use of the FFT followed by ellipse fitting [Bri+15 ; Tan+14 ; Wu+11] gives one value corresponding to the dominant orientation in the considered stack or ROI. Single orientation values can also be extracted using texture analysis which is applied locally [Hu+12]. It is also possible to extract an orientation distribution histogram from the FFT by the application of a Radon transform for example [McL15 ; Meg+12] or by extracting the orientation distribution from the FFT and fit a Von Mises distribution on it [Pol+13 ; Sch+13 ; APB19 ; Nie+16]. Histogram of the frequency of occurrence is another representation of the orientation. It has been used in [Wen+14].

III.6.2 Composition information (density)

Fiber density estimation is important for collagen characterization. In the literature, there are two ways to define the density: the volume occupied by the fibers in the stack (i.e. volume fraction) or the number of fibers in a considered region.

III.6.2.1 Scale of measure

The scale of measure depends on what has to be quantified. For volume fraction estimation, the procedure is global and applied to the entire stack. It may be interesting for some applications to focus on a ROI in the stack and calculate its volume fraction (for example to characterize the evolution of tumor density). The same reasoning is applicable to calculate the density as the number of fibers in the entire stack or in a ROI. However, for an accurate estimation of the density, it is important to choose a ROI that covers up to 10 times the collagen fiber diameter.

In order to evaluate the fiber density, it is mandatory to enhance the SHG image by improving the signal to noise ratio. For this matter, it is important to filter the image and to recover an accurate representation of the fiber network through segmentation [Hom+08] or fiber extraction [Weg+17].

Gade et al. [GRC19] performed a segmentation on the SHG stack using the Otsu thresholding. Then they computed the area of segmented pixels in every slice and sum up the segmented area across the volume to calculate total areal density in the image stack. The same procedure was followed by Balu et al. [Bal+14] and Tjin et al. [Tji+14] where they performed a thresholding based on the mean and the standard deviation of the considered image to exclude background emissions. Then they computed the collagen area (which corresponds to our definition of density) as the sum of the pixels that have intensity values greater than a certain threshold.

It is sometimes interesting to proceed to a complete image enhancement step, because of the diminution of the pixel intensity when one goes deeper in the stack. For this matter, it is useful to apply a CLAHE on the SHG images. Cai et al. [Cai+14] enhanced the dermal layer of human skin SHG images using the CLAHE algorithm. Then, they applied the Frangi filter and a segmentation using Otsu's tresholding in order to capture a representation of both the fibers and the holes in

the images to finally have the best evaluation of the collagen fiber volume fraction.

CT-FIRE was used in [Bes+19], [Weg+17] and [Zho+17] to extract the collagen fibers. For example, in [Bes+19], the authors extracted the collagen in renal cell carcinoma in order to evaluate the density of the collagen in low and high grade tumors. The density can be calculated as the number of pixels corresponding to the fiber network with respect to the image or to the entire stack.

Second-order statistics in general and the Grey Level Co-Occurrence Matrix in particular have been used to estimate the density of collagen fibers. In [Krö+21], the authors used the GLCM and especially the homogeneity parameter to determine the density of features in an image.

Some papers such as [AH10 ; Lin+05 ; Koe+06] focused on the estimation of the ratio of both collagen and elastin fibers in SHG stacks. In [AH10], the authors started by filtering the images to reduce the noise. Then, they segmented the images and estimated the volume fraction of the fiber network as the sum of all the pixels belonging to the segmented region.

III.6.2.2 Input data nature (2D / projected 3D / 3D)

The computation of the fibers density (also referred to as the volume fraction) requires the entire stack. The evaluation of the density can be done in 2D (i.e. slice per slice) or directly on the entire stack. It depends on how the segmentation is performed (in 2D or 3D).

Cai et al. [Cai+14] were interested in 2D virtual biopsy images and not stacks. So, they tested their approach only on single 2D images. In [Zho+17], the authors focused on single SHG images and, thus, calculated the collagen density in the 2D plane.

In general, SHG images are segmented separately. For example, in [GRC19] and [Bal+14], the authors segmented the SHG images using a thresholding technique. Then, they calculated the amount of white pixels in every image and summed them up across the volume to calculate total 3D density.

A global overview of the stack gives more accurate estimations of the collagen density. Abraham et al. [AH10] implemented their method on the entire SHG stack.

III.6.2.3 Output data nature

The estimation of the density is a single value. This measure can whether represent the density of the entire stack [AH10] or the density of a specific SHG image [GRC19 ; Bal+14].

III.6.3 Morphologic information (fiber's size)

In addition to geometric and composition information, it is necessary to know the fiber morphology in order to have a complete picture of the considered microstructure. For this matter, the intersections between the collagen fibers and the fiber size have been investigated in the literature.

III.6.3.1 Scale of measure

The study of the intersection between the collagen fibers and even the estimation of their size are done locally because they are specific to a fiber (size) or a region (intersection). In order to be able to extract those information from the SHG images, it is important to enhance them.

For example, Koch et al. [Koc+14] used segmented SHG images to estimate the fiber diameter. They performed some mathematical morphology operators (erosion and dilation) to obtain a 1-pixel thick fiber skeleton. This skeleton was later used to calculate the fibers radii from the initial segmented image.

In some cases depending on the application, only the characterization of the evolution of the morphology is needed. For this matter, texture analysis is used. In [Wu+16], the authors used this technique to study the impact of aging on the skin microstructure. They computed the contrast, correlation and entropy from the GLCM of the image and analyzed them to estimate the fiber structure and morphology. The contrast was computed to assess the presence of a fine structure of collagen fibrils. Wu et al. [Wu+16] characterized how the collagen matrix is distinct from its surrounding and if there is loss in collagen through time using the computation of correlation. This can be generalized to distinguish between the collagen fibers and thus, estimate their diameter [Cic+09]. It is also possible to deduce if there are linear fibers and a fine structure through the computation of the entropy [Wu+16].

Some researchers showed interest in evaluating the fibers length. In [SM17], the authors extracted the centers of each fiber assuming that they correspond to a maximum intensity value and then estimated the fiber length as the sum of the distances between their centers. The fiber length can be evaluated manually from the SHG images of collagen gels after segmentation and using ImageJ drawing tool [Aje+11].

Moreover, collagen fibers that are extracted using the CT-FIRE algorithm can be used to extract manually the length and the fibers diameter [Ros+20 ; Zho+17 ; Dri+16 ; Weg+17]. In [Ros+20], the collagen fibers in every SHG image of feline mammary adenocarcinoma were identified by the mean of the CT-FIRE algorithm. Once the fiber extraction achieved, each fiber was analyzed and its length and width were extracted in addition to the percentage of straight fibers.

Some out-of the box techniques were used. For instance, Robinson et al. [Rob+16] estimated the collagen fibers thickness using the BoneJ plugin for ImageJ [Dou+10] which was initially developed to measure bones geometry. This algorithm gives the thickness of a considered fiber.

III.6.3.2 Input data nature (2D / projected 3D / 3D)

For texture analysis, the application is done usually on 2D images. Indeed, Wu et al. [Wu+16] were only interested in investigating some layers of the dermis with the strongest collagen intensity. In [Cic+09], the investigation was also limited to 2D SHG images of human dermis.

In the case of a skeletonization such as in [Koc+14], the authors used 2 2D images (one of the fibers skeleton and one of the enhanced image) to determine the

fibers radii. In addition, to estimate the fibers length, they used the skeleton of the fibers. Sugita et al. [SM17] focused also on the fiber length and used 2D SHG images since the fiber centers were determined in the 2D plane. It is also possible to extract the fiber network using the CT-FIRE algorithm and determine the fiber length and diameter [Zho+17], [Dri+16].

Papers that considered segmentation of the SHG images focused on each image individually and did not apply the segmentation to the entire stack [Aje+11].

III.6.3.3 Output data nature

The estimation of the length and the thickness of the collagen fibers from SHG images is usually done manually after some operations to extract the center line of the fibers (using skeletonization or local maximum intensity). The result is, thus, a numerical value for each measure and each fiber.

III.6.4 Summary

Table III.3 – Main methods used in the literature

Measure		Methods	References
Waviness	Locally	local maximum intensity	[SM17]
		Manual (ImageJ, Imaris)	[Hil+12], [APB19]
		CT-FIRE	[Bes+19], [Zho+17], [Bre+14]
		Skeletonization	[Koc+14], [LCK17]
		NeuronJ	[Zya+17], [Cho+14], [Zei+13]
		FMM	[Hil+12]
Orientation	Locally	Segmentation + Hough transform	[Bay+09]
		skeletonization	[Koc+14]
		FFT	[Siv+10], [RMT09], [Amb+12a], [LAT12], [SM17]
		Wavelet transform	[Til+14]
		Gradient	[Hil+12], [Phi+14], [Kab+13], [SBZ15], [Cav+17], [ÁB15]
		3D directional variance	[Liu+18]

Measure		Methods	References
	Globally	FFT	[Bue+13], [Chi10] [Cho+14], [LCD19], [LAT12], [Rob+16], [Zei+17] [Siv+10], [Wu+11], [Pij+19], [GMM18]
		FFT + Von Mises	[APB19]
		FFT + Wedge filter + Von Mises	[Pol+13], [Sch+13], [Nie+16]
		FFT + Gaussian	[Amb+12b]
		FFT + ellipse fitting	[Bri+15], [Tan+14], [Wu+11]
		FFT + Radon transform	[McL15], [Meg+12]
		Directional filters	[Wen+14]
		Texture analysis	[Hu+12]
Density		Segmentation	[GRC19], [Bal+14], [Tji+14], [Cai+14], [AH10], [Lin+05], [Koe+06]
		CT-FIRE	[Bes+19], [Weg+17] [Zho+17]
Size		Manual	[Aje+11]
		BoneJ	[Rob+16]
		Skeletonization	[Koc+14]
		Local maximum intensity	[SM17]
		Texture analysis	[Wu+16], [Cic+09]
		CT-FIRE	[Ros+20], [Zho+17], [Dri+16] [Weg+17]

III.7 Conclusion

The quantitative analysis of collagen fibers through SHG images can be very challenging considering the large number of possibilities among available image processing methods. These methods can be divided with respect to the quantitative metric we want to extract from the images (information about the geometry, the morphology or the composition of collagen fibers). However, through our review of the state of the art, we noticed that machine learning techniques and especially deep learning algorithms were missing despite the outstanding results that these algorithms showed in different applications such as object detection, medical image segmentation and image denoising. Besides, most of the proposed approaches in the literature focused on 2D images and neglected the 3D aspect of the fibers. The second part of this thesis aims at dealing with these problems by realizing the following

aspects:

Propose a new approach based on deep learning to estimate collagen fibers orientation in the 3D space: For this matter, we developed a synthetic dataset containing 3D images of fibers. We made sure that these images resemble as much as possible the original ones. Then, we propose a CNN aiming at estimating the global orientations of collagen fibers. In chapter 4, different tested deep networks will be presented as well as the obtained results.

Compare our approach with existing methods: The estimation of global orientations from 3D images may differ from the one from 2D images. In fact, when the orientation is estimated in the 2D plan, it only takes into consideration the fibers of that plan. However, when the fibers orientation estimation is performed in the 3D space, it takes into consideration all the fibers in the space. If these fibers do not have the same orientation as the ones in the 2D plan, the global orientation estimation will be different. In chapter 5, the efficiency of the final network presented in chapter 4 will be tested and compared.

Chapter IV

Orientation estimation of collagen fibers using deep learning

Contents of the chapter

IV.1 Résumé du chapitre

Les réseaux de fibres de collagène sont connus pour jouer un rôle important dans la réponse mécanique des tissus biologiques quand ils sont soumis à certaines charges. Afin d'étudier cette réponse, l'orientation des fibres de collagène est souvent estimée. Plusieurs techniques ont été développées à cette fin mais, à notre connaissance, l'utilisation de l'apprentissage profond reste limitée. De plus, la majorité de ces méthodes traitent uniquement des images 2D. Dans le but de proposer une première tentative d'estimation des orientations des fibres de collagène à partir d'image de seconde harmonique 3D utilisant l'apprentissage profond, un jeu de données contenant des milliers d'images 3D de fibres synthétiques a été crée et utilisé pour entrainer deux réseaux de neurones convolutionnels. L'estimation de l'orientation des fibres dans le plan (x,y) est réussie et donne de bons résultats sur des images réelles. Par contre, l'orientation suivant l'axe z ne fonctionne pas proprement à cause de la présence du bruit selon cette direction.

IV.2 Abstract of the chapter

Fibrous collagen networks are well known to play an important role in the mechanical response of biological tissue when they are under some loads. In order to study this response, collagen fiber orientation is usually estimated. Multiple techniques have been developed for this purpose but, to our knowledge, did not include deep learning approaches and in general focused on 2D. To propose a first attempt to estimate fiber orientations from 3D images using deep learning, a dataset of synthetic fibers was developed and was used to train two convolutional neural networks in order to estimate fiber orientations (along x and z axes). Only the estimation of the orientation in the (x,y) plan succeeded and showed satisfying results when tested on real stacks.

IV.3 Introduction

Collagen is the most abundant protein in the human body. It is considered as structural since it is responsible of the maintain of the strength and the elasticity of the body's connective tissues. Thus, directionality and orientation information of collagen fibers are very useful for the determination of bio-mechanical properties of biological tissues.

Recently, computational and experimental methods have been combined to model soft tissues mechanical behaviour and SHG imaging became the new standard in analyzing collagen fiber networks [Cav+17 ; APB19]. Collecting SHG images of collagen networks was made possible through two-photon microscopes and powerful infrared lasers. Most of the published papers focus on the quantitative analysis of collagen fibers especially the estimation of their orientations in the 2D space. The most common method used for this purpose is the Fast Fourier Transform (FFT) [SM17 ; Amb+12a ; Rob+16] which is sometimes combined with other techniques

such as the Radon transform [Dea07] and ellipse fitting distribution [Bri+15]. However, since SHG imaging provides 3D stacks of collagen fibers, it is interesting to consider evaluating fiber orientations in space. Besides, modern techniques, such as deep learning, proved their efficiency in dealing with large data but their use on SHG images is still limited.

In this chapter, we start by introducing a developed dataset of synthetic fibers. This dataset is used in a new approach to estimate collagen fibes orientations from SHG images. This approach is based on deep convolutional neural network. Then, we describe different architectures that have been tested as well as their corresponding results.

IV.4 Strategy

Orientation estimation of collagen fibers can be sometimes challenging when the images are noisy. In addition, improving the images is also as challenging as the previously mentioned task and the result is not always adequate. In fact, the result depends on the used microscope and image processing techniques. In order to deal with this issue, it may be interesting to use a deep learning approach to resolve it. This approach consists in using some 3D synthetic images where fiber orientations are known to estimate fibers orientations in real images. Figure IV.1 gives an overview this strategy.

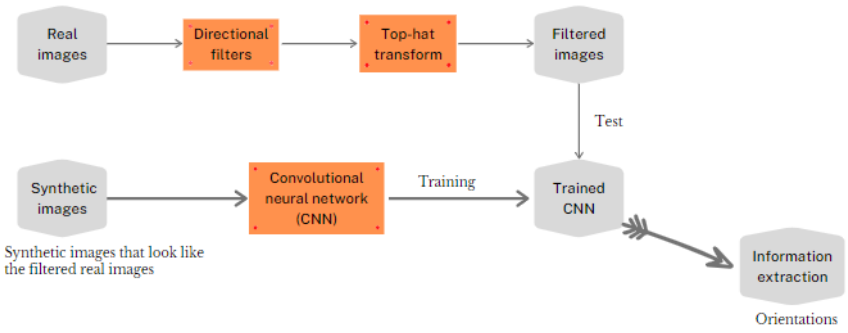

FIGURE IV.1 – Overview of the proposed approach

Our method consists in using deep learning and more precisely Convolutional Neural Networks (CNN) to estimate collagen fiber orientations from SHG images. We chose to propose a neural network for each orientation estimation. For this matter, we need a consistent amount of data to train the network. This phase is only feasible when an annotated dataset is available. In fact, we are following a supervised learning approach where our network is trained with 3D images and the corresponding orientation of collagen fibers.

In order to describe the collagen fibers in the 3D space, two angles must be estimated: θ the angle in the plan and ϕ the fiber orientation along the z axis (see figure IV.2). In the following, all orientations are estimated in degrees.

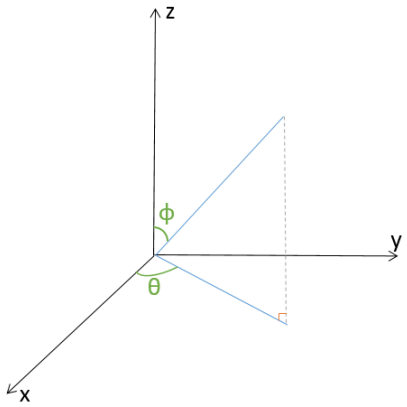

FIGURE IV.2 – Representation of the angles to estimate

IV.4.1 Annotated dataset

We dispose of a set of 3D SHG images of collagen fibers captured from the adventitial layer of human and animal aortas. These stacks could not be used for the training process of our network since information about collagen fiber orientations is not labelled. For this matter, a new synthetic dataset was elaborated.

The creation of this dataset was based on collagen fiber characteristics in biological tissues. In fact, those fibers are usually undulated in a resting state and they form straighter lines when they are under a mechanical load. Thus, in the creation process of our synthetic stacks, we chose to have random fibers representations in each stack. Here is a list of the global parameters that are randomly chosen to generate a 3D stack of fibers:

— The number of fibers: in a given stack, there are between 20 and 99 fibers.

— The mean and the standard deviation values for θ (θ is assumed to follow a normal distribution).

— The mean and the standard deviation values for ϕ (ϕ is assumed to follow a normal distribution).

— The density of the synthetic fibers. This value is calculated after the creation of the image. Thus, it is not linked to the generation process.

In addition to the above mentioned global parameters, we need some information about each one of the fibers in the stack. These information are:

— Starting point X: it corresponds to the x coordinate of the starting point of the considered fiber.

— Starting point Y: it corresponds to the y coordinate of the starting point of the considered fiber.

— Starting point Z: it corresponds to the z coordinate of the starting point of the considered fiber.

— θ: the orientation of the considered fiber along the x axis. θ varies between 0 and 360 degrees.

— ϕ: the orientation of the considered fiber along the z axis. ϕ varies between 0 and 180 degrees. Certainly, ϕ is very small (around 5°) but here we exagge-

rate this angle in order to generalize our network to any orientation or stack rotation.

— Fiber length: the length of the considered fiber. This measure needs to be greater than 10 pixels in order to be easily visible to the human eye.

— Radius: in the creation process of the fibers, we assume the collagen fibers have circular section so the radius corresponds to this section. It varies between 1 and 3 pixels.

— Amplitude, Frequency and the Phase: since the fibers are usually undulated, we assume that this undulation can be approximated by a sine wave. Thus, it can be expressed as: $z = Asin(2\pi fn + \xi)$, where n describes the direction to follow. To have an acceptable configuration without exaggerations, the amplitude A is set to vary between 1 and 3, the phase ξ is set to vary between 0 and 180 degrees and the frequency f is set to vary between 0 (the fiber is linear if it is too short (i.e. less than 15 pixels)) and $\frac{fiberlength}{10}$

These information are saved into a JSON file to make its use easier. Figure IV.3 shows an example of information used to create a synthetic fibers stack.


```
{"Number of fibers": 20,
"Fiber 0": {"Starting pointX": 46, "Starting pointY": 1, "Starting pointZ": 62,
"Theta": 293.7235148507031, "Phi": 150.63297161241357, "Amplitude": 3,
"Frequency": 3, "Radius": 2, "Fiber length": 72, "Phase": 15},

...

"Fiber 19": {"Starting pointX": 117, "Starting pointY": 35, "Starting pointZ": 52,
"Theta": 292.3451433860117, "Phi": 150.6921315494187, "Amplitude": 0,
"Frequency": 0, "Radius": 3, "Fiber length": 15, "Phase": 0},

"density": 666.3648319244385,
"theta_mean": 294,
"theta_std": 2,
"phi_mean": 152,
"phi_std": 1}
```


FIGURE IV.3 – Example of parameters used to create a synthetic stack

Because the training process of deep neural networks necessitates a consistent amount of data, we generated 4000 3D stacks containing between 20 and 99 fibers which corresponds to 50 stacks per number of fibers. For hardware and time considerations, the choice of the images dimensions is set to 128x128x64 pixels. Figure IV.4 shows some examples of generated stacks.

IV.4.2 Make real and synthetic images similar

The goal of the present chapter is to estimate collagen fiber orientations from real images. For this matter, the available images of the adventitial layer are pre-processed using the top-hat transform and the directional filter previously presented (see chapter 2). Certainly, the resulting images may sometimes still present some issues especially due to the directional filter.

On the other hand, the synthetic images contains sharp and well defined fibers. It is then essential to downgrade the synthetic dataset to make its images' regularity

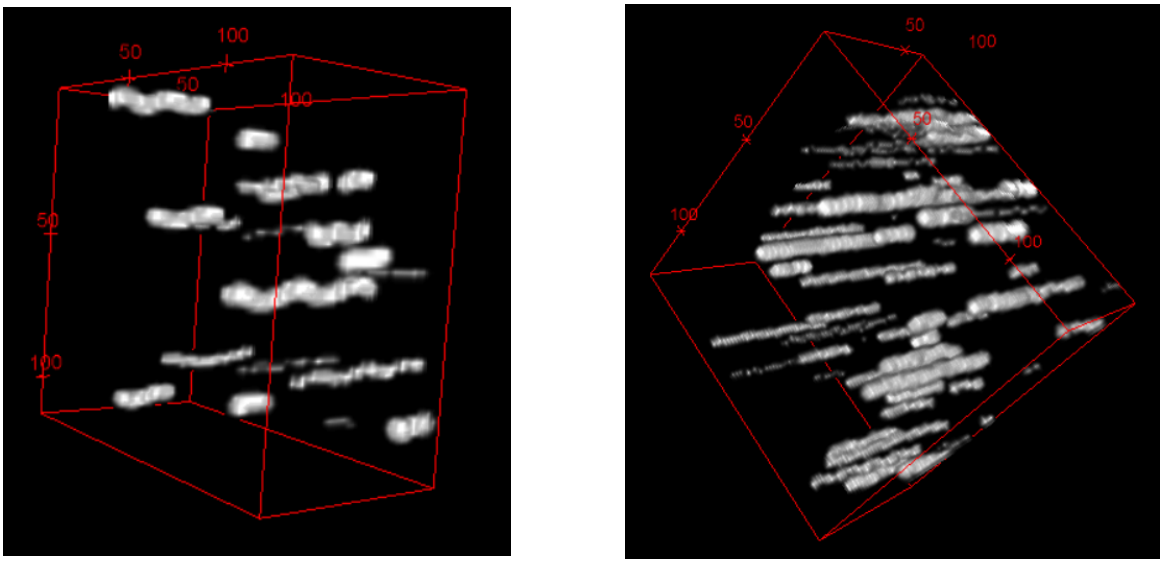

(a) (b)

FIGURE IV.4 – (a) Original image, (b) Result after 3D Directional filter

similar to the real ones. We decided to apply a Gaussian filter to the synthetic images. This Gaussian filter is applied to mimic the effect of the directional filter and any additional noise left after the application of the top-hat transform. Besides, training the network with images having some noise participates in making the network more robust and allows it to be more accurate in estimating collagen fiber orientations from fibrous tissues in general.

Because of the dimensions we chose for the training dataset, synthetic images may be compared to real image regions with the same dimensions. Thus, orientations obtained from synthetic images can be considered as local for real stacks.

Meanwhile, some configurations of fiber orientations can not be obtained with our algorithms. Figure IV.5 shows an example of SHG image of collagen fibers captured from the adventitial layer of carotid artery of a rabbit. The global fiber orientation is not even clear for the human eye.

IV.4.3 Estimation

For collagen fiber orientations estimation, we decided to use a regressive form of a CNN. It is also possible to perform a classification, however, in order to have a fine estimation, it is necessary to set a high number of classes which may cause the computation to be expensive and slow. The developed dataset was used to apply a supervised learning approach on our network.

As far as we know, there are no other publications that addressed the question of orientation estimation by using regressive neural networks. Thus, we tested several architectures. Meanwhile, all the tested architectures were composed of two parts: some convolutional layers and some fully connected layers. The main differences affect two aspects:

— The structure of convolutional layers: the term convolutional layer refers to a block of 3 components namely a certain number (1 or 2) of convolutions, a

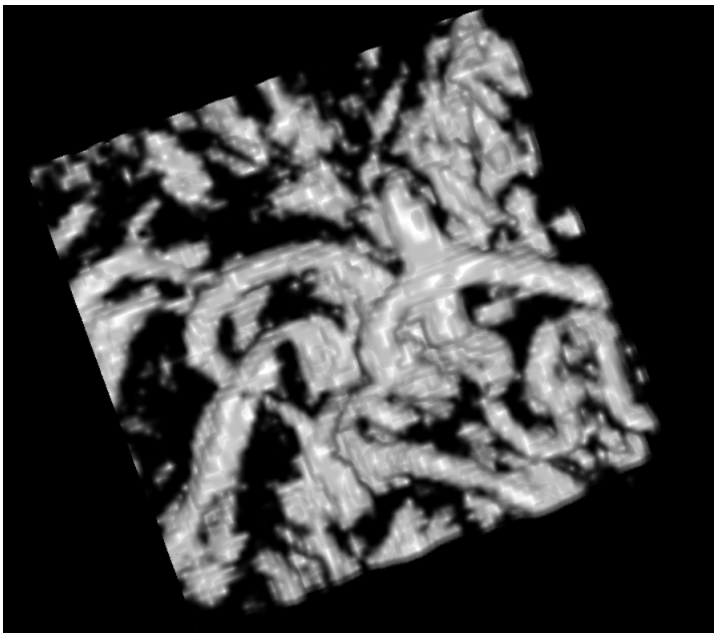

Figure IV.5 – Example of real stack where the fibers do not have a pre-dominant orientation

max pooling and a normalization.

— The number of convolutional layers: this parameter usually depends on the image dimensions and the number of convolutions per layer.

— The number of fully connected layers: it has an impact on the complexity of the network however, it may make the architecture converge faster.

We started our tests with an example of 3D CNN published in keras website by Hasib Zunair [Zun]. This network aimed at classifying some medical images to say if there is cancer or not. Obviously, in our application, we change the output to have an estimation of fibers orientations. More details of the conducted tests are presented in the following section.

The choice of the learning rate, the optimizer and the loss function were driven by the results of multiple tests. We chose to work with a learning rate that decays as long as the training progresses. The learning rate intervenes when computing the loss. The loss is based on a minimization. The starting learning rate (a high value) helps in reaching the minimum fast while small values allow to make a fine minimization to reach the exact minimum value. In our case, the learning rate starts with the value of 0.0001 and then decreases following an exponential shape. Regarding the optimizer, it is the Adam algorithm [KB17] that was chosen. Adam stands for adaptive moment estimation. It aims at optimizing stochastic objective function through first-order gradient. The advantage of this optimizer is that it adapts the learning rate for each weight of the neural network through the learning process. This algorithm offers multiple benefits such as computational efficiency, little memory requirements, suitability to problems with large data and even more. On the other hand, the chosen loss function is the Mean Squared Logarithmic Error (MSLE). It is computed as the mean squared logarithmic error between the predicted value and the ground truth. This loss function is used for regression problems. It is mainly used when the targeted

value has a spread of values and when there is no need to heavily punish the model when predicting large values.

IV.5 Orientation estimation

Once the main parameters of the network are set, the training phase can be initiated. But before that, it is important to define the nature of the targeted output. There are two possibilities: (i) predicting the two angles simultaneously or (ii) proposing a deep neural network for each angle to estimate. In the following, the conducted tests will be detailed. For all the training phases, the input to the tested networks is a fixed-size 128x128x64 image. These images contain artificial fibers and are downgraded through the application of a Gaussian filter. Regarding the Gaussian filter, we applied one with a standard deviation of $(1, 1, 2)$. It is wider along the z axis to mimic the effect of the PSF. It is important to mention that, during the testing on real images, these images were improved using a unidirectional top-hat transform. For the different output configurations, we proceeded to a fine tuning using tensorboard in order to find the best parameters.

IV.5.1 Estimation of two angles simultaneously

The first tested approach is the prediction of both angles simultaneously. For the training process, inputs are 3D synthetic stacks and outputs are vectors of two coordinates, namely θ and ϕ.

IV.5.1.1 Network architecture

Multiple tests were conducted to determine the best architecture for this application. The choice was set to include four convolutional layers. The kernel size is set to 3x3x3. The convolution stride and the spatial padding are both equal to 1 pixel. This way, the result of the convolution has the same dimensions as its input. After each convolution, there is a max pooling layer of size 2 and a batch normalization layer. These 4 convolutional layers in addition to the max pooling allow the reduction of the input dimensions which reaches 6x6x2. Regarding the fully connected (FC) layers, the choice fell on the use of only two FCs. The first one has 8 channels while the second has 4 channels. In fact, we noticed that too many FCs tend to make the algorithm computationally expensive and may also cause overfitting. Figure IV.6 shows a global architecture of the proposed network. The activation function of all neurons of the proposed network is the Rectified Linear Unit (ReLU) activation function. This function outputs the input directly if it is positive and returns zero if it is negative. It is the most commonly used activation function. The reason behind its success is its computational simplicity, its linear behaviour and its representational sparsity.

The proposed architecture needs around 25 epochs to converge with a batch of size 8. The size of the batch is constrained by the available memory on the GPU.

The dataset was set as follows: 3800 images were used for the training phase and 200 were used for the testing process.

IV.5.1.2 Results and discussion

The multiple conducted tests showed that the estimation of both angles does not work properly. In fact, usually, we succeed in having a good approximation of only one angle. The evolution of the loss during the training and the testing phases is exposed in figure IV.7. The figure shows that both curves converges to a value around 1. The value 1 may seem to be high since it is different from 0 but it allows us to obtain θ values modulo 180. In fact, when the 3D images were created, the mean value of θ was set randomly between 0 and 360 degrees. However, for mean θ values of α and $\alpha + 180$, the network will not see any difference and we will have as output one of those two values.

After the training and the testing processes, we validate our model using another synthetic stack of fibers that was never used before. This stack, in addition to the stacks used for training and testing, are chosen randomly from our dataset. Figure IV.8 shows an example of result that we obtained using the architecture described above. The estimation of θ is good since it is equal to the real value modulo 180 (i.e. $318 \simeq 137 + 180$). However, for ϕ estimation, the result is not good enough. The difference between the predicted value and the ground truth is around 20 degrees which is very high.

The retained network was also tested on real images. To start, we focused on a 3D portion of an SHG stack of collagen fibers where most of the fibers are aligned and straight. θ is extracted manually using ImageJ and its value is around 110°. Meanwhile, the proposed network gives a prediction of 139°. This gap between the ground truth value and the predicted one can be explained by the fact that in the considered portion of stack, we can distinguish between 2 sets of fibers, each set having a proper dominant orientation. In order to deal with this issue, we kept only the slices where all the fibers have the same direction and we replaced the rest with empty slices. Unfortunately, the problem remains the same. Several other tests on different real stacks were carried out but the results were not conclusive.

Regarding the estimation of ϕ, the proposed network gave an estimation of 73°. Here also the prediction is far from the reality since the fibers are quite planer so the prediction needs to be close to 90°.

IV.5.2 Estimation of θ

Since the simultaneous estimation of both angles did not work properly, we decided to estimate one angle at a time. Here, we focus on the estimation of θ. For this matter, two scenarios were tested: (i) the estimation of both the cosine and sine of the desired angle and (ii) the straightforward estimation of the considered angle. In the following, we will expose the different tested architectures and the main results.

IV.5.2.1 Estimation of cos and sin

In order to obtain a good estimation of θ, it is interesting to try to predict its sine and cosine values. For this prediction, we use the mean squared error as a loss function.

IV.5.2.1.a Network architecture

Multiple tests were carried out to determine the best architecture to estimate the sine and cosine values of θ. These tests included networks having four convolutional blocks or three blocks containing two successive convolutional layers. Several variations in the kernel size were tested. The convolution stride and the spatial padding are both equal to 1 pixel in order to maintain the same dimensions as its input. Each convolution block contains a max pooling layer of size 2 and a batch normalization layer. These convolutional layers in addition to the max pooling allow the reduction of the input dimensions. This last tensor is then flattened before being fed to the first fully connected layer. Only two fully connected layers with varying number of neurons were included in the tested architectures. The activation function of all neurons of the tested architectures is the ReLU activation function except for the output layer where the used activation function is the hyperbolic tangent. This way, we ensure that the output values will range between -1 and 1. All architectures were trained and tested on around 25 epochs with a batch of size 8. The dataset was set as follow: 80% of the images are used for the training phase while 20% are used for the testing process. Regarding the loss function, we used the classical mean squared error function which works well with the output of our application.

IV.5.2.1.b Results and discussion

The conducted tests were not conclusive. Unfortunately, we were not able to make any network converge. In fact, in most of the tests, the loss continuously decreases during the training process while it remains globally constant (around 0.5) during the testing process. Figure IV.9 shows an example of the evolution of the loss function. Most of the tested networks showed an evolution similar to what is exhibited here.

When we try to estimate the sine and cosine values of θ, we aim at estimating two values related to our angle. This means that if the tested network fails to estimate one value, it will affect the loss result. However, since the network does not distinguish between fibers oriented at θ and $\theta + 180$, the probability of wrongly predicting the sine, the cosine or both is high. Thus, during the testing process, the loss can be elevated which explains why the tested networks do not converge.

IV.5.2.2 Direct estimation

The estimation of the cosine and sine values of θ was not conclusive and, just like the simultaneous estimation of both angles, only one angle is at best correctly estimated. That is why we decided to try the straight forward estimation of θ.

IV.5.2.2.a Network architecture

Same as previously, several tests were carried out to determine the best architecture for θ estimation. The final choice was set to include four convolutional layers. The kernel size is set to 3x3x3 for all convolutions. The convolution stride and the spatial padding are both equal to 1 pixel in order to maintain the same dimensions as its input. Each convolution is followed by a max pooling layer of size 2 and a batch normalization layer. These 4 convolutional layers in addition to the max pooling allow the reduction of the input dimensions which reaches 6x6x2. This last tensor is then flattened before being fed to the first fully connected layer. Two fully connected layers are enough to make the network converge without over-fitting. The first one has 512 channels while the second has 2 channels. Figure IV.10 shows the global architecture of the proposed network. The activation function of all neurons of the proposed network is the ReLU activation function.

The proposed architecture needs around 25 epochs to converge with a batch of size 8. The size of the batch is constrained by the available memory on the GPU. The dataset was set as follows: 3800 images were used for the training phase and 200 were used for the testing process.

IV.5.2.2.b Results and discussion

The carried out tests showed that the estimation of θ gives satisfying results. The evolution of the loss during the training and the testing phases is showed in figure IV.11. The figure shows that both curves converges to a value around 1.1. This value may seem to be high since it is different from 0 but, again, it allows us to obtain θ values modulo 180.

After the training and the testing processes, we validate our model using another synthetic stack of fibers that was never used before. This stack, in addition to the stacks used for training and testing, are chosen randomly from our dataset. Figure IV.12 shows an example of result that we obtained using the architecture described above. The estimation of θ is good since it is equal to the real value modulo 180 (i.e. $198 \simeq 19 + 180$.

Afterwards, the retained network was tested on real images. First, we used the same portion of the SHG stack of collagen fibers which was used in the previous section. θ is extracted manually using ImageJ and its value is around 110°. Meanwhile, the proposed network gives a prediction of 293° which corresponds also to an orientation of 113°. The few degrees difference between the predicted value and the one extracted manually from one slice of the stack can be explained by the fact that our network estimates the global orientation of collagen fibers in a volume and the fibers orientations have some variances. Thus, an error of 3° is acceptable.

IV.5.3 Estimation of ϕ

Once the estimation of θ is completed, we focus of the estimation of ϕ. For this matter, we followed the same process as for θ which is based on evaluating the results

of two architectures, one to estimate the cosine and sine values of ϕ and the other one to straight forward estimate the value of ϕ.

IV.5.3.1 Estimation of cos and sin

In this section, the output of the proposed deep network is a vector of two values: $\sin(\phi)$ and $\cos(\phi)$. It is interesting to mention that, since it is difficult to distinguish between fibers oriented at ϕ and $\phi + 180$, if the prediction of the proposed network corresponds to $-\sin(\phi)$ and $-\cos(\phi)$ (where ϕ is the ground truth), we will consider it as a proper prediction.

IV.5.3.1.a Network architecture

Several tests were conducted in order to determine the best architecture capable of estimating the sine and cosine values of θ. These tests included networks with four convolutional blocks or three blocks each containing two successive convolutional layers. During these tests, the kernel size of the convolutions varied and included several variations. The convolution stride and the spatial padding are both equal to 1 pixel in order to maintain the same dimensions as its input. Each convolution block is composed, in addition to the convolution layer(s), of a max pooling layer of size 2 and a batch normalization layer. Convolutional layers as well as the max pooling layer allow the reduction of the input dimensions. This last tensor is then flattened before being fed to the first fully connected layer. Only two fully connected layers with varying number of neurons were included in the tested architectures. The activation function of all neurons of these architectures is the ReLU activation function except for the output layer where the used activation function is the hyperbolic tangent to have output values ranging between -1 and 1. All architectures were trained and tested on around 25 epochs with a batch size of 8. The dataset was set as follow: 80% of the images are used for the training phase while 20% are used for the testing process. Regarding the loss function, we used the classical mean squared error function which works well with the output of our application.

IV.5.3.1.b Results and discussion

Same as for θ, we were not able to make any of the tested architectures converge. The reasons of this divergence, which were mentioned before, are not applicable in this case. In fact, since ϕ is initially defined between 0 and 180 degrees, the network can not confuse it with $\phi + 180$. It can not predict values that it did not encounter during the training process.

For all tested networks, the loss function decreased continuously during the training process but settled down between 0.3 and 0.4 during the testing process. We noticed also that, in the best case scenarios, we have a good estimation of only one value between the sine and the cosine. The issue with ϕ estimation is probably due to the effect of the used Gaussian filter to mimic the PSF of the microscope. In fact the Gaussian filter is wider along the z axis which may add some difficulties to train the network. This makes the fibers wider along the z axis and can possibly make

two or more fibers touch. It would be interesting to carry out more tests related to this application but using another dataset where we make sure that fibers do not touch and maybe try with straight fibers before introducing undulated ones.

IV.5.3.2 Direct estimation

After the estimation of the sine and cosine values of ϕ, we proceed to the direct estimation of this angle. For this matter, many architectures were tested. An overview of this architectures as well as the related results will be exhibited in the following.

IV.5.3.2.a Network architecture

In order to estimate the value of collagen fibers orientations along the z axis, we tested several network architectures. These tests included multiple sizes of kernels, multiple numbers of convolutional layer and two pooling functions. The convolution stride and the spatial padding are both equal to 1 pixel in order to maintain the same dimensions as its input. Meanwhile, the number of FC layers was fixed to 2. The number of filters for the convolutional layers as well as the number of neurons in the FC layers vary also with the different tested architectures. The activation function of all neurons of the tested network is the ReLU activation function.

IV.5.3.2.b Results and discussion

Regrettably, the conducted tests did not give any good result in estimating ϕ. When analyzing the evolution of the loss value during the training and the testing phases, we can notice that some architectures tend to fit exactly its training data but it has trouble with the testing data. It is the overfitting phenomena. In table IV.1, we present a summary of the different architectures where the loss evolution of the training and testing processes converges as well as the result of an example of prediction using them. The stack used for the last prediction is a synthetic stack which was not used during the training nor the testing.

Table IV.1 – Different tested architectures for ϕ estimation

CNN architecture	Kernel	Pooling	FC	Validation
Conv(16)+BN+pooling+	(7x7x7)	max	FC(16) + FC(8)	ground truth = 60°
Conv(16)+BN+pooling+	(5x5x5)	max		prediction = 92°
Conv(32)+BN+pooling+	(5x5x5)	max		
Conv(64)+BN+pooling	(3x3x3)	max		
Conv(16)+BN+pooling+	(3x3x5)	max	FC(16) + FC(8)	ground truth = 7°

CNN architecture	Kernel	Pooling	FC	Validation
Conv(16)+BN+pooling+	(3x3x5)	max		prediction = 71°
Conv(32)+BN+pooling+	(3x3x5)	max		
Conv(64)+BN+pooling	(3x3x5)	max		
Conv(16)+BN+pooling+	(3x3x5)	average	FC(16) + FC(8)	ground truth = 85°
Conv(16)+BN+pooling+	(3x3x5)	average		prediction = 65°
Conv(32)+BN+pooling+	(3x3x5)	average		
Conv(64)+BN+pooling	(3x3x5)	average		
Conv(16)+BN+pooling+	(7x7x7)	max	FC(16) + FC(8)	ground truth = 175°
Conv(32)+BN+pooling+	(5x5x5)	max		prediction = 83°
Conv(32)+BN+pooling+	(5x5x5)	max		
Conv(64)+BN+pooling	(3x3x3)	max		
Conv(4)+BN+pooling+	(3x3x3)	max	FC(32) + FC(16)	ground truth = 100°
Conv(4)+BN+pooling+	(3x3x3)	max		prediction = 89°
Conv(8)+BN+pooling+	(3x3x3)	max		
Conv(8)+BN+pooling+	(3x3x3)	max		
Conv(16)+BN+pooling	(1x1x1)	max		
Conv(8)+BN+pooling+	(3x3x3)	max	FC(16) + FC(8)	ground truth = 85°
Conv(8)+BN+pooling+	(3x3x3)	max		prediction = 70°
Conv(16)+BN+pooling+	(3x3x3)	max		
Conv(16)+BN+pooling+	(3x3x3)	max		
Conv(32)+BN+pooling	(1x1x1)	max		
Conv(16)+Conv(16)+BN +pooling+	(3x3x3)	max	FC(4) + FC(2)	ground truth = 32°
Conv(4)+Conv(4)+BN +pooling	(3x3x3)	max		prediction = 64°

CNN architecture	Kernel	Pooling	FC	Validation
Conv(16)+Conv(16)+BN +pooling+	(3x3x3)	max	FC(512) + FC(4)	ground truth = 133°
Conv(128)+Conv(128)+BN +pooling	(3x3x3)	max		prediction = 77°
Conv(64)+Conv(64)+BN +pooling+	(1x1x1)	max	FC(16) + FC(8)	ground truth = 19°
Conv(128)+Conv(128)+BN +pooling	(1x1x1)	max		prediction = 84°
Conv(4)+Conv(4)+BN +pooling+	(3x3x3)	max	FC(4) + FC(2)	ground truth = 180°
Conv(8)+Conv(8)+BN +pooling+	(3x3x3)	max		prediction = 64°
Conv(16)+Conv(16)+BN +pooling+	(3x3x3)	max		
Conv(32)+BN+pooling	(1x1x1)	max		
Conv(4)+Conv(4)+BN +pooling+	(5x5x5)	max	FC(4) + FC(2)	ground truth = 97°
Conv(8)+Conv(8)+BN +pooling+	(3x3x3)	max		prediction = 78°
Conv(16)+Conv(16)+BN +pooling+	(3x3x3)	max		
Conv(32)+BN+pooling	(1x1x1)	max		

The results of the predictions show that ϕ estimation is very limited. In fact, in best case scenario, there is a gap of 11° between the ground truth and the predicted value. Because of the bad results during the testing process on synthetic data, no tests were carried out on real stacks of collagen fibers.

IV.6 Conclusion

In this chapter, we described different approaches to estimate collagen fibers orientations. For this matter, we introduced a new dataset of synthetic fibers. Each stack of this dataset contains a certain number of fibers oriented following two angles θ and ϕ. These stacks were then downgraded by convolving it with a Gaussian filter in order to mimic the effect of the PSF and the noise that may be introduced by the directional filter on real SHG images. Certainly, raw images are pre-processed using the top-hat transform but we added some noise to the synthetic images to make the network robust to noise. This way, it will properly work even when raw images

still have some noise. The resulting dataset was used to train multiple deep neural networks aiming at estimating fiber orientations. We were able to find a network that correctly estimates θ on synthetic and real images. Unfortunately, the estimation of ϕ was not successful and, despite all the tested architectures, we were not able to have a proper estimation of the considered angle.

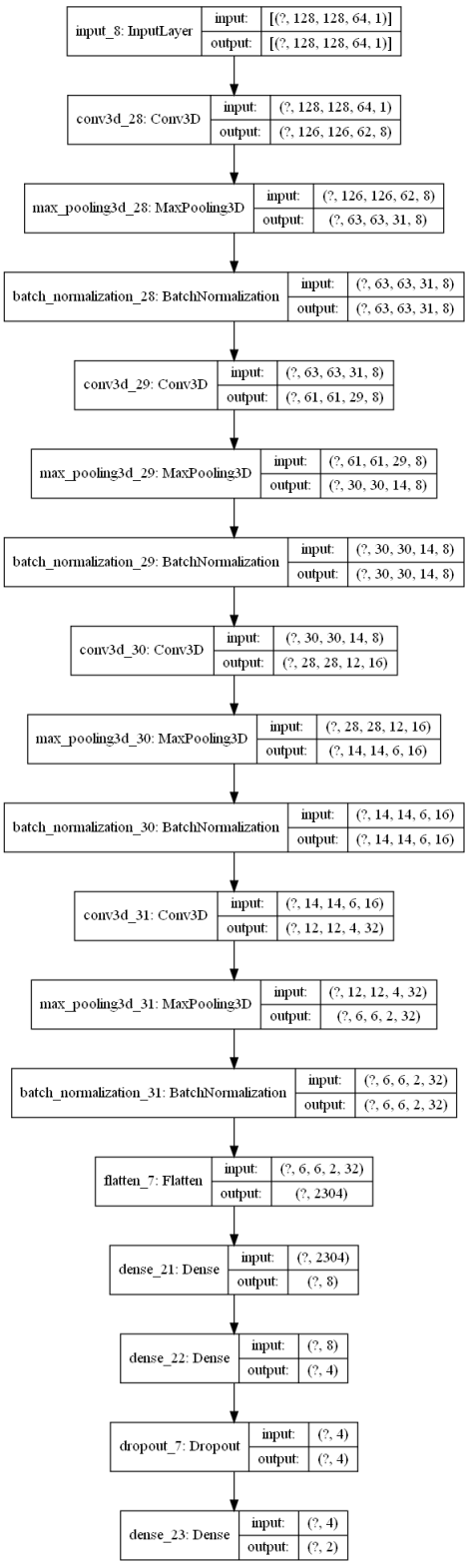

FIGURE IV.6 – Architecture of the proposed network to estimate both θ and ϕ

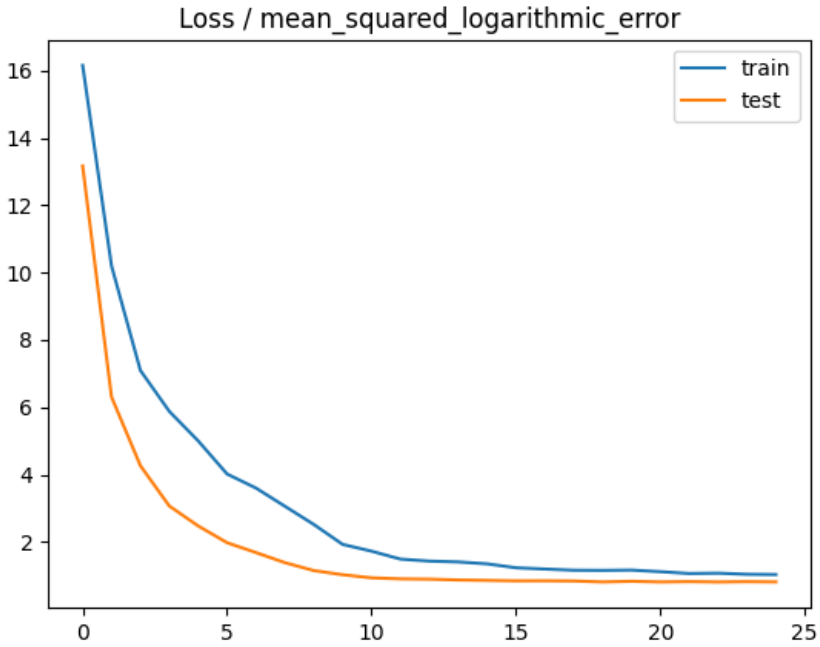

FIGURE IV.7 – Evolution of the loss during the training and the testing phases when estimating both θ and ϕ

```
result of the prediction [[137.0973   75.48358]]
the correct value: tf.Tensor([318  52], shape=(2,), dtype=int64)
```

FIGURE IV.8 – Example of the prediction of the orientations of synthetic fibers, the firs angle corresponds to ϕ while the second one corresponds to θ

.

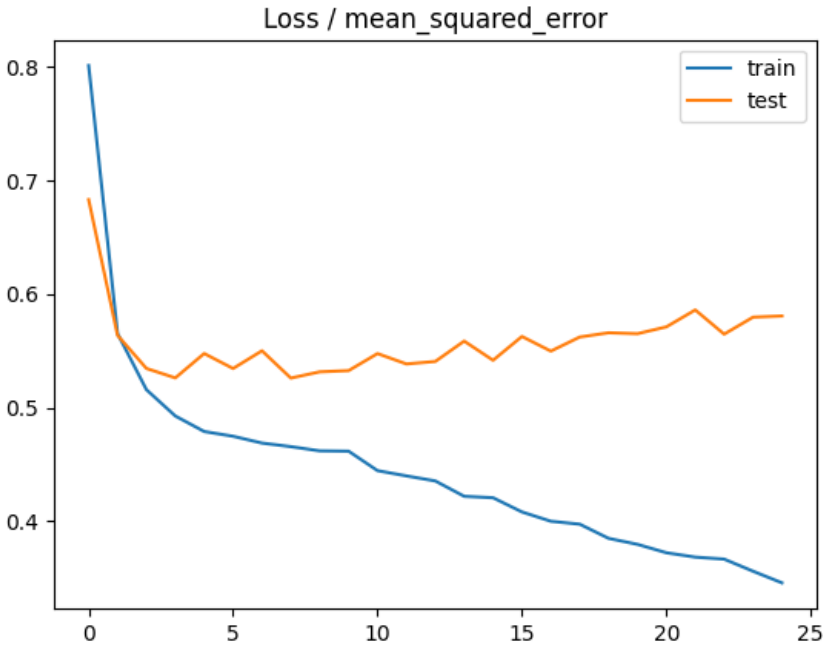

FIGURE IV.9 – Example of the evolution of the loss function when estimating both the cosine and sine values of θ

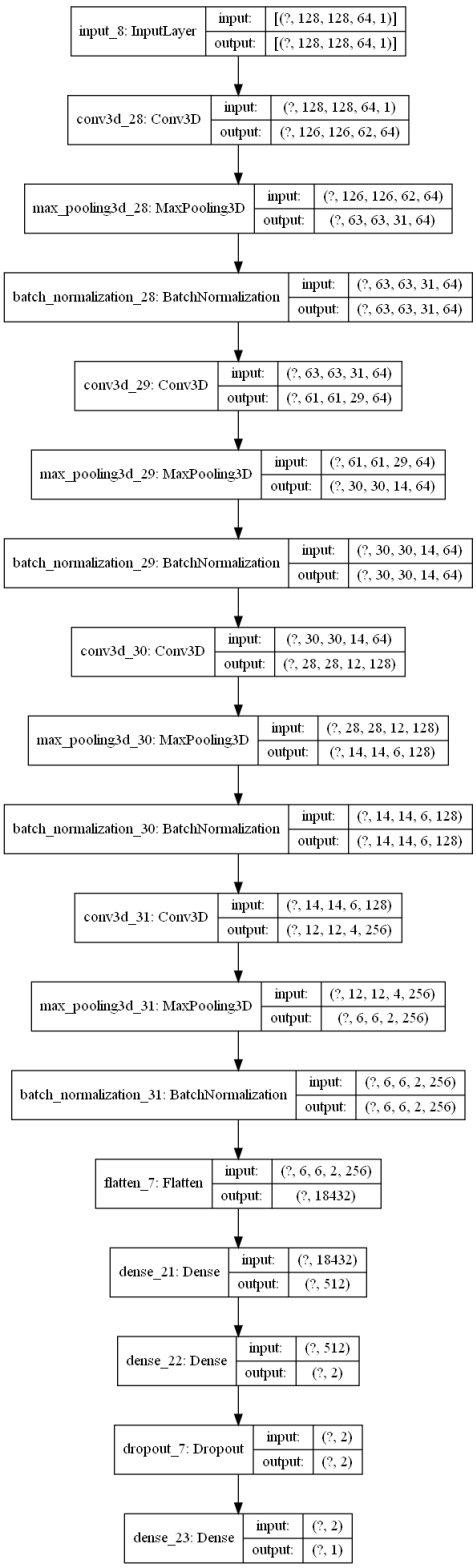

FIGURE IV.10 – Architecture of the proposed network to estimate θ

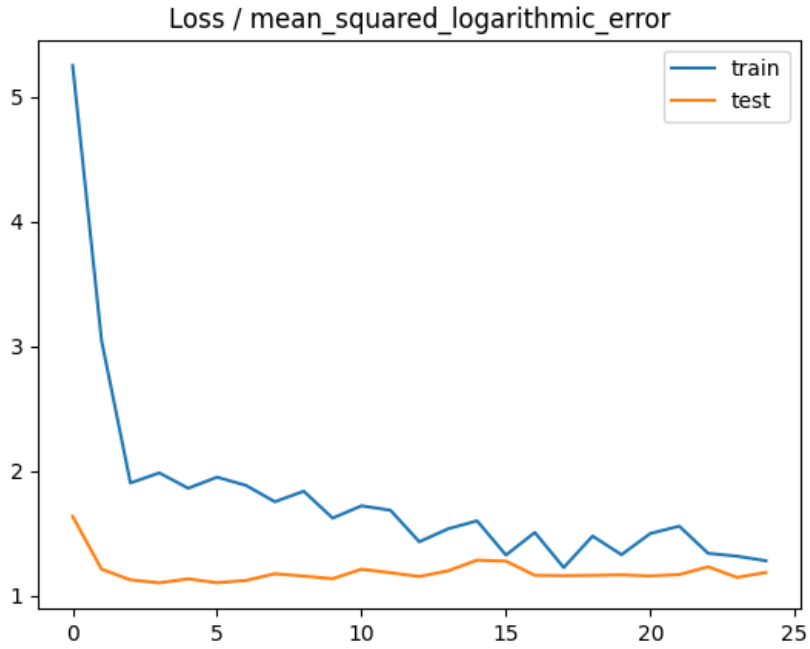

FIGURE IV.11 – Evolution of the loss during the training and the testing phases when estimating θ

```
result of the prediction [[198.28734]]
the correct value: tf.Tensor(19, shape=(), dtype=int64)
```

FIGURE IV.12 – Example of the prediction of θ of synthetic fibers

.

Chapter V

Comparison with other methods

Contents of the chapter

V.1 Résumé du chapitre

L'analyse quantitative des images de seconde harmonique et précisément l'estimation de l'orientation des fibres de collagène dans les tissus biologiques est importante en vue de l'étude de la nature et du comportement de cette protéine. Ainsi, plusieurs approches ont été développées dans la littérature et ont été testées principalement sur des images 2D. Le réseau de neurones proposé et décrit dans la section IV.5.2.2 du chapitre précédent considère le volume 3D en entier dans l'estimation de l'orientation. Une comparaison entre ce réseau de neurones et quelques unes des méthodes les plus utilisées à cette fin est présentée. Ce réseau a montré des résultats

assez satisfaisants pour l'estimation de l'orientation des fibres droites et ondulées.

V.2 Abstract of the chapter

The quantitative analysis and especially the orientation's estimation of collagen fibers in biological tissue is important to study the nature and behaviour of this protein. For this purpose, several approaches were developed in the literature and were tested on mainly 2D images. The proposed neural network takes into consideration the entire stack when evaluating the average orientation. A comparison between the proposed network and some common orientation estimation methods is exposed. This network showed satisfying and coherent results whether for straight or undulated fibers.

V.3 Introduction

Orientation estimation of collagen fibers from SHG images has been in the center of bio-mechanical research since it is an interesting information to have in order to characterize these fibers. For this matter, multiple methods have been developed. However, most of these methods focused on 2D images from the SHG stack and not the entire volume. Thus, it is interesting to compare the estimation results of our deep network to some of the most used approaches in the literature in order to validate it as well as to see if the inclusion of the 3D aspect of the stack has any effect on the estimated orientation.

In this chapter, we will start by introducing the elected stacks which will be used to test the accuracy of the proposed deep network. On the second part, we will present the results of θ estimation through multiple techniques from the literature. The methods that will be covered in the present chapter are the 3D FFT, the CT-FIRE algorithm in addition to Cavinato et al. technique which is based on the 2D FFT.

V.4 Data preparation

For comparison purposes, we chose to use the same collagen fiber SHG stacks to test some approaches aiming at estimating fiber orientations. In this chapter, we will present the results of three different stacks containing fibers with different shapes. These stacks will be referenced to as:

— stack 1: it corresponds to a rabbit's carotid artery. Collagen fibers are straight because this stack was captured when the specimen was under a certain mechanical load. These fibers have almost the same orientation.

— stack 2: it corresponds to a human ascending thoracic aorta. Collagen fibers are quite undulated. These fibers have slightly different orientations but the average orientation will be considered.

— stack 3: it corresponds to a rabbit's carotid artery. Collagen fibers are undulated but they do not have a dominant orientation. Even for the human eye, it is difficult to distinguish between the different fibers in the stack.

A slice from each one of these stacks is exhibited in figure V.1. These stacks are pre-processed using the white top-hat transform to reduce the noise. This way, the fibers become clearer especially along the z axis. These stacks were chosen to validate our deep learning approach on different types of fibers: straight, undulated and random ones.

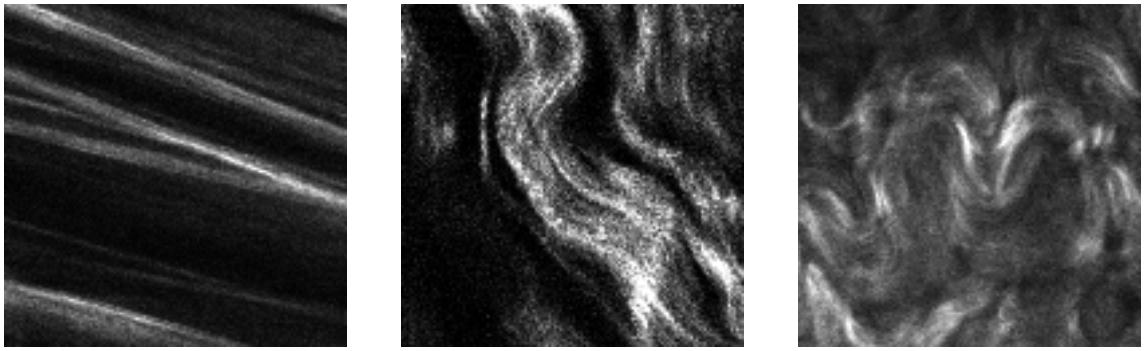

(a) (b) (c)

Figure V.1 – An image from (a) stack 1, (b) stack 2 and (c) stack 3

These stacks are portions from bigger stacks. In fact, since the proposed network need inputs of dimensions (128, 128, 64) and the available stacks have usually dimensions of (1024, 1024, z) where z varies from a stack to another, we had to work with small portions from original stacks. We chose portions that contain multiple fibers having a common orientation. To ensure this condition, the depth of the selected portion is usually smaller than 64. To deal with this issue, we pad the extracted portion with zeros before feeding it to our network.

V.5 Orientation estimation using different methods

Once the data is preprocessed, we can proceed to the validation of our method by comparing it with other approaches.

V.5.1 Orientation's estimation results

In order to validate our approach based on deep learning to estimate collagen fiber's orientation from SHG images, we compare it to different other techniques from the literature. In the following, we are presenting results of some commonly used ones, namely the 3D FFT, the CT-FIRE algorithm in addition to an approach developed by Cavinato et al. in our lab. Certainly, we focus on the estimation of θ. It is important to mention that the CT-FIRE and the approach developed by Cavinato et al. are performed in 2D (i.e. on a single image of the stack). In the following, for comparison purposes, we will only consider the orientation along the x axis.

V.5.1.1 Deep learning

We present the results of the proposed method described in chapter 4. Here, the deep neural network is already trained using the previously developed synthetic dataset.

We start our tests by using stack 1. It was pre-processed using a top-hat transform with a structuring element of size 15. In this stack, fibers are straight. The proposed deep network estimates θ to be roughly equal to 283°. This value is equivalent to 103° (i.e. $103° = 283° - 180$) since the network does not distinguish between θ and $\theta + 180$. This estimation seems to be accurate especially when we compare it to the angle extracted manually from one image of the stack using ImageJ (around 110°). Regarding stack 2, it was pre-processed using a top-hat transform with a structuring element of size 15. Our network gave an estimation of θ around 333°. This angle is equivalent to 153° (i.e. $153° = 333° - 180$). This estimation seems to be accurate especially when we compare it to the angle extracted manually from one image of the stack using ImageJ (around 150°). We end up with stack 3 where collagen fibers do not have any preferential orientation. Certainly, the proposed network will give an estimation of θ but it will not have any significance. Same as for both previous stacks, stack 3 was pre-processed with a top-hat transform with a structuring element of 15. The estimation given by our network is around 276° which equivalent to the value 96°. Table V.1 summarizes the different estimated values of θ.

stack index	1	2	3
θ estimation	103°	153°	96°

Table V.1 – Estimation results using deep learning

V.5.1.2 3D FFT

The application of the 3D FFT on collagen SHG images was performed using the plugin "FFTJ" of ImageJ. For each stack, we calculate its 3D FFT and we plot the logarithmic power spectrum where the origin of the Fourier domain is placed on the volume-center. In the center slice of the recovered spectrum, we find a white line which direction corresponds to the dominant orientation minus 180. Figure V.2 shows the power spectra of the three considered stacks.

For stack 1, the angle drawn in figure V.2a is equal to 20°. Thus, the orientation of collagen fibers is estimated to be around 110° (i.e. $110° = 20° + 90°$). Regarding stack 2, from its power spectrum, we can extract and angle around 48°. Therefore, the fiber orientation corresponds to 138° (i.e. $138° = 48° + 90°$). Meanwhile, for the last stack, we were not able to extract any distinguishable line from its power spectrum. This is not surprising because stack 3 contains fibers that do not have a dominant direction. Thus, no orientation's estimation was possible.

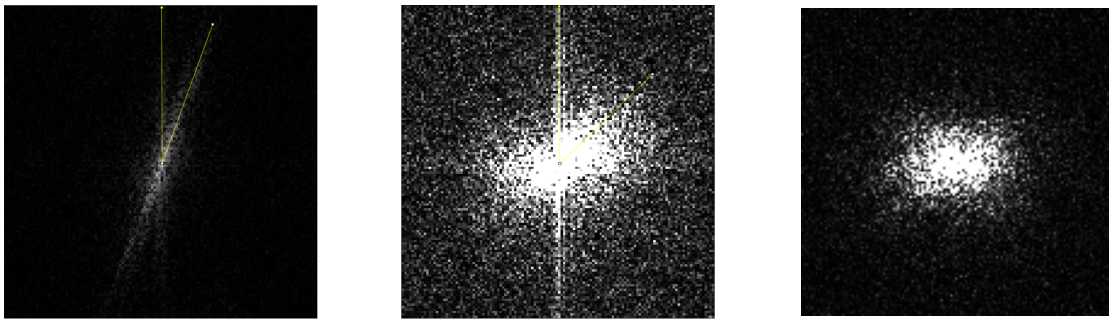

(a) (b) (c)

FIGURE V.2 – Power spectra of: (a) stack 1, (b) stack 2 and (c) stack 3

stack index	1	2	3
θ estimation	110°	138°	−−

TABLE V.2 – Estimation results using 3D FFT

V.5.1.3 CT-FIRE

For the CT-FIRE algorithm, we proceeded to two different tests: one with one raw image from the considered stack and one with this image being pre-processed using the top-hat transform. This transform certainly reduces the noise and makes fibers clearer in the 3D space. However, it does not suppresses all the noise which can cause some inaccuracies when trying to estimate the orientation.

The CT-FIRE algorithm already proceeds to a noise reduction through the curvelet transform. It also allows extracting the fibers network from the image. Each extracted fiber is characterized by several parameters including the orientation. Thus, we will consider the average orientation for comparison purposes. However, as can be seen in figure V.3, fiber extractions were very noisy. The estimated average orientation based on the pre-processed image is equal to 117.3°.

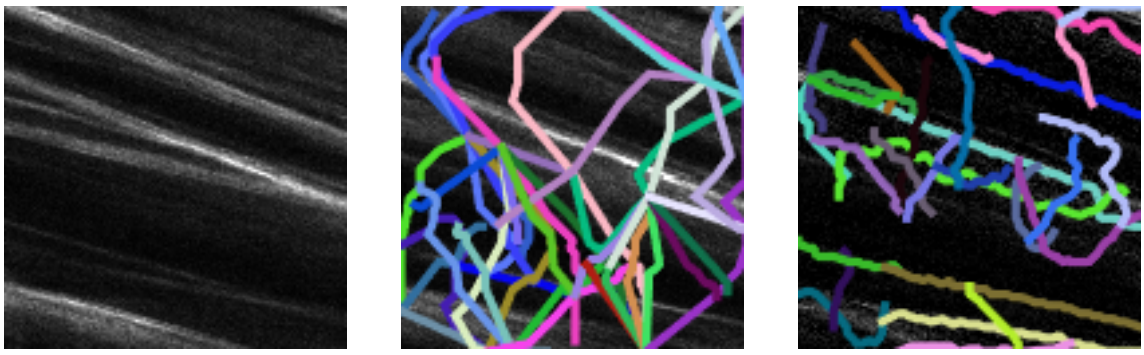

(a) (b) (c)

FIGURE V.3 – Stack 1: (a) original image, (b) fibers extraction from raw image and (c) fiber extraction from pre-processed image

For stack 2 and stack 3, we applied the CT-FIRE algorithm only on pre-processed images using the white top-hat transform. Regarding stack 2, the result of the ex-

traction is showed in figure V.4. The considered algorithm extracted fibers that do not exist (the ones in pink for example in figure V.4b). Unfortunately, CT-FIRE was not able to properly extract undulated fibers. The estimated global orientation is equal to 109.1°

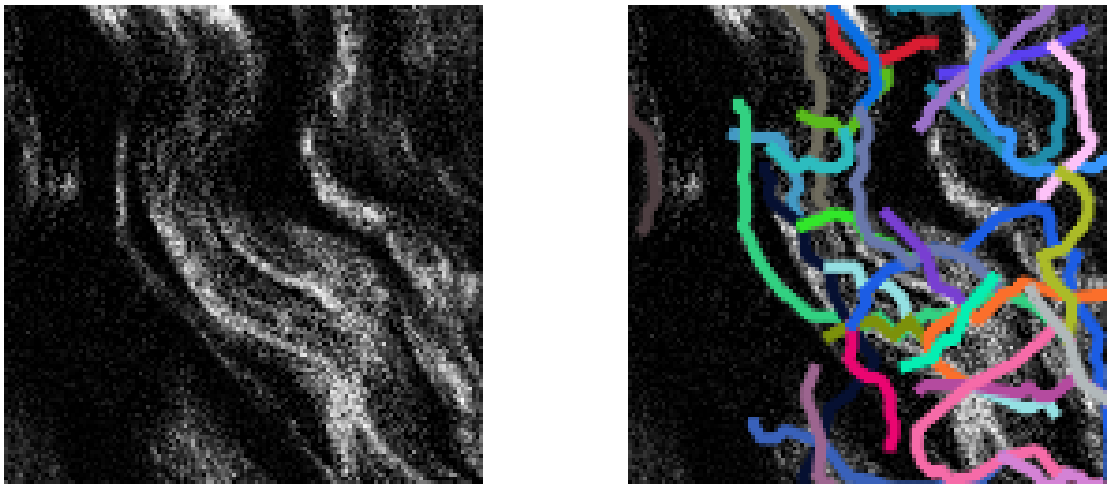

(a) (b)

FIGURE V.4 – Stack 2: (a) pre-processed image and (b) fibers extraction using CT-FIRE

For the last stack where the fibers are undulated and have no preferential orientation, the fiber extraction was really bad, see figure V.5. It is important to mention that, even for the human eye, it is quite complicated to properly distinguish between collagen fibers, especially after the top-hat transform. In fact, since this transform is more oriented into the 3D volume, there is less information in pre-processed slices than in raw ones. Still, CT-FIRE gave a global orientation estimation of 88.4°. All the presented results are summed up in table V.3.

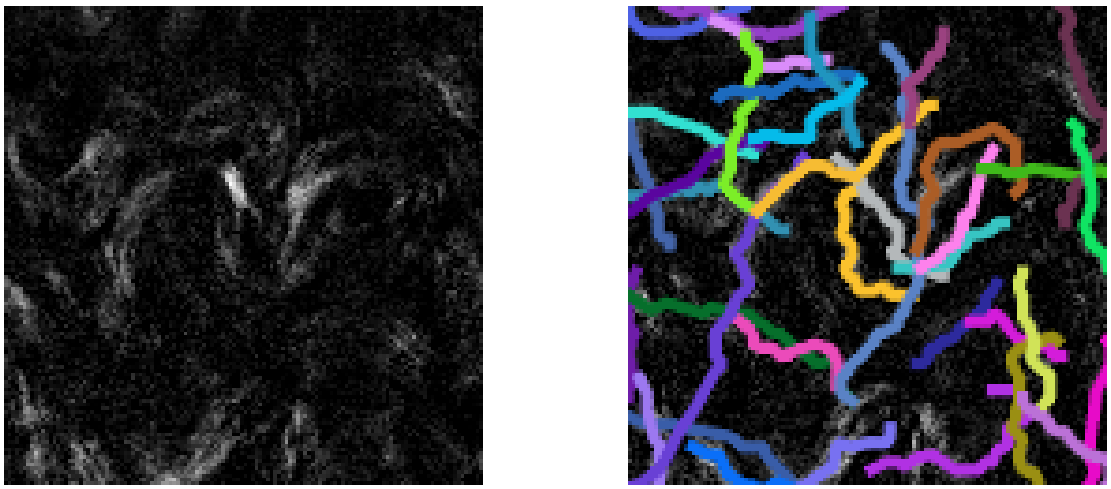

(a) (b)

FIGURE V.5 – Stack 3: (a) pre-processed image and (b) fibers extraction using CT-FIRE

stack index	1	2	3
θ estimation	117°	109°	88°

Table V.3 – Estimation results using CT-FIRE

V.5.1.4 Cavinato et al. method

The method used in this section was exposed by Cavinato et al. in 2020 [Zha20]. It is used to estimate planar orientation distributions of collagen fibers. For this matter, the authors considered the projection of 3D stacks of SHG images of collagen fibers and applied a 2D FFT on them. In order to extract the orientation distribution, the power spectrum is is integrated through the use of a wedge-shape sum approach. We applied this methodology on projections from pre-processed stacks using the white top-hat. This available code for this method estimates angles with respect to the horizontal axis. Thus, some changes are necessary to recover an orientation expressed with respect to the vertical axis.

Figure V.6 shows the different resulting orientation distributions of the 3 considered stacks. From each distribution, the maximum is extracted and it corresponds to the fibers orientation with respect to the horizontal axis. For stack 1, the fibers orientation is equal 62° which corresponds to 118° with respect to the vertical axis. Regarding stack 2, we can see that there is no absolute max since the probability of every angle between 0° and 90° is high and constant to a certain point. Meanwhile, the maximum probability corresponds to an angle of 32°. The value is equivalent to 148° with respect to the vertical axis. For stack 3, we notice that the probabilities of the majority of possible orientations is low and it is hard to define a maximum to this curve. This is not surprising because the fibers in the considered stack are not organized in the space. However, the maximum probability corresponds to 0° which is equivalent to an angle of 90° with respect to the vertical axis. These results are summed up in table V.4.

stack index	1	2	3
θ estimation	118°	148°	90°

Table V.4 – Estimation results using Cavinato's method

V.5.2 Additional tests

We performed more tests on additional 5 stacks containing straight fibers and another 5 stacks containing undulated stacks. These tests included stacks with wide and thin fibers as well as stacks with a single or multiple fibers. The results of the orientation estimation are summed up in the table V.5. The chosen stacks are presented in appendix A. Stacks *Undulated 4*, *Undulated 5* and *Straight 5* correspond to images of rabbit carotids where all the other stacks correspond to human aortae.

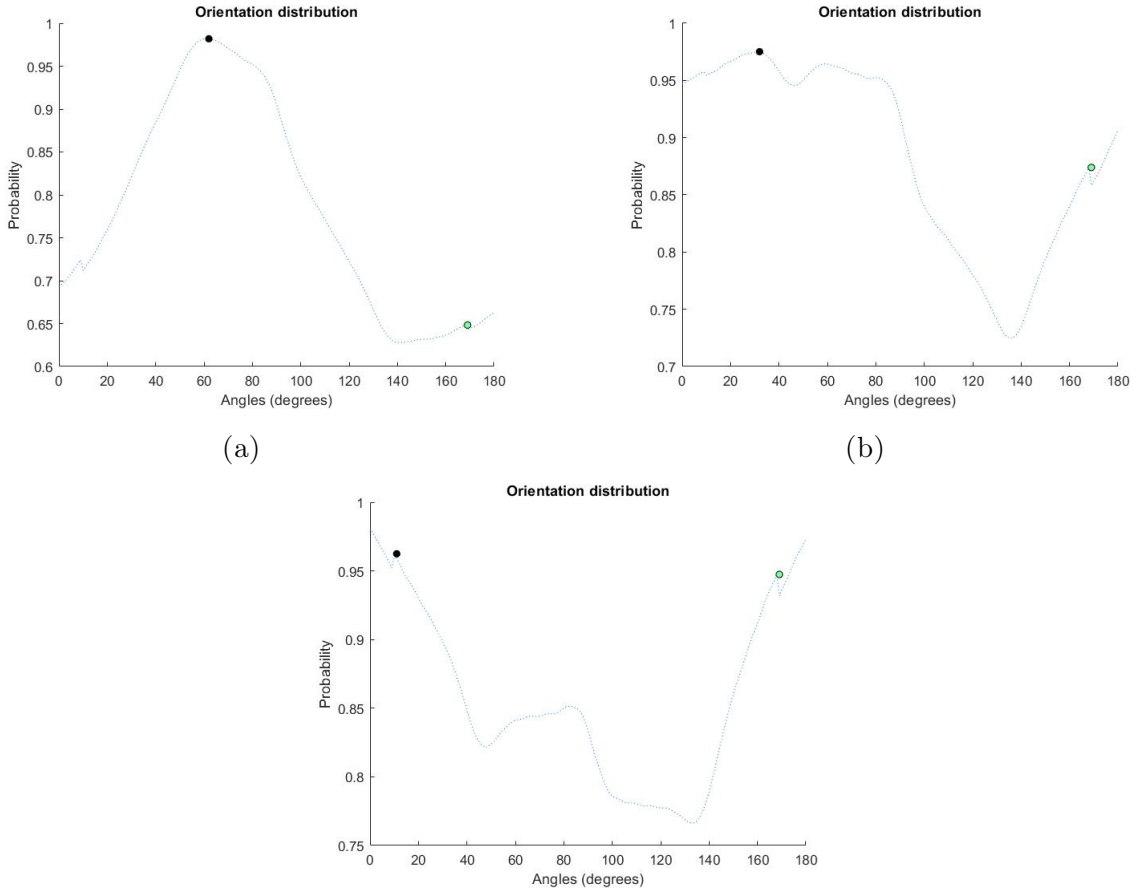

FIGURE V.6 – Orientation distributions of: (a) stack 1 (b) stack 2 and (c) stack 3

TABLE V.5 – Results of the orientation estimation on using different methods

Stacks		DL	3DFFT	CT-FIRE	Cavinato et al.	Visually
Straight	1	116°	112°	101°	114°	113°
	2	110°	170°	97°	107°	175°
	3	107°	148°	119°	143°	153°
	4	97°	93°	94°	93°	90°
	5	106°	49°	62°	51°	50°
Undulated	1	118°	130°	133.7°	119°	130°
	2	123°	180°	95°	148°	180°
	3	110°	140°	90°	148°	150°
	4	90°	135°	70°	169°	80°
	5	115°	–	103°	156°	150°

V.5.3 Discussion

The previously presented orientation estimation methods proved their efficiency. However, there is some differences between their results.

For the deep learning approach, it is important to mention that the included slices in the considered stack have a strong impact on the result of the orientation's estimation. In fact, if we include other fibers that have a totally different orientation, the estimation will be an approximation of the mean orientation. In stack 1, collagen fibers have close but different orientations. That is why, the estimated orientation is different from the one estimated using the 3D FFT for example where the orientation corresponds to the most frequent one. Besides, deep learning performs better when using noisy images. As a matter of fact, the noise that is present in the background of the fibers is taken into consideration when calculating the FFT. However, the advantage of the deep learning approach is that it considers fibers as a whole. Since the proposed network was trained using noisy images, it is able to estimate orientation from noisy images. Meanwhile, from the additional tests, we noticed that our deep network works better with thin fibers (see stacks *Straight 1* and *Straight 4* and *Undulated 4* in appendix A). However, for thick fibers, the orientation's estimation is completely wrong. This is explained by the fact that the network was trained using stacks containing thin fibers and not bundles. It is important to say that, for this type of stacks, even other methods such as the CT-FIRE algorithm and Cavinato et al. approach have trouble estimating the fiber orientation (e.g. for stacks *Straight 2* and *Undulated 2*).

Regarding the 3D FFT, it allows the identification of the most frequent orientation since it converts the stack to the frequency domain. Thus, the noise can affect the result of this transformation. However, usually the resulting orientation estimation is still coherent with the reality. For example, for stack 1, θ estimation using the 3D FFT (110°) and the deep learning approach (103°) are quite close. The difference can be explained by the fact that the deep learning approach consider the fiber network in 3D, thus, it estimates the average orientation while the 3D FFT estimates the most frequent orientation. For stack 2, we tried to extract the most frequent orientation but it was not as clear as for the first stack. It is more of an approximation than a good estimation. It is even possible to say that the orientation is somewhere between 120° and 170° where we can find the whiter pixels in the power spectrum. This is coherent with the estimation using the deep learning approach. On the other hand, for the stack *Undulated 4*, the 3D FFT did not correctly estimate the orientation. This is caused by the multiple fibers and their high waviness. Meanwhile, the 3D FFT is still the most robust technique to estimate orientations.

As regards the CT-FIRE algorithm, the result of the fibers extraction is highly-dependent on the quality of the image. In fact, any noisy pixels that are present outside the fibers can be considered as a fiber and will be included in the network extraction. This has been showed when the CT-FIRE algorithm was applied on both raw and pre-processed images. Thus, the result of the orientation estimation is biased by the non-existent extracted fibers. Besides, since it is applied on one slice of the stack, the result of the orientation's estimation may be different from the one

based on deep learning where the entire stack in taken into consideration. This may explains the differences in θ estimation for all three stacks especially for stacks 1 and 2. Meanwhile, this approach works well with stacks with dominant fibers such as *Straight 1*, *Straight 4* and *Undulated 4*.

The method of Cavinato et al. is also based on the FFT except that it is applied on the projection along the z axis of one stack and not on the 3D volume. The results of θ estimation for both stack 1 and stack 2 are quite similar. The small differences (around $8 - 10°$) are due to the dimension of the performed FFT. In fact, the most frequent frequency in the 3D volume is certainly different from the most frequent one in a 2D projection. Besides, we noticed that this approach do not work properly on noisy data such as on stacks *Straight 3* and *Undulated 2*. In fact, noise has a strong impact on changes in the pixels intensity and, thus, the spatial frequency. On the other hand, for the stack *Undulated 4*, the projection along the z axis contained too many fibers with different orientations which confuses the algorithm.

Stack 3 is initially considered as a 3D volume where collagen fibers are not organized in the space. However, all the tested orientation estimation methods gave close results. It is also important to mention that it is difficult to compare between approaches that use different types of inputs (2D or 3D). Besides, we chose to use the same pre-processed stacks for all the tested methods which may have caused some bias for some techniques (namely the CT-FIRE algorithm). In fact, to properly function, this algorithm needs an image with minimum noise.

V.6 Conclusion

In this chapter, in order to validate our deep learning approach, we presented the results of θ estimation using several techniques from the literature as well as ours. Despite the fact that the chosen techniques do not use the same type of inputs (2D or 3D), the various estimations were consistent and coherent. In fact, for straight fibers, our deep network gives a satisfying estimation which is close to the one estimated using the FFT for example. Regarding undulated and thick fibers, our neural network performs good and the result is consistent with the reality. It is even possible to say that it outperforms other approaches since it gives an average estimation of θ while the FFT for example tends to find the most frequent spatial frequency. And because of the thickness of the fibers, it is difficult to determine this frequency. However, for thick noisy fibers, the estimation using deep learning faces some issues. On the other hand, for disorganized fibers, all the tested methods gave similar estimation even if it does not really have any significance. Finally, the comparison of the deep learning approach with other methods to estimate θ is conclusive and proves that the proposed network can be used to this end especially for straight and relatively thin fibers.

General conclusion

Main findings

This summary briefly recalls the aspects of the literature that have been highlighted in the present work as well as the major novel advances resulting from it.

— ***3D Micro-structural imaging:*** After reviewing the state of the art in chapter 1, it was shown the study of collagen fibers is closely related to the used imaging modality and the quality of the acquired images. Multi-photon microscopy through second harmonic generation is proved to be the best imaging modality to capture 3D images of biological tissues containing collagen fibers. However, these images may present some artifacts. To deal with it, several image processing techniques, mainly in 2D, were used.

— ***SHG image improvement:*** SHG images suffers in general from three types of artifacts: (i) fibers discontinuities due to shadows effect or the presence of black regions caused by the presence of air or dust during the acquisition, (ii) the blur introduced by the PSF of the used microscope in addition to (iii) the Poisson noise caused during the acquisition. Both the blur and the Poisson noise were dealt with using a uni-dimensional top-hat transform along the z axis. On the other hand, fibers discontinuities were overcome by the use of a 3D directional filter. Certainly, the proposed filter introduces some additional noise. However, the application of a 3D top-hat transform after the directional filter was able to suppress most of the noise and reconstruct a proper collagen fiber network.

— ***Quantitative analysis:*** The study of collagen fibers is based on quantitative analysis. For this purpose, several image processing techniques were used whether to transform the initial image to another domain where it is possible to extract some information (e.g. FFT, HT, etc.) or to select and extract directly information from the SHG image (e.g. segmentation, CT-FIRE, statistics, etc.). After reviewing the state of the art related to which quantitative information to extract, it was shown that the choice of the image processing technique is dependent on the metric to extract. Despite their great potential, deep learning applications are still very limited on SHG images and collagen fibers. Besides, most of the available methods in the literature focused on 2D

images while neglecting the depth of the tissue.

— ***Collagen fiber orientation estimation from 3D images:*** Improved SHG images demonstrated a good 3D representation of the collagen fiber network. From these stacks, it is possible to extract two angles to describe fiber orientations in the 3D space. Deep learning was used for this purpose. The training process was performed using a dataset of synthetic fibers which were downgraded to look like real SHG images. At the end, only the orientation in the 2D plan was estimated correctly.

— ***Deep learning and orientation estimation:*** The proposed deep neural network was compared to other orientation estimation techniques from the literature and it provided coherent results. This network has the advantage to determine the average orientation in a stack while most of the literature focuses only on the most frequent one. Thus, this method works better on small stacks of undulated fibers to estimates their global orientation than other techniques introduces in the literature.

Limitations

The study presented in this thesis is not without limitations. In the following, these limitations are exposed:

— ***Computational expenses:*** In order to have a good fiber reconstruction, the 3D directional filter needs to cover a large number of directions. This necessity makes the algorithm computationally expensive. In fact, it takes around 5 hours on a cluster (CPU Intel Xeon E5-2660 v3 of 10 cores at 2,6 GHz) to process a 3D image of dimension (128,128,15) with a length of 120 pixels and 101 directions covered. Besides, to apply this filter on bigger images, it needs a large memory.

— ***Adaptability of the size of the filter:*** The three dimensional directional filter as proposed is characterized by a constant length and a constant number of directions. However, fiber discontinuities are not all the same. Besides, the directional filter is applied on all the pixels of the stack even when there is no need to any reconstruction.

— ***First orientation estimation:*** The result of the estimation of θ is highly dependent on the considered stack. In fact, when this stack contains only fibers that have almost the same direction, the proposed network gives a good estimation. Meanwhile, if other slices, where fibers are oriented in a completely different direction, are introduced the result changes and becomes irrelevant.

— ***Second orientation estimation:*** Unfortunately, the different tested architectures of deep neural networks did not succeed in estimating ϕ. The fact that the stacks present more noise along the z axis made the orientation estimation along this axis more complex.

Prospects

The limitations cited before can be overcome through different approaches which includes:

— It is possible to deal with the computational expenses of the three dimensional directional filter by parallelizing it on the GPU. It is necessary to have a powerful GPU with a large memory since the available stacks are big (around 105 million pixels). Regarding the adaptability of the proposed filter, it would be interesting to develop a new version which will be oriented toward the size of fiber discontinuities.

— For ϕ estimation, it is necessary to reduce the noise along the z axis as much as possible. A new dataset of synthetic fibers without the addition of any type of noise can be used to train a deep neural network. This way, it will be used on filtered (even segmented) real images. Thus, the noise along the z axis is dealt with and ϕ estimation can potentially work.

— Deep learning in general and convolutional neural networks in particular show a great potential in dealing with heavy 3D images for multiple purposes. Since volume fraction is an important quantitative information to have, developing a neural network aiming at estimating that metric can be interesting.

— Deep learning potential can be exploited to different applications related to SHG images (e.g. segmentation, denoising, etc.). For these application an appropriate dataset needs to be available.

Conclusion générale

Principaux résultats

Ce succinct résumé rappelle les différents aspects de la littérature qui ont été soulignés par le présent travail ainsi que les principales avancées qui en résultent.

— ***Imagerie micro-structurale 3D:*** Après la revue de l'état de l'art dans le chapitre 1, il a été montré que l'étude des fibres de collagène est étroitement liée à la technique d'imagerie utilisée et la qualité de images acquises. La microscopie multi-photonique à travers la génération de seconde harmonique est considérée comme la meilleure modalité d'imagerie pour acquérir des images 3D de tissus biologiques contenant des fibres de collagène. Cependant, ces images peuvent contenir plusieurs artéfacts. Plusieurs méthodes de traitement d'images ont été proposées dans la littérature pour remédier à ce problème mais la majorité s'est focalisé sur des tranches 2D.

— ***Amélioration des images de seconde harmonique:*** Les images de seconde harmonique souffrent en général de 3 types d'artéfacts: (i) de la discontinuité au niveau de certaines fibres causée par un effet d'ombre ou la présence de poussière lors de l'acquisition, (ii) du flou introduit par la fonction d'étalement du point propre au microscope et (iii) du bruit de Poisson causé lors de l'acquisition. Le flou et le bruit de Poisson ont été traités par l'application d'une transformée "top-hat" unidimensionnelle suivant l'axe z. D'autre part, un filtre directionnel 3D a été utilisé pour reconstruire les fibres discontinues. Certainement, ce filtre introduit encore du bruit mais il est possible de l'enlever en appliquant une transformée "top-hat" 3D. Ainsi, il est possible de reconstruire un réseau de fibres de collagène net.

— ***Analyse quantitative:*** L'étude des fibres de collagène est basée sur l'analyse quantitative. A cette fin, plusieurs méthodes de traitement d'images peuvent être utilisées, d'une part pour transformer l'image brute dans un autre domaine où il est possible d'extraire certaines informations (FFT, HT, etc.) et d'autre part pour sélectionner et extraire directement des métriques des images brutes (segmentation, CT-FIRE, etc.). Après la revue de l'état de l'art relatif au choix de la technique de traitement d'image en fonction de l'information à extraire, il a été prouvé que ce choix est étroitement lié à la métrique à évaluer. Malgré

son potentiel, l'apprentissage profond est rarement utilisé sur des images de seconde harmonique de fibres de collagène. En plus, la majorité des méthodes de la littérature est focalisée sur des images 2D en négligeant la composante 3D du tissu biologique considéré.

— ***Estimation des orientations des fibres de collagène à partir d'images de seconde harmonique 3D:*** Les images de seconde harmonique filtrées montrent une bonne représentation 3D du réseau de collagène. De ces images, il est possible d'extraire deux angles décrivant l'orientation du réseau de fibres dans l'espace. L'apprentissage profond a été utilisé pour l'estimation de ces angles. Un jeu de données contenant des images 3D de fibres synthétiques qui ont été bruitées pour ressembler à des images de seconde harmonique réelles a été utilisé pour entrainer le réseau proposé. Cependant, seulement l'estimation de l'orientation des fibres dans le plan (x,y) a abouti à un résultat correct.

— ***Apprentissage profond et estimation d'orientation:*** Le réseau profond proposé a été comparé à d'autres techniques d'estimation d'orientation parues dans la littérature et a montré des résultats cohérents. Ce réseau a l'avantage de déterminer une orientation moyenne à partir d'une image 3D tandis que le reste de la litérature cherche l'orientation la plus fréquente dans l'image. Par conséquent, cette méthode fonctionne proprement sur de petites images contenant des fibres droites ou ondulées pour estimer leur orientation globale.

Limites

L'étude présentée dans cette thèse présente certaines limites. Ces limites peuvent se résumer en:

— ***Besoin matériel:*** Afin d'avoir une bonne reconstitution de fibres, il faut considérer un nombre assez important de directions pour le filtre directionnel 3D à appliquer. Cette nécessité augmente forcément le temps de calcul. En effet, l'application d'un filtre directionnel 3D d'une longueur de 120 pixels et couvrant 101 directions sur une image de dimension (128,128,15) dure autour de 5 heures sur un cluster de calcul (CPU Intel Xeon E5-2660 v3 de 10 cœurs à 2,6 GHz). De plus, ce type de filtres nécessite la disponibilité d'encore plus de mémoire pour permettre son utilisation sur des images plus grandes.

— ***Adaptabilité de la longueur du filtre directionnel:*** Le filtre directionnel 3D comme proposé est caractérisé par une longueur constante et un nombre de directions constant. Le filtre est appliqué sur tous les pixels de l'image sans prendre en considération si ce pixel correspond à une discontinuité ou pas. De plus, les discontinuités ne figurent pas sur toutes les fibres du réseau et ne sont pas toutes similaires.

— ***Estimation de θ:*** Le résultat de l'estimation de θ dépend fortement de l'image 3D considérée. En effet, si l'on inclut des tranches qui contiennent des fibres dont l'orientation est complètement différente du reste du volume, le résultat de l'estimation est impacté. Ceci est dû au fait que le réseau estime une orientation moyenne.

— ***Estimation de ϕ:*** Malheureusement, les différentes architectures testées pour estimer cet angle n'ont pas permis de l'estimer correctement. du fait que les images (réelles et synthétiques) présentent plus de bruit suivant l'axe z, l'estimation devient plus complexe.

Perspectives

Les limites citées précédemment peuvent être palliées via plusieurs approches. Ceci peut inclure:

— Il est possible de surmonter les besoins matériels par l'utilisation d'une carte graphique performante qui possède une large mémoire puisque les images utilisées peuvent atteindre 105 millions de pixels. Pour ce faire, il est nécessaire de paralléliser l'algorithme déjà écrit. Par rapport à l'adaptabilité du filtre, il serait intéressant de développer une version qui traite uniquement les discontinuités et non l'image entière.

— Pour l'estimation de ϕ, il est nécessaire de réduire le bruit suivant l'axe z autant que possible. Il serait possible de développer un autre jeu de données sans l'ajout de bruit afin de l'utiliser pour entrainer un autre réseau de neurones. Dans ce cas, lors du test sur des images réelles, il faudrait les filtrer. Par conséquent, l'estimation de ϕ pourrait éventuellement fonctionner.

— L'apprentissage profond en général et les réseaux convolutionnels en particulier ont montré un grand potentiel dans le traitement de larges images 3D pour différentes applications. La fraction volumique est une grandeur qu'on cherche souvent à estimer. Il serait possible de développer un réseau de neurones convolutionnel qui assure cette tâche.

— L'apprentissage profond peut être utilisé dans plusieurs autres applications relatives aux images de seconde harmonique 3D, comme par exemple la segmentation ou le dé-bruitage. Pour ce faire, un jeu de données adéquat est nécessaire.

Appendix: Stacks included in the orientation estimation tests

Here, we present the stacks used in the additional tests were some orientation estimation methods are compared.

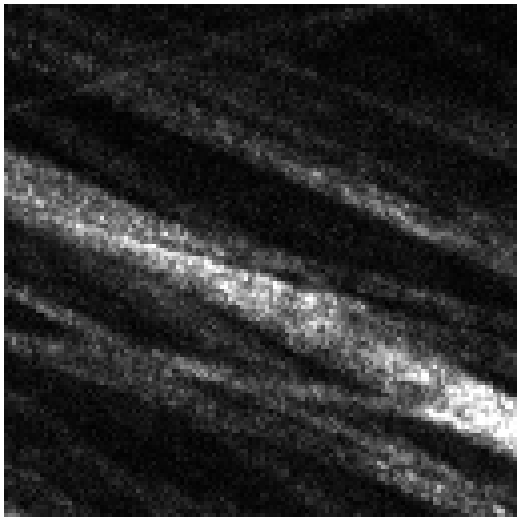

Straight 1

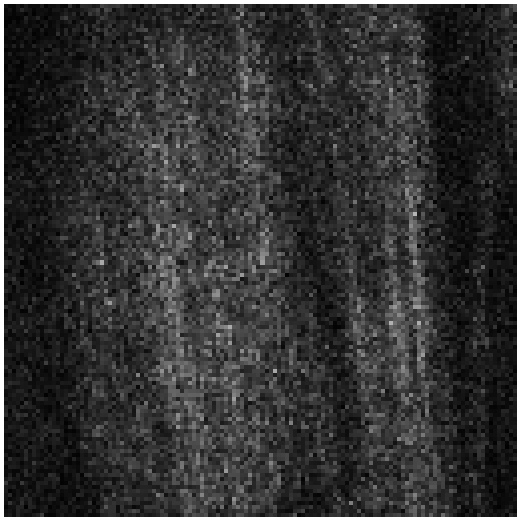

Straight 2

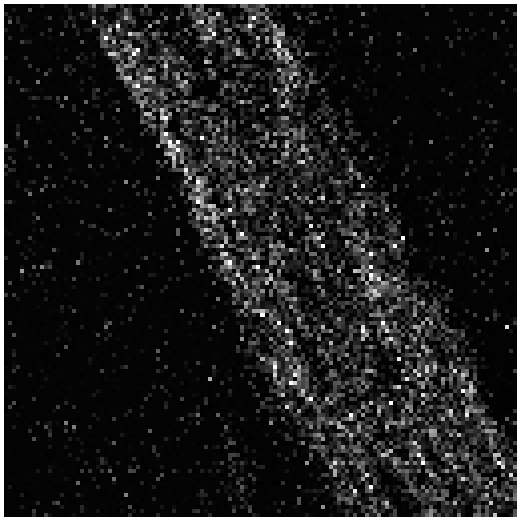

Straight 3

Straight 4

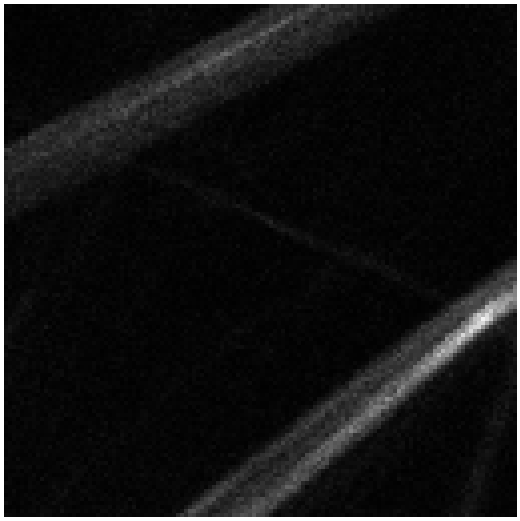

Straight 5

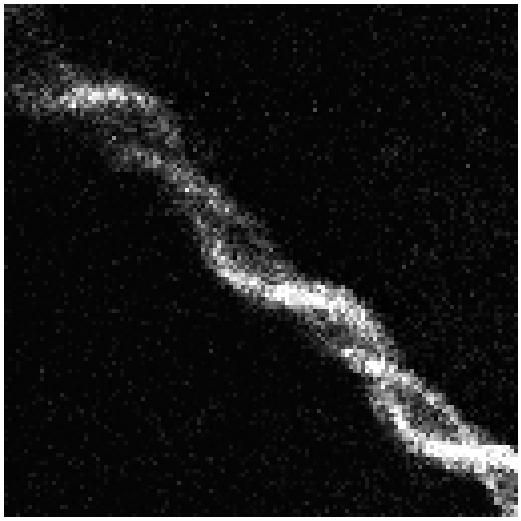

Undulated 1

Undulated 2

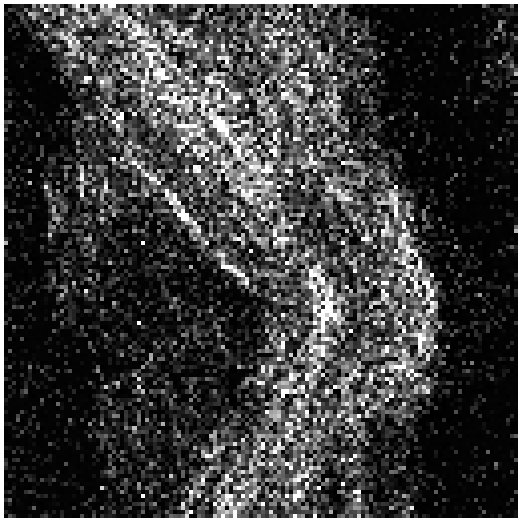

Undulated 3

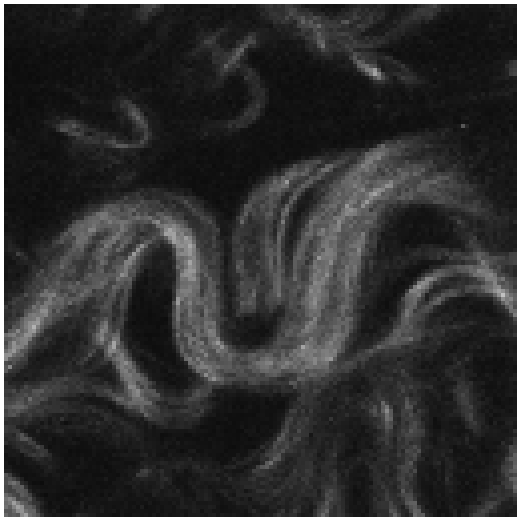

Undulated 4

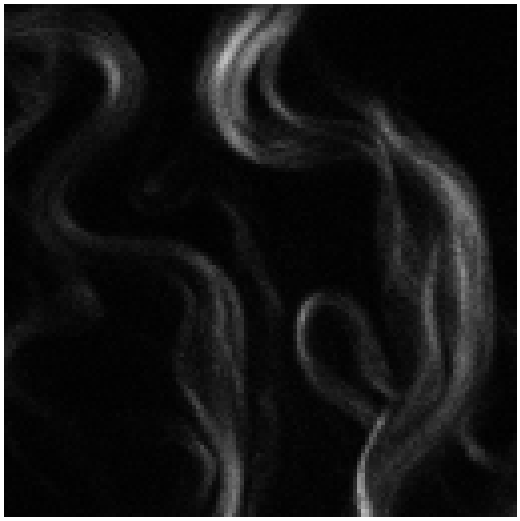

Undulated 5

References

[ÁB15] Francisco J. Ávila et Juan M. Bueno. « Analysis and quantification of collagen organization with the structure tensor in second harmonic microscopy images of ocular tissues ». In : *Applied Optics* 54.33 (2015), p. 9848-9854.

[AB94] R. Adams et L. Bischof. « Seeded region growing ». In : *IEEE Transactions on Pattern Analysis and Machine Intelligence* 16.6 (1994), p. 641-647.

[Aco+18] Víctor A. Acosta Santamaría, María Flechas García, Jérôme Molimard et Stephane Avril. « Three-Dimensional Full-Field Strain Measurements across a Whole Porcine Aorta Subjected to Tensile Loading Using Optical Coherence Tomography–Digital Volume Correlation ». en. In : *Frontiers in Mechanical Engineering* 4 (2018). ISSN : 2297-3079. DOI : 10.3389/fmech.2018.00003.

[AFM17] Lambros S. Athanasiou, Dimitrios I. Fotiadis et Lampros K. Michalis. « Introduction ». en. In : *Atherosclerotic Plaque Characterization Methods Based on Coronary Imaging*. Elsevier, 2017, p. 1-21. ISBN : 978-0-12-804734-7. DOI : 10.1016/B978-0-12-804734-7.00001-4.

[Agg+09] Constantina Aggeli, Konstantinos Toutouzas, Harisios Boudoulas et Christodoulos Stefanadis. « Atherosclerosis: aortic wall thickness and atherosclerotic plaques ». en. In : *THE AORTA STRUCTURE, FUNCTION, DYSFUNCTION, AND DISEASES*. Harisios Boudoulas and Christodoulos Stefanadis. Informa Healthcare, 2009.

[AH10] Thomas Abraham et James Hogg. « Extracellular matrix remodeling of lung alveolar walls in three dimensional space identified using second harmonic generation and multiphoton excitation fluorescence ». In : *Journal of Structural Biology* 171.2 (2010), p. 189-196.

[Aje+11] Visar Ajeti, Oleg Nadiarnykh, Suzanne M. Ponik, Patricia J. Keely, Kevin W. Eliceiri et Paul J. Campagnola. « Structural changes in mixed Col I/Col V collagen gels probed by SHG microscopy: implications for probing stromal alterations in human breast cancer ». In : *Biomedical Optics Express* 2 (2011), p. 2307-2316.

[Aka01] A. N. Akansu. *Multiresolution Signal Decomposition - Transforms, Subbands, and Wavelets*. 2nd edition. Elsevier, 2001.

[Alt92] N. S. Altman. « An Introduction to Kernel and Nearest-Neighbor Nonparametric Regression ». In : *The American Statistician* 46.3 (1992), p. 175-185.

[Amb+12a] Raghu Ambekar, Michael Chittenden, Iwona Jasiuk et Kimani C. Toussaint. « Quantitative second-harmonic generation microscopy for imaging porcine cortical bone: Comparison to SEM and its potential to investigate age-related changes ». In : *Bone* 50.3 (2012), p. 643-650.

[Amb+12b] Raghu Ambekar, Tung-Yuen Lau, Michael Walsh, Rohit Bhargava et Kimani C. Toussaint. « Quantifying collagen structure in breast biopsies using second-harmonic generation imaging ». In : *Biomedical Optics Express* 3 (2012), p. 2021-2035.

[APB19] Venkat Ayyalasomayajula, Baptiste Pierrat et Pierre Badel. « A computational model for understanding the micro-mechanics of collagen fiber network in the tunica adventitia ». In : *Biomechanics and Modeling in Mechanobiology* 18.5 (2019), p. 1507-1528.

[AR05] Tinku Acharya et Ajoy K. Ray. *Image processing: principles and applications*. Hoboken, N.J : John Wiley, 2005.

[Åst+03] Håkan Åstrand, Thomas Sandgren, Åsa Rydén Ahlgren et Toste Länne. « Noninvasive ultrasound measurements of aortic intima-media thickness: implications for in vivo study of aortic wall stress1 1Competition of interest: none. » en. In : *Journal of Vascular Surgery* 37.6 (juin 2003), p. 1270-1276. issn : 07415214. doi : 10.1016/S0741-5214(02)75344-5.

[Bab+14] Olubukola Babalola, Andrew Mamalis, Hadar Lev-Tov et Jared Jagdeo. « Optical coherence tomography (OCT) of collagen in normal skin and skin fibrosis ». In : *Archives of Dermatological Research* 306.1 (2014), p. 1-9.

[Bai+18] Lucie Bailly, Thibaud Cochereau, Laurent Orgéas, Nathalie Henrich Bernardoni, Sabine Rolland du Roscoat, Anne McLeer-Florin, Yohann Robert, Xavier Laval, Tanguy Laurencin, Philippe Chaffanjon, Barbara Fayard et Elodie Boller. « 3D multiscale imaging of human vocal folds using synchrotron X-ray microtomography in phase retrieval mode ». In : *Scientific Reports* 8.1 (2018).

[Bal+14] M. Balu, K. M. Kelly, C. B. Zachary, R. M. Harris, T. B. Krasieva, K. Konig, A. J. Durkin et B. J. Tromberg. « Distinguishing between Benign and Malignant Melanocytic Nevi by In Vivo Multiphoton Microscopy ». In : *Cancer Research* 74.10 (2014), p. 2688-2697.

[Bar+] Andrea Barbetta, Rossella Bedini, Raffaella Pecci et Mariella Dentini. « Role of X-ray microtomography in tissue engineering ». en. In : ().

[Bay+09] Christopher Bayan, Jonathan M. Levitt, Eric Miller, David Kaplan et Irene Georgakoudi. « Fully automated, quantitative, noninvasive assessment of collagen fiber content and organization in thick collagen gels ». In : *Journal of Applied Physics* 105.10 (2009), p. 102042-1-102042-11.

[Ber13] Panagiotis Berillis. « The Role of Collagen in the Aorta's Structure ». en. In : *The Open Circulation and Vascular Journal* 6.1 (2013), p. 1-8. issn : 18773826. doi : 10.2174/1877382601306010001.

[Ber60] DH Bergel. « THE VISCO-ELASTIC PROPERTIES OF THE ARTERIAL WALL ». en. In : (1960), p. 252.

[Ber69] G. D. Bergland. « A guided tour of the fast Fourier transform ». In : *IEEE Spectrum* 6.7 (1969), p. 41-52.

[Bes+19] Sara L. Best, Yuming Liu, Adib Keikhosravi, Cole R. Drifka, Kaitlin M. Woo, Guneet S. Mehta, Marie Altwegg, Terra N. Thimm, Matthew Houlihan, Jeremy S. Bredfeldt, E. Jason Abel, Wei Huang et Kevin W. Eliceiri. « Collagen organization of renal cell carcinoma differs between low and high grade tumors ». In : *BMC Cancer* 19.1 (2019).

[Blu70] L. Bluestein. « A linear filtering approach to the computation of discrete Fourier transform ». In : *IEEE Transactions on Audio and Electroacoustics* 18.4 (1970), p. 451-455.

[Boy08] Robert W. Boyd. *Nonlinear optics*. 3rd ed. Amsterdam ; Boston : Academic Press, 2008. isbn : 978-0-12-369470-6.

[Bre+14] Jeremy S. Bredfeldt, Yuming Liu, Carolyn A. Pehlke, Matthew W. Conklin, Joseph M. Szulczewski, David R. Inman, Patricia J. Keely, Robert D. Nowak, Thomas R. Mackie et Kevin W. Eliceiri. « Computational segmentation of collagen fibers from second-harmonic generation images of breast cancer ». In : *Journal of Biomedical Optics* 19.1 (2014).

[Bri+15] Becky K. Brisson, Elizabeth A. Mauldin, Weiwei Lei, Laurie K. Vogel, Ashley M. Power, Albert Lo, Derek Dopkin, Chand Khanna, Rebecca G. Wells, Ellen Puré et Susan W. Volk. « Type III Collagen Directs Stromal Organization and Limits Metastasis in a Murine Model of Breast Cancer ». In : *The American Journal of Pathology* 185.5 (2015), p. 1471-1486.

[Bro+03] Edward Brown, Trevor McKee, Emmanuelle diTomaso, Alain Pluen, Brian Seed, Yves Boucher et Rakesh K. Jain. « Dynamic imaging of collagen and its modulation in tumors in vivo using second-harmonic generation ». In : *Nature Medicine* 9.6 (2003), p. 796-800.

[Bru78] G. Bruun. « z-transform DFT filters and FFT's ». In : *IEEE Transactions on Acoustics, Speech, and Signal Processing* 26.1 (1978), p. 56-63.

[BS92] R.H. Bamberger et M.J.T. Smith. « A filter bank for the directional decomposition of images: theory and design ». In : *IEEE Transactions on Signal Processing* 40.4 (1992), p. 882-893.

[BT02] Brett E. Bouma et Guillermo J. Tearney, éd. *Handbook of optical coherence tomography*. New York : Marcel Dekker, 2002. isbn : 978-0-8247-0558-9.

[Bue+13] Juan M. Bueno, Raquel Palacios, Mary K. Chessey et Harilaos Ginis. « Analysis of spatial lamellar distribution from adaptive-optics second harmonic generation corneal images ». In : *Biomedical Optics Express* 4.7 (2013).

[CA10] D. Chaudhuri et A. Agrawal. « Split-and-merge Procedure for Image Segmentation using Bimodality Detection Approach ». In : *Defence Science Journal* 60.3 (2010), p. 290-301.

[Cai+14] Cheng-Syun Cai, Chun-Fu Chen, Gwo Giun Lee, Guan-Liang Lin, Sin-Yo Chou, Ming-Rung Tsai, Yi-Hua Liao et Chi-Kuang Sun. « Density analysis of collagen fibers based on enhanced frangi filter in Second Harmonic Generation virtual biopsy images ». In : *2014 IEEE China Summit International Conference on Signal and Information Processing (ChinaSIP)*. IEEE, 2014, p. 465-469. doi : 10.1109/ChinaSIP.2014.6889286.

[Cam+02] Paul J. Campagnola, Andrew C. Millard, Mark Terasaki, Pamela E. Hoppe, Christian J. Malone et William A. Mohler. « Three-Dimensional High-Resolution Second-Harmonic Generation Imaging of Endogenous Structural Proteins in Biological Tissues ». en. In : *Biophysical Journal* 82.1 (2002), p. 493-508. issn : 00063495. doi : 10.1016/S0006-3495(02)75414-3.

[Cam11] Paul Campagnola. « Second Harmonic Generation Imaging Microscopy: Applications to Diseases Diagnostics ». In : *Analytical Chemistry* 83.9 (2011), p. 3224-3231.

[Car+09] L. Cardamone, A. Valentín, J. F. Eberth et J. D. Humphrey. « Origin of axial prestretch and residual stress in arteries ». en. In : *Biomechanics and Modeling in Mechanobiology* 8.6 (déc. 2009), p. 431-446. issn : 1617-7959, 1617-7940. doi : 10.1007/s10237-008-0146-x.

[Car10] Marie-Hélène Roy Cardinal. « Fast-marching segmentation of three-dimensional intravascular ultrasound images: A pre- and post-intervention study ». In : *Medical Physics* 37.7 (2010).

[Cav+17] Cristina Cavinato, Clementine Helfenstein-Didier, Thomas Olivier, Sabine Rolland du Roscoat, Norbert Laroche et Pierre Badel. « Biaxial loading of arterial tissues with 3D in situ observations of adventitia fibrous microstructure: A method coupling multi-photon confocal microscopy and bulge inflation test ». In : *Journal of the Mechanical Behavior of Biomedical Materials* 74 (2017), p. 488-498.

[Cav+19] Cristina Cavinato, Jerome Molimard, Nicolas Curt, Salvatore Campisi, Laurent Orgéas et Pierre Badel. « Does the Knowledge of the Local Thickness of Human Ascending Thoracic Aneurysm Walls Improve Their Mechanical Analysis? » In : *Frontiers in Bioengineering and Biotechnology* 7 (juill. 2019), p. 169. issn : 2296-4185. doi : 10.3389/fbioe.2019.00169.

[CG85] J M Clark et S Glagov. « Transmural organization of the arterial media. The lamellar unit revisited. » en. In : *Arteriosclerosis: An Official Journal of the American Heart Association, Inc.* 5.1 (1985), p. 19-34. issn : 0276-5047. doi : 10.1161/01.ATV.5.1.19.

[Che+12] Xiyi Chen, Oleg Nadiarynkh, Sergey Plotnikov et Paul J Campagnola. « Second harmonic generation microscopy for quantitative analysis of collagen fibrillar structure ». In : *Nature Protocols* 7.4 (2012), p. 654-669.

[Che+17] Mingzhe Chen, Ursula Challita, Walid Saad et Changchuan Yin. « Machine Learning for Wireless Networks with Artificial Intelligence: A Tutorial on Neural Networks ». en. In : (2017).

[CHH77] William H. Carnes, Mary Lou Hart et Norman M. Hodgkin. « Conformation of Aortic Elastin Revealed by Scanning Electronmicroscopy of Dissected Surfaces ». In : *Elastin and Elastic Tissue*. Sous la dir. de Lawrence B. Sandberg, William R. Gray et Carl Franzblau. T. 79. Series Title: Advances in Experimental Medicine and Biology. Boston, MA : Springer US, 1977, p. 61-70. doi : 10.1007/978-1-4684-9093-0_7.

[Chi10] Yu-Wei Chiu. « Second-harmonic generation imaging of collagen fibers in myocardium for atrial fibrillation diagnosis ». In : *Journal of Biomedical Optics* 15.2 (2010).

[Cho+09] Nusrat Choudhury, Olivier Bouchot, Leonie Rouleau, Dominique Tremblay, Raymond Cartier, Jagdish Butany, Rosaire Mongrain et Richard L. Leask. « Local mechanical and structural properties of healthy and diseased human ascending aorta tissue ». en. In : *Cardiovascular Pathology* 18.2 (mars 2009), p. 83-91. issn : 10548807. doi : 10.1016/j.carpath.2008.01.001.

[Cho+14] Ming-Jay Chow, Raphaël Turcotte, Charles. P. Lin et Yanhang Zhang. « Arterial Extracellular Matrix: A Mechanobiological Study of the Contributions and Interactions of Elastin and Collagen ». In : *Biophysical Journal* 106.12 (2014), p. 2684-2692.

[CHP] National Center for Chronic Disease Prevention, Division for Heart Disease Health Promotion et Stroke Prevention. *Aortic Aneurysm*. https://www.cdc.gov/heartdisease/aortic_aneurysm.htm. Accessed: 2021-10-15.

[Cic+09] Riccardo Cicchi, Dimitrios Kapsokalyvas, Vincenzo De Giorgi, Vincenza Maio, Annelies Van Wiechen, Daniela Massi, Torello Lotti et Francesco S. Pavone. « Scoring of collagen organization in healthy and diseased human dermis by multiphoton microscopy ». In : *Journal of Biophotonics* 3.1-2 (2009), p. 34-43.

[CKS93] B.B. Chaudhuri, Pulak Kundu et Nirupam Sarkar. « Detection and gradation of oriented texture ». In : *Pattern Recognition Letters* 14.2 (1993), p. 147-153.

[Clo+99] William Darrin Clouse, John W. Hallett, Hartzell V. Schaff, Michelle M. Gayari, Duane M. Ilstrup et Joseph Melton. « Improved Prognosis of Thoracic Aortic Aneurysms: a Population- Based Study: » en. In : *Survey of Anesthesiology* 43.4 (1999), p. 198-199. ISSN : 0039-6206. DOI : 10.1097/00132586-199908000-00011.

[CLW69] James W. Cooley, Peter A. W. Lewis et Peter D. Welch. « The Fast Fourier Transform and Its Applications ». In : *IEEE Transactions on Education* 12.1 (1969), p. 27-34.

[Cri09] Emiliano Cristiani. « A Fast Marching Method for Hamilton-Jacobi Equations Modeling Monotone Front Propagations ». In : *Journal of Scientific Computing* 39.2 (2009), p. 189-205.

[Dag11] François Dagenais. « Anatomy of the Thoracic Aorta and of Its Branches ». en. In : *Thoracic Surgery Clinics* 21.2 (2011), p. 219-227. ISSN : 15474127. DOI : 10.1016/j.thorsurg.2010.12.004.

[Dah+08] Rainer Dahlhaus, Jürgen Kurths, Peter Maass et Jens Timmer. *Mathematical methods in signal processing and digital image analysis*. Sous la dir. de Rainer Dahlhaus. Understanding complex systems. Berlin : Springer, 2008.

[Dav+16] Frances M. Davis, Yuanming Luo, Stéphane Avril, Ambroise Duprey et Jia Lu. « Local mechanical properties of human ascending thoracic aneurysms ». en. In : *Journal of the Mechanical Behavior of Biomedical Materials* 61 (août 2016), p. 235-249. ISSN : 17516161. DOI : 10.1016/j.jmbbm.2016.03.025.

[DDD19] Robert S. Dieter, Raymond A. Dieter et Raymond A. Dieter III, éd. *Diseases of the Aorta*. en. Cham : Springer International Publishing, 2019. DOI : 10.1007/978-3-030-11322-3.

[DE69] Paul Davidovits et M. David Egger. « Scanning Laser Microscope ». en. In : *Nature* 223.5208 (1969), p. 831-831. ISSN : 0028-0836, 1476-4687. DOI : 10.1038/223831a0.

[Dea07] Stanley R. Deans. *The radon transform and some of its applications*. Mineola, N.Y : Dover Publications, 2007.

[Den+94] S. X. Deng, J. Tomioka, J. C. Debes et Y. C. Fung. « New experiments on shear modulus of elasticity of arteries ». en. In : *American Journal of Physiology-Heart and Circulatory Physiology* 266.1 (jan. 1994), H1-H10. issn : 0363-6135, 1522-1539. doi : 10.1152/ajpheart.1994.266.1.H1.

[DF08] Wolfgang Drexler et James G. Fujimoto, éd. *Optical coherence tomography: technology and applications*. en. Biological and medical physics, biomedical engineering. OCLC: ocn212327728. Berlin : Springer, 2008. isbn : 978-3-540-77549-2.

[DH72] Richard O. Duda et Peter E. Hart. « Use of the Hough transformation to detect lines and curves in pictures ». In : *Communications of the ACM* 15.1 (1972), p. 11-15.

[Dis+17] C. M. Disney, K. Madi, A. J. Bodey, P. D. Lee, J. A. Hoyland et M. J. Sherratt. « Visualising the 3D microstructure of stained and native intervertebral discs using X-ray microtomography ». In : *Scientific Reports* 7.1 (2017).

[Dis+20] Emiel M.J. van Disseldorp, Julia J. van Dronkelaar, Josien P.W. Pluim, Frans N. van de Vosse, Marc R.H.M. van Sambeek et Richard G.P. Lopata. « Ultrasound Based Wall Stress Analysis of Abdominal Aortic Aneurysms using Multiperspective Imaging ». en. In : *European Journal of Vascular and Endovascular Surgery* 59.1 (jan. 2020), p. 81-91. issn : 10785884. doi : 10.1016/j.ejvs.2019.01.026.

[Dou+10] Michael Doube, Michał M. Kłosowski, Ignacio Arganda-Carreras, Fabrice P. Cordelières, Robert P. Dougherty, Jonathan S. Jackson, Benjamin Schmid, John R. Hutchinson et Sandra J. Shefelbine. « BoneJ: Free and extensible bone image analysis in ImageJ ». In : *Bone* 47.6 (2010), p. 1076-1079.

[DR03] Guillaume Damiand et Patrick Resch. « Split-and-merge algorithms defined on topological maps for 3D image segmentation ». In : *Graphical Models* 65.1-3 (2003), p. 149-167.

[Dra+02] Mary T. Draney, Robert J. Herfkens, Thomas J. R. Hughes, Norbert J. Pelc, Kristin L. Wedding, Christopher K. Zarins et Charles A. Taylor. « Quantification of Vessel Wall Cyclic Strain Using Cine Phase Contrast Magnetic Resonance Imaging ». en. In : *Annals of Biomedical Engineering* 30.8 (sept. 2002), p. 1033-1045. issn : 0090-6964. doi : 10.1114/1.1513566.

[Dri+16] Cole R. Drifka, Agnes G. Loeffler, Kara Mathewson, Guneet Mehta, Adib Keikhosravi, Yuming Liu, Stephanie Lemancik, William A. Ricke, Sharon M. Weber, W. John Kao et Kevin W. Eliceiri. « Comparison of Picrosirius Red Staining With Second Harmonic Generation Imaging for the Quantification of Clinically Relevant Collagen

Fiber Features in Histopathology Samples ». In : *Journal of Histochemistry & Cytochemistry* 64.9 (2016), p. 519-529.

[Dud+19] V. V. Dudenkova, M. V. Shirmanova, M. M. Lukina, F. I. Feldshtein, A. Virkin et E. V. Zagainova. « Examination of Collagen Structure and State by the Second Harmonic Generation Microscopy ». In : *Biochemistry (Moscow)* 84.S1 (2019), p. 89-107.

[Dup+16] Ambroise Duprey, Olfa Trabelsi, Marco Vola, Jean-Pierre Favre et Stéphane Avril. « Biaxial rupture properties of ascending thoracic aortic aneurysms ». en. In : *Acta Biomaterialia* 42 (sept. 2016), p. 273-285. issn : 17427061. doi : 10.1016/j.actbio.2016.06.028.

[Erb01] R Erbel. « Diagnosis and management of aortic dissection Task Force on Aortic Dissection, European Society of Cardiology ». en. In : *European Heart Journal* 22.18 (2001), p. 1642-1681. issn : 0195668X. doi : 10.1053/euhj.2001.2782.

[FDS86] I. Freund, M. Deutsch et A. Sprecher. « Connective tissue polarity. Optical second-harmonic microscopy, crossed-beam summation, and small-angle scattering in rat-tail tendon ». en. In : *Biophysical Journal* 50.4 (1986), p. 693-712. issn : 00063495. doi : 10.1016/S0006-3495(86)83510-X.

[Fer+22] Edward Ferdian, David J. Dubowitz, Charlene A. Mauger, Alan Wang et Alistair A. Young. « WSSNet: Aortic Wall Shear Stress Estimation Using Deep Learning on 4D Flow MRI ». In : *Frontiers in Cardiovascular Medicine* 8 (jan. 2022), p. 769927. issn : 2297-055X. doi : 10.3389/fcvm.2021.769927.

[FFP79] Y. C. Fung, K. Fronek et P. Patitucci. « Pseudoelasticity of arteries and the choice of its mathematical expression ». en. In : *American Journal of Physiology-Heart and Circulatory Physiology* 237.5 (nov. 1979), H620-H631. issn : 0363-6135, 1522-1539. doi : 10.1152/ajpheart.1979.237.5.H620.

[Fis53] R. Fisher. « Dispersion on a Sphere ». In : *Proceedings of the Royal Society A: Mathematical, Physical and Engineering Sciences* 217.1130 (1953), p. 295-305.

[Fog] Richard N. Fogoros. *An Overview of Atherosclerosis*. https://www.verywellhealth.com/what-is-atherosclerosis-1745908. Accessed: 2021-10-12.

[For+21] Kayvan Forouhesh Tehrani, Emily G. Pendleton, W. Michael Southern, Jarrod A. Call et Luke J. Mortensen. « Spatial frequency metrics for analysis of microscopic images of musculoskeletal tissues ». en. In : *Connective Tissue Research* 62.1 (2021), p. 4-14. issn : 0300-8207, 1607-8438. doi : 10.1080/03008207.2020.1828381.

[Fra+61] P. A. Franken, A. E. Hill, C. W. Peters et G. Weinreich. « Generation of Optical Harmonics ». en. In : *Physical Review Letters* 7.4 (1961), p. 118-119. issn : 0031-9007. doi : 10.1103/PhysRevLett.7.118.

[Fra+98] Alejandro F. Frangi, Wiro J. Niessen, Koen L. Vincken et Max A. Viergever. « Multiscale vessel enhancement filtering ». In : *Medical Image Computing and Computer-Assisted Intervention — MICCAI'98*. Sous la dir. de William M. Wells, Alan Colchester et Scott Delp. T. 1496. Berlin, Heidelberg : Springer Berlin Heidelberg, 1998, p. 130-137.

[FRW17] Samantha Fowler, Rebecca Roush et James Wise. *Concepts of Biology*. en. Houston, Texas, 2017. isbn : 1-947172-03-4.

[Fuj+00] James G. Fujimoto, Costas Pitris, Stephen A. Boppart et Mark E. Brezinski. « Optical Coherence Tomography: An Emerging Technology for Biomedical Imaging and Optical Biopsy ». en. In : *Neoplasia* 2.1-2 (2000), p. 9-25. issn : 14765586. doi : 10.1038/sj.neo.7900071.

[Gar+12] C. M. García-Herrera, J. M. Atienza, F. J. Rojo, E. Claes, G. V. Guinea, D. J. Celentano, C. García-Montero et R. L. Burgos. « Mechanical behaviour and rupture of normal and pathological human ascending aortic wall ». en. In : *Medical & Biological Engineering & Computing* 50.6 (juin 2012), p. 559-566. issn : 0140-0118, 1741-0444. doi : 10.1007/s11517-012-0876-x.

[GB10] Ashima Gulati et Arvind Bagga. « Large vessel vasculitis ». en. In : *Pediatric Nephrology* 25.6 (2010), p. 1037-1048. issn : 0931-041X, 1432-198X. doi : 10.1007/s00467-009-1312-9.

[GC08] Heather L. Gornik et Mark A. Creager. « Aortitis ». en. In : *Circulation* 117.23 (2008), p. 3039-3051. issn : 0009-7322, 1524-4539. doi : 10.1161/CIRCULATIONAHA.107.760686.

[Gen+13] K. Genovese, Y-U. Lee, A.Y. Lee et J.D. Humphrey. « An improved panoramic digital image correlation method for vascular strain analysis and material characterization ». en. In : *Journal of the Mechanical Behavior of Biomedical Materials* 27 (nov. 2013), p. 132-142. issn : 17516161. doi : 10.1016/j.jmbbm.2012.11.015.

[Gir+92] X. J. Girerd, C. Acar, J. J. Mourad, P. Boutouyrie, M. E. Safar et S. Laurent. « Incompressibility of the human arterial wall: an in vitro ultrasound study ». eng. In : *Journal of Hypertension. Supplement: Official Journal of the International Society of Hypertension* 10.6 (août 1992), S111-114. issn : 0952-1178.

[GL91] Sarah Frisken Gibson et Frederick Lanni. « Experimental test of an analytical model of aberration in an oil-immersion objective lens used in three-dimensional light microscopy ». In : *J. Opt. Soc. Am. A* 8.10 (1991), p. 1601-1613. doi : 10.1364/JOSAA.8.001601.

[GM84] A. Grossmann et J. Morlet. « Decomposition of hardy functions into square integrable wavelets of constant shape ». In : *Siam Journal on Mathematical Analysis* 15.4 (1984), p. 723-736.

[GMM18] James A. Germann, Eduardo Martinez-Enriquez et Susana Marcos. « Quantization of collagen organization in the stroma with a new order coefficient ». In : *Biomedical Optics Express* 9.1 (2018), p. 173-189.

[GOH06] T Christian Gasser, Ray W Ogden et Gerhard A Holzapfel. « Hyperelastic modelling of arterial layers with distributed collagen fibre orientations ». en. In : *J. R. Soc. Interface* (2006).

[Gol+14] Judith Z. Goldfinger, Jonathan L. Halperin, Michael L. Marin, Allan S. Stewart, Kim A. Eagle et Valentin Fuster. « Thoracic Aortic Aneurysm and Dissection ». en. In : *Journal of the American College of Cardiology* 64.16 (2014), p. 1725-1739. issn : 07351097. doi : 10.1016/j.jacc.2014.08.025.

[Got+16] Will Goth, John Lesicko, Michael S. Sacks et James W. Tunnell. « Optical-Based Analysis of Soft Tissue Structures ». en. In : *Annual Review of Biomedical Engineering* 18.1 (2016), p. 357-385. issn : 1523-9829, 1545-4274. doi : 10.1146/annurev-bioeng-071114-040625.

[GRC19] Piyusha S. Gade, Anne M. Robertson et Chih-Yuan Chuang. « Multiphoton Imaging of Collagen, Elastin, and Calcification in Intact Soft-Tissue Samples ». In : *Current Protocols in Cytometry* 87.1 (2019).

[GST19] Jan-Lucas Gade, Jonas Stålhand et Carl-Johan Thore. « An *in vivo* parameter identification method for arteries: numerical validation for the human abdominal aorta ». en. In : *Computer Methods in Biomechanics and Biomedical Engineering* 22.4 (mars 2019), p. 426-441. issn : 1025-5842, 1476-8259. doi : 10.1080/10255842.2018.1561878.

[GW18] Rafael C. Gonzalez et Richard E. Woods. *Digital image processing*. New York, NY : Pearson, 2018.

[HCC16] Christopher Harris, Beth Croce et Christopher Cao. « Type A aortic dissection ». eng. In : *Annals of Cardiothoracic Surgery* 5.3 (2016). issn : 2225-319X. doi : 10.21037/acs.2016.05.04.

[Hel+18] Clémentine Helfenstein-Didier, Damien Taïnoff, Julien Viville, Jérôme Adrien, Éric Maire et Pierre Badel. « Tensile rupture of medial arterial tissue studied by X-ray micro-tomography on stained samples ». en. In : *Journal of the Mechanical Behavior of Biomedical Materials* 78 (2018), p. 362-368. issn : 17516161. doi : 10.1016/j.jmbbm.2017.11.032.

[HGO00] Gerhard A. Holzapfel, Thomas C. Gasser et Ray W. Ogden. « A New Constitutive Framework for Arterial Wall Mechanics and a Comparative Study of Material Models ». In : *Journal of Elasticity* 61.1/3 (2000), p. 1-48. issn : 03743535. doi : 10.1023/A:1010835316564.

[HH12] J.D. Humphrey et G.A. Holzapfel. « Mechanics, mechanobiology, and modeling of human abdominal aorta and aneurysms ». In : *Journal of Biomechanics* 45.5 (2012), p. 805-814.

[HHH09] Aapo Hyvärinen, Jarmo Hurri et Patrik O. Hoyer. *Natural Image Statistics*. T. 39. Computational Imaging and Vision. London : Springer London, 2009.

[Hil+12] Michael R. Hill, Xinjie Duan, Gregory A. Gibson, Simon Watkins et Anne M. Robertson. « A theoretical and non-destructive experimental approach for direct inclusion of measured collagen orientation and recruitment into mechanical models of the artery wall ». In : *Journal of Biomechanics* 45.5 (2012), p. 762-771.

[Hol+05] Gerhard A. Holzapfel, Gerhard Sommer, Christian T. Gasser et Peter Regitnig. « Determination of layer-specific mechanical properties of human coronary arteries with nonatherosclerotic intimal thickening and related constitutive modeling ». en. In : *American Journal of Physiology-Heart and Circulatory Physiology* 289.5 (nov. 2005), H2048-H2058. issn : 0363-6135, 1522-1539. doi : 10.1152/ajpheart.00934.2004.

[Hom+08] Tord Hompland, Arne Erikson, Mikael Lindgren, Tore Lindmo et Catharina de Lange Davies. « Second-harmonic generation in collagen as a potential cancer diagnostic parameter ». In : *Journal of Biomedical Optics* 13.5 (2008).

[Hou62] Paul VC Hough. *Method and means for recognizing complex patterns*. US Patent 3,069,654. 1962.

[HR02] J. D. Humphrey et K. R. Rajagopal. « A CONSTRAINED MIXTURE MODEL FOR GROWTH AND REMODELING OF SOFT TISSUES ». en. In : *Mathematical Models and Methods in Applied Sciences* 12.03 (mars 2002), p. 407-430. issn : 0218-2025, 1793-6314. doi : 10.1142/S0218202502001714.

[Hri+18] Radu Hristu, Lucian G. Eftimie, Stefan G. Stanciu, Denis E. Tranca, Bogdan Paun, Maria Sajin et George A. Stanciu. « Quantitative second harmonic generation microscopy for the structural characterization of capsular collagen in thyroid neoplasms ». In : *Biomedical Optics Express* 9.8 (2018), p. 3923-3936.

[HSD73] Robert M. Haralick, K. Shanmugam et Its'Hak Dinstein. « Textural Features for Image Classification ». In : *IEEE Transactions on Systems, Man, and Cybernetics* SMC-3.6 (1973), p. 610-621.

[Hu+12] Wenyan Hu, Hui Li, Chunyou Wang, Shanmiao Gou et Ling Fu. « Characterization of collagen fibers by means of texture analysis of second harmonic generation images using orientation-dependent gray level co-occurrence matrix method ». In : *Journal of Biomedical Optics* 17.2 (2012).

[Hu+19] Desheng Hu, Changjun Yin, Shanshan Luo, Andreas J. R. Habenicht et Sarajo K. Mohanta. « Vascular Smooth Muscle Cells Contribute to Atherosclerosis Immunity ». en. In : *Frontiers in Immunology* 10 (2019). issn : 1664-3224. doi : 10.3389/fimmu.2019.01101.

[Hua+91] David Huang, Eric A Swanson, Charles P Lin, Joel S Schuman, William G Stinson, Warren Chang, Michael R Hee, Thomas Flotte, Kenton Gregory et Carmen A Puliafito. « Optical Coherence Tomography ». en. In : Sciences 254 (1991), p. 1178-1181.

[Hum02] Jay D. Humphrey. *Cardiovascular Solid Mechanics*. en. New York, NY : Springer New York, 2002. doi : 10.1007/978-0-387-21576-1.

[Hut+18] Mikko J. Huttunen, Abdurahman Hassan, Curtis W. McCloskey, Sijyl Fasih, Jeremy Upham, Barbara C. Vanderhyden, Robert W. Boyd et Sangeeta Murugkar. « Automated classification of multiphoton microscopy images of ovarian tissue using deep learning ». en. In : *Journal of Biomedical Optics* 23.06 (2018), p. 066002-1-066002-7. issn : 1083-3668. doi : 10.1117/1.JBO.23.6.066002.

[HYT79] T. Huang, G. Yang et G. Tang. « A fast two-dimensional median filtering algorithm ». In : *IEEE Transactions on Acoustics, Speech, and Signal Processing* 27.1 (1979), p. 13-18.

[Iqb+21] Naveed Iqbal, Rafia Mumtaz, Uferah Shafi et Syed Mohammad Hassan Zaidi. « Gray level co-occurrence matrix (GLCM) texture based crop classification using low altitude remote sensing platforms ». en. In : *PeerJ Computer Science* 7 (2021). issn : 2376-5992. doi : 10.7717/peerj-cs.536.

[Iss05] Eric M. Isselbacher. « Thoracic and Abdominal Aortic Aneurysms ». en. In : *Circulation* 111.6 (2005), p. 816-828. issn : 0009-7322, 1524-4539. doi : 10.1161/01.CIR.0000154569.08857.7A.

[Ita+02] Yasutaka Itani, Shigeru Watanabe, Yoshiaki Masuda, Kazuhisa Hanamura, Kazuhiro Asakura, Shusuke Sone, Yuko Sunami et Tadaaki Miyamoto. « Measurement of aortic diameters and detection of asymptomatic aortic aneurysms in a mass screening program using a mobile helical computed tomography unit ». en. In : *Heart and Vessels* 16.2 (2002), p. 42-45. issn : 0910-8327, 1615-2573. doi : 10.1007/s380-002-8315-1.

[JD05] Daniel P. Judge et Harry C. Dietz. « Marfan's syndrome ». In : 366.9501 (2005), p. 1965-1976.

[JH13] A.H.M. Jaffar Iqbal Barbhuiya et K. Hemachandran. « Wavelet Tranformations & Its Major Applications In Digital Image Processing ». In : *International Journal of Engineering Research* 2.3 (2013).

[Jin+20] Cheng Jin, Lingjie Kong, Hod Dana, Hao Xie, Liangcai Cao, Guofan Jin et Qionghai Dai. « Advances in point spread function engineering for functional imaging of neural circuits *in vivo* ». en. In : *Journal of Physics D: Applied Physics* 53.38 (2020). issn : 0022-3727, 1361-6463. doi : 10.1088/1361-6463/ab946e.

[JKR18] Jens Jordan, Christine Kurschat et Hannes Reuter. « Arterial Hypertension ». en. In : *Deutsches Aerzteblatt Online* (2018). issn : 1866-0452. doi : 10.3238/arztebl.2018.0557.

[JLG02] S L Johnston, R J Lock et M M Gompels. « Takayasu arteritis: a review ». en. In : 55 (2002), p. 481-486.

[Kab+13] Mohammad M. Kabir, V. V. G. Krishna Inavalli, Tung-Yuen Lau et Kimani C. Toussaint. « Application of quantitative second-harmonic generation microscopy to dynamic conditions ». In : *Biomedical Optics Express* 4.11 (2013).

[Kar+17] N. Karathanasopoulos, P. Angelikopoulos, C. Papadimitriou et P. Koumoutsakos. « Bayesian identification of the tendon fascicle's structural composition using finite element models for helical geometries ». In : *Computer Methods in Applied Mechanics and Engineering* 313 (2017), p. 744-758.

[Kar+98] William J Karlon, James W Covell, Andrew D Mcculloch, John J Hunter et Jeffrey H Omens. « Automated measurement of myofiber disarray in transgenic mice with ventricular expression of ras ». In : *The anatomical record* (1998), p. 612-625.

[KB17] Diederik P. Kingma et Jimmy Ba. « Adam: A Method for Stochastic Optimization ». en. In : *arXiv:1412.6980 [cs]* (2017). arXiv: 1412.6980.

[KE10] Nilufer Kale et Eric Eggenberger. « Diagnosis and management of giant cell arteritis: a review ». en. In : *Current Opinion in Ophthalmology* 21.6 (2010), p. 417-422. issn : 1040-8738. doi : 10.1097/ICU.0b013e32833eae8b.

[Kha+15] Sheema Shuja Khattak, Gule Saman, Imran Khan et Abdus Salam. « Maximum Entropy Based Image Segmentation of Human Skin Lesion ». In : *International Journal of Computer, Control, Quantum and Information Engineering* 9.5 (2015), p. 667-671.

[KHX11] Demirhan Kobat, Nicholas G. Horton et Chris Xu. « In vivo two-photon microscopy to 1.6-mm depth in mouse cortex ». en. In : *Journal of Biomedical Optics* 16.10 (2011). issn : 10833668. doi : 10.1117/1.3646209.

[KI86] J. Kittler et J. Illingworth. « Minimum error thresholding ». In : *Pattern Recognition* 19.1 (1986), p. 41-47.

[Kir71] Russell A. Kirsch. « Computer determination of the constituent structure of biological images ». In : *Computers and Biomedical Research* 4.3 (1971), p. 315-328.

[KKA21] Jonathan D. Kelley, Connor C. Kerndt et John V. Ashurst. « Anatomy, Thorax, Aortic Arch ». eng. In : *StatPearls*. Treasure Island (FL) : StatPearls Publishing, 2021.

[KMW13] Thomas E. Kruger, Andrew H. Miller et Jinxi Wang. « Collagen Scaffolds in Bone Sialoprotein-Mediated Bone Regeneration ». In : *The Scientific World Journal* 2013 (2013). Sous la dir. d'A. Bandyopadhyay et C.-H. Yao. Publisher: Hindawi Publishing Corporation. issn : 2356-6140. doi : 10.1155/2013/812718.

[Koc+14] Ryan G. Koch, Alkiviadis Tsamis, Antonio D'Amore, William R. Wagner, Simon C. Watkins, Thomas G. Gleason et David A. Vorp. « A custom image-based analysis tool for quantifying elastin and collagen micro-architecture in the wall of the human aorta from multi-photon microscopy ». In : *Journal of Biomechanics* 47.5 (2014), p. 935-943.

[Koe+06] Martin Johannes Koehler, Karsten König, Peter Elsner, Rainer Bückle et Martin Kaatz. « In vivo assessment of human skin aging by multiphoton laser scanning tomography ». In : *Optics Letters* 31.19 (2006).

[Kra+17] Witold Krasny, Claire Morin, Hélène Magoariec et Stéphane Avril. « A comprehensive study of layer-specific morphological changes in the microstructure of carotid arteries under uniaxial load ». en. In : *Acta Biomaterialia* 57 (2017), p. 342-351. issn : 17427061. doi : 10.1016/j.actbio.2017.04.033.

[Krö+21] Marius Kröger, Johannes Schleusener, Sora Jung et Maxim E. Darvin. « Characterization of Collagen I Fiber Thickness, Density, and Orientation in the Human Skin In Vivo Using Second-Harmonic Generation Imaging ». en. In : *Photonics* 8.9 (2021). issn : 2304-6732. doi : 10.3390/photonics8090404.

[Lar+11] Emma Larsson, Fausto Labruto, T. Christian Gasser, Jesper Swedenborg et Rebecka Hultgren. « Analysis of aortic wall stress and rupture risk in patients with abdominal aortic aneurysm with a gender perspective ». en. In : *Journal of Vascular Surgery* 54.2 (août 2011), p. 295-299. issn : 07415214. doi : 10.1016/j.jvs.2010.12.053.

[LAS15] J. S. Lowe, Peter G. Anderson et Alan Stevens. *Stevens & Lowe's human histology*. 4th edition. Philadelphia, PA : Elsevier/Mosby, 2015.

[LAT12] Tung Yuen Lau, Raghu Ambekar et Kimani C. Toussaint. « Quantification of collagen fiber organization using three-dimensional Fourier transform-second-harmonic generation imaging ». In : *Optics Express* 20.19 (2012), p. 21821-21832.

[LCD19] Sheng-Lin Lee, Yang-Fang Chen et Chen-Yuan Dong. « Second harmonic generation imaging reveals asymmetry in the rotational helicity of collagen lamellae in chicken corneas ». In : *Biomedical Optics Express* 10.10 (2019).

[LCK17] Tong Luo, Huan Chen et Ghassan S. Kassab. « Resliced image space construction for coronary artery collagen fibers ». In : *PLOS ONE* 12.9 (2017), p. 1-15.

[Lea92] V. F. Leavers. *Shape Detection in Computer Vision Using the Hough Transform*. London : Springer, 1992. Chap. Computer Vision: Shape Detection, p. 1-18.

[Lef+21] Claire Lefort, Mathieu Chalvidal, Alexis Parenté, Véronique Blanquet, Henri Massias, Laetitia Magnol et Emilie Chouzenoux. « FAMOUS: a fast instrumental and computational pipeline for multiphoton microscopy applied to 3D imaging of muscle ultrastructure ». en. In : *Journal of Physics D: Applied Physics* 54.27 (2021). issn : 0022-3727, 1361-6463. doi : 10.1088/1361-6463/abf8f2.

[Lin+05] Sung-Jan Lin, Ruei-Jr Wu, Hsin-Yuan Tan, Wen Lo, Wei-Chou Lin, Tai-Horng Young, Chih-Jung Hsu, Jau-Shiuh Chen, Shiou-Hwa Jee et Chen-Yuan Dong. « Evaluating cutaneous photoaging by use of multiphoton fluorescence and second-harmonic generation microscopy ». In : *Optics Letters* 30.17 (2005), p. 2275-2277.

[Liu+18] Zhiyi Liu, Lucia Speroni, Kyle P. Quinn, Carlo Alonzo, Dimitra Pouli, Yang Zhang, Emily Stuntz, Carlos Sonnenschein, Ana M. Soto et Irene Georgakoudi. « 3D organizational mapping of collagen fibers elucidates matrix remodeling in a hormone-sensitive 3D breast tissue model ». In : *Biomaterials* 179 (2018), p. 96-108.

[LL96] J.Michael Lee et Shari E. Langdon. « Thickness measurement of soft tissue biomaterials: A comparison of five methods ». en. In : *Journal of Biomechanics* 29.6 (1996), p. 829-832. issn : 00219290. doi : 10.1016/0021-9290(95)00121-2.

[LLF04] Franck Luthon, Marc Liévin et Francis Faux. « On the use of entropy power for threshold selection ». In : *Signal Processing* 84.10 (2004), p. 1789-1804.

[LLS17] Liang Liang, Minliang Liu et Wei Sun. « A deep learning approach to estimate chemically-treated collagenous tissue nonlinear anisotropic stress-strain responses from microscopy images ». en. In : *Acta Biomaterialia* 63 (2017), p. 227-235. issn : 17427061. doi : 10.1016/j.actbio.2017.09.025.

[Lod+00] Harvey Lodish, Arnold Berk, S Lawrence Zipursky, Paul Matsudaira, David Baltimore et James Darnell. *Molecular cell biology*. Sous la dir. d'Harvey F. Lodish. 4th ed. New York : W.H. Freeman, 2000.

[LV17] Christophe Ley et Thomas Verdebout. *Modern Directional Statistics*. Interdisciplinary statistics. CRC Press, 2017.

[MA18] Wan Azani Mustafa et Mohamed Mydin M. Abdul Kader. « A Review of Histogram Equalization Techniques in Image Enhancement Application ». In : *Journal of Physics: Conference Series* 1019 (2018).

[Mad02] Sylvia S. Mader. *Human biology*. 7th ed. Boston, [MA] : McGraw-Hill, 2002. isbn : 978-0-07-232481-5.

[MAH18] Claire Morin, Stéphane Avril et Christian Hellmich. « Non-affine fiber kinematics in arterial mechanics: a continuum micromechanical investigation ». en. In : *ZAMM - Journal of Applied Mathematics and Mechanics / Zeitschrift für Angewandte Mathematik und Mechanik* 98.12 (déc. 2018), p. 2101-2121. issn : 0044-2267, 1521-4001. doi : 10.1002/zamm.201700360.

[Mar+08] Kanti V. Mardia, Gareth Hughes, Charles C. Taylor et Harshinder Singh. « A multivariate von mises distribution with applications to bioinformatics ». In : *Canadian Journal of Statistics* 36.1 (2008), p. 99-109.

[Mat+09] Takeo Matsumoto, Tomohiro Fukui, Toshihiro Tanaka, Naoko Ikuta, Toshiro Ohashi, Kiichiro Kumagai, Hiroji Akimoto, Koichi Tabayashi et Masaaki Sato. « Biaxial Tensile Properties of Thoracic Aortic Aneurysm Tissues ». en. In : *Journal of Biomechanical Science and Engineering* 4.4 (2009), p. 518-529. issn : 1880-9863. doi : 10.1299/jbse.4.518.

[McL15] J. McLean. « A linear method for quantification of collagen fiber orientation in Cornea ». In : *2015 41st Annual Northeast Biomedical Engineering Conference (NEBEC)*. 2015, p. 1-2.

[Meg+12] Yair Mega, Mike Robitaille, Ramin Zareian, James McLean, Jeffrey Ruberti et Charles DiMarzio. « Quantification of lamellar orientation in corneal collagen using second harmonic generation images ». In : *Optics Letters* 37 (2012).

[Mei+04] E. Meijering, M. Jacob, J.-C.F. Sarria, P. Steiner, H. Hirling et M. Unser. « Design and validation of a tool for neurite tracing and analysis in fluorescence microscopy images ». In : *Cytometry* 58A.2 (2004), p. 167-176.

[Mey+20] Olivier Meyrignac, Laurence Bal, Charline Zadro, Adrien Vavasseur, Anou Sewonu, Marine Gaudry, Bertrand Saint-Lebes, Mariangela De Masi, Paul Revel-Mouroz, Agnès Sommet, Jean Darcourt, Anne Negre-Salvayre, Alexis Jacquier, Jean-Michel Bartoli, Philippe Piquet, Hervé Rousseau et Ramiro Moreno. « Combining Volumetric and Wall Shear Stress Analysis from CT to Assess Risk of Abdominal Aortic Aneurysm Progression ». en. In : *Radiology* 295.3 (juin 2020), p. 722-729. issn : 0033-8419, 1527-1315. doi : 10.1148/radiol.2020192112.

[MGM06] Matei Mancas, Bernard Gosselin et Benoit Macq. « Segmentation using a region growing thresholding ». In : *Image Processing: Algorithms and Systems IV*. T. 5672. 2006, p. 388-398.

[Mic] MicroscopyU. *Numerical Aperture and Image Resolution*. https://www.microscopyu.com/tutorials/imageformation-airyna. Accessed: 2021-10-25.

[Min19] Marvin Minsky. *Microscopy apparatus*. U.S. 3013467A, 1961-12-19.

[MJ00] K. V. Mardia et Peter E. Jupp. *Directional statistics*. Wiley series in probability and statistics. Chichester ; New York : J. Wiley, 2000.

[Mor+21] Claire Morin, Christian Hellmich, Zeineb Nejim et Stéphane Avril. « Fiber Rearrangement and Matrix Compression in Soft Tissues: Multiscale Hypoelasticity and Application to Tendon ». en. In : *Frontiers in Bioengineering and Biotechnology* 9 (oct. 2021), p. 725047. issn : 2296-4185. doi : 10.3389/fbioe.2021.725047.

[Mos+13] Leila B. Mostaço-Guidolin, Alex C.-T. Ko, Fei Wang, Bo Xiang, Mark Hewko, Ganghong Tian, Arkady Major, Masashi Shiomi et Michael G. Sowa. « Collagen morphology and texture analysis: from statistics to classification ». In : *Scientific Reports* 3.1 (2013).

[MS96] R. Malladi et J.A. Sethian. « Level set and fast marching methods in image processing and computer vision ». In : *Proceedings of 3rd IEEE International Conference on Image Processing*. T. 1. Lausanne, Switzerland : IEEE, 1996, p. 489-492.

[Nat+09] Konstantinos I. Natsis, Ioannis A. Tsitouridis, Matthaios V. Didagelos, Andis A. Fillipidis, Konstantinos G. Vlasis et Prokopios D. Tsikaras. « Anatomical variations in the branches of the human aortic arch in 633 angiographies: clinical significance and literature review ». en. In : *Surgical and Radiologic Anatomy* 31.5 (2009), p. 319-323. issn : 0930-1038, 1279-8517. doi : 10.1007/s00276-008-0442-2.

[Nie+16] Justyna A. Niestrawska, Christian Viertler, Peter Regitnig, Tina U. Cohnert, Gerhard Sommer et Gerhard A. Holzapfel. « Microstructure and mechanics of healthy and aneurysmatic abdominal aortas: experimental analysis and modelling ». In : *Journal of The Royal Society Interface* 13.124 (2016).

[Nis+99] S Nistri, M D Sorbo, M Marin, M Palisi, R Scognamiglio et G Thiene. « Aortic root dilatation in young men with normally functioning bicuspid aortic valves ». en. In : *Heart* 82.1 (1999), p. 19-22. issn : 1355-6037. doi : 10.1136/hrt.82.1.19.

[Oka+02] Ruth J. Okamoto, Jessica E. Wagenseil, William R. DeLong, Sara J. Peterson, Nicholas T. Kouchoukos et Thoralf M. Sundt III. « Mechanical Properties of Dilated Human Ascending Aorta ». en. In : *Annals of Biomedical Engineering* 30.5 (mai 2002), p. 624-635. issn : 0090-6964. doi : 10.1114/1.1484220.

[OKH82] J. W. Orberg, L. Klein et A. Hiltner. « Scanning Electron Microscopy of Collagen Fibers in Intestine ». In : *Connective Tissue Research* 9.3 (1982), p. 187-193.

[Oly] Olympus. *Numerical Aperture and Resolution*. https://www.olympus-lifescience.com/en/microscope-resource/primer/anatomy/numaperture/. Accessed: 2021-10-25.

[OS88] Stanley Osher et James A Sethian. « Fronts propagating with curvature-dependent speed: Algorithms based on Hamilton-Jacobi formulations ». In : *Journal of Computational Physics* 79.1 (1988), p. 12-49.

[Ost13] Oksana Ostroverkhova. *Handbook of organic materials for optical and (opto)electronic devices*. en. Woodhead Publishing Limited, 2013. isbn : 978-0-85709-265-6. doi : 10.1533/9780857098764.

[Ots79] Nobuyuki Otsu. « A Threshold Selection Method from Gray-Level Histograms ». In : *IEEE Transactions on Systems, Man, and Cybernetics* 9.1 (1979), p. 62-66.

[OZV95] Makoto Ohki, Michael E. Zervakis et Anastasios N. Venetsanopoulos. « 3-D Digital Filters ». In : *Control and Dynamic Systems*. T. 69. Elsevier, 1995, p. 49-88.

[Pea01] Karl Pearson. « LIII. *On lines and planes of closest fit to systems of points in space* ». In : *The London, Edinburgh, and Dublin Philosophical Magazine and Journal of Science* 2.11 (1901), p. 559-572.

[Pet+68] Mojmír Petráň, Milan Hadravský, M. David Egger et Robert Galambos. « Tandem-Scanning Reflected-Light Microscope* ». en. In : *Journal of the Optical Society of America* 58.5 (1968). issn : 0030-3941. doi : 10.1364/JOSA.58.000661.

[PFJ69] Dali J. Patel, Donald L. Fry et Joseph S. Janicki. « The Elastic Symmetry of Arterial Segments in Dogs ». en. In : *Circulation Research* 24.1 (jan. 1969), p. 1-8. issn : 0009-7330, 1524-4571. doi : 10.1161/01.RES.24.1.1.

[PG20] Arthur Pewsey et Eduardo García-Portugués. « Recent advances in directional statistics ». In : *arXiv:2005.06889 [stat]* (2020).

[Phi+14] Julie A. Phillippi, Benjamin R. Green, Michael A. Eskay, Mary P. Kotlarczyk, Michael R. Hill, Anne M. Robertson, Simon C. Watkins, David A. Vorp et Thomas G. Gleason. « Mechanism of aortic medial matrix remodeling is distinct in patients with bicuspid aortic valve ». In : *The Journal of Thoracic and Cardiovascular Surgery* 147.3 (2014), p. 1056-1064.

[Pij+19] Jacek K. Pijanka, Petar P. Markov, Dan Midgett, Neil G. Paterson, Nick White, Emma J. Blain, Thao D. Nguyen, Harry A. Quigley et Craig Boote. « Quantification of collagen fiber structure using second harmonic generation imaging and two-dimensional discrete Fourier transform analysis: Application to the human optic nerve head ». In : *Journal of Biophotonics* 12.5 (2019).

[Piz+87] Stephen M Pizer, E Philip Amburn, John D Austin, Robert Cromartie, Ari Geselowitz, Trey Greer et Arel Zuiderveld. « Adaptive Histogram Equalization and Its Variations ». In : *Computer Vision, Graphics and Image Processing* 39 (1987), p. 355-368.

[PJ08] Liakat A. Parapia et Carolyn Jackson. « Ehlers-Danlos syndrome – a historical review ». en. In : *British Journal of Haematology* 141.1 (2008), p. 32-35. issn : 0007-1048, 1365-2141. doi : 10.1111/j.1365-2141.2008.06994.x.

[Pol+13] Stanislav Polzer, T. Christian Gasser, Caroline Forsell, Hana Druckmüllerova, Michal Tichy, Robert Staffa, Robert Vlachovsky et Jiri Bursa. « Automatic Identification and Validation of Planar Collagen Organization in the Aorta Wall with Application to Abdominal Aortic Aneurysm ». In : *Microscopy and Microanalysis* 19.6 (2013), p. 1395-1404.

[Pra+03] Isaura M.M. Prado, Liberato J.A. Di Dio, Marcílio Hubner Miranda-Neto, Sonia Lucy Molinari, Tiziana Stallone, Guido Macchiarelli et Pietro M. Motta. « Distribution of collagen fibers in the aggregated lymphoid follicles of swine terminal ileum ». In : *Annals of Anatomy - Anatomischer Anzeiger* 185.1 (2003), p. 73-80.

[Pre70] Judith M. S. Prewitt. « Object enhancement and extraction ». In : *Picture processing and Psychopictorics* (1970).

[Rad68] C.M. Rader. « Discrete Fourier transforms when the number of data samples is prime ». In : *Proceedings of the IEEE* 56.6 (1968), p. 1107-1108.

[Rad83] Johann Radon. « Über die Bestimmung von Funktionen durch ihre Integralwerte längs gewisser Mannigfaltigkeiten ». de. In : *Proceedings of Symposia in Applied Mathematics*. Sous la dir. de Lawrence Shepp. T. 27. Providence, Rhode Island : American Mathematical Society, 1983, p. 71-86. doi : 10.1090/psapm/027/692055.

[RB11] Kara Rogers et Britannica Educational Publishing. *The Cardiovascular System.* English. OCLC: 630543487. Chicago : Britannica Educational Pub., 2011. isbn : 978-1-61530-251-2.

[Rea+13] Eusebio Real, Alma Eguizabal, Alejandro Pontón, Marta Calvo Díez, José Fernando Val-Bernal, Marta Mayorga, José M. Revuelta, José M. López-Higuera et Olga M. Conde. « Optical coherence tomography assessment of vessel wall degradation in thoracic aortic

aneurysms ». en. In : *Journal of Biomedical Optics* 18.12 (2013). ISSN : 1083-3668. DOI : 10.1117/1.JBO.18.12.126003.

[RF95] Werner Risau et Ingo Flamme. « Vasculogenesis ». en. In : *Annual Review of Cell and Developmental Biology* 11.1 (1995), p. 73-91. ISSN : 1081-0706, 1530-8995. DOI : 10.1146/annurev.cb.11.110195.000445.

[Riv77] G. Rivard. « Direct fast Fourier transform of bivariate functions ». In : *IEEE Transactions on Acoustics, Speech, and Signal Processing* 25.3 (1977), p. 250-252.

[RMT09] Raghu Ambekar Ramachandra Rao, Monal R. Mehta et Kimani C. Toussaint. « Fourier transform-second-harmonic generation imaging of biological tissues ». In : *Optics Express* 17.17 (2009).

[Rob+16] Benjamin K. Robinson, Ernesto Cortes, Alistair J. Rice, Muge Sarper et Armando del Río Hernández. « Quantitative analysis of 3D extracellular matrix remodelling by pancreatic stellate cells ». In : *Biology Open* 5.6 (2016), p. 875-882.

[Rom+14] Aaron Romo, Pierre Badel, Ambroise Duprey, Jean-Pierre Favre et Stéphane Avril. « In vitro analysis of localized aneurysm rupture ». en. In : *Journal of Biomechanics* 47.3 (fév. 2014), p. 607-616. ISSN : 00219290. DOI : 10.1016/j.jbiomech.2013.12.012.

[Ros+20] Suzanne Rosen, Becky K. Brisson, Amy C. Durham, Clare M. Munroe, Conor J. McNeill, Darko Stefanovski, Karin U. Sørenmo et Susan W. Volk. « Intratumoral collagen signatures predict clinical outcomes in feline mammary carcinoma ». In : *PLOS ONE* 15.8 (2020), p. 1-22.

[Sal+15] Emile Saliba, Ying Sia, Annie Dore et Ismael El Hamamsy. « The ascending aortic aneurysm: When to intervene? » en. In : *IJC Heart & Vasculature* 6 (2015), p. 91-100. ISSN : 23529067. DOI : 10.1016/j.ijcha.2015.01.009.

[SBZ15] Meng Sun, Alexander B. Bloom et Muhammad H. Zaman. « Rapid Quantification of 3D Collagen Fiber Alignment and Fiber Intersection Correlations with High Sensitivity ». In : *PLOS ONE* 10.7 (2015). Sous la dir. d'Arrate Muñoz-Barrutia.

[SCD02] Jean-Luc Starck, Emmanuel J Candès et David L Donoho. « The Curvelet Transform for Image Denoising ». In : *IEEE TRANSACTIONS ON IMAGE PROCESSING* 11.6 (2002).

[Sch+13] Andreas J. Schriefl, Heimo Wolinski, Peter Regitnig, Sepp D. Kohlwein et Gerhard A. Holzapfel. « An automated approach for three-dimensional quantification of fibrillar structures in optically cleared soft biological tissues ». In : *Journal of The Royal Society Interface* 10.80 (2013).

[Sch+19] Lars SCHMARJE, Claudius ZELENKA, Ulf GEISEN, Claus-C. GLÜER et Reinhard KOCH. « 2D and 3D Segmentation of uncertain local collagen fiber orientations in SHG microscopy ». In : *arXiv:1907.12868 [cs]* 11824 (2019). arXiv: 1907.12868, p. 374-386. DOI : 10.1007/978-3-030-33676-9_26.

[SF96] E.P. SIMONCELLI et H. FARID. « Steerable wedge filters for local orientation analysis ». In : *IEEE Transactions on Image Processing* 5.9 (1996).

[SHB08] Milan SONKA, Vaclav HLAVAC et Roger BOYLE. *Image processing, analysis, and machine vision*. 3. ed., internat. student ed. Stamford, Conn. : Cengage Learning, 2008.

[She+16] Tom SHEARER, Robert S. BRADLEY, L. Araida HIDALGO-BASTIDA, Michael J. SHERRATT et Sarah H. CARTMELL. « Three-dimensional visualisation of soft biological structures by X-ray computed microtomography ». en. In : *Journal of Cell Science* (2016). ISSN : 1477-9137, 0021-9533. DOI : 10.1242/jcs.179077.

[She89] Y. R. SHEN. « Surface properties probed by second-harmonic and sum-frequency generation ». en. In : *Nature* 337.6207 (1989), p. 519-525. ISSN : 0028-0836, 1476-4687. DOI : 10.1038/337519a0.

[Siv+10] Mayandi SIVAGURU, Sushmitha DURGAM, Raghu AMBEKAR, David LUEDTKE, Glenn FRIED, Allison STEWART et Kimani C. TOUSSAINT. « Quantitative analysis of collagen fiber organization in injured tendons using Fourier transform-second harmonic generation imaging ». In : *Optics Express* 18.24 (2010), p. 24983-24993.

[SKK04] Jonas STALHAND, Anders KLARBRING et Matts KARLSSON. « Towards in vivo aorta material identification and stress estimation ». In : *Biomechanics and modeling in mechanobiology* 2 (avr. 2004), p. 169-86. DOI : 10.1007/s10237-003-0038-z.

[Slo] Lutz SLOMIANKA. *Blue Histology - Vascular System*. URL : http://lecannabiculteur.free.fr/SITES/UNIV%5C%20W.AUSTRALIA/mb140/CorePages/Vascular/Vascular.htm. (accessed: 19.05.2021).

[SM17] Shukei SUGITA et Takeo MATSUMOTO. « Multiphoton microscopy observations of 3D elastin and collagen fiber microstructure changes during pressurization in aortic media ». In : *Biomechanics and Modeling in Mechanobiology* 16.3 (2017), p. 763-773.

[Smo+17] Marija SMOLJKIĆ, Heleen FEHERVARY, Philip VAN DEN BERGH, Alvaro JORGE-PEÑAS, Louis KLUYSKENS, Steven DYMARKOWSKI, Peter VERBRUGGHE, Bart MEURIS, Jos VANDER SLOTEN et Nele FAMAEY. « Biomechanical Characterization of Ascending Aortic Aneurysms ». en. In : *Biomechanics and Modeling in Mechanobiology* 16.2 (2017), p. 705-720. ISSN : 1617-7959, 1617-7940. DOI : 10.1007/s10237-016-0848-4.

[So02] Peter T. C. So. *Two-photon light microscopy*. 2002.

[Sob14] Irwin Sobel. « An Isotropic 3x3 Image Gradient Operator ». In : *Presentation at Stanford A.I. Project 1968* (2014).

[Som+10] Gerhard Sommer, Peter Regitnig, Lukas Költringer et Gerhard A. Holzapfel. « Biaxial mechanical properties of intact and layer-dissected human carotid arteries at physiological and supraphysiological loadings ». en. In : *American Journal of Physiology-Heart and Circulatory Physiology* 298.3 (mars 2010), H898-H912. issn : 0363-6135, 1522-1539. doi : 10.1152/ajpheart.00378.2009.

[SR09] N Senthilkumaran et R Rajesh. « Edge Detection Techniques for Image Segmentation – A Survey of Soft Computing Approaches ». In : *INFORMATION PAPER International Journal of Recent Trends in Engineering* 1.2 (2009).

[Ste+08] Andrew M. Stein, David A. Vader, Louise M. Jawerth, David A. Weitz et Leonard M. Sander. « An algorithm for extracting the network geometry of three-dimensional collagen gels ». In : *Journal of Microscopy* 232.3 (2008), p. 463-475.

[Ste99] Aneta Stefanovska. « Physics of the human cardiovascular system ». en. In : *Contemporary Physics* 40.1 (1999), p. 31-55. issn : 0010-7514, 1366-5812. doi : 10.1080/001075199181693.

[Str+07] M. Strupler, A.-M. Pena, M. Hernest, P.-L. Tharaux, J.-L. Martin, E. Beaurepaire et M.-C. Schanne-Klein. « Second harmonic imaging and scoring of collagen in fibrotic tissues ». In : *Optics Express* 15.7 (2007).

[Sur+96] Chitra Suri, Pamela F Jones, Sybill Patan, Sona Bartunkova, Peter C Maisonpierre, Samuel Davis, Thomas N Sato et George D Yancopoulos. « Requisite Role of Angiopoietin-1, a Ligand for the TIE2 Receptor, during Embryonic Angiogenesis ». en. In : *Cell* 87.7 (1996), p. 1171-1180. issn : 00928674. doi : 10.1016/S0092-8674(00)81813-9.

[SW05] Denis Semwogerere et Eric R. Weeks. « Confocal Microscopy ». In : *Encyclopedia of Biomaterials and Biomedical Engineering*. 2005.

[SY06] Karel Svoboda et Ryohei Yasuda. « Principles of Two-Photon Excitation Microscopy and Its Applications to Neuroscience ». en. In : *Neuron* 50.6 (2006), p. 823-839. issn : 08966273. doi : 10.1016/j.neuron.2006.05.019.

[Tan+13] Ryosuke Tanaka, Shu-ichiro Fukushima, Kunihiko Sasaki, Yuji Tanaka, Hiroyuki Murota, Kenji Matsumoto, Tsutomu Araki et Takeshi Yasui. « In vivo visualization of dermal collagen fiber in skin burn by collagen-sensitive second-harmonic-generation microscopy ». In : *Journal of Biomedical Optics* 18.06 (avr. 2013), p. 1. issn : 1083-3668. doi : 10.1117/1.JBO.18.6.061231.

[Tan+14] Soon Yew Tang, James Monslow, Leslie Todd, John Lawson, Ellen Puré et Garret A. FitzGerald. « Cyclooxygenase-2 in Endothelial and Vascular Smooth Muscle Cells Restrains Atherogenesis in Hyperlipidemic Mice ». In : *Circulation* 129.17 (2014), p. 1761-1769.

[TH87] Keiichi Takamizawa et Kozaburo Hayashi. « Strain energy density function and uniform strain hypothesis for arterial mechanics ». en. In : *Journal of Biomechanics* 20.1 (jan. 1987), p. 7-17. issn : 00219290. doi : 10.1016/0021-9290(87)90262-4.

[The+06] Theodossis A. Theodossiou, Christopher Thrasivoulou, Chidi Ekwobi et David L. Becker. « Second Harmonic Generation Confocal Microscopy of Collagen Type I from Rat Tendon Cryosections ». In : *Biophysical Journal* 91.12 (2006), p. 4665-4677.

[Til+14] Karissa Tilbury, James Hocker, Bruce L. Wen, Nathan Sandbo, Vikas Singh et Paul J. Campagnola. « Second harmonic generation microscopy analysis of extracellular matrix changes in human idiopathic pulmonary fibrosis ». In : *Journal of Biomedical Optics* 19.8 (2014).

[Tiz05] Hamid R. Tizhoosh. « Image thresholding using type II fuzzy sets ». In : *Pattern Recognition* 38.12 (2005), p. 2363-2372.

[Tji+14] Gavin Tjin, Paul Xu, Scott H. Kable, Eleanor P. W. Kable et Janette K. Burgess. « Quantification of collagen I in airway tissues using second harmonic generation ». In : *Journal of Biomedical Optics* 19.3 (2014).

[TS11] S Thilagamani et N Shanthi. « A Survey on Image Segmentation Through Clustering ». In : *International Journal of Research and Reviews in Information Sciences* 1 (2011).

[Tsa85] Wen-Hsiang Tsai. « Moment-preserving thresolding: A new approach ». In : *Computer Vision, Graphics, and Image Processing* 29.3 (1985), p. 377-393.

[Tya18] Vipin Tyagi. *Understanding Digital Image Processing*. 1re éd. CRC Press, 2018.

[Ugr+09] N. Ugryumova, J. Jacobs, M. Bonesi et S.J. Matcher. « Novel optical imaging technique to determine the 3-D orientation of collagen fibers in cartilage: variable-incidence angle polarization-sensitive optical coherence tomography ». In : *Osteoarthritis and Cartilage* 17.1 (2009), p. 33-42.

[Van02] Kent M Van De Graaff. *Human anatomy*. English. OCLC: 926911217. Boston; London : McGraw Hill, 2002.

[VG91] Michel Van Der Rest et Robert Garrone. « Collagen family of proteins ». en. In : *The FASEB Journal* 5.13 (1991), p. 2814-2823. issn : 0892-6638, 1530-6860. doi : 10.1096/fasebj.5.13.1916105.

[VH18] Jan Vychytil et Miroslav Holeček. « Development of a constitutive model of soft tissues for FE analyses using a bottom-up approach ». In : *Applied and Computational Mechanics* 12.2 (2018). issn : 1802680X, 23361182. doi : 10.24132/acm.2018.330.

[VYP73] Ramesh N. Vaishnav, John T. Young et Dali J. Patel. « Distribution of Stresses and of Strain-Energy Density through the Wall Thickness in a Canine Aortic Segment ». en. In : *Circulation Research* 32.5 (mai 1973), p. 577-583. issn : 0009-7330, 1524-4571. doi : 10.1161/01.RES.32.5.577.

[Wal+15] Lucy A. Walton, Robert S. Bradley, Philip J. Withers, Victoria L. Newton, Rachel E. B. Watson, Clare Austin et Michael J. Sherratt. « Morphological Characterisation of Unstained and Intact Tissue Micro-architecture by X-ray Computed Micro- and Nano-Tomography ». en. In : *Scientific Reports* 5.1 (2015). issn : 2045-2322. doi : 10.1038/srep10074.

[Weg+17] Kyle A. Wegner, Adib Keikhosravi, Kevin W. Eliceiri et Chad M. Vezina. « Fluorescence of Picrosirius Red Multiplexed With Immunohistochemistry for the Quantitative Assessment of Collagen in Tissue Sections ». In : *Journal of Histochemistry & Cytochemistry* 65.8 (2017), p. 479-490.

[Wen+14] Bruce L. Wen, Molly A. Brewer, Oleg Nadiarnykh, James Hocker, Vikas Singh, Thomas R. Mackie et Paul J. Campagnola. « Texture analysis applied to second harmonic generation image data for ovarian cancer classification ». In : *Journal of Biomedical Optics* 19.9 (2014).

[WM09] Jessica E. Wagenseil et Robert P. Mecham. « Vascular Extracellular Matrix and Arterial Mechanics ». In : *Physiological Reviews* 89.3 (2009), p. 957-989.

[WP88] Hans W. Weizsacker et John G. Pinto. « Isotropy and anisotropy of the arterial wall ». en. In : *Journal of Biomechanics* 21.6 (jan. 1988), p. 477-487. issn : 00219290. doi : 10.1016/0021-9290(88)90240-0.

[Wu+03] J Wu, B Rajwa, D L Filmer et C M Hof Fmann. « Automated BlackwellPublishingLtd. quantification and reconstruction of collagen matrix from 3D confocal datasets ». In : *Journal of Microscopy* (2003), p. 158-165.

[Wu+11] Shulian Wu, Hui Li, Hongqin Yang, Xiaoman Zhang, Zhifang Li et Shufei Xu. « Quantitative analysis on collagen morphology in aging skin based on multiphoton microscopy ». In : *Journal of Biomedical Optics* 16.4 (2011).

[Wu+16] Shulian Wu, Yuanyuan Peng, Liangjun Hu, Xiaoman Zhang et Hui Li. « Classification and recognition of texture collagen obtaining by multiphoton microscope with neural network analysis ». In : *Journal of Physics: Conference Series* 680 (2016).

[Yas+18] Takeshi Yasui, Eiji Hase, Ryosuke Tanaka et Shu-ichiro Fukushima. « In vivo time-series monitoring of dermal collagen fiber during skin burn healing using second-harmonic-generation microscopy ». In : *Biomedical Imaging and Sensing Conference*. Sous la dir. d'Osamu Matoba, Yasuhiro Awatsuji, Yuan Luo, Toyohiko Yatagai et Yoshihisa Aizu. Yokohama, Japan : SPIE, avr. 2018, p. 42. isbn : 978-1-5106-1979-1 978-1-5106-1980-7. doi : 10.1117/12.2316748.

[Yeh+02] Alvin T. Yeh, Nader Nassif, Aikaterini Zoumi et Bruce J. Tromberg. « Selective corneal imaging using combined second-harmonic generation and two-photon excited fluorescence ». In : *Optics Letters* 27.23 (2002).

[YH17] Song Yuheng et Yan Hao. « Image Segmentation Algorithms Overview ». In : *ArXiv* abs/1707.02051 (2017).

[YLP14] Miko Yamada, Lynlee L. Lin et Tarl W. Prow. « Multiphoton Microscopy Applications in Biology ». In : *Fluorescence Microscopy*. Elsevier, 2014, p. 185-197.

[ZBD09] Miroslav Zemanek, Ji˘rı Bur˘sa et Michal D˘etak. « Biaxial Tension Tests With Ssoft Tissues Of Arterial Wall ». en. In : (2009), p. 10.

[Zei+13] Shahrokh Zeinali-Davarani, Ming-Jay Chow, Raphaël Turcotte et Yanhang Zhang. « Characterization of Biaxial Mechanical Behavior of Porcine Aorta under Gradual Elastin Degradation ». In : *Annals of Biomedical Engineering* 41.7 (2013), p. 1528-1538.

[Zei+17] Angel A. Zeitoune, Luciana A. Erbes, Victor H. Casco et Javier F. Adur. « Improvement of co-occurrence matrix calculation and collagen fibers orientation estimation ». In : *12th International Symposium on Medical Information Processing and Analysis*. Sous la dir. d'Eduardo Romero, Natasha Lepore, Jorge Brieva, Jorge Brieva et Ignacio Larrabide and. T. 10160. International Society for Optics et Photonics. SPIE, 2017, p. 381-389.

[Zha20] Yanhang Zhang, éd. *Multi-scale Extracellular Matrix Mechanics and Mechanobiology*. T. 23. Studies in Mechanobiology, Tissue Engineering and Biomaterials. Switzerland : Springer, 2020.

[Zho+17] Zhi-Hua Zhou, Cheng-Dong Ji, Hua-Liang Xiao, Hai-Bin Zhao, You-Hong Cui et Xiu-Wu Bian. « Reorganized Collagen in the Tumor Microenvironment of Gastric Cancer and Its Association with Prognosis ». In : *Journal of Cancer* 8.8 (2017), p. 1466-1476.

[Zon04] Anders E. Zonst. *Understanding the fast Fourier transform*. Titusville, Florida : Citrus press, 2004.

[Zun] Hasib Zunair. *3D image classification from CT scans*. https://keras.io/examples/vision/3D_image_classification/. Accessed: 2021-12-03.

[ZWW03] Warren R Zipfel, Rebecca M Williams et Watt W Webb. « Nonlinear magic: multiphoton microscopy in the biosciences ». en. In : *Nature Biotechnology* 21.11 (2003), p. 1369-1377. issn : 1087-0156, 1546-1696. doi : 10.1038/nbt899.

[Zya+17] Mariya Zyablitskaya, Anna Takaoka, Emilia L. Munteanu, Takayuki Nagasaki, Stephen L. Trokel et David C. Paik. « Evaluation of Therapeutic Tissue Crosslinking (TXL) for Myopia Using Second Harmonic Generation Signal Microscopy in Rabbit Sclera ». In : *Investigative Opthalmology & Visual Science* 58.1 (2017).

École Nationale Supérieure des Mines
de Saint-Étienne

NNT: 2022LYSEM016

Author: Zeineb Nejim

Title: 3D microscopy image analysis: from image enhancement to quantitative analysis of arterial tissues

Speciality: Sciences of images and patterns

Keywords: Second harmonic generation, collagen fibers, orientation estimation, image enhancement

Abstract

The human body is a complex structure composed of multiple cells, organs and tissues. The cardiovascular system is responsible of transferring nutrients and oxygen to all the body and the aorta plays an essential role. The upper portion of the aorta, called ascending thoracic aorta, is a critical section since it has to support the high pressure blood pumped by the heart. This is made possible thanks to the micro-structure of the aortic wall, mainly composed of fibers (collagen and elastin). With aging, changes may occur on the aortic micro-structure and may cause some diseases such as aneurysms. Studying this microstructure is helpful to understand its functions. To this end, several imaging modalities were used in the literature especially the multi-photon microscopy and Second Harmonic Generation (SHG) because of its good resolution in 3D. However, SHG images may present some artifacts such as noise in addition to some discontinuities on certain fibers. The study of this micro-structure is based on the quantitative analysis of acquired 3D images in order to extract information related to the geometry and the morphology of collagen fibers as well as the composition of the considered specimen.

The goal of this thesis is, in the first place, to enhance 3D second harmonic generated images of collagen fibers in order to make them more suited for a potential quantitative analysis. To this end, a combination of a 3D directional filter (to deal with fibers discontinuities) and a 1D and a 3D top-hat transforms (to reduce the noise) is proposed. The second part of this thesis is focused on the quantitative analysis of these images and in particular, orientations' estimation of collagen fibers in the 3D space. A new approach based on deep learning is introduced. A dataset of 3D images of synthetic fibers is developed to ensure the learning phase of the proposed neural network.

École Nationale Supérieure des Mines
de Saint-Étienne

NNT: 2022LYSEM016

Auteur: Zeineb Nejim

Titre: Analyse d'images de microscopie 3D : de l'amélioration des images à l'analyse quantitative des tissus artériels

Spécialité: Sciences des images et des formes

Mots-Clefs: Génération de seconde harmonique, fibres de collagène, estimation d'orientation, amélioration d'image

Résumé

Le corps humain est une structure complexe composée de plusieurs cellules, tissus et organes. Le système cardiovasculaire est responsable du transfert de l'oxygène et des nutriments vers tout le corps et l'aorte y joue un rôle essentiel. La portion supérieure de l'aorte, appelée aorte thoracique ascendante, est assez critique puisqu'elle doit supporter la pression élevée du sang pompé par le cœur. Ceci est possible grâce à la micro-structure de l'aorte qui est principalement composée de fibres (collagène et élastine). Cependant, avec le vieillissement, des changements peuvent toucher cette micro-structure et causer des pathologies comme les anévrismes. L'étude de cette micro-structure est nécessaire pour comprendre ses fonctions. Ceci est possible grâce à plusieurs modalités d'imagerie notamment la microscopie à deux photons et la génération de seconde harmonique puisqu'elle offre une bonne résolution en 3D. Cependant, les images collectées peuvent présenter plusieurs artéfacts comme du bruit et des discontinuités au niveau de quelques fibres. L'étude de cette micro-structure est basée sur l'analyse quantitative des images acquises afin d'extraire des informations relatives à la géométrie et la morphologie des fibres ainsi que la composition du spécimen considéré.

Cette thèse a pour objectif, en premier lieu, d'améliorer des images 3D de seconde harmonique de fibres de collagène afin de les rendre exploitables pour une éventuelle analyse quantitative. Pour se faire, une combinaison d'un filtre directionnel 3D (pour remédier au problème de discontinuité) et de transformées "top-hat" à une et trois dimensions (pour réduire le bruit) est proposée. En second lieu, l'intérêt est porté sur l'analyse quantitative de ces images et en particulier l'estimation de l'orientation des fibres de collagène dans l'espace 3D. Une nouvelle approche basée sur l'apprentissage profond est présentée. Une base de données contenant des images 3D de fibres synthétiques est développée pour assurer la phase d'apprentissage du réseau de neurones proposé.

ÉCOLE DES MINES DE SAINT-ÉTIENNE
158, cours Fauriel – CS 62362
42023 Saint-Étienne Cedex 2 – France
Tél. +33(0)4 77 42 01 23
www.mines-stetienne.fr